Lawrence Berkeley National Laboratory
Recent Work

Title
The Synthesis, Characterization and Catalytic Reaction Studies of Monodisperse Platinum Nanoparticles in Mesoporous Oxide Materials

Permalink
https://escholarship.org/uc/item/1ff6v4td

Author
Rioux, Robert M.

Publication Date
2006-01-15

The Synthesis, Characterization and Catalytic Reaction Studies of Monodisperse
Platinum Nanoparticles in Mesoporous Oxide Materials

by

Robert M. Rioux

B.S. (Worcester Polytechnic Institute) 1999
M. S. (The Pennsylvania State University) 2001

A dissertation submitted in partial satisfaction of the

requirements for the degree of

Doctor of Philosophy
in

Chemistry

in the

GRADUATE DIVISION

of the

UNIVERSITY OF CALIFORNIA, BERKELEY

Committee in charge:

Professor Gabor A. Somorjai, Chair
Professor Herbert L. Strauss
Professor Kyriakos Komvopoulos

Spring 2006

The dissertation of Robert M. Rioux is approved:

_____

Professor Gabor A. Somorjai, Chair   Date

_____

Professor Herbert L. Strauss   Date

_____

Professor Kyriakos Komvopoulos   Date

University of California, Berkeley

Spring 2006

The Synthesis, Characterization and Catalytic Reaction studies of Monodisperse Platinum
Nanoparticles in Mesoporous Oxide Materials

Abstract

The Synthesis, Characterization and Catalytic Reaction studies of Monodisperse Platinum

Nanoparticles in Mesoporous Oxide Materials

by

Robert M Rioux

Doctor of Philosophy in Chemistry

University of California, Berkeley

Professor Gabor A. Somorjai, Chair

A catalyst design program was implemented in which Pt nanoparticles, either of

monodisperse size and/or shape were synthesized, characterized and studied in a number

of hydrocarbon conversion reactions. The novel preparation of these materials enables

exquisite control over their physical and chemical properties that could be controlled (and

therefore rationally tuned) during synthesis. The ability to synthesize rather than prepare

catalysts followed by thorough characterization enable accurate structure-function

relationships to be elucidated. Pt nanoparticles (1.7-7.1 nm) are synthesized by solution

phase reduction methods in which Pt precursors are reduced in protic solvents in the

presence of a surface templating polymer, which serves to stabilize the metal

nanoparticles in solution. Particle size can be controlled during synthesis by altering

either the PVP: Pt salt ratio, reaction media and by seeded growth methods. After Pt

nanoparticles are synthesized, their size and morphology are confirmed with transmission

electron microscopy and x-ray diffraction. Low power sonication in either aqueous or

organic solvent was utilized to disperse Pt nanoparticles within the mesoporous metal oxide matrix. This method of catalyst synthesis is named capillary inclusion (CI). An alternative approach to catalyst synthesis combines the hydrothermal synthesis of mesoporous silica with Pt nanoparticle synthesis in the same solution. Synthesis under neutral conditions led to a catalyst in which the nanoparticles were highly dispersed throughout the catalyst matrix. This method of catalyst synthesis called nanoparticle encapsulation (NE) ensured that Pt nanoparticles were located on the internal pore surface of the mesoporous silica. Catalysts were characterized by transmission electron microscopy (TEM), x-ray diffraction (XRD), small angle x-ray scattering (SAXS) and physical adsorption to determine metal particle size and mesoporous structure. The surface chemistry of the nanoparticle surface was studied by infrared spectroscopy, selective gas adsorption (chemisorption) and catalytic reactivity studies. During nanoparticle synthesis, PVP is added to the solution to stabilize the platinum nanoparticles against aggregation. This polymer remains bound to the nanoparticle surface after catalyst synthesis and must be removed before catalytic reactions. Calcination of the catalyst at high temperature (623-723 K) for long time periods (24-36 hours) followed by reduction was initially used to clean the Pt surface. While calcination-reduction treatment is a standard procedure for catalyst activation, the need for long treatments was due to the high molecular weight (~55,000) of the surface-stabilizing polymer. Polymer removal was confirmed by selective gas adsorption, infrared spectroscopy investigation of CO adsorption as well as ethylene hydrogenation. Metallic surface area determined by chemisorption was not in agreement with XRD or TEM results and turnover rates for ethylene hydrogenation results were lower than those

measured on classically prepared heterogeneous catalysts. Particle sizes measured by chemisorption were larger than determined by XRD or TEM suggesting that PVP or carbon still covered a fraction of the Pt surface or was inaccessible to gas adsorption due to Pt encapsulation in amorphous silica plugs. An alternative approach to catalyst activation employed *in-situ* cyclic oxidation-reduction pretreatments. Calcination of small catalyst samples for short times (~ 1h) followed by reduction at the same temperature was more effective at polymer removal than calcination of large catalyst quantities as it avoids possible readsorption of volatile organic fragments. Cyclic oxidation reductions (up to five cycles) at temperatures between 373 and 673 K had metal surface areas up to 5 times higher than samples calcined for long times as verified by ethylene hydrogenation.

Catalysts with monodisperse particles and platinum surface areas of ~ 1 m^2 g^{-1} catalyst were active for several hydrocarbon conversion reactions. The structure sensitive, ethane hydrogenolysis reaction was studied over both the CI and NE catalyst series as a function of particle size. The rate of ethane hydrogenolysis was structure sensitive on both catalysts, although the NE series showed a two order of magnitude difference in rate (methane formation) as the particle size was varied from 1 to 7 nm, while the rate on the CI catalyst only varied by a factor of two over the same size range. Apparent activation energies for both catalysts varied considerably. Both catalyst series demonstrated partial pressure dependencies on ethane and hydrogen that were indicative of the rate-determining step being the cleavage of the C-C bond of a highly hydrogenated intermediate. Higher rates were observed on smaller particles for both catalyst series and

were attributed to coordinatively unsaturated metal atoms which are more prevalent in smaller particles.

The influence of particle size on selectivity was examined with cyclohexene hydrogenation/dehydrogenation. Under excess hydrogen, the hydrogenation of cyclohexene to cyclohexane is favored at low temperatures, while the dehydrogenation of cyclohexene to benzene is favored at higher temperatures. Selectivity to either product is controlled by kinetics of the heterogeneous reaction, not by thermodynamics. Reaction studies on Pt single crystals suggest that selectivity can be influenced by surface structure. On a series of ~1 % Pt/SBA-15 catalysts, benzene selectivity decreases with increasing particle size at comparable conversion levels and reaction temperature. Increased apparent activation energies for benzene formation are observed as the particle size is increased. At particle sizes greater than ~ 7 nm, there is no change in apparent activation energy for dehydrogenation and selectivity to benzene remains constant.

The influence of particle size on the poisoning of ethylene hydrogenation by low pressures (0.1-1 Torr) of carbon monoxide was examined. Introduction of CO led to a decrease in turnover frequency of six orders of magnitude at 0.5 Torr CO when compared to the unpoisoned reaction. Reaction orders in C_2H_4 and H_2 were 1st order and ½ order, respectively, while CO inversely inhibits the reaction. The increase in C_2H_4 reaction order from zero in the unpoisoned reaction to 1st order in the poisoned reaction suggested that CO and C_2H_4 competed for the same sites on the catalyst surface. Volumetric adsorption and infrared spectroscopy studies of sequential and co-adsorption of CO and C_2H_4 at 298 and 413 K confirmed that adsorption was competitive. Ethylene adsorption was reduced to greater extent on a CO covered surface than CO adsorption on an

ethylidyne-covered surface. It was observed that ethylidyne formed on a CO covered surface at a surface concentration significantly lower than that of a clean surface. It was determined that the bonding of CO was only slightly perturbed by the presence of coadsorbed ethylene and the particle size had little influence on the extent of CO poisoning. All particle sizes were poisoned to the same extent.

The addition of surface templating polymer and Pt precursors to refluxing ethylene glycol solutions containing small amounts of sacrificial metal ions led to the growth of Pt nanoparticles with different shapes. The ratio of Ag ions to Pt ions in solution led to selective growth of Pt nanoparticles with shape selectivity $\geq$ 80% in all cases. The addition of 1.1 mol. % AgNO$_3$ (relative to Pt salt concentration) led to the formation of cubes, while 11 mol. % led to the exclusive formation of cuboctahedra. Increasing the silver concentration up to 32 mol. % led to the formation of octahedra, particles terminated entirely by (111) surfaces. The cubes are terminated by (100) surfaces, while cuboctahedra terminate with both surfaces. The addition of silver ion enhances the crystal growth rate along the <100> direction and ultimately determines the shape and surface structure of the Pt nanoparticles. These nanoparticles were encapsulated in mesoporous silica by the NE method and surfaces cleaned by low temperature oxidation-reduction cycles. Catalysts were activated at low temperatures in order to avoid changes in Pt nanoparticle surface structure. All Pt nanoparticles contained ppm levels of Ag, levels significantly lower than the starting synthetic concentrations. The catalysts are active for ethylene hydrogenation and are promising materials for future studies on the influence of catalyst particle shape on reaction selectivity during the low temperature catalytic reactions. The hydrogenation of α,β

unsaturated aldehydes, such as crotonaldehyde and cinnamaldehyde were chosen as probe reactions for Pt cubes, cuboctahedra and octahedra. Surface science studies and particle size dependent reaction studies have demonstrated that (111) surfaces are more selective for carbonyl bond hydrogenation, while (100) and highly corrugated surfaces hydrogenate both the C=C and C=O double bond.

This thesis emphasizes all three aspects of catalyst design: synthesis, characterization and reactivity studies. The precise control of metal nanoparticle size, surface structure and composition may enable the development of highly active and selective heterogeneous catalysts.

Dedicated to Lincoln H. Randall

Table of Contents

List of Figures

List of Tables

Acknowledgements

First and foremost, I would like to thank my advisor, Professor Gabor A. Somorjai for his guidance throughout the years. I came to Berkeley with the intention of working for Professor Somorjai. One of his first pieces of advice was to visit with the other Berkeley chemistry professors because Berkeley is a place full of amazing science. He certainly was right and in the end (and the reason why you are reading this) I decided to join Professor Somorjai's group. His enthusiasm and love for science is truly amazing. I have learned as much about life as science from him. He has always supported me in my efforts inside and outside of laboratory. Professionally, he has been my biggest supporter and for this I am most grateful. I would also like to thank his wife, Mrs. Judy Somorjai, who has been very supportive of me and my wife, Julie during our time at Berkeley. She is truly a wonderful woman.

I need to thank my former undergraduate advisor and friend, Professor Fabio H. Ribeiro. You have always believed in me and helped me along every step of the way. The three years I spent your lab have had the biggest impact on my scientific career. Now that this thesis is finished, I hope we can finish the hydrodechlorination review!!! Professor M. A. Vannice of Pennsylvania State University deserves a thank you for understanding my reason for leaving Pennsylvania for Berkeley. He has supported me my entire time while at Berkeley. I wish him a happy and healthy retirement.

The Somorjai machine is kept running by none other than Ms. Inger Coble, the most dedicated administrative assistant and surrogate mother while at Berkeley. I had the opportunity to spend a large amount of time on campus and get to know her and her son,

Tommy, a future major league baseball player, maybe? Her patience and acceptance of all those green purchase order sheets is much appreciated. I hope our paths cross again in some capacity.

During my third year at Berkeley I received the Ford Catalysis Fellowship administered by the Berkeley Catalysis Center. I would like to thank Ford Motor Company for sponsoring the fellowship. Thank you to Dr. Robert McCabe from Ford Motor for the award and Professor Enrique Iglesia, director of the Berkeley Catalysis Center for supporting this fellowship.

The Somorjai group is large and there are so many to thank. There are a few Somorjai group members that I would like to thank in particular. I've made two very good friends in Berkeley; James Hoefelmeyer and David Chi-Wai Tang. I thank James Hoefelmeyer (Professor Hoefelmeyer, I mean) for his all his help in the laboratory. We spent many late nights and weekends in the lab trying to meet deadlines and figure out why things weren't working. The memory of that one very eventful night at The Ivy Room will never be forgotten. David Tang is a funny guy, who morphed into someone else after four years of graduate school or was because of four years of Berkeley. One will never know? Thanks for all the trips to Club Mallard and Barclays; they made graduate school a heck of a lot of fun. I have to thank Aric Opdahl, one of the first people I met in the Somorjai group. I wish him well as a professor at the University of Wisconsin, Lacrosse. Special thanks to the Berkeley-Szeged connection, Professors Imre Kirisci and Zoltan Kónya for starting the nanocatalyst project and laying the groundwork on which I built upon. The last of the Berkeley-Szeged connection, Dr. Krisztian Niesz has been a valuable asset to the Somorjai group and he and his wife, Agi have become

great friends. Other nanocatalyst coworkers worthy of thanks are Dr. Changxi Miao, Dr. Hyunjoon Song, Susan Habas and the newest member of the Somorjai group to join the project, Michael Grass. Michael, you are now the leader of the project and I can wish you the best of luck with the Quantachrome. Other members of the Somorjai group which I need to thank our Dr. Yuri Borodko, Dr. Keng Chou, Dr. Mike Ferguson, Dr. Lucio Flores, Dr. Jessica (Parker) Gaughan, Dr. Jeff Grunes, Sasha Kweskin, Dr. Telly Koffas, Dr. Andy Marsh, Dr. Keith McCrea, Dr. Minchul Yang, Roger "no clothes" York and of course Anthony Contreras. I wish him and his family the best of luck in the future and I hope that we don't lose contact. Thanks to Dr. Christian Mohr and his extremely hip wife, Silvana for their friendship. I promise Julie, Lincoln and I will visit Germany very soon. There are so many other fellow students and colleagues to thank at Berkeley; Libby, Jennifer, Andy, Morgan, Tim, Howard, Patty, Bjorn, Mark, Ian, Elon, Alex, and Henry to name a few.

Thanks to Dr. Yadong Yin and Professor Alivisatos including me in the coreshell work which was eventually published in Science! I also have the opportunity to work and learn from Professor T. D. Tilley which I sincerely enjoyed. Thanks to his graduate student, Dan Ruddy for involving me in his single site Pt project.

While I was at Berkeley, I was able to work with two great Berkeley chemical engineering undergraduate students, Bryan Hsu and Russ Komor. We had quite a few good times in the lab and a few more outside the lab. Bryan, you persevered through the summer and <u>almost</u> got the campus UHV chamber working. Congratulations and good luck in graduate school, wherever that may be. If you come to Boston, look me up.

months until Mr. Jim Breen replaced him. Jim is one of the nicest guys I've ever met. I wish him the best of luck and hope we stay in touch after my time in Berkeley has ended. Thanks to Sue Gettinger, administrative assistant for the machine shop for hours of great conversation about folk music and for keeping me abreast of the Bay Area folk music scene. Henry Chan and Steve Hoagland in the electronic shop deserve mention for all their help building boxes, repairing boxes and teaching me a lot about electronics. Mike Brateng and the eclectic bunch of guys in the wood shop need to be thanked for always having Unistrut$^®$ pieces in stock and their willingness to cut it on demand. The Somorjai group had an arsenal of broken vacuum pumps, many thanks to Yi-Min Hsieh for their repair and the many electrical issues he fixed in our campus laboratories.

I would like to thank my family for all their support. Life in Berkeley hasn't always been smooth sailing but I knew that I always had the support of my family, which I am very grateful for. Mom and Dad, it's finally over and now I can get a real job and stop borrowing money from you. Well, not a real job quite yet, its time to postdoc. I want to thank my sister, her husband and my nephew and niece, Bobby and Emily. Thanks to Pat, Ed and Marty and the rest of Julie's family for their support.

To my wife, Julie Meiser thanks for everything you did for me and us while living in Berkeley. I will always appreciate your understanding of how important this has been to me. We became parents while writing this thesis. Our new baby, Lincoln Daniel is the greatest thing that has happened in either of our lives and officially makes us a family. I am lucky to have such a wonderful family.

Lincoln Daniel Meiser-Rioux
9.22.05

To the future, as my family and I move onto Cambridge, MA for a postdoctoral position with Professor George Whitesides, I say thank you to all in Berkeley and I hope to see y'all real soon.

Chapter 1

Introduction

1.1 Implications of catalyst structure on the kinetics (activity, selectivity) of heterogeneous catalytic reactions

The influence of particle size on the activity and selectivity of heterogeneous catalytic reactions has been studied for over 70 years. Early attempts to approach this problem were made by Kobosev and co-workers [1-3] in the 1930s from the viewpoint of atomic dispersion and active ensembles. They studied the behavior of catalysts containing very small amounts of supported metal and were able to derive the number of atoms within the ensembles that were active for specific reactions (for example, one atom for SO_2 oxidation, 2 atoms for benzene hydrogenation, and 3 atoms for ammonia synthesis). The first comprehensive study of the relationship between particle size and catalytic activity was by Boreskov *et al*. [4, 5]. They showed that the specific activity of platinum in the oxidation of sulfur dioxide and hydrogen varied by less than one order of magnitude for catalyst samples differing in platinum surface area by four orders of magnitude. This observation is in agreement with Kobosev's observations of SO_2 oxidation. Kobosev's ideas were further investigated and tested by Poltorak and Boronin [6] on highly dispersed metals who demonstrated rates for certain reactions varied little with large changes in metal surface area. Their studies led to many of the same

conclusions reached independently by Boudart *et al.* [7] for the hydrogenolysis of cyclopropane. They showed that the rate per unit surface area of metal seemed for certain catalytic reactions is insensitive to the degree of dispersion of the metal. Boudart called these reactions facile or structure insensitive [8]. The term structure refers to the coordination number of surface atoms that can be varied by exposing different crystallographic planes and making them imperfect by means of introducing steps and kinks or by varying the particle size of supported metals.

Apparent exceptions to the insensitivity of particular reactions to changes in particle size were also observed. Boreskov *et al.* [9] observed that the low temperature H_2-D_2 exchange was sensitive to the size of the platinum nanoparticles. Other examples of the sensitivity of specific activity to particle size were reported later on. Hydrogenolysis of ethane was found to depend on particle size on both Ni and Rh systems [10, 11]. In the former case, the catalytic activity per unit surface area decreased with increasing particle size, whereas with the latter, an optimum particle size was associated with a maximum specific activity. There reactions were called "demanding" or structure sensitive by Boudart [8]. Numerous observations of the influence of particle size on the specific catalytic activity for various reactions have led to the classification of reactions into four distinct categories depending on how the turnover frequency (TOF, the rate of reaction expressed in moles per exposed metal atom per unit time) varies as a function of the particle size, *d*, as shown in Figure 1. The TOF of structure insensitive reactions does not depend on the particle size (curve 1). The TOF of structure sensitive reactions can vary in two opposite ways with particle size: it decreases when the particle size decreases (*i.e.* larger particles are more active than small particles). This is termed a

negative particle size effect of antipathetic structure sensitivity (curve 2); or it may increase for decreasing particle sizes, *i.e.*, smaller particles are more active than larger ones. This is called a positive particle size effect or sympathetic structure sensitivity (curve 4). The TOF may go through a maximum (curve 3), in which particles of intermediate size will have maximum specific activity.
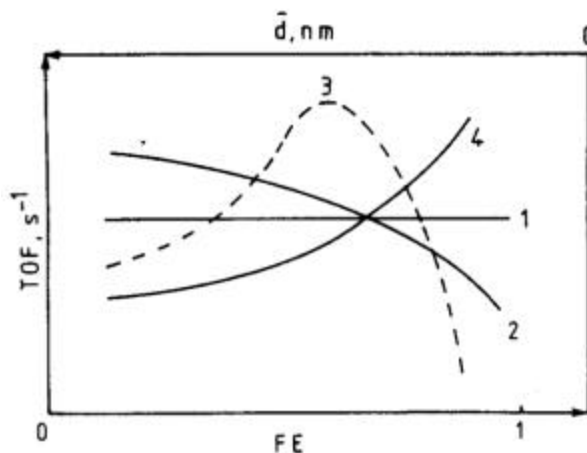
Figure 1.1. Variations of turnover frequency with particle size. From ref. [12].

The study of low pressure (ultrahigh vacuum (UHV)) catalytic phenomena on well defined transition metal single crystals has enabled a vast compilation of literature documenting the influence of surface structure on adsorption, surface reaction and desorption [13]. While these experiments have provided tremendous insight into nature of adsorbate-surface interactions, the extrapolation of these low pressure results to high pressure conditions of industrial catalytic processes for interpretive purposes has been met with skepticism. This difference in pressure has been termed the "pressure gap" of UHV surface science. The pioneering studies by Professors G. A. Somorjai [14] and G. Ertl [15] of catalytic phenomena on transition metal single crystal surfaces under high

pressure reaction conditions coupled with *ex-situ* low pressure characterization before and after reaction by electron and ion based techniques has closed the "pressure gap" and defined a new area of science, high pressure surface science. The first apparatus for studying high pressure (atmospheric) reactions on single crystals was designed by Somorjai and co-workers in 1976 in which they studied the hydrogenolysis of cyclopropane on a stepped Pt single crystal [16]. Their results were significant because they agreed with Boudart's hypothesis that this reaction was structure-insensitive when studied over a series of Pt/Al$_2$O$_3$ catalysts with varying dispersion [7]. One of the most well-studied examples of a structure sensitive reaction is ammonia synthesis from N$_2$ and H$_2$, *i.e.* N$_2$ +3H$_2$ $\rightarrow$ 2NH$_3$. Studies of ammonia synthesis on Fe/MgO catalysts with varying particle size (1 – 30 nm) demonstrated that the rate of ammonia synthesis increased with particle size (measured by chemisorption) [17]. Figure 2 demonstrates that the rate of ammonia production varies by four orders of magnitude over the stated particle size range.
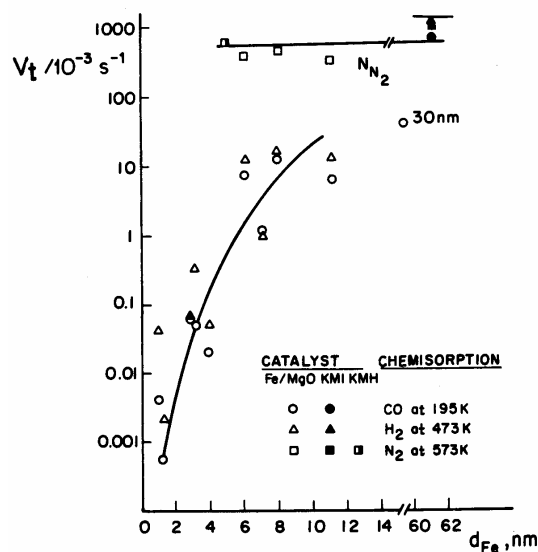
Figure 1.2. Ammonia synthesis turnover frequency versus Fe particle size at 673 K, atmospheric pressure, stoichiometric mixture. From ref. [17].

Figure 2 unequivocally demonstrates (after rejection of catalytic activity decrease due to metal-support interaction influence on the small iron particles) that the surface atoms or sites involved in ammonia formation become more abundant as the cluster size grows. Since these are clusters with ill-defined crystallographic planes (*i.e.* single crystals), it is better to describe the surface structure in terms of the number of surface atoms, C_i with coordination number, *i*. Numerous observations by Boudart and coworkers have shown that the chemical and physical properties of Fe clusters change with particle size which suggested that the surface concentrations of C_7 sites increased with cluster size and are therefore responsible for higher activity in ammonia synthesis [18]. The fraction of C_7 sites on the surface of bcc metals with different atomic arrangement is shown in Figure 3.
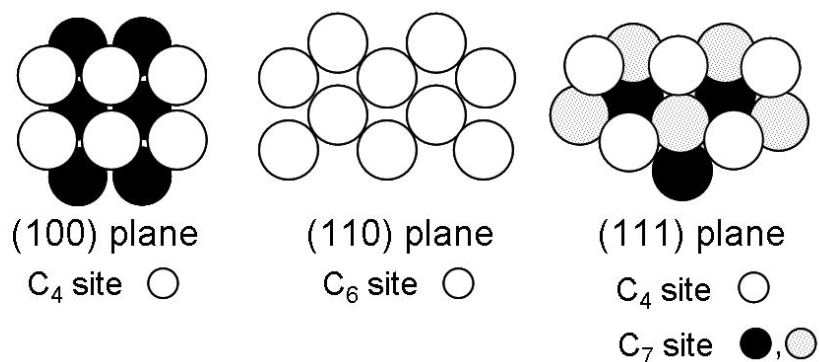
Figure 1.3. Relationship between C_i and low Miller index planes of a body-centered cubic lattice. From ref. [18].

Figure 3 demonstrates that the Fe(111) surface has the highest fraction of surface atoms with C_7 coordination. In fact, Brill *et al.* [19] found that the (111) plane of iron is preferentially formed upon exposure of the (110) and (100) planes of iron to nitrogen at 673 K. Since the (111) plane of a bcc metal, such as iron, has a high concentration of C_7, atoms (Fig. 3), the results of Boudart agrees well with those of Brill *et al.* Shortly after Boudart published his series of papers on the structure sensitivity of ammonia synthesis

on supported Fe particles, Somorjai and co-workers [20] demonstrated that the rate of ammonia synthesis was structure sensitive on series of Fe single crystals. Specifically, at 20 atm., the relative areal rates of ammonia synthesis on the (111), (100) and (110) planes of Fe at 798 K were 418, 25 and unity, respectively. Later studies by Somorjai over five Fe single crystals with differing surface structure again confirmed that the (111) and (211) surface were most active for ammonia synthesis [21].
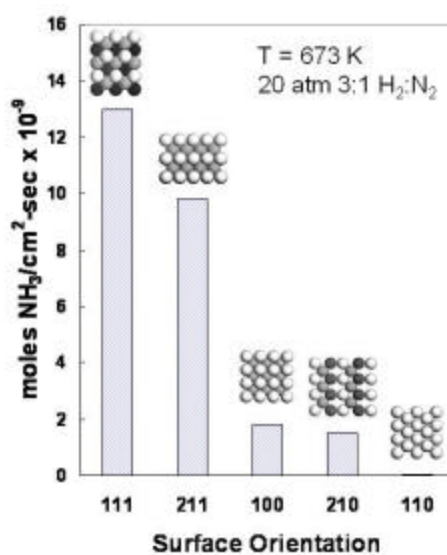
Figure 1.4. Rate of ammonia synthesis over the five surfaces studied exhibiting the structure sensitivity of the reaction. From ref. [21].

Ammonia synthesis is the most documented study of the influence of surface structure (and therefore particle size) on the rate of a catalytic reaction but many others have been documented [12, 22].

There are also a number of examples demonstrating the influence of particle size on reaction selectivity. The role of particle size on the selectivity to cyclohexane and benzene during the hydrogenation/dehydrogenation of cyclohexene is presented in Chapter 8. The selectivity of Co based Fischer-Tropsch catalyst has been studied as a

function of particle size [23]. Larger particles favor a higher production of larger hydrocarbons (C_n, $n \geq 6$). Isomerization of *n*-pentane is favored over Pt/SiO_2 catalysts with larger particles, while smaller particles favor hydrogenolysis [24]. Particle size was also shown to influence selectivity during the hydrogenation of α,β unsaturated aldehydes (*i.e.* crotonaldehyde), with larger particles more selective for the formation of the unsaturated alcohol, requiring preferential hydrogenation of the C=O group over the C=C double bond [25, 26]. Conversely, Mohr *et al*. [27] have shown that the edges of single crystalline gold particles are the active sites for the preferred C=O hydrogenation in acrolein suggesting that smaller particles with a greater number of edge sites are more selective for the unsaturated alcohol. Reaction studies on Pt single crystals have shown that close-packed planes such as Pt(111) are selective for C=O bond hydrogenation, while corrugated surfaces such as Pt(110) are more selective for hydrogenation of the conjugated C=C bond of 3-methylcrotonaldehyde [28]. The number of examples of particle size selectivity correlations is fewer in number compared to particle size-activity correlations but it is apparent that such correlations exist and will become better defined as catalyst structures are synthesized with more uniform properties.

1.2   Explanations of particle size effect: Electronic versus geometric

Two general ideas have been proposed to explain the influence of particle size on catalytic activity. Both electronic and geometric effects have been proposed to be responsible, but in most cases, electronic and geometric effects cannot be decoupled from one another.

Nanoparticles are larger than clusters and show properties that differ between the molecular and the bulk. A significant fraction of the total number of atoms in a

nanostructure are coordinatively unsaturated with respect to the equilibrium bulk structure. These coordinatively unsaturated sites exhibit local electronic structures that are decoupled from the band structure of the interior [29]. The electronic structure of a nanoparticle depends critically on its size. For small particles, the electronic energy levels are not continuous as in bulk materials, but discrete, due to the confinement of the electron wavefunction because of the physical dimensions of the particle (Figure 5) [30].
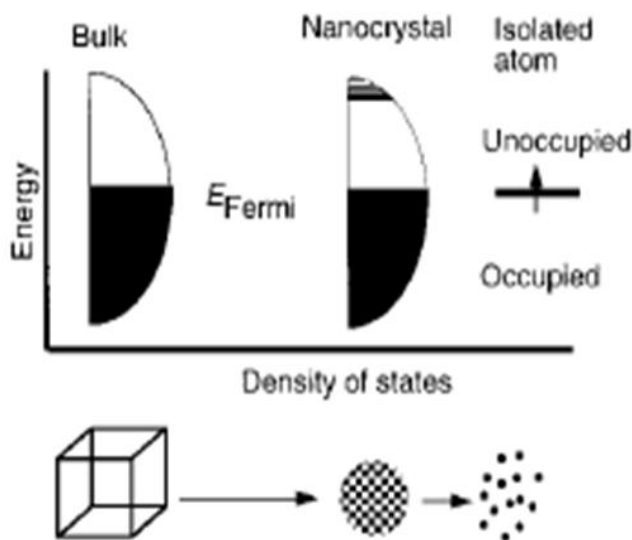
Figure 1.5. Density of states for a metal nanoparticle compared with bulk and isolated atom. The Fermi level, E_f, is at the center of the band in a metal, and kT may exceed the electronic energy level spacings even at room temperature or small sizes. From ref. [30].

The average energy spacing of the successive quantum states, δ at the band edge is known as the Kubo gap [31] and is given by $\delta = 4E_f/3n$, where E_f is the Fermi energy of the bulk material and n is the total number of valence electrons in the nanoparticle. At low enough temperatures and small enough particle sizes, $\delta \approx k$T, the nanoparticle will demonstrate non-metallic behavior. Consequently, an energy gap exists between the valence and conduction bands with its width depending on the number of valence

electrons in the nanostructure [29]. This size effect on the integral electronic structure is significant for small clusters with a few atoms but the band gap vanishes at 300 K for nanostructures comprised of ~300 atoms. The closure of the band gap has been predicted from photoelectron spectroscopic measurements of Hg_n nanoparticles (n = 3 to 250) in the gas phase to ~ 400 atom nanoparticles. The HOMO-LUMO (s–p) energy gap decreases gradually from ~ 3.5 eV for n = 3 to ~ 0.2 eV for n = 250 [32]. Extensive investigations of metal nanoparticles (Au, Ag, Pd, Ni, Cu) of various sizes by X-ray photoelectron spectroscopy (XPS) have shown that as the metal particle size decreases, the core level binding energy of the metal increases sharply by over 1 eV (23 kcal mol^{-1}) at small size [33]. This is shown for Au particles deposited on NaCl (Figure 6) [34].
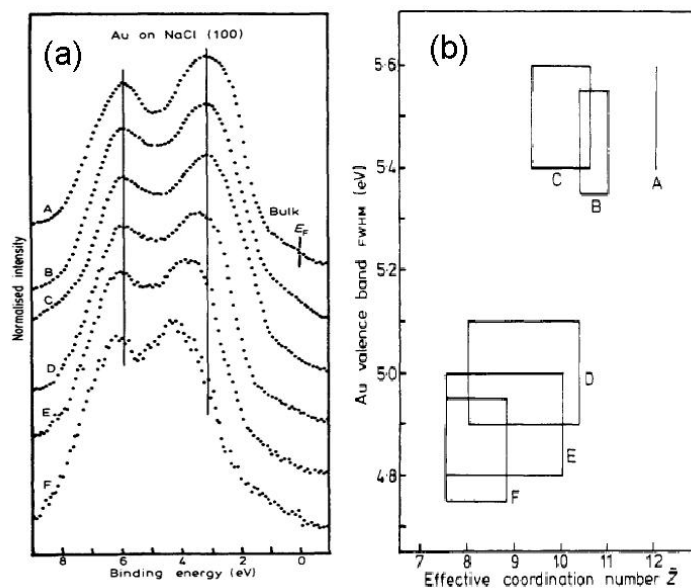
Figure 1.6. (a) XPS spectra of Au valence band and (b) Full width at half maximum (FWHM) of the Au valence band as function of effective coordination number. (A) bulk metal, (B) 60, (C) 40, (D) 30, (E) 25, and (F) 15 Å clusters. From ref. [34].

The variation in binding energy is negligible at larger particle sizes and similar to the bulk metal. The increase in the core-level binding energy in small particles occurs due to

the poor screening of the core-hole and is a manifestation of the size-induced metal–nonmetal transitions in nanocrystals. Thus, a variation in the catalytic properties of small particles would be expected because of this electronic effect. The width of the valence band is related to the effective coordination number of the atoms in the cluster. For example, for clusters of 6 and 4 nm, although they have reduced coordination number (10 relative to 12 for bulk samples), these nanoparticles behave like bulk Au atoms, while the decrease in size demonstrates that width of the valence band decreases and the whole particle is electronically perturbed (Figure 6).

However, the situation is complicated because the proportion of the total atoms present on the surface changes with particle size and the coordination sphere with respect to other metal atoms will also change. The electronic configuration of these surface atoms is changed, leading to changes in catalytic properties. This second electronic effect may be viewed as having a geometric origin, so that the usual division of size effects is somewhat arbitrary. Most catalytic reactions occur at temperatures above 300 K, therefore it is believed that modification of the average ground state electronic structure is in most cases not responsible for the enhanced catalytic activity seen on nanostructures [29].

Hartog and van Hardeveld [35] have developed mathematical models describing the arrangement of atoms within the crystallites. An example of a face centered cubic (fcc) octahedron is shown in Figure 7. Figure 7 demonstrates that three types of surface atoms are identified on an octahedron. The symbol, C_9 represents a face atom; C_7 an edge atom and C_4 a corner atom, while a bulk atom in an fcc metal has 12 nearest neighbors and is denoted as C_{12}. All surface atoms have lower coordination than the bulk
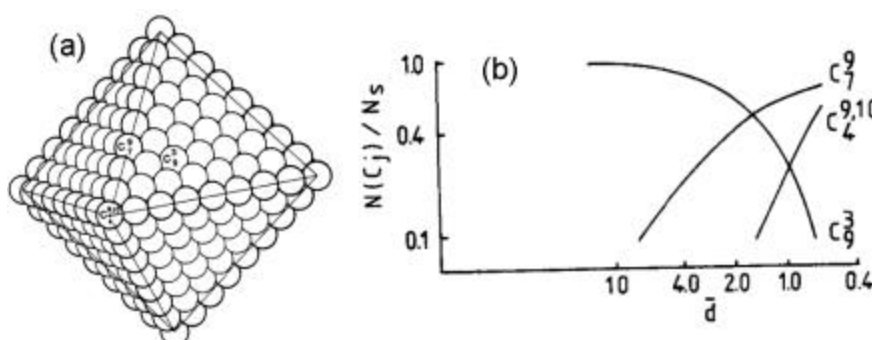
Figure 1.7. (a) Face centered cubic octahedron with m = 9, where m is the number of atoms along an edge. (b) Coordination of surface atoms versus the mean particle size, $\bar{d}$. The symbols refer to the different types of surface atoms in the fcc octahedron. From ref. [35].

and are termed coordinatively unsaturated atoms. The surface atom statistics ($N(C_j)/N_s$) for a number of small octahedron (0.4–10 nm) have been calculated and shown in Figure 7b. The fraction of face atoms C_9 becomes about 0.9 at ~ 6 nm but falls to zero at ~ 0.6 nm, where all the atoms are at edges and corners. Figure 7b demonstrates that effect of surface atom coordination is most important for particles smaller than 4 nm. As mentioned in the beginning of this subsection, these changes in coordination are linked to changes in the electronic characteristics of the particle.

The octahedron is Figure 7a is a complete octahedron, the outer shell of atoms is complete. As a model of a small crystallite is built one atom at a time, a complete octahedron or other regular shape is reached only periodically [36]. For a complete octahedron, 6, 19, and 44 atom clusters are necessary. Addition of the 20th and 21st atom starts a new layer and creates atoms of different coordination. At the edges of added layers, a particular ensemble composed of five atoms (B_5) is assembled (Figure 8). If the number of B_5 ensembles is maximized in an fcc octahedron, there will be some atoms in coordination states that do not exist in the complete octahedron [37]. The concentration
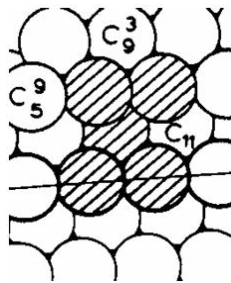
Figure 1.8. Striped atoms represent B_5 ensemble which may be important for catalysis. From ref. [35, 37].

of B_5 site are believed to be particular important in catalysis and their concentration depends critically on the shape of the particle. Comparison of a cube, cuboctahedron and sphere comprised of 683 atoms, the cube has 13 B_5 sites, the cuboctahedron has 76 and the sphere has 13 [37]. Depending on the metal, the number of B_5 sites often goes through a maximum at ~1.5-2.5 nm, and therefore serves as a popular explanation for structure sensitivity, for TOF versus $\bar{d}$ for a number reactions which pass through a maximum in the range around 2-3 nm (see Figure 3c) [12]. Most small fcc nanoparticles $(\bar{d} \leq 10 \text{ nm})$ crystallize in a cuboctahedral arrangement as illustrated in Figure 9.
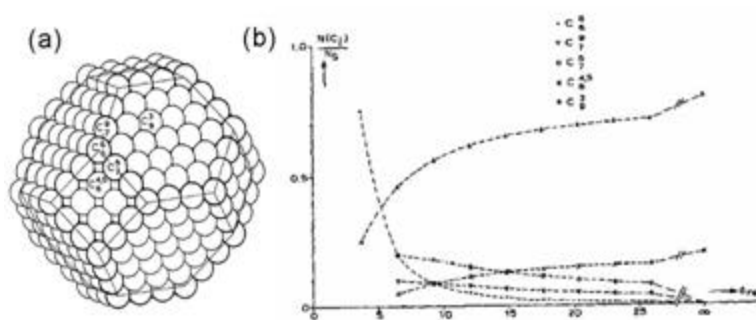
Figure 1.9. (a) Face centered cube (fcc) cuboctahedron. (b) Coordination of surface atoms versus the mean particle size, $\bar{d}$. The symbols refer to the different types of surface atoms in the fcc cuboctahedron. From ref. [35].

A complete fcc cuboctahedron with m = 4 is shown in Figure 9a. This particle shape has five different types surface atoms; a (111) face atom, (100) face atom, a corner atom and two types of edge atoms. One type of edge site is found at the intersection of two (111) oriented faces, while the second type is located at the intersection of (111) and (100) faces. The surface atom statistics (Figure 9b) demonstrate that the edge and corner atoms represent a significant fraction at small particle sizes but as at larger sizes, (100) and particularly (111) face atoms dominate the surface atom distribution. For even smaller crystallites, an icosahedral non-fcc arrangement may become more stable and the differences in energy between icosahedrons and cuboctahedron are small, so that the diameter below which the former are stable varies considerably from one metal to another [38, 39].

The catalytic properties of a metal are linked to $N(C_j)/N_s$ of Figures 7 and 9 if a geometric effect is the reason for the observed catalytic activity. For example, if catalysis is favored by atoms of low coordination, small particles would give higher rates (Figures 7b and 9b) simply because the concentration of the sites (corners and edges) is maximized. If catalysis is favored by face atoms, large particles would give higher rates [8]. The two scenarios are shown graphically in trace 4 and 2 of Figure 1, respectively. While it is difficult to decouple geometric from electronic effects, there are examples of antipathetic structure sensitive reactions requiring multi-atom active sites, which when diluted with inert metal atoms, the activity decreases dramatically due to the dilution of large ensembles of metal atoms of the same nuclearity. Within that ensemble, the atoms must be properly oriented and may include atoms of varying coordinative unsaturation [40]. The most appropriate approach to understand the electronic and geometric effects

on catalytic rates is to produce catalysts containing nanoparticles which are nearly monodisperse such that all particles have similar properties (both electronic and geometric). Geometric effects may be probed by dilution of metal atom ensembles with inert metals [41, 42] and electronic effects may be probed by changing the character of the support as long as all other catalyst parameters are remain identical. This is certainly a significant challenge and a number of them have been discussed in a recent review [12]. The development of nearly monodisperse nanoparticles and shape-controlled nanoparticles should enable the influence of both parameters on reaction selectivity to be deduced [43].

1.3 Applications of nanoscience methods to catalyst synthesis for the formulation of a model 3-dimensional heterogeneous catalyst

New methods of synthesis of nanoscale size materials are finding applications and potential use in the field of nanotechnology, heterogeneous catalysis represents one of the oldest commercial applications of nanotechnology [43, 44]. The ability to create heterogeneous catalysts with at least one precise parameter (particle size, shape, location in support matrix, etc.) which can be rationally designed and controlled during synthesis is the first impact that nanotechnology has had on heterogeneous catalysis. This has been realized in a number of synthetic structures to date, whether its control of the metal particle size and/or shape, composition and location of active site in an organic matrix (inorganic-hybrid catalytic material synthesis) or the composition/structure of the environment surrounding the active site (*i.e.* molecular imprinting). In this thesis, we utilize methods developed in the colloidal chemistry field to synthesize monodisperse

transition metal nanoparticles and introduce these as-synthesized nanoparticles into a mesoporous oxide matrix. These colloidal nanoparticle synthesis methods have been known for quite some time [45], but the nanotechnology/nanoscience revolution has reignited an interest in the production of monodisperse, multi-functional particles of nanometer dimensions. Many researchers have suggested that research in nanoscience and nanotechnology present great opportunities for research in heterogeneous catalysis [29, 43, 46-48]. Kung and Kung have written a perspective on the impact of nanotechnology on heterogeneous catalysis. In this perspective, one of the most important impacts of nanotechnology is the design and control of the surface atomic arrangement in order to optimize the desired structure and density of the active sites. These authors contend this would include the ability to manipulate the deposition of atoms in a specific location with a specific order. However, the authors do note that there are a number of obstacles to practical applications of such an atom-by-atom approach of catalyst synthesis. For example, if one were to synthesize active sites one at a time, and sites on the order of 10^{16}-10^{17} are needed for testing, an extremely efficient synthetic method will be needed to prepare sufficient quantities of samples. Kung and Kung [46-48] have suggested that nanotechnology may enable the production of catalysts by an atom-by-atom or unit-by-unit approach. This they believe will enable control of the structure and composition of the active site, but also the same parameters of the environment around the active site. The relative positions of the binding and active site play a critical role in enzymatic catalysis and therefore are likely to be important for the design of highly selective synthetic catalysts. Schlögl and Hamid [29] have emphasize in their review that nanocatalysis will enable catalysts to be "synthesized" rather than

prepared because classical catalyst preparation methods (see Chapter 2) are empirical recipes which are followed that do not describe the kinetic boundary conditions of the reactions performed. Therefore, each batch of material consequently must be characterized for their functional properties because they can not be predicted. It is barely possible to predefine properties in heterogeneous catalysis in a rational manner. Schlögl and Hamid emphasize that nanocatalysts require structural control over several dimension scales and that multidimensional structural control is exerted by considering catalysts as inorganic polymers rather than as closed packed crystals. Primary, secondary, and tertiary structural hierarchies translate into molecular building blocks and linkers, the defect structure of crystals and particle morphology. Therefore, these authors define nanocatalysis as the science of the synthesis of supramolecular materials and the control of the kinetics of their chemical transformation. It differs from traditional catalysis since the materials are explicitly designed over length scales larger than that of a single active site. The similarity of the approaches to that of biocatalysis or enzyme catalysis put forth separately by Kung and Schlögl is rather apparent, but Schlögl acknowledges that the degree of sophistication with which active sites in enzymes are fine-tuned by incorporation into complex networks of an organic polymer (i.e. proteins) made of chemically simple basic structural units is much higher than one can hope to achieve in purely inorganic systems [29].

We emphasize in this thesis that our utilization of colloidal chemistry to synthesize heterogeneous catalysts comprised of monodisperse Pt nanoparticles is done not to explore the development of a new catalyst synthesis method with the goal of practical applications, but rather the purpose was to synthesize a material that enables the

development of a better understanding of a catalytic phenomenon. In this example, we use a less stringent definition of nanocatalysis put forth by Schlögl and Hamid, and suggest that nanoscience methods can be utilized to design the next generation model catalyst [29]. Boudart has defined a model catalyst as "one that is prepared for the purpose of investigating a complex phenomenon that cannot be quantified or explained by working with practical complex catalysts" [49]. Boudart states that the purpose of making and studying a model catalyst is to understand a catalytic phenomenon. In this thesis, methods of nanoscience (*i.e.* monodisperse nanoparticles) are utilized to produce the next generation model heterogeneous catalyst.

The evolution of the model heterogeneous catalyst is exemplified by the work of Gabor A. Somorjai and co-workers which has closed the so-called "materials gap" between model systems and industrially relevant heterogeneous catalysis [14]. The evolution of more complex model catalysts has been paralleled by the discovery of analytical techniques which enable catalytic phenomena to be studied under relevant reaction conditions (*i.e.* high pressure and temperature) [50]. The evolution of model catalyst within the Somorjai group is shown in Figure 10. Other research groups have suggested that model systems beyond those represented in Figure 10. Single crystal surfaces are prepared and cleaved to expose a particular crystal. Cleavage within the stereographic triangle enables with varying defect concentrations (steps and kinks) to be prepared as well as the most stable low index faces. The two-dimensional nanoparticles using electron beam lithography (EBL) was applied to the synthesis of well-ordered nanoparticle arrays on planar metal oxides [51]. The most recent evolution of the model

catalyst in the Somorjai group is the synthesis of monodisperse metal nanoparticles and

their incorporation in a high surface
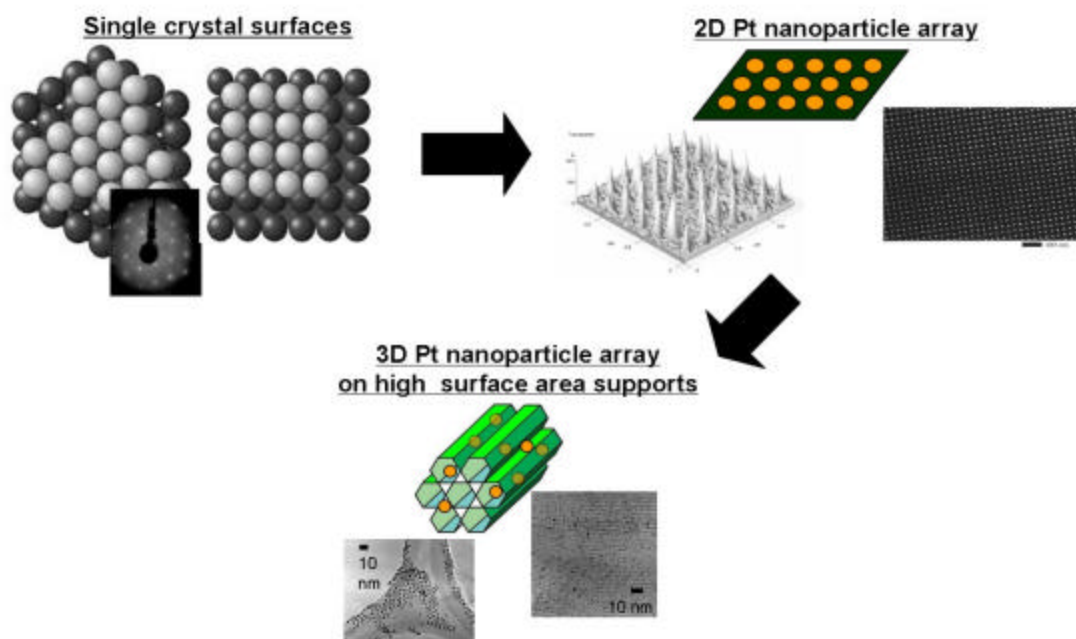
Figure 1.10. Model catalyst evolution in the Somorjai group. Single crystals are prepared and cut to expose a particular crystal plane (*i.e.* (111) and (100)) and characterized by electron based techniques (LEED crystallography for example).

area stable support. The inherent advantage of the three model systems are rather

apparent; single crystals and their preparative technology allows surface with practically

any orientation to be prepared, while the 2-dimensional nanoparticle arrays have a

geometrically "well-defined" metal-metal oxide interface which has been implicated as a

very active catalytic entity and the high surface area catalysts afford metallic surface

areas > 1 m^2 g^{-1}, four orders of magnitude larger than a single crystal surface.

The advantages and disadvantages of each type of model catalyst as well as other

catalysts which are considered models of industrial relevant catalysts are summarized in

Table 1, which demonstrates that a number of model systems have been developed.

1.4   Motivation to combine synthesis, characterization, and reaction studies of supported metal catalysts

Heterogeneous catalysis is a multi disciplinary science requiring knowledge from chemistry (physical, organic and inorganic), physics (solid state, condensed matter), and engineering (materials, reactor design, modeling).   The heterogeneous catalysis community spans both academia and industry and plays a major role in many traditional industries (commodity chemicals, pharmaceuticals, and energy) and significantly impacting some unconventional areas (microelectronics, nanotechnology, information storage, etc.).   One of the significant challenges in heterogeneous catalysis is to develop the skills and technology to synthesize, characterize and perform reaction studies on the synthesized materials.   Characterization of the catalysts is significant as it enables the determination of a catalyst structure and therefore the formulation of structure-function relationships in heterogeneous catalysis.   Specifically, this thesis concentrates on the influence of particle size on reaction activity and selectivity.   The importance and earlier observations of particle size-activity (and/or selectivity) relationships have been discussed in section 1.1.

The field of heterogeneous catalysis is plagued by thorough kinetic studies and mechanism formulations on poorly characterized catalysts or externally obtained catalysts with little to no characterization information available.   The opposite scenario involves the highly controlled synthesis of catalytic materials and their thorough characterization with very little to no catalytic data on the materials.   Therefore in this thesis, it is emphasized that materials synthesis, thorough physical and chemical characterization and catalytic studies have been performed in one laboratory.

Table 1.1. Types of catalysts and their use as model systems in heterogeneous catalysis

Class of catalyst	Typical preparation method	Example	Advantages for fundamental understanding	Limitations for fundamental understanding
Film	Evaporation and deposition of metal	Pt film	Applicable to many metals; surface area easily measured	Surface structure; not uniform; no support
Single crystal	Preparation of single crystal and cleavage to expose a particular crystal plane	Pt(111)	Applicable to many metals; surface structure/composition easily measured; many experimental techniques applicable	No support
Metal particles on high area porous support	Impregnation of support (or ion exchange) with metal salt followed by calcination and/or reduction	Pt/Al_2O_3, Pt/SiO_2, etc.	Applicable to many metals and supports; wide range of particle sizes attainable	Metal structures nonuniform; support surface nonuniform; metal-support interface nonuniform
Metal particles on low-area planar support	Vapor deposition of metal on a single crystal of ultrathin film oxide support	Pt deposited in Al_2O_3 under UHV conditions	Applicable to many metals and supports; wide range of particle size obtainable	Metal particles nonuniform; metal-support interface nonuniform
	Vapor deposition of metal on lithographically defined ultrathin film oxide support	2D Pt nanoparticle arrays prepared by electron beam lithography (EBL)	Applicable to many metals and many supports; nearly monodisperse particle sizes obtained, well-defined metal-support interface	Metal particle sizes are large (low S:V ratio), metal-support interfacial area represent very small fraction of metal surface area
Metal clusters on high-area porous support	Synthesis of molecular or ionic metal carbonyl cluster precursor on support followed by treatment to remove CO ligands	Rh_6, Ir_6, Ir_4 clusters on MgO, TiO_2, etc.	Applicable to many supports; extremely small clusters producible for maximizing metal-support interactions; possibility of forming nearly uniform metal clusters	Restricted to few metals and few cluster sizes; uniform clusters stable only at relatively low temperatures
Metal clusters on low-area planar support	Vapor deposition of size-selected metal clusters from gas phase onto single-crystal or ultrathin film support	$Pt/Al_2O_3(0001)$	Applicable to many metals and supports; wide range of particle sizes attainable; possibility of structurally near uniform clusters and supports	Question whether preparation can be carried out without changes in cluster size
Metal clusters on high-area crystalline support	Synthesis of molecular or ionic metal carbonyl cluster precursor in zeolite pores followed by treatment to remove CO ligands	Rh_6/NaY	Extremely small clusters can be made; both clusters and zeolite support may be structurally nearly uniform	Restricted to small number of metals and molecular sieve supports; uniform clusters stable only at relatively low temperatures
Prepared monodisperse nanoparticles encapsulated into high-area porous support	Preparation of nanoparticles in presence of surfactant in solution followed by encapsulation of mesoporous oxide matrix	Pt(X)/SBA-15, where X = 1.7, 2.6, 2.9, 3.6 or 7.1 nm	Monodisperse particle sizes attainable; wide range of particle sizes attainable; applicable to many supports	Question whether polymer/ molecular stabilizing agent can be completely removed from nanoparticle surface

1.5   Summary of thesis contents

The thesis is divided into eleven chapters, seven of which have or will become publications. The current chapter, Chapter 1 explains summarizes the motivation for this project, the approaches utilized and scope of the project. Chapter 2 summarizes classical catalyst synthetic methods with an emphasis on the advantage and disadvantage of each method in its ability to produce monodisperse particles and controlled placement within the support matrix. This chapter also includes an introduction to solution phase synthesis of colloidal metal nanoparticles, as well as the synthesis of ordered, mesoporous oxide materials and an introduction to two novel catalytic synthetic methods developed in this thesis, namely capillary inclusion and nanoparticle encapsulation methods. Chapter 3 summarizes all of the experimental techniques utilized in this thesis for the characterization of as-synthesized nanoparticles and supported nanoparticles as well as the techniques used to determine and quantify the catalytic activity of the nanoparticle catalysts. Chapter 4 introduces the capillary inclusion (CI) synthetic scheme, and characterization and reactivity studies of these materials. Chapter 5 introduces the nanoparticle encapsulation (NE) method of catalyst synthesis and the characterization of these materials. Also included in this chapter are reactivity studies of these catalysts for the hydrocarbon conversion reactions, ethylene hydrogenation and ethane hydrogenolysis. In Chapter 6, the adsorption and co-adsorption of carbon monoxide and ethylene are studied by volumetric adsorption and infrared spectroscopy on the nanoparticle encapsulation catalysts synthesized and characterized in Chapter 5. The influence of low pressures of CO on the kinetics of ethylene hydrogenation on the nanoparticle encapsulation series catalysts is investigated in Chapter 7 and a kinetic model is

formulated which captures the measured kinetics of the poisoned hydrogenation reaction. Chapter 8 is a systematic study of the decomposition and removal of templating polymer from the nanoparticle surface. Combining infrared spectroscopy, thermal analysis and temperature programmed desorption, the structure of adsorbed polymer as well as the onset and degree of decomposition were assessed in both inert and reactive (oxidative, reductive) atmospheres. Chapter 9 introduces the synthesis, characterization and catalytic studies of shape controlled Pt nanoparticles. The introduction of varying amounts of silver nitrate to the 7 nm Pt particle synthesis (see Chapter 4) led to the production of well defined cubes, cuboctahedra and octahedra of catalytic relevant particle size (~ 9 nm). The catalytic activity for ethylene hydrogenation demonstrated that residual Ag, potentially in the form of small crystallites on the Pt nanoparticle surface is responsible for the diminished catalytic activity. The thesis ends with Chapter 10, conclusions and recommendations for future work. The final chapter also includes a summary of on-going projects which are relevant to work presented in this thesis.

1.6   References and Notes

1.   N. I. Kobosev, *Acta. Physicochim. URSS* 9 (1938) 1.

2.   L. Klichko-Gurwich, N. I. Kobosev, *Acta. Physicochim. URSS* 10 (1939) 1.

3.   N. I. Kobosev, *Usp. Khim.* 25 (1958) 245.

4.   G. K. Boreskov, V. S. Chesalova, *Zh. Fiz. Khim*.30 (1956) 2560.

5.   G. K. Boreskov, M. G. Slinko, Z. S. Chesalova, *Zh. Fiz. Khim*.30 (1956) 2787.

6.   O. M. Poltorak, V. S. Boronin, *Zh. Fiz. Khim*. 39 (1965) 1476.

7.   M. Boudart, A. Aldag, J. E. Benson, N. A. Dougharty, C. Harkins Givens, *J. Catal.* 6 (1966) 92.

8.   M. Boudart, *Adv. Catal*. 20 (1969) 153.

9.   M. A. Abdeenko, G. K. Boreskov, M. G. Slinko, *Probl. Kinet. Katal*. 9 (1957) 61.

10.   J. L. Carter, J. A. Cusumano, J. H. Sinfelt, *J. Phys. Chem*. 70 (1966) 2257.

11.   D. J. C. Yates, J. H. Sinfelt, *J. Catal*. 8 (1967) 348.

12.   M. Che, C. O. Bennett, *Adv. Catal*. 36 (1989) 55.

13.   G. A. Somorjai, *Introduction to Surface Chemistry and Catalysis*, Wiley, New York, 1994.

14.   G. A. Somorjai, *J. Phys. Chem. B* 104 (2000) 2969.

15.   G. Ertl, *Angew. Chem. Int. Ed*. 15 (1976) 391.

16.   D. R. Kahn, E. E. Petersen, G. A. Somorjai *J. Catal*. 34 (1974) 294.

17.   H. Topsøe, N. Topsøe, H. Bohlbro, J. A. Dumesic, *Proc. 7th Intl. Cong. Catalysis*, ed. T. Seiyama and K. Tanabe, Tokyo, 1981.

18.   J. A. Dumesic, H. Topsøe, M. Boudart, *J. Catal*. 37 (1975) 513.

19.   R. Brill, E. L. Richter, E. Ruch, *Angew. Chem. Intl. Ed. Engl.* 6 (1967) 882.

20.   N.O. Spencer, R.C. Schoonmaker and G.A. Somorjai, *Nature* 294 (1981) 643.

21.   D. R. Strongin, J. Carrazza, S. R. Bare, G. A. Somorjai, *J. Catal*. 103 (1987) 213.

22.   M. Boudart, G. Djéga-Mariadassou, *Kinetics of Heterogeneous Catalytic Reactions*, Princeton University Press, Princeton, 1984.

23.   R. C. Reuel, C. H. Bartholomew, *J. Catal*. 85 (1984) 78.

24.   J. P. Brunelle, A. Sugier, J. F. Le Page, *J. Catal*. 43 (1976) 273.

25.   P. Gallezot, D. Richard, *Catal. Rev. –Sci. Eng*. 40 (1998) 81.

26.   B. Coq, F. Figueras, Coord. *Chem. Rev*. 178-180 (1991) 1753.

27.   C. Mohr, H. Hofmeister, J. Radnik, P. Claus, *J. Am. Chem. Soc*. 125 (2003) 1905.

28.   C. M. Pradier, T. Birchem, Y. Berthier, G. Cordier, *Catal. Lett*. 29 (1994) 371.

29.   R. Schlögl, S. B. A. Hamid, *Angew. Chem. Int. Ed*. 43 (2004) 1628.

30.   C. N. R. Rao, G. U. Kulkarni, P. J. Thomas, P. P. Edwards, *Chem. Eur. J.* 8 (2002) 29.

31.   R. Kubo, *J. Phys. Soc., Jpn*. 17 (1962) 975.

32.   R. Busani, M. Folkers, O. Cheshnovsky, *Phys. Rev. Lett*. 81 (1998) 3836.

33.   H. N. Aiyer, V. Vijayakrishnan, G. N. Subbanna, C. N. R. Rao, *Surf. Sci*. 313 (1994) 392.

34.   H. Roulet, J. –M. Mariot, G. Dufour, C. F. Hague, *J. Phys. F., Metal Phys*. 10 (1980) 1025.

35.	R. van Hardeveld, F. Hartog, *Surf. Sci*. 15 (1969) 189.

36.	O. L. Perez, D. Romeu, M. J. Yacaman, *Appl. Surf. Sci*. 13 (1982) 402.

37.	R. van Hardeveld, F. Hartog, *Adv. Catal*. 22 (1972) 75.

38.	M. Gillet, *Surf. Sci*. 67 (1977) 139.

39.	M. R. Hoare, P. Pal, *J. Cryst. Growth*, 17 (1972) 77.

40.	J. G. Goodwin, S. Kim, W. D. Rhodes, *Catalysis*, Vol. 17, ed. J. J. Spivey, Royal Society of Chemistry, 2004.

41.	J. H. Sinfelt, *AIChE J.* 19 (1973) 673.

42.	J. H. Sinfelt, *Acc. Chem. Res*. 4 (1987) 134.

43.	G. A. Somorjai, Y. G. Borodko, *Catal. Lett*. 76 (2001) 1.

44.	A. T. Bell, *Science* 299 (2003) 1688.

45.	J. Turkevich, G. Kim, *Science* 169 (1970) 875.

46.	H. H. Kung, M. C. Kung, *Appl. Catal.* 246 (2003) 193.

47.	H. H. Kung, M. C. Kung, *Catal. Today* 97 (2004) 219.

48.	H. H. Kung, M. C. Kung, *Top. Catal*. 34 (2005) 77.

49.	M. Boudart, *Top. Catal*. 13 (2000) 147.

50.	G. A. Somorjai, R. M. Rioux, *Catal. Today* 100 (2005) 201.

51.	F.H. Ribeiro, G.A. Somorjai, *Recl. Trav. Chim. Pays-Bas* 113 (1994) 419.

Chapter 2

Heterogeneous catalyst synthesis: Comparison of classical preparation methods with novel methods

This chapter introduces classical catalyst preparation techniques, such as coprecipitation, impregnation, incipient wetness, ion exchange, and metal precursor decomposition (Section 2.1). The basics of the preparation method are given, as well as the advantages and disadvantages of each method. The synthesis of monodisperse nanoparticles in solution phase is discussed in section 2.2 with emphasis on a nucleation-growth mechanism of nanoparticle formation. Section 2.3 focuses on the synthesis of mesoporous metal oxides, concentrating on SBA and MSU silica materials and a discussion of the proposed formation mechanism. Section 2.4 introduces the techniques developed in this thesis for the synthesis of catalysts containing monodisperse Pt particles, namely capillary inclusion (CI) and nanoparticle encapsulation (NE), respectively. The chapter concludes with section 2.5, where the synthetic methods are compared and contrasted.

2.1   Classical methods of catalyst synthesis

2.1.1 Co-precipitation

Co-precipitation is a preparative method in which precursor forms of both support and active phase are precipitated from solution [1-3]. An inherent advantage is the intimate mixing of metal precursor and support. Upon calcination, the precipitate becomes the support with the active component dispersed throughout the bulk as well as at the surface. After reduction it is difficult to obtain metal crystallites of uniform size because of the presence of both oxides (support and active phase) and other intermediate compounds (form example Ni silicate formation for the Ni/SiO_2 system) which have different reducibilities. This heterogeneity may be avoided in the superhomogeneous coprecipitation method which consists of two steps [4]. The first step involves the superposition of layers of salt solutions followed by their mixing to instantaneously from a supersaturated solution.   The second step consists of forming a homogeneous precipitate form the supersaturated solution. The disadvantage of this method is that the precursor ions are also distributed within the bulk of the support oxide [3] and that the pore structure of the final catalyst is more difficult to control than when one starts from a separately produced carrier.

2.1.2 Impregnation

Impregnation is defined as a means of catalyst preparation by the adsorption of a catalyst precursor salt from solution onto a support material [5]. This process is sometimes referred to as wet impregnation because the pores of the support are filled with solvent before coming in contact with the precursor salt. One of the problems associated with impregnation is the number of variables which influence precursor salt adsorption and the final metal loading and location of the metal in the support particle.

Variables which are important include the concentration of the precursor salt, type of salt, solvent, temperature, nature of the support, time of contact with the support and the presence of other materials. When impregnating a porous material with a metal salt from solution, four different conditions can be envisaged for a system consisting of external solution and a single pore. There are numerous scenarios for the distribution of metal precursor in the system where the solution arrives at the end of the pore [6]. Consider the situation depicted in Figure 1A. The assumption made is that the penetration and rate of diffusion of the solute into the pore is slow compared to the rate of adsorption. All metal precursor material in the penetrating liquid adsorbs on the walls of the first part of the pore through which it passes. The liquid which passes further into the pore contains no active material. At this time if the solvent is removed by drying, metal precursor will only be found in part of the pore nearest the external solution. If instead of
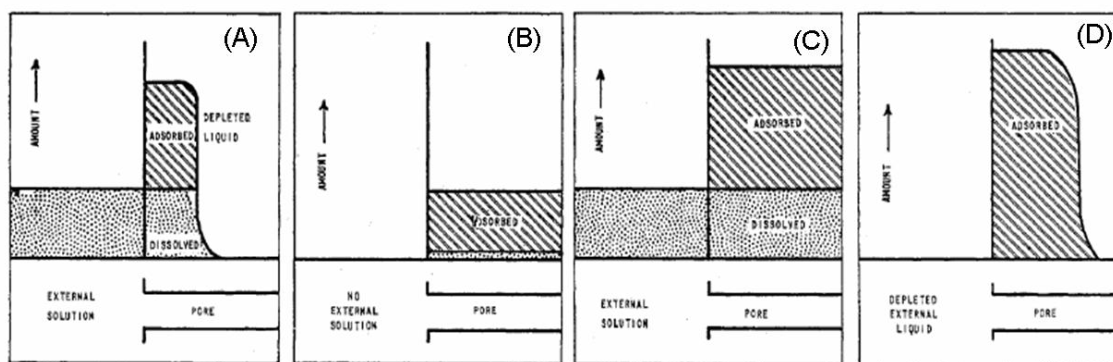
Figure 2.1. Conditions of a pore adsorbing metal precursor in solution. From ref. [6].

drying at this time, the pore is simply removed from contact with external solution but left filled with liquid, redistribution of the metal precursors will occur because of precursor desorption from the pore wall and migration by diffusion. This ultimately yields a uniform distribution of precursor within the pore (Figure 1B). This process can

be used in catalyst synthesis if the rate of desorption is sufficiently rapid. The third and fourth scenarios are depicted in Figure 1C and 1D, respectively. Figure 1C is a situation in which the pore is left in contact with the external solution, additional activating material is supplied by the external solution by diffusion to the adsorption sites until either equilibrium with the external impregnating solution is reached, bring about a uniform distribution of metal salt in the pore. Figure 1D is the example of Figure 1C when the external solution is depleted of metal precursor before the distribution is uniform.

The advantages of impregnation are its synthetic simplicity, no intricate equipment is necessary for catalyst preparation by impregnation. It works with any porous material and metal salt combination as long as a solvent compatible with both is available. The simplicity of the preparation method enables large quantities of catalysts to be prepared. The primary disadvantage of the technique is poor control of the distribution of metal nanoparticles in the pores (Figure 1) and activation steps such as evaporation of the solvent require special attention as these procedures generally cause agglomeration of metal precursors and the formation of large particles after reduction. Another inherent disadvantage is the inability to produce highly dispersed catalysts at high metal weight loadings.

2.1.3   Incipient wetness

Incipient wetness, also referred to as dry impregnation involves contacting a dry support with only enough solution of the impregnant to fill the pores of the support [3, 5]. The volume of liquid needed to reach this stage of incipient wetness is usually determined by slowly adding small quantities of solvent to a well stirred weighed amount

of support until the mixture turns slightly liquid. This weight:volume ratio is then used to prepare a solution of the precursor salt having the appropriate concentration to give the desired metal loading. Since all of the impregnant solution is adsorbed into the pores of the support, this procedure can be used to prepare specific, predetermined metal loadings on the catalyst.

Incipient wetness has the same advantages and disadvantages of impregnation. Similar to catalysts prepared by impregnation, reduction of the precursor to metal nanoparticle must be done at low temperatures due the weak interaction between metal precursor and support.

2.1.4   Ion exchange

This technique is used when the precursor interacts with the support via electrostatic interactions. The interactions are basically controlled by the type of support and state of the surface (number and nature of the functional groups, their acid-base properties) and the impregnating solution (pH, type and concentration of the metal precursor, and presence of competing ions) [7]. In this method, the support is immersed in a solution containing precursor, stirred for a given time, and filtered. Depending on the strength and conditions of adsorption of the precursor species, the concentration of active phase may vary. For exchange on a support, two conditions must be met: (1) the pH of the impregnating solution must be either sufficiently high or low to provide the appropriate surface potential and the adsorbent must have the proper charge. This technique is widely used in the preparation of laboratory and industrial catalysts.

The primary advantage of this method is a greater control over the dispersion and distribution of the active species with the catalyst pore. The metal loading is governed by

the concentration of adsorption exchange sites and as a consequence the weight of the active component that can be incorporated is limited, an inherent disadvantage of the technique. A disadvantage of the technique is related to its applicability with various metal precursors and supports. For example, the chloroplatinate ion ($PtCl_6^{2-}$) is negative so this material does not adsorb on silica (isoelectric point of $\approx$ 2). The only way of incorporating chloroplatinic acid onto silica is to use the incipient wetness procedure [8]. Unfortunately, this method leads to large platinum crystallites upon reduction because the $PtCl_6^{2-}$ ion is not held on the silica support and therefore the platinum particles agglomerate. Catalysts prepared by ion exchange between the cationic $Pt(NH_3)_4^{2+}$ and the silica have a strong bond between the silica surface and the platinum. On reduction, these ion exchanged species gave highly dispersed catalysts with small metal crystallites regardless of Pt loading.

2.1.5   Decomposition of metal clusters

The decomposition of metal clusters on solid porous supports was first demonstrated with the decomposition of Ni carbonyl of Al_2O_3 and SiO_2 [9]. Metal cluster compounds were initially employed for the two following reasons: (1) formation of heterogeneous analogs of homogeneous active catalysts, and (2) the production of clusters or small metal particles of well-defined nuclearity.   Recently, Gates has published a review on the preparation and reactivity of supported metal clusters for applications in heterogeneous catalysis [10].   The major advantages of metal cluster decomposition for the creation of small particles is the temperatures usually required to decompose the metal cluster compounds and produce small metal particles are substantially lower than those needed for the reduction of metal salts involved in

conventional methods so that the number of atoms initially present in the complex is preserved. Metal cluster compounds are usually anchored onto an oxide surface via the two following routes [11]. Reaction involving surface hydroxyl groups, Si–OH leading to surface reactions of the form, $nS - OH + MX_m \rightleftharpoons [S - O]_nMX_{m-n} + nHX$. The metal content is controlled by the concentration of surface $S - OH$ groups, the stoichiometry of the reaction and the number of metal atoms in the cluster. The second method involves preparing oxide surfaces with specific functional groups upon which the metal cluster compound will anchor to, commonly referred to as grafting.

The main advantage of this catalyst preparation technique is the ability to produce small metal clusters composed of only a few metal atoms, but in the case where precursors are anchored to the surface through functional groups, metal clusters may be in both the zero-valent and partially oxidized states. The other disadvantage of the metal cluster compound decomposition is that the ligands have to be removed to produce the metal particles and the organic solvent used to impregnate the support by the precursor compound may remain on the surface and thus interfere with the catalytic reaction.

2.1.6   Activation after synthesis: Calcination and reduction

Most catalyst synthetic methods require additional activation steps in order to produce a catalytically active disperse phase. The type of activation necessary depends on whether the metal is in its zerovalent state (decomposition of metal cluster, vapor phase deposition) or in an oxidized state (coprecipitation, impregnation and ion exchange) [12]. For the latter case, a reduction step is necessary to reduce the ions to obtain zerovalent metal. The two primary activation steps are calcination and reduction. Calcination is carried out in air or oxygen to decompose the metal precursor compound

and induce subsequent bonding of the formed oxide with the support. It is useful for the removal of some of the elements introduced during the preparation by formation of volatile compounds, decomposition of the precursor ionic complex and further ligand exchange reactions between surface groups and ligands bound to the metal ion, elimination of carboneacous impurities possibly introduced during preparation and the intentional sintering of the precursor compound or of the formed oxide system. Consequently, calcination may have a pronounced effect on the reducibility, dispersion and distribution of the metal in the final catalyst. There have been relatively few studies on the influence of treatment conditions on metal dispersion, but a study by Kubo *et al*. [13] reported that the temperature of calcination in air before hydrogen reduction was the key parameter in determining the dispersion of Pt in Pt/NaY and Pt/NH$_4$Y zeolites.

The second activation step that generally follows calcination is reduction, the conditions of which are particularly important since they can strongly affect the final distribution of the metal particles (see Figure 2). Figure 2 demonstrates that mean particle size increases as the reduction temperature (and time) are increased. It is also evident that the particle size distributions are broad and overlapping. The study of particle size effects with these four catalyst samples may lead to anomalous results with regards to structure sensitivity/insensitivity of a particular catalytic reaction. In the case of nucleation in metal oxide reduction, higher temperatures favor more rapid initial reduction of the metal oxide and higher density of nuclei but also coalescence or sintering of the particles. An intermediate temperature is necessary to maximize nuclei
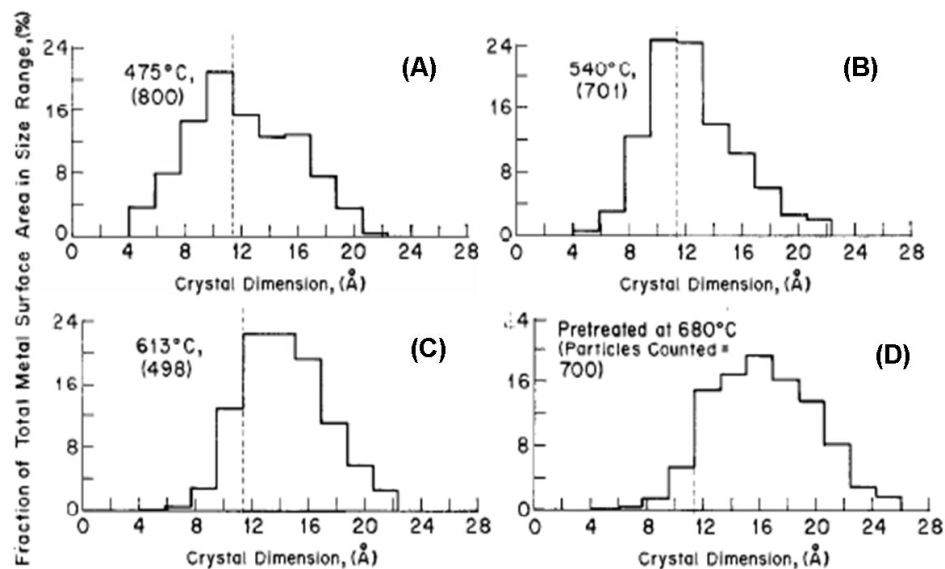
Figure 2.2. Particle size distribution for Pt/Al_2O_3 after reduction in H_2 at various temperatures. Number is parentheses refers to the number of particles counted. From ref. [14].

without any appreciable coalescence. It is anticipated that using support materials with a maximum number of defects and reducing catalysts at low temperatures and high H_2 flowrates (to reduce the partial pressure of H_2O) will lead to smaller particles [15].

2.2 Synthesis via the design and control of catalytic structures

2.2.1 Synthesis of monodisperse nanoparticles

The ability to synthesize nanoparticles of well-defined size (*i.e.* monodisperse) with high yield is due to intensified research in the chemistry and physics of nanoparticle growth in solution. Over the last 15 years, techniques for the synthesis of nanoparticles have developed dramatically. The experimental apparatus for nanoparticle synthesis is very simple. Figure 3 is an example of three prong flask for solution phase synthesis of nanoparticles.
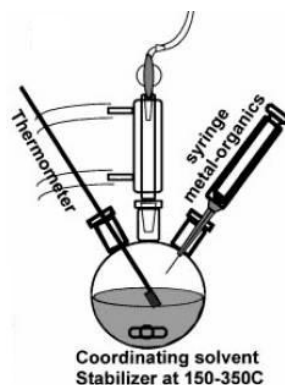
Figure 2.3. Synthetic apparatus employed for the synthesis of monodisperse Pt nanoparticles. From ref. [16].

The most successful strategy for synthesis involves the decomposition of metal precursors in high temperature reaction medium containing surface stabilizers, which in general are molecular surfactants or polymers (Figure 4).
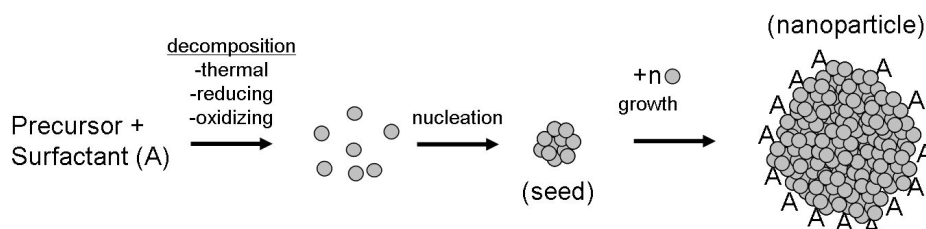
Figure 2.4. Solution phase nanoparticle synthesis in the presence of surfactant (which can be either polymeric or molecular).

Particle formation proceeds according to the LaMer model [17]. Decomposition of the precursor occurs thermally, oxidatively, or reductively to generate atomic species in solution. At a critical concentration, these atomic species undergo nucleation, resulting in a seed particle of approximately 1 nm diameter. Seed formation has a high activation energy barrier. Following formation of the seed, the concentration of atomic species in solution decreases rapidly until it is below the critical concentration for seed formation. After the nucleation event, subsequently generated atomic species in solution participate

in an autocatalytic growth process, whereby atoms are individually added to the seed (Ostwald ripening). The surface of the seed, or growing particle, catalyzes the transformation of precursor to adatom, consequently the energy barrier for the autocatalytic growth process is much lower than required for seed formation. In this way, as long as precursor concentration is kept below the critical concentration for seed formation, growth occurs exclusively. This mechanism leads to the formation of monodisperse particles, since the nucleation event occurs at a distinct point in time, followed by slow continuous autocatalytic uniform growth. This process is shown schematically in Figure 5.
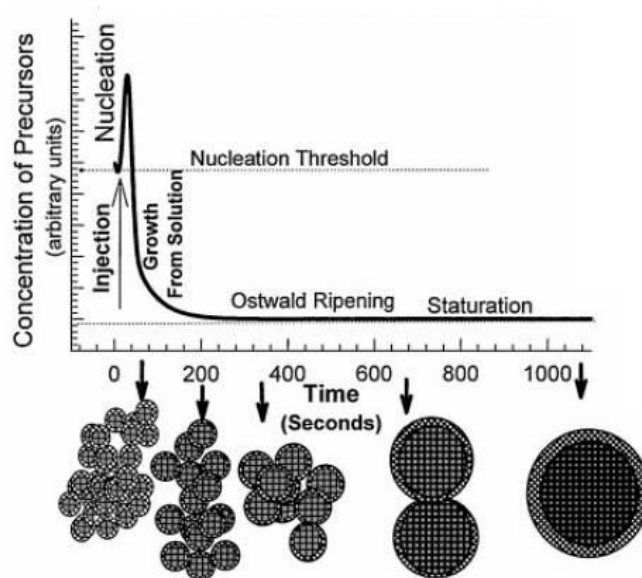
Figure 2.5. Schematic depicting stages of nucleation and growth for the preparation of monodisperse nanoparticles in the framework of the La Mer model [17]. As NCs grow with time, a size series of NCs may be isolated by periodically removing aliquots from the reaction vessel. Reproduced from ref. [16].

In general, the rapid addition via a syringe (Figure 3) to the reaction vessel raises the precursor concentration above the nucleation threshold, followed by a short nucleation burst which partially relieves the supersaturation. Classic studies by LaMer

[17] demonstrated that the production of monodisperse colloids requires a temporally discrete nucleation event. The fast nucleation event is followed by slow continuous growth on the existing nuclei, so called Ostwald ripening. In this second, distinct growth phase, the high surface energy of the small nanoparticles promotes their dissolution, whereas material is redeposited on the larger particles. The average nanoparticle size increases over time (Figure 5) with a compensating decrease in nanoparticle number, as a consequence of the law of mass action. Removal of raw material at different time intervals during the growth from solution phase demonstrates that the initial particle size distribution is $10 < \sigma < 15\%$, which is narrowed to $\leq 5\%$ through size selective processing. The nucleation burst maybe replaced by the addition of seed particles [18]. It is of interest to understand if seeding or early nucleation always leads to monodisperse particles because from nucleation theory [19], it is known that nuclei are normally very small and grow to different sizes during the brief nucleation burst and therefore initially the system is non-monodispersed. The rate determining step for particle growth can be limited by surface reaction processes or by diffusion [18].

Particle shapes can be tuned during the synthesis according to the relative surface free energies of crystal facets in the growing particle, and as a function of the interaction of a surface stabilizer with the different crystal facets of the particle. The thermodynamically favored geometry is spherical, where sufficient free energy in the system causes differences in free energies of facets, or in binding energy of the stabilizer to facets to be of no consequence. Kinetic control of particle shape occurs when the surface free energy differences are large relative to the energy available in the system. Typically, particles are bound by the most stable low-index crystal planes in proportion to

the difference in their surface free energy. Low index planes have the minimum number of surface atoms with exposed coordination spheres on corner or edge sites. The balance of surface free energy can be greatly perturbed through the interaction of the surface stabilizer. If a stabilizer preferentially binds to one facet, then the surface of the growing particle will be terminated by this specially stabilized case. Growth occurs in directions in which the surface stabilizer weakly passivates the crystal plane. Figure 6 demonstrates a number of potential situations which arise in the attempt to control particle shape during solution phase synthesis.

Surfactant effect:

1) binding energy of A is equal for all surface directions; surface energy of faces is equivalent

....if the surface energy of faces is not equivalent, then faceting occurs

A

growth

A

(spheres)

2) A binds face (1) tightly, face (2) weakly, growth is primarily along (2) directionv

(1)

(2)
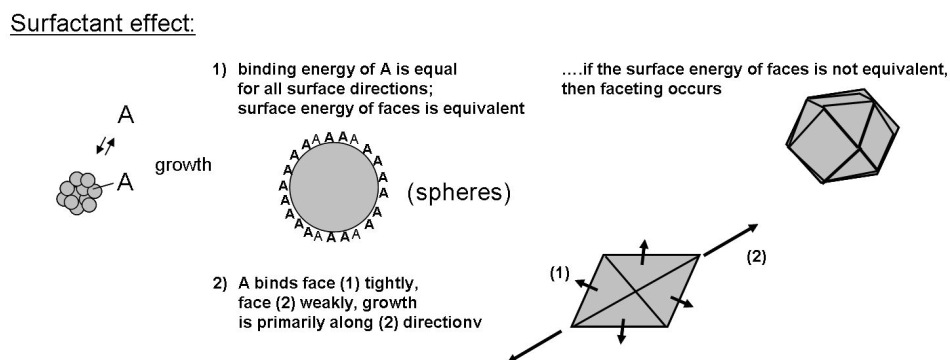
Figure 2.6. Surfactant effect on the final shape of nanoparticles during solution phase synthesis.

Shape control has been demonstrated in a number of materials (Figure 7 and Chapter 9). In most examples, foreign agents whether metal or other inorganic ions have led to enhanced anisotropic growth for the preparation of well defined nanoparticles. The final geometry of the nanoparticle is determined by several parameters during the nucleation and growth processes. Initially, the crystalline phase of the seed at the nucleating stage is the critical parameter for directing nanocrystal (previously referred to as nanoparticles) shapes due to its characteristic unit cell structure. Once nanocrystal
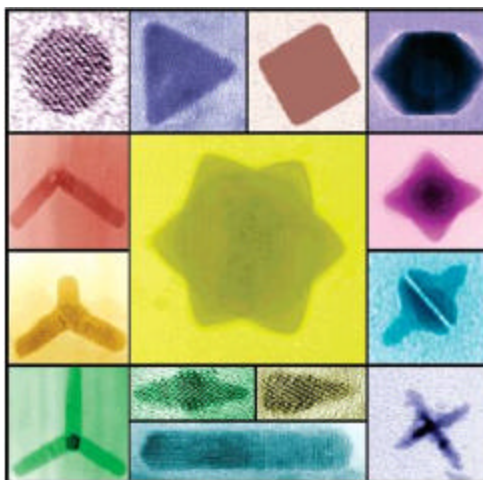
Figure 2.7. Examples of shape control during various nanoparticle syntheses. From ref. [20].

seeds are formed with a specific crystalline phase, several other factors for controlling the subsequent growth processes will affect the final geometry of the nanocrystals. These factors include intrinsic surface energy of different crystallographic surfaces, the role of selective capping molecules, and the choice of the nanocrystal growth regime between thermodynamic and kinetic processes. One of the most critical parameters influencing the growth patterns of nanocrystals is the surface energy of the crystallographic faces of the seed. Anisotropic crystal growth rate is closely related to surface energy, as shown in Figure 8, which demonstrates the role of surface energy for the anisotropic growth of ZnS rods with wurtzite structures. The surface energy of {001} faces of the wurtzite structure is much larger than either {100} or {110} due a large number of under coordinated atoms on the {001} face. Such surface energy differences result in significant growth rate differences between two crystallographic directions, since the growth rate is exponential proportional to the surface energy. The growth rate along the ⟨001⟩ directions is much faster compared to other directions, which eventually results in progressive elongation
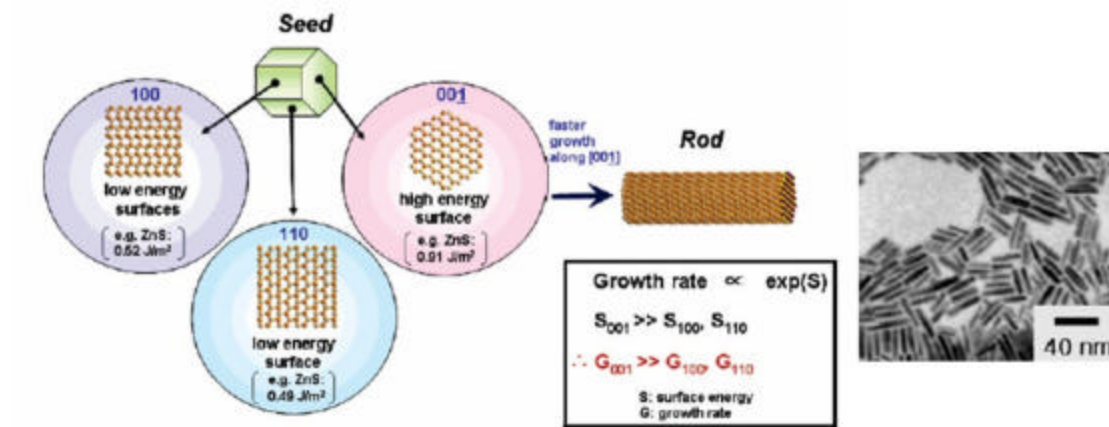
Figure 2.8. Surface initiated anisotropic growth of nanocrystals. An example of one-dimensional growth of semiconductor nanorods with wurtzite structure. From ref [20].

along the $\langle 001 \rangle$ directions of the nanocrystals and in this case, the formation of one-dimensional rod structures. A similar surface energy effect induced by foreign transition metal ions has been used to explain the growth of Pt nanoparticles of well-defined shapes [21-23]. The introduction of Ag ions to Pt seed solution led to the anistropic growth where the addition of Ag in increasing amounts led to enhanced growth along the $\langle 100 \rangle$ direction. As the silver concentration (relative to Pt salt concentration) is increased from 1.1 to 32 mol. %, the shape evolves from cubes to cuboctahedra to octahedra. This induced anisotropic growth is assumed to be related to stronger adsorption of Ag onto the (100) face of Pt, thereby inhibiting growth along that direction. Growth is inhibited and the adatom to nanocrystal surface reaction can only occur on the (111) seed faces.

The use of polymer and foreign ions to direct anisotropic growth as well as stabilize higher surface energy surfaces has enabled the synthesis of nanocrystals with a variety of shapes (see Figure 7), but with regards to the application of these materials in catalysis, it is still unknown whether their structure will influence catalytic chemistry due to the presence of residual metal or inorganic ions or polymer residues. One area of

concern related to these nanocrystals and their applications in catalysis is their surface chemistry and the ability of their surfaces to catalyze heterogeneous chemistry. We have focused extensively on the removal of polymer from the surface of monodisperse Pt nanoparticles (Chapter 9) and the removal of Ag from the surface of Pt nanocrystals for applications in catalysis (Chapter 10).

2.2.2 *Synthesis of ordered catalyst supports*

Since the discovery of the M41S family of molecular sieves by researchers at the Mobil Research and Development Corporation [24, 25], one of the most exciting potential applications envisioned for this class of materials was catalysis, whether used as a support for transition metal nanoparticles or as the actual catalyst itself. These materials contain pores with diameters of 2-50 nm; considered mesopores according to the International Union of Pure and Applied Chemistry (IUPAC) definition [26], which breaks past the size constraint of zeolites and represent the main reason why there was an initial excitement in the catalysis community about using these materials as catalyst supports. They can have larger surfaces areas (up to 1000 m^2 g^{-1}) ; an ideal trait of a catalyst support. It must be stated that while many of these mesoporous materials have long range ordering of the pore packing, the pore walls are amorphous, lack long range order and are therefore not crystalline [27]. The M41S materials were synthesized by novel approach in materials science, where instead of using single molecule templating agents (as is done with zeolites), self assembled molecular aggregates or supramolecular assemblies are employed as the structure directing agents (SDAs). There have been a number of models proposed to explain the formation of mesoporous materials. On the

most common level, all models predict that surfactants in solution guide the formation of

the inorganic mesostructure from solubilized inorganic precursors (Figure 9).
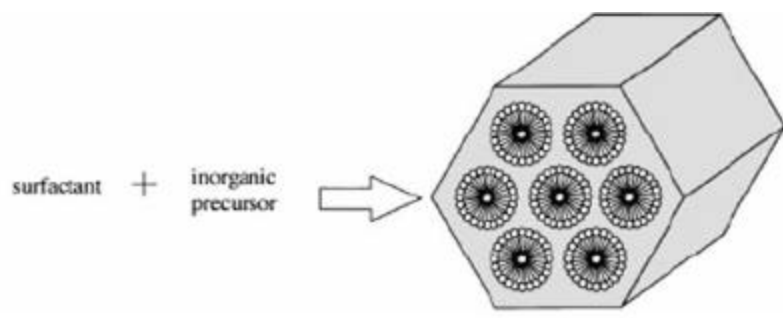
Figure 2.9. Schematic representation of the formation of SBA-15 type materials from inorganic precursors and organic surfactants. From ref. [27].

Surfactants contain a hydrophilic head group and a long hydrophobic group within the

same molecule and will self organize in such a way to minimize contact between the two

incompatible ends. The mechanism for formation of mesoporous silicate was initially

outlined in two possible pathways by Beck *et al.* [24]. The first model assumes that the

primary structure-directing element is the water-surfactant liquid crystal phase (pathway

(1) of Figure 10), while the second model suggests that the addition of the silicate orders

the subsequent silicate encased surfactant micelles.
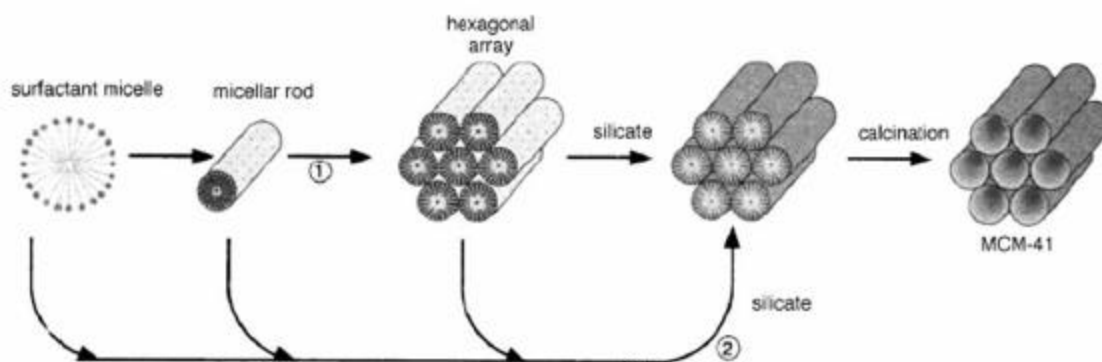
Figure 2.10. Two possible pathways for the liquid crystal templating (LCT) mechanism for the formation of MCM-41. From ref. [24].

In both pathways, the inorganic components (which are negatively charged due to the high pH used) preferentially interact with the positively charged ammonium head groups of the surfactants and condense into a solid, continuous framework. The resulting organic-inorganic mesostructure could be alternatively viewed as a hexagonal array of surfactant micellar rods embedded in a silica matrix and upon removal of the surfactants, an open, mesoporous framework is realized. This constitutes pathway (1), and it has recently been determined that surfactant concentrations used were far below the critical micelle concentration (CMC) required for hexagonal liquid crystal (LC) formation [28]. The second pathway for LCT is postulated as a cooperative self-assembly of the surfactant and silicate precursor species below the CMC. This pathway is rather vague and no support for its validity is known, except that no preformed LC phase is necessary for MCM-41 formation. Stucky and co-workers have suggested a generalized mechanism of formation based on the specific type of electrostatic interaction between a given inorganic precursor, denoted I and surfactant head group, denoted S [29, 30]. In the case of pathway (2) of Figure 10, involved anionic silicate species and cationic quaternary ammonium surfactant if we consider the formation of MCM-41, would be classified as a S^+I^- pathway. Conversely, if the solution was held at a pH below the isoelectric point of silica (pH ≈ 2), the silicate species would be cationic, I^+. The same ammonium surfactant, S^+ could be used as a templating agent but the halide counterion X^- would become involved in this pathway in order to buffer the repulsion between I^+ and S^+ by means of weak hydrogen bonding. These examples demonstrate that this classification system (S, I) can be used to describe various types of inorganic-organic

interactions. This mechanism is based on electrostatic interaction and referred to as the generalized LCT mechanism; it is shown schematically in Figure 11.
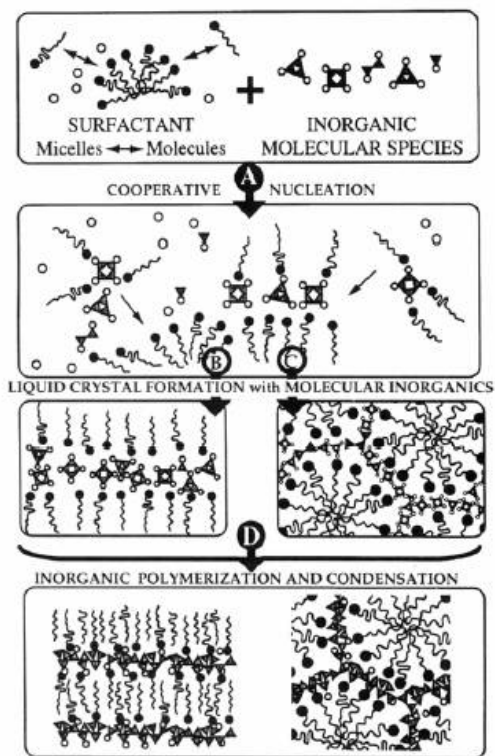
Figure 2.11. Cooperative templating of the generalized LCT mechanism. From ref. [29].

In frame (A) of Figure 11, single chain reactant molecules react preferentially with silicate polyanions (e.g. dimers, double three and four rings) which displace the original surfactant monoanions. Micelles serve as a surfactant molecule source or are rearranged according to the anion charge density and shape requirements. Nucleation and rapid precipitation (frames B and C) of organized arrays takes place with configurations determined by the cooperative interactions of ion-pair charges, geometries, and organic van der Waals forces. Condensation of the silicate phase (frame D) with increasing time and temperature leads to a decrease silicate framework charge and this

may lead to liquid crystal like phase transitions as the surfactant phase tries to reorganize the changing interface density [31, 32].

Stucky and co-workers have found that balanced coulombic, hydrogen bonding and van der Waals interactions with charge matching in aqueous syntheses provide an effective means for enhancing long range order. These interactions are particularly important at the inorganic-organic interface and can be realized by working with cationic silica species below the aqueous isoelectric point of silica. Conducting syntheses with cationic surfactants in HCl below the aqueous isoelectric point of silica the key interactions are among the cationic surfactant (S^+), chloride ion (X^-) and cationic silica species (I^+), which is Si-OH. This interaction is designated as $S^+X^-I^+$ and the overall charge balance is provided by association with an additional halide ion. Solubilization of nonionic poly(alkyene oxide) surfactants and block copolymers in aqueous media is due to the association of water molecules with the alkylene oxide moieties through hydrogen bonding, which should be enhanced in acidic media where hydronium ions (H_3O^+), instead of water molecules are associated with the alkylene oxygen atoms, thus enhancing long range coulombic interactions. If conducted below the aqueous isoelectric point of silica, cationic silica will be present as precursors and the assembly should proceed through a $(S^0H^+)(X^-I^+)$ intermediate. Under these conditions, Stucky *et al*. synthesized highly ordered hexagonal mesoporous silica structures in the presence of triblock poly(ethylene oxide) – poly(propylene oxide) – poly(ethylene oxide) (PEO – PPO – PEO) copolymers [33]. The mesoporous silica was named SBA-15 and is the support used for the synthesis of catalysts by the capillary inclusion method.

The assembly of mesoporous silica organized by nonionic poly(alkene oxide) triblock copolymer species in acidic media occurs by the hydrolysis of alkoxysilane species,

$$\text{Si}(\text{OEt})_4 + n\text{H}_3\text{O}^+ \xrightarrow{\text{hydrolysis(pH<2)}} \text{Si}(\text{OEt})_{4-n}(\text{OH}_2^+)_n + n\text{EtOH}$$
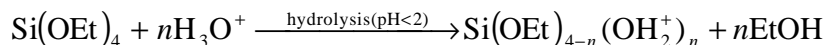
which is followed by the partial oligomerization at the silica. $\text{Si}(\text{OEt})_4$ is shorthand for tetraethoxysilane and EtOH for ethanol, respectively. The EO moieties of the surfactant in strong acid media associate with hydronium ioins

$$\text{REO}_m + y\text{HX} \xrightarrow{\text{H}_2\text{O}} \text{REO}_{m-y}\left[(\text{EO})\cdot \text{H}_3\text{O}^+\right]_y \cdots y\text{X}^-$$

where R is poly(propylene oxide) and X^- is Cl^- in the case of SBA-15 synthesis [34]. It is proposed that the charge associated EO units and the cationic silica species are assembled together by a combination of electrostatic, hydrogen bonding, and van der Waals interactions, of the form, $\text{REO}_{m-y}\left[(\text{EO})\cdot \text{H}_3\text{O}^+\right]_y \cdots y\text{X}^- \cdots \text{I}^+$. Further condensation of the silica species and organization of the surfactant and inorganic species results in the formation of the lowest energy silica-surfactant mesophase allowed by the solidifying network.

Another route to LC templating and the formation of mesoporous silica is through the use of nonionic surfactant (N^0) and a nonionic inorganic precursor (I^0) [35]. The materials lack the long range ordering of pores and have a higher amount on interparticle mesoporosity because the lack of electrostatic interactions prevents long range effects from controlling the micelle packing. The driving force for assembly is hydrogen bonding. Pinnavaia has utilized a hydrogen-bonding synthesis route using surfactants with a polyethylene oxide head group with adjustable head group and tail group lengths enabling pores as large as 5.8 nm to be synthesized. The nonionic route produces pores

that our more wormlike than rodlike cylinders. The material is referred to as MSU-H

[36] and many of the physical properties of the nanoparticle encapsulation silica (Chapter

6) are similar to the MSU materials.

2.2.3   Combined solution phase nanoparticle synthesis and ordered mesoporous oxide

supports

The synthesis of nanoparticles and their incorporation into mesoporous silica

matrices by sonication or encapsulation represent two novel methods of catalyst synthesis.

Both methods differ considerable from the methods outlined in section 2.1 because the

size of the nanoparticle and its size distribution are not determined by random physical

forces but rather by well-controlled nucleation-growth kinetics.   The methods are

discussed in more detail in Chapters 4 and 5 but introduced here to emphasize the

difference between our synthetic scheme and classical catalyst synthesis methods.   The

application of mesoporous materials in catalysis has recently been reviewed [37, 38].

The first method developed in our group for the preparation of high surface area

silica catalysts with monodisperse Pt particle was capillary inclusion (CI) (Figure 12) [39,

40].
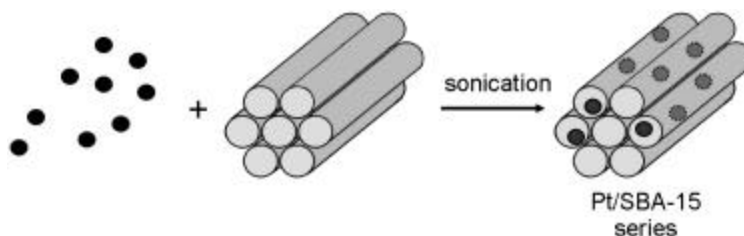
Figure 2.12. Schematic of capillary inclusion (CI) catalyst synthetic method. Sonication of calcined SBA-15 and Pt(X)-PVP particle, where X = 1.7, 2.6, 2.9, 3.6 and 7.1 nm leads to catalyst samples with high loading and excellent dispersion of Pt nanoparticles within the silica matrix.

The application of sonication led to the primary inclusion of nanoparticles within the channels of the calcined SBA-15. Sonication increased the rate of nanoparticle transport into the pore by mechanical agitation which influenced the random diffusion of the nanoparticles, enhanced the pressure drop in the silica pores or supplied the required energy for nanoparticles to diffuse on the outer surface of the silica particles until it was able to diffuse into the pore. Initial observations suggest that within the first minute of sonication, all nanoparticles adsorb to the outer surface of the silica, as if the silica behaves as a sponge. Evaluation of catalyst samples by electron microscopy demonstrate that after a ½ h, the particles have accumulated on the edge of the silica particles or begun entering the channel. Little change occurs after 90 minutes of sonication. The method is effective at achieving low (0.2 % by weight) or high (~14 % by weight) loadings of Pt, with most particles located within the pores. One of the primary disadvantages of the technique, as it appears that sonication (even at the low powers used here) disrupts the mesoporous material [41].

The second method is a "one pot" synthesis in which PVP stabilized Pt nanoparticles are encapsulated in mesoporous silica by the addition of silica precursors and triblock copolymers followed by *in-situ* hydrothermal synthesis. A schematic representation of the nanoparticle encapsulation (NE) method [42, 43] is shown in Figure 13. In solution it is believe the Pt-PVP nanoparticles are located within the triblock copolymer micelles and therefore all Pt nanoparticles should be located within the internal volume of the hexagonally arranged pores (see Chapter 5 for postulated mechanism). This synthetic method is similar to co-precipitation (Section 2.1.1) in that
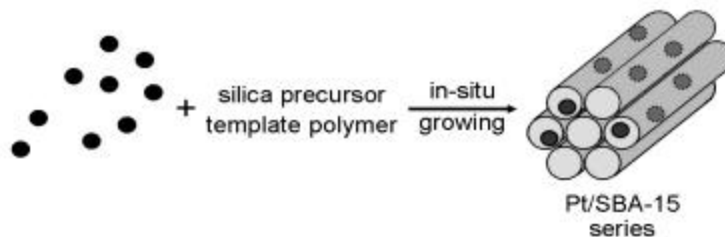
Figure 2.13. Schematic of nanoparticle encapsulation (NE) catalyst synthetic method. Addition of silica precursor and mesoporous silica matrix template polymer leads to a Pt-PVP nanoparticle solution leads to the encapsulation of Pt-PVP nanoparticles by mesoporous silica.

the active component and support matrix are precipitated from solution and leads to intimate contact between the two phases, but has the inherent advantage of preformed monodisperse nanoparticles. One disadvantage that may be apparent with the nanoparticle encapsulation method is the inclusion of the active component in the bulk of the support matrix. This is a major disadvantage of catalysts prepared from co-precipitation and maybe a problem with nanoparticle encapsulated Pt/SBA-15.

2.2.4 Comparison of classical catalyst preparation methods with capillary inclusion and nanoparticle encapsulation methods

There are numerous methods to synthesize catalysts, many of which are only applicable under certain circumstances. The method of synthesis vary by the solvent in which synthesis occurs, the type of metal precursor used, whether other species are present during synthesis (support precursor, counter ions, etc.). Table 1 is a compilation of the different catalyst synthesis methods and the required activation steps required to obtain dispersed metallic nanoparticles. One goal of catalyst synthesis is to develop protocols which produce monodisperse nanoparticles (see Chapter 1). It has been shown that activation steps such as drying, calcination and reduction can influence the particle size to a greater extent than the synthetic method itself. The two methods developed here

Table 1. Comparison of catalyst preparation methods

Method	Solvent	Metal Precursor	Other species present	Further activation steps[b]			
				Washing, hydrolysis, or evacuation	Drying	Calcination	Reduction
Coprecipitation	Inorganic	Salt	Support precursor	+	+	+ (-)	+ (-)
Impregnation	Inorganic	Solvated cation	Counteranion	-	+	+ (-)	+
		Complex anion	Counteraction	-	+	+ (-)	+
Ion exchange	Inorganic	Complex cation	Counteranion / Competing cation	+	+	+ (-)	+
	Inorganic	Complex anion	Countercation / Competing anion	+	+	+ (-)	+
Metal precursor decomposition	Organic	Metal cluster compound	--	-	-	+ (-)	+
Vapor phase deposition	--	Atoms (metal vapor)	--	+	+	-	-
Capillary Inclusion (CI)[c]	**Inorganic/ Organic**	**Metal colloids**	--	+	+	+	+
Nanoparticle Encapsulation (NE)	**Inorganic**	**Metal Colloids**	**Support precursors**	+	+	+	+

[a]All catalyst preparation methods have been discussed in sections 2.1 and 2.2.

[b]+ or − indicates whether or not the corresponding activation step has been performed.

[c]Also referred to as chemical deposition. From ref. [12].

require washing, drying, calcination and reduction. The influence of washing and drying on nanoparticle stability (*i.e.* agglomeration) has been determined minimal, but the impact of calcination and reduction pretreatments has not been entirely elucidated. It appears that calcination is the most important activation step for both the CI and NE catalysts solely for the purpose of removing the adsorbed surface templating polymer, PVP. Ideally, one would like to produce "naked" or surfactant free nanoparticles [44]. This is a difficult task due to the inability to stabilize the particles in solution and prevent them from aggregating. The preparation, stabilization and catalytic activity of naked Au particles for the aerobic oxidation of glucose to gluconate have recently been demonstrated [44]. The authors found that a water dispersed Au colloidal sol was much more active for the oxidation reaction than polyvinyl alcohol (PVA), polyvinylpyrrlidone (PVP) or tetrahydroxymethylphosphonium chloride (THPC) protected nanoparticles. Two alternative methods to polymer stabilization have been suggested in the literature. Klabunde and Tanaka [45] have suggested that metal atoms can be stabilized in solution by solvation with organic solvent molecules. Solvation of metal atoms and subsequent nanoparticle formation has been confirmed by other researchers [46 – 48]. The solvation mechanism of Klabunde and Tanaka [45] suggests from extensive studies of Ni-pentane and Ni-toluene systems that the primary species on the catalyst surface are C_1 fragments. Bönnemann and co-workes [47] have shown that Mn, Pd and Pt organosols can be stabilized in tetrahydrothiopene (Figure 14). If the small organic molecule can be removed from the nanoparticle surface, which should be rather facile compared with removal of a polymer, such as PVP, this method represents a rather clean method for the synthesis of monodisperse nanoparticles.

Figure 2.14. Reprensenation of Mn, Pd, and Pt organosol stabilized by tetrahydrothiopene. From ref. [47].

A second method that has been developed is the electrostatic stabilization of metal nanoparticles. Electrostatic adsorption shown schematically in Figure 15 [49] is the adsorption of ions (such as Br^- and Cl^-) to the often electrophilic metal surface [50].
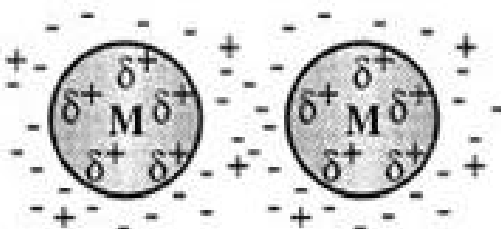
Figure 2.15. Schematic image of two electrostatically stabilized nanoparticles. Ions adsorb onto the surface of the nanoparticles creating an electrical double layer which provides Coulombic repulsion and thus stabilization against aggregation. From ref. [51].

The charge on the nanoparticle surface is partially positive, δ^+ and doesn't possess a full positive charge but is an electrostatic charge mirror produced by the adsorption on X ions [52]. Therefore, the resultant stabilized nanoparticle is anionic. Finke and co-workers have proven that the schematic in Figure 15 is a good representation of Ir^0 clusters composed of ~ 300 atoms stabilized by adsorbed polyoxoanions which render the surface anionic as determined by electrophoresis [53]. The electrostatically stabilized

particles have a number of advantages over the sterically (polymer) stabilized and solvation stabilized nanoparticles. After deposition on a surface, the removal counter anion should be relatively facile as compared to removal of large polymeric molecules. The further development of naked nanoparticle synthesis or the electrostatic stabilization of nanoparticles may eliminate the need for a calcination step and require only a reduction or a washing step.

2.3   References and Notes

1.   K. Morikawa, T. Shirasaki, M. Okada, *Adv. Catal*. 20 (1967) 97.

2.   A. G. Walton, *The Formation and Properties of Precipitates*. Interscience, London, 1967.

3.   R. L. Augustine, *Heterogeneous Catalysis for the Synthetic Chemist*. Marcel Dekker, New York, 1996.

4.   S. J. Teichner, G. A. Nicolaon, M. A. Vicarini, G. E. Gardes, *Adv. Coll. Inter. Sci*. 5 (1976) 245.

5.   J. Haber, J. H. Block, B. Delmon, *Pure Appl. Chem.* 67 (1995) 1257.

6.   R. W. Maatman, C. D. Prater, *Ind. Eng. Chem*. 49 (1957) 253.

7.   J. P. Brunelle, *Pure Appl. Chem.* 50 (1978) 1211.

8.   J. P. Brunelle, *Stud. Surf. Sci. Catal*. 3 (1979) 211.

9.   J. Phillips, J. A. Dumesic, *Appl. Catal*. 9 (1984) 1.

10.   B. C. Gates, *Chem. Rev*. 95 (1995) 511.

11.   Y. I. Yermakov, B. N. Kuznetsov, V. A. Zakharov, *Catalysis by Supported Complexes*. Elsevier, Amsterdam, 1981.

12.   M. Che, C. O. Bennett, *Adv. Catal*. 36 (1989) 55.

13.   T. Kubo, H. Arai, H. Tominaga, T. Kunugi, *Bull. Chem. Soc. Jpn*. 45 (1972) 607.

14.   G. R. Wilson, W. K. Hall, *J. Catal*. 17 (1970) 190.

15.   S. C. Davis, K. J. Klabunde, *Chem. Rev*. 82 (1982) 153.

16. C. B Murray, C. R. Kagan, M. G. Bawendi, *Annu. Rev. Mater. Sci*. 30 (2000) 545.

17. V. K. La Mer, R. H. Dinegar, *J. Am. Chem. Soc*. 72 (1950) 4847.

18. J. Th. G. Overbeek, *Adv. Coll. Inter. Sci*. 15 (1982) 251.

19. A. W. Adamson, A. P. Gast, *Physical Chemistry of Surfaces*. 6th Ed., Wiley Interscience, New York, 1997.

20. Y.-wook Jun, J. –H. Lee, J.-sil Choi, J. Cheon, *J. Phys. Chem. B* 109 (2005) 14795.

21. H. Song, F. Kim, S. Connor, G. A. Somorjai, P. Yang, *J. Phys. Chem. B* 109 (2005) 188.

22. R. M. Rioux, PhD Thesis, Chapter 9, University of California, Berkeley, 2005.

23. R. M. Rioux, H. Song, S. Habas, M. Grass, K. Niesz, J. D. Hoefelmeyer, P. Yang, G. A. Somorjai. Accepted in *Top. Catal*. 2005.

24. J. S. Beck, J. C. Vartuli, W. J. Roth, M. E. Leonowicz, C. T. Kresge, K. D. Schmitt, C. T. –W. Chu, D. H. Olsen, E. W. Sheppard, S. B. McCullen, J. B. Higgins, J. L. Schlenker, *J. Am. Chem. Soc*. 224 (1992) 10834.

25. C. T. Kresge, M. E. Leonowicz, W. J. Roght, J. C. Vartuli, J. S. Beck, *Nature* 359 (1992) 710.

26. J. Rouquérol, D. Avnir, C. W. Fairbridge, D. H. Everett, J. H. Haynes, N. Pericone, J. D. F. Ramsay, K. S. W. Sing, K. K. Unger, *Pure Appl. Chem*. 66 (1994) 1739.

27. J. Y. Ying, C. P. Mehnert, M. S. Wong, *Angew. Chem. Int. Ed*. 38 (1999) 56.

28.	J. C. Vartuli, C. T. Kresge, M. E. Leonowicz, A. S. Chu, S. B. McCullen, I. D. Johnson, E. W. Sheppard, *Chem. Mater*. 6 (1994) 2070.

29.	Q. Huo, D. I. Margolese, U. Ciesla, D. G. Demuth, P. Feng, T. E. Gier, P. Sieger, A. Firouzi, B. F. Chmelka, F. Schüth, G. D. Stucky, *Chem. Mater*. 6 (1994) 1176.

30.	Q. Huo, D. I. Margolese, U. Ciesla, P. Feng, T. E. Gier, P. Sieger, R. Leon, P. M. Petroff, F. Schüth, G. D. Stucky, *Nature* 368 (1994) 317.

31.	G. D. Stucky, A. Monnier, F. Schüth, Q. Huo, D. Margolese, D. Kumar, M. Krishamurty, P. Petroff, A. Firouzi, M. Janicke, B. F. Chmelka, *Mol. Cryst. Liq. Cryst*. 240 (1994) 187.

32.	A. Monnier, F. Schüth, Q. Huo, D. Kumar, D. Margolese, R. S. Maxwell, G. D. Stucky, M. Krishnamurty, P. Petroff, A. Firouzi, M. Janicke, B. F. Chmelka, *Science* 261 (1993) 1299.

33.	D. Zhao, J. Feng, Q. Huo, N. Melosh, G. H. Fredrickson, B. F. Chmelka, G. D. Stucky, *Science* 279 (1998) 548.

34.	D. Zhao, Q. Huo, J. Feng, B. F. Chmelka, G. D. Stucky, *J. Am. Chem. Soc*. 120 (1998) 6024.

35.	S. A. Bradshaw, E. Prouzet, T. J. Pinnavaia, *Science* 269 (1995) 1242.

36.	S. S. Kim, A. Karkamkar, T. J. Pinnavaia, M. Kruk, M. Jaroniec, *J. Phys. Chem. B* 105 (2001) 7663.

37.	T. Linssen, K. Cassiers, E. F. Vansant, *Adv. Coll. Inter. Sci.* 103 (2003) 121.

38.	D. Trong On, D. Desplantier-Giscard, C. Danumah, S. Kaliaguine, *Appl. Catal. A Gen*. 222 (2001) 299.

39. R. M. Rioux, PhD Thesis, Chapter 4, University of California, Berkeley, 2005.

40. R. M. Rioux, H. Song, J. D. Hoefelmeyer, P. Yang, G. A. Somorjai, *J. Phys. Chem. B* 109 (2005) 2172.

41. Y. Borodko, J. W. Ager, G. E. Marti, H. Song, K. Niesz, G. A. Somorjai, *J. Phys. Chem. B* 109 (2005) 17386.

42. R. M. Rioux, PhD Thesis, Chapter 5, University of California, Berkeley, 2005.

43. H. Song, R. M. Rioux, J. D. Hoefelmeyer, K. Niesz, M. Grass, P. Yang, G. A. Somorjai, Submitted to *J. Am. Chem. Soc*. 2005.

44. M. Commotti, C. D. Pina, R. Matarrese, M. Rossi, *Angew. Chem. Int. Ed*. 43 (2004) 5812.

45. K. J. Klabunde, Y. Tanaka, *J. Mol. Catal*. 21 (1983) 57.

46. M. T. Reetz, G. Lohmer, *J. Chem. Soc., Chem. Commun*. (1996) 1921.

47. H. Bönnemann, G. Braun, W. Brijoux, R. Brinkmann, A. Schulze Tilling, K. Seevogel, K. Siepen, *J. Organomet. Chem*. 420 (1996) 143.

48. R. A. T. M. van Benthem, H. Heimstra, P. W. N. M. van Leeuwen, J. W. Geus, W. N. Speckamp, *Angew. Chem., Int. Ed. Engl*. 34 (1995) 547.

49. J. D. Aiken III, Y. Lin, R. G. Finke, *J. Mol. Catal. A Chem*. 114 (1996) 29.

50. R. J. Hunter, *Foundations of Colloid Science*. Vol. 1, Oxford Univ. Press, New York, 1987.

51. J. D. Aiken III, R. G. Finke, *J. Mol. Catal. A Chem*. 146 (1999) 1.

52. M. E. Labib, *Coll. Surf.* 29 (1988) 293.

53. Y. Lin, R. G. Finke, *J. Am. Chem. Soc*. 116 (1994) 8335.

Chapter 3

Experimental Methods and Techniques

3.1   Experimental Techniques of Catalyst Characterization

A variety of techniques were used in this thesis for the characterization of as-synthesized colloidal Pt nanoparticles and mesoporous SBA-15 silica, as well the composite Pt/SBA-15 materials. The complexity of the materials requires a number of combined physical and chemical characterization to fully understand the solid state and catalytic chemistry of such materials. In most cases, catalysts were studied *ex-situ* before and after reaction, although infrared spectroscopy and thermal analysis were used *in-situ* to study the removal of structure directing polymer during oxidative and reductive activation steps.

3.1.1   Transmission electron microscopy (TEM)

Electron microscopy is a straightforward technique for the determination of the size of supported nanoparticles. However, since the wavelength associated with high energy electrons is on the order of interatomic distances or smaller, diffraction effects are important and may cause the image to not necessarily represent the shape of a particle [1]. Therefore, one must be careful when interpreting electron microscopy images. Transmission electron and a related technique, scanning electron microscopy (SEM) have

been widely used in the characterization of catalytic materials. Several books have been published on transmission electron microscopy experimental and theoretical topics [2], as well as a recent book published on the application of TEM in heterogeneous catalysis [3].

TEM uses transmitted and diffracted electrons to image a catalytic material. The instrument is very similar to an optical microscope, in that optical lenses are essentially replaced with electromagnetic lenses. In TEM, a primary electron beam of high energy (100-300 keV) and intensity passes through a condenser to produce parallel rays which impinge on the sample. In TEM, electrons which do not deviate far from the incident electron direction are those which provide the most information [2a]. Incident electrons ionize the samples that they impinge upon causing removal of one of the tightly bound inner-shell electrons from the attractive field of the nucleus. This process causes a number of secondary signals, which are summarized in Figure 1 and can be used to gain
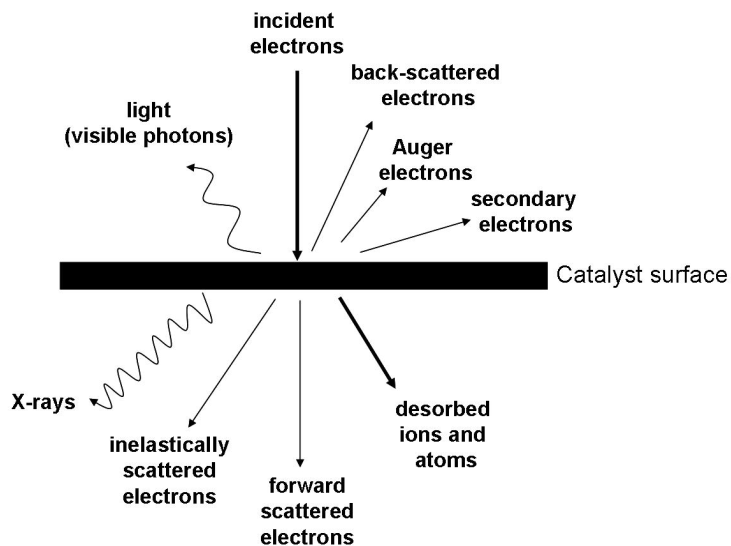
Figure 3.1. Signals generated when high energy electrons interacts with a thin specimen. The directions shown for each signal do not always represent the physical direction of the signal but indicate, in a relative manner, where the signal is the strongest or where it is detected. From reference [3].

further information on sample, including elemental analysis, as long as the TEM has the appropriate detection equipment. Figure 1 demonstrates that signals can be detected on both sides of the samples, but as the name of the technique implies, electrons which transmit through the samples are the most informative. The attenuation of the beam by the sample depends on the density and thickness. Transmitted electrons form a two-dimensional projection of the sample mass, which is subsequently magnified by electron optics to produce a bright field image. The dark field image is obtained from the diffracted electron beams, which are slightly off angle from the transmitted beam. TEM experiments are generally conducted in vacuum, although a few instruments with *in-situ* capabilities exist. Magnification in TEM instruments is ~$10^5 - 10^6$. TEM is a local probe of the material, as the incident electron beam has a diameter of ~1-10 nm.

Transmission electron microscopy (TEM) is the primary electron microscopy technique used in catalysis research. Detection of supported particles is possible provided that there is sufficient contrast between particle and support. Contrast in transmission mode is not only caused by attenuation of electrons due to density and thickness variations over the sample, but also to diffraction and interference. Particles in TEM often show less constrast than other identical particles because it is favorably oriented for Bragg diffraction (see following section on x-ray diffraction) by its lattice planes, such that the diffracted beam does not contribute to the image. Tilting the sample changes the orientation of the particle and 3-dimensional reconstruction of particles embedded within amorphous supports allows the shape of the nanoparticle to be determined and the location of the particles within the support. Images in dark field emphasize crystalline particles, but very small clusters may not be distinguishable from

the support. The capability of TEM imaging particles supported on an oxide support is shown in Figure 2.
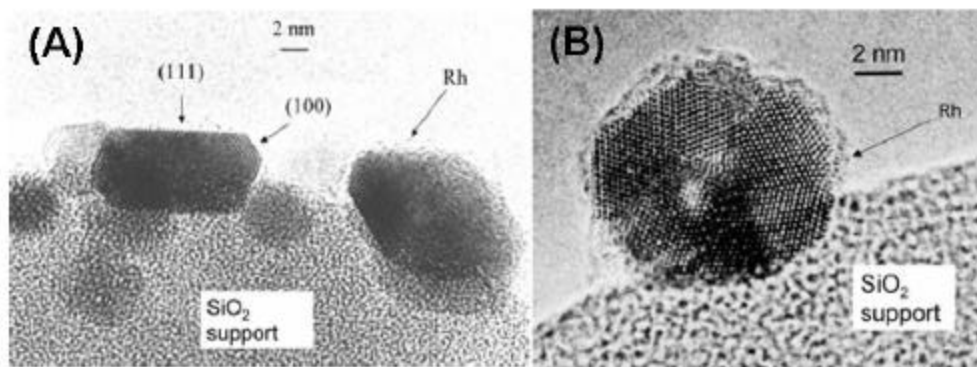
Figure 3.2. (A) Transmission electron microscopy image of Rh nanoparticles supported on nonporous SiO_2 spheres.   The image demonstrates that some particles are nearly cuboctahedral.   (B) High resolution TEM (HRTEM) image of Rh nanoparticle on nonporous silica sphere. From ref. [4].

Figure 2 demonstrates that the shape of these particles can be discerned from high quality images void of any artifacts. TEM is one of the only catalyst characterization techniques which enables the determination of particle size distributions (PSDs) [5], in ideal cases small angle x-ray scattering may also be used.   Other primary techniques used to determine particle size of supported nanoparticles are x-ray diffraction and selective gas adsorption which yield volume and surface average particle sizes, respectively. Ideally, meaningful PSDs are determined when a large number of particles are counted (≥ 300) from multiple samples. Three types of size distributions can be determined by measuring the particle sizes in TEM images. The number average or the mean particle size is

defined as $d_{mean} = \dfrac{\sum_i n_i d_i}{\sum_i n_i}$ where n_i is the number of particles with size d_i. The mean has

the property of being the diameter such that deviations sum to zero: $\sum_i n_i (d_i - d_{mean}) = 0$.

Two other commonly defined PSDs are the surface-area weighted average diameter,

$$d_s = \frac{\sum_i n_i d_i^3}{\sum_i n_i d_i^2}$$ and the volume weighted average diameter, $$d_v = \frac{\sum_i n_i d_i^4}{\sum_i n_i d_i^3}$$. For any

distribution of particle sizes, d_s will be larger than d_{mean}, d_v will be larger than d_s. In the

case of a monodisperse particle size distribution, $d_{mean} = d_s = d_v$. The relative values of

d_{mean}, d_s, and d_v indicate the breadth of the particle size distribution because the nth

moment involves d_n, the higher moments are strongly influenced by large values of d and

the sensitivity of high moments to the high end of the particle size distribution will be

shown to have great importance in particle size measurements. An example of a TEM

image of a Pt/Al$_2$O$_3$ catalyst and the corresponding number average PSD is shown in

Figure 3.
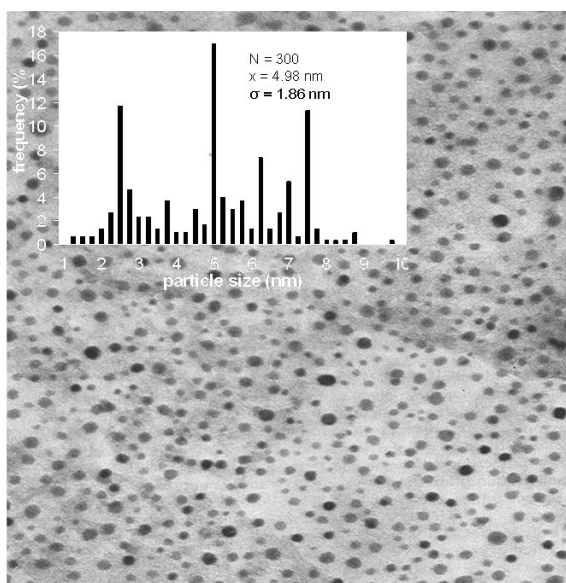
Figure 3.3. TEM micrograph of Pt/Al$_2$O$_3$ reforming catalyst from Exxon Research and Engineering Company. One millimeter represents 2.5 nm. Reproduced from ref. [6].

The mean particle size from counting 200 particles was 4.5 nm, but more informative

from the PSD is the indication that the PSD is actually trimodal with a high frequency of

particle sizes occurring at ~ 2.5 nm, 5 nm and ~7.5 nm. This indicates that the particles are far from monodisperse and may display very distinct catalytic chemistry if the reaction is sensitive to the structure of the catalyst.

Transmission electron microscopy was used in **Chapter 4** and **Chapter 5** for the determination of particle size distributions and in **Chapter 9** for determination of particle size and shape.

3.1.2   X-Ray diffraction (XRD)

X-rays have wavelengths in the angstrom range, and therefore are sufficiently energetic enough to penetrate solids and are well-suited to probe their internal structure [1]. X-ray diffraction is used to identify bulk phases, characterize defects and to estimate particle sizes. X-ray diffraction is the elastic scattering of x-ray photons by atoms in a periodic lattice (Figure 4A).
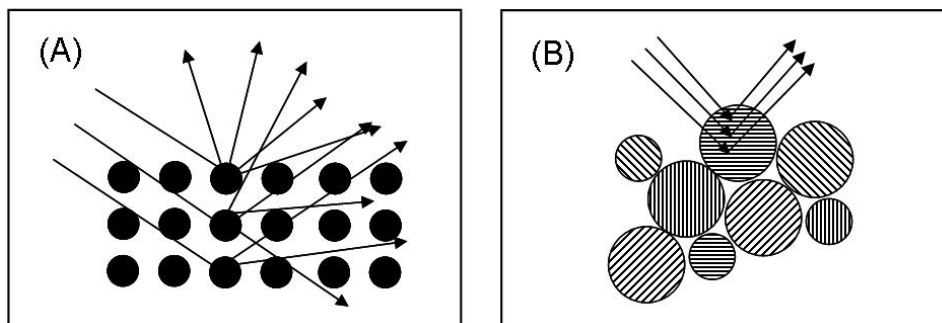
Figure 3.4. (A) X-ray scattering from periodic lattice. Two such waves will interfere constructively if the path difference is equal to an integer number of wavelengths. (B) Constructive interference may only arise from selected particle sizes in a powdered sample. Reproduced from ref. [1].

X-ray diffraction is based on the principles of constructive interference of radiation that is scattered by relatively large parts of the sample, therefore requiring long range order. There are two types of scattering of energy incident on atoms constituting a solid material.

They are (1) scattering in a very few directions, those satisfying the Bragg law, the scattering is strong and is called diffraction and (2) scattering in most directions, those not satisfying the Bragg law, there is no diffraction because the scattered rays cancel one another. In the former case, the scattering amplitudes add, and a diffracted beam may be defined as a beam composed of a large number of scattered rays mutually reinforcing one another [7].

In deriving Bragg's law for determining the periodicity of a particular material, two geometrical facts should be mentioned. The incident beam, the normal to the reflecting plane and the diffracted beam are always coplanar and the angle between the diffracted beam and the transmitted beam is always 2θ. Diffraction from a periodic lattice with lattice spacing, d is shown in Figure 5.
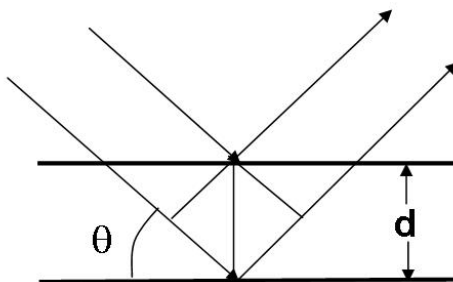
Figure 3.5. Diffraction of x-rays from a periodic lattice with spacing d. Reproduced from ref. [7].

Figure 5 demonstrates that scattered rays will be completely in phase if the path difference is equal to a whole number, n of wavelengths or if $n? = 2d_{hkl}\sin(?)$ where λ is the wavelength of the X-rays (1.54 Å for CuK_α radiation), d_{hkl} is the distance between two lattice planes, θ is the angle between the incoming X-rays and the normal to the reflecting lattice plane and n is the order of the reflection (integer value and generally taken as unity) [8]. The above equation is known as Braggs Law and was first

formulated by W. L. Bragg. It states the essential condition which must be met if diffraction is to occur. n may take on any integral value consistent with $\sin(\theta)$ not exceeding unity and is equal to the number of wavelengths in the path difference between rays scattered by adjacent planes. For example the two scattered rays of Figure 5 would differ in length of path (and in phase) by one wavelength, a so-called first order reflection. The rays scatted by all the atoms in the planes are therefore completely in phase and reinforce one another (constructive interference) to form a diffracted beam in the direction shown. In all other directions of space the scattered beams are out of phase and annul one another (destructive interference). The diffracted beam is rather strong compared to the sum of all the rays scattered in the same direction, simply because of the reinforcement which occurs. This diffracted beam is still very weak compared to the incident beam since the atoms of a crystal scatter only a small fraction of the energy incident on them. Measuring the angle, 2θ under which constructively interfering X-rays leave the crystal, the Bragg relation yields the corresponding lattice spacings, d. The XRD pattern of a powdered sample is measured with a stationary X-ray source and a movable detector, which scans the intensity of the diffracted radiation as a function of the angle 2θ between the incoming and the diffracted beams.

There is a case of when diffraction occurs under nonideal conditions, that is a case where Braggs law is not entirely correct. In the derivation of Braggs law, a perfect crystal and an incident beam composed of perfectly parallel and strictly monochromatic radiation was assumed. These conditions never actually exist because only an infinite crystal is really perfect and no radiation is strictly monochromatic. Deviations from Braggs law are important when dealing with metal particles of nanometer dimensions,

because small size alone of an otherwise perfect crystal can be considered a crystal imperfection because it is not infinite. This theoretical knowledge can be used to determine the particle size of nanoparticles from an x-ray diffraction spectrum. Previously, in the derivation of Braggs law, it was shown that scattered rays will be completely in phase if the path difference is equal to a integral values of wavelength. If the path difference between rays scatted by the first two planes differ only slightly from an integral number of wavelengths, then the plane scattering a ray exactly out of phase with the ray from the first plane will lie deep within the crystal. If the crystal is so small that this plane does not exist, then complete cancellation of all the scattered rays will not result. Therefore, it is evident that there is a connection between the amount of "out of phaseness" and crystallite size; very small crystallites cause broadening (a small angular divergence) of the diffracted beam. This implies diffraction occurs at angles near to, but not equal to, the exact Bragg angle. Consideration of the scattering of rays incident on the crystal planes at angles deviating slightly from the exact Bragg angle [7], it is found that the width of the diffraction curve increases as the thickness of the crystal decreases, because the angular range ($2\theta_1$-$2\theta_2$) increases as the number of planes decrease. Figure 6a demonstrates the effect of finite particle size on a diffraction curve, while Figure 6b illustrates the hypothetical case of diffraction occurring only at the exact Bragg angle. Figure 6a demonstrates that the diffracted intensity at angles near $2\theta_B$, but not greater than $2\theta_1$ or less than $2\theta_2$, is not zero but has a value intermediate between zero and the maximum intensity of the beam diffracted at an angle $2\theta_B$. The width, B is measured in radians at an intensity equal to the full width at half maximum (FHWM). It is
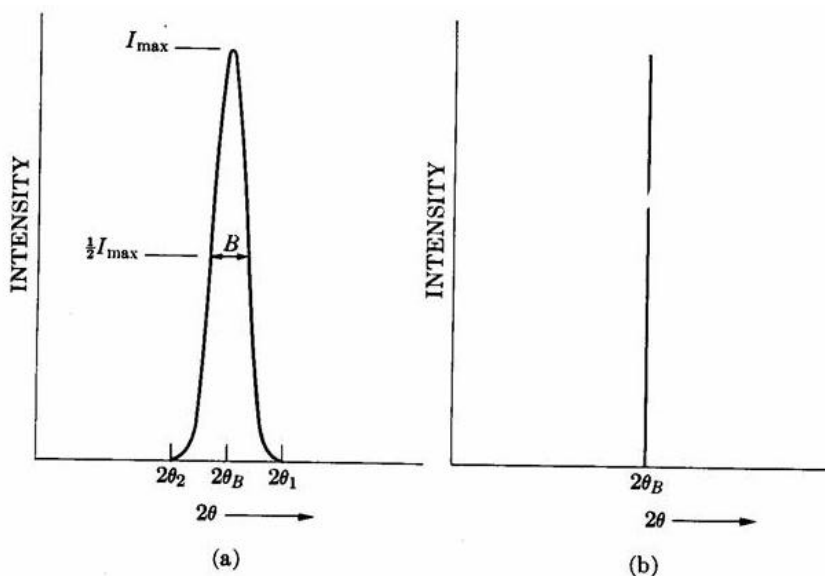
Figure 3.6. Effect of finite particle size on diffraction curves. (a) Influence of crystallite size on width of diffraction peak, (b) hypothetical case of diffraction occurring only at the exact Bragg angle. From ref. [7].

emphasized that B is an angular width, in terms of 2θ and not a linear width. If B is considered to be a measure of half the difference between the two extreme angles at which the intensity is zero, path difference equations, which are related to the entire thickness of the crystal rather than to the distance between adjacent planes, a formula known as the Scherrer equation [7] is derived which allows the estimation of particle size of very small crystallites from the measured width of their diffraction curves. The Scherrer equation is written as $d = \dfrac{0.9\lambda}{\beta\cos(\theta_B)}$, where d is a measure of the particle dimension in the direction perpendicular to the reflecting plane, β is the peak width, and λ and θ have the same previous meaning. The Scherrer equation indicates that measuring at smaller wavelengths yields sharper peaks because λ becomes smaller and the diffraction lines shift to lower angles, which decreases the $1/\cos(\theta_B)$ term. The particle size determined by XRD is a volume average size because the measured particle size is

merely the ratio of two moments in the particle size distribution, $\langle L^2 \rangle / \langle L \rangle$, which are weighted by the volume of the particles, and not by number or by surface area [1]. Line broadening due to the diffractometer itself has to be determined as a function of 2θ using a well defined crystalline material and β must then be corrected for this. The most common correction is Warren's correction [9], where $\beta = (B^2 - b^2)^{1/2}$ where B is the peak width at half maximum and b is the instrumental broadening [10]. The broadening of diffraction peaks for a series of Pt nanoparticles of various sizes is shown in Figure 7.
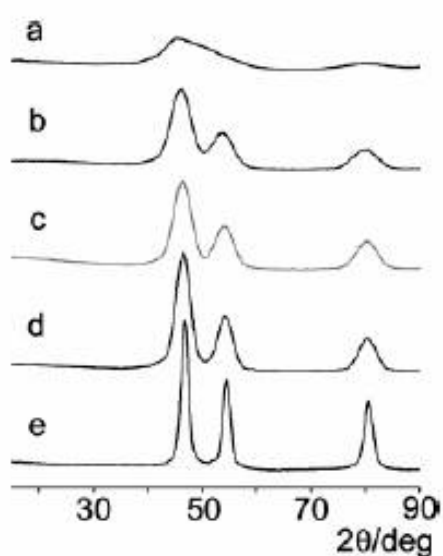
Figure 3.7. XRD data for free-standing Pt particles. (a) 1.7 nm, (b) 2.6 nm, (c) 2.9 nm, (d) 3.6 nm and (e) 7.1 nm. From ref. [11].

The experimental difficulties involved in measuring particle size from line broadening increases with the size of the particles measured. Accurate particle sizes are measured in the range 5–50 nm, but very good experimental technique is needed in the range of 50 – 100 nm. The maximum size measurement by line broadening techniques is ~ 200 nm. Peak broadening may also occur due to internal strain within the particle. Non-uniform

strain within a particle may give anomalously smaller particle sizes due to peak broadening.

When working with powdered samples, the high surface area support material usually has quite broad diffraction peaks because in its amorphous state it has limited long-range, translational order. An image of diffraction lines occurs because a small fraction of the powder particles are oriented such that by chance a certain crystal plane is at the right angle θ with the incident beam for constructive interference (Figure 4B). An inherent disadvantage of XRD is that it is more sensitive to particles that are sufficiently large (more crystalline), but it does not see particles that are either too small or amorphous. XRD is essentially insensitive to particles with a diameter $= 2.5$ nm when embedded in a high surface area amorphous support.

X-ray diffraction was used in **Chapter 4**, **Chapter 5** and **Chapter 9** for the determination of volume averaged particle sizes.

3.1.3   *Thermogravimetric analysis (TGA)*

Thermogravimetry (TG) is one of the most used techniques in thermal analysis, in which changes in the sample mass under a programmed temperature change is recorded as a function of temperature or time [12]. Thermogravimetry can be used to determine the thermal stability of a material (*i.e.* decomposition of molecular precursor grafted on solid support), kinetics of a reaction (surface catalyzed, solid state) and quantification of bulk composition. A TG apparatus is composed of an electric microbalance and a programmable heating unit. TG systems are classified according to the arrangement of the balance system and heating unit. Three common types of TG units exist, suspending, top-loading, or horizontal arrangement type. Both TGA instruments used in this

dissertation were based on a null point balance with an electric resistance furnace connected to a programmable temperature controller. A schematic of a suspending type TG instrument with a null point balance is shown in Figure 8.
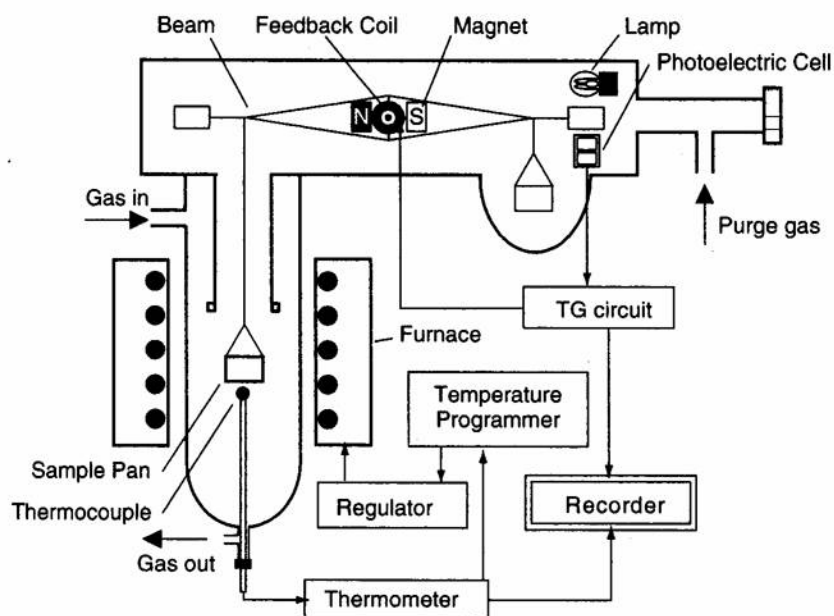
Figure 3.8. Schematic illustration of a suspending type TG apparatus. From ref. [12].

The operation of a TG apparatus includes sample heating with a furnace according to a temperature program (linear with the ability to change heating rates). As the sample mass changes, the beam will list which is detected by one of the photoelectric cells. The signals from the photoelectric cells are input into a differential amplifier, which outputs a current to the feedback coil for providing a counter torque to recover the balance of the beam. The current output is proportional to the mass change, therefore the change in sample mass can be recorded by measuring the current. This enables a TG curve to be obtained by recording the mass change and the sample temperature

continuously as a function of time. An example of the decomposition of a nanoparticle

encapsulation catalyst prepared in this thesis (Chapter 5) is shown in Figure 9.
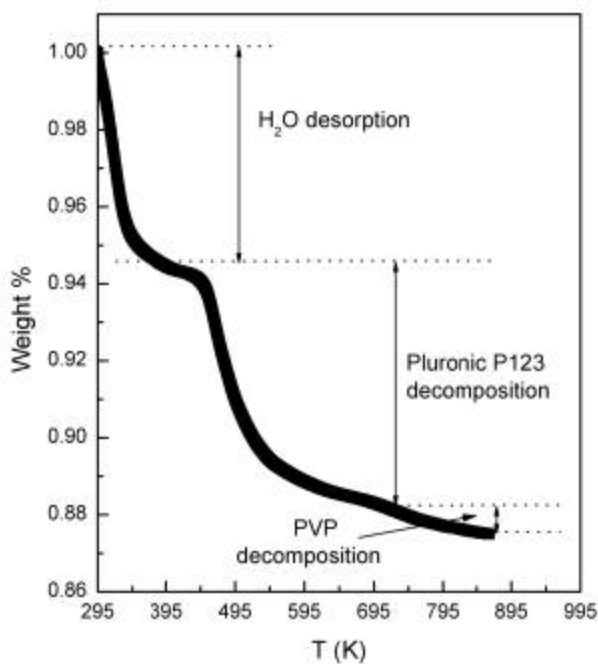
Figure 3.9. Thermogravimetry curve for decomposition of Pluronic triblock copolymer and PVP from 0.77% Pt(2.9 nm)/SBA-15 in oxygen. From ref. [13].

TG is a versatile experimental technique and various measuring conditions can be

applied depending on the sample and the purpose of measurements. In many cases, the

experimentally resolved TG curves change with measuring conditions and in order to

obtain a meaningful TG curve, conditions at which the thermal analysis is performed

should be chosen carefully. Sample amount is a critical parameter and depends on the

sample type and purpose of measurement. For reproducible results, smaller sample

amounts are preferred. Interpretation of TG traces from powdered samples can be

difficult due to the influence of particle size and its distribution on the shape and position

of the TG curve [14]. Practical measurements are carried out under isothermal or

nonisothermal conditions. In the case of isothermal measurement, the mass change at

constant temperature is recorded as a function of time. Measurements under nonisothermal conditions are the most frequently employed method, where the mass change of sample during a linear heating scheme. In order to reduce thermal gradients within the sample bed and influences of reaction heat (*i.e.* exothermic or endothermic processes), low heating rates are preferred (= 10 K min^{-1}). Measurements are usually conducted in inert gas (He, N$_2$, Ar) atmosphere, although reactive gases, such as hydrogen or oxygen can be used when studying sample weight loss under reducing or oxidizing conditions, respectively. When introducing reactive gases, the gas is introduced directly to the reaction chamber and removed at the end of the reaction chamber with a purge gas.

The type of thermal behavior occurring during a TG experiment can be more readily discerned when combined with information from a DTA curve. Quantitative analysis of the TG curve is achieved by correcting the fraction of mass change for the respective reaction steps by baseline data with reference to the original sample mass. The first derivative curve of the TG with respect to time or temperature is known as derivative TG, which enables detection of small mass changes and partially overlapped multi-step reactions.

Thermogravimetric analysis was used in **Chapter 5, Chapter 6, Chapter 8** and **Chapter 9** for the investigation of PVP removal from as-synthesized and encapsulated Pt particles.

3.1.4 Differential Thermal Analysis (DTA) and Differential Scanning Calorimetry (DSC)

Differential thermal analysis (DTA) and differential scanning calorimetry (DSC) are useful thermal analysis techniques for the study of endothermic or exothermic phenomena occurring on the surface or within the bulk of a substance. In DTA and DSC, the difference in temperature (ΔT) between the sample and reference material is measured while both are subjected to the same temperature program.   The basic principles of DTA and DSC are explained below. If a sample is heated at a constant rate (dT_p/dt = constant), the temperature of furnace (T_p), reference (T_R) and sample (T_S) change with time (t) according to Figure 10.
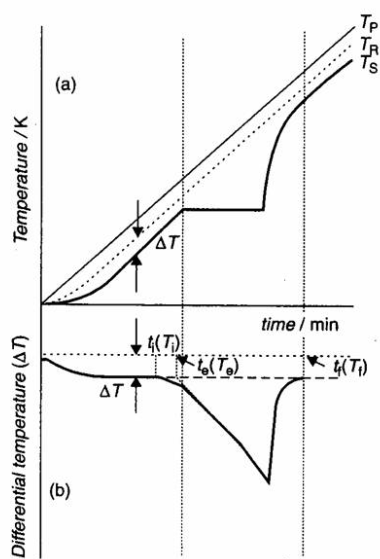
Figure 3.10. Basic principle of DTA and DSC. (a) Change in temperature of reference T_R and sample T_S with increasing furnace temperature, T_p. (b) Typical signal output converted to differential temperature, ΔT with passage of time. From ref. [15].

Steady state requires that T_R and T_S change at a constant rate of dT_p/dt, and according to Newton's law of cooling, the heat transferred from the furnace to the sample side can be written as

$$\frac{dq_s}{dt} = \frac{1}{R}(T_p - T_s) \qquad\qquad (1)$$

where R represents the heat resistance between the furnace and the sample. The heat resistance is the reciprocal of the heat transfer coefficient (lumped convection, conduction and radiation). Since heat transferred to the sample is used for heating of the sample (this also includes the sample cell), the rate of heat flow is such a system is

$$\frac{dq_s}{dt} = [C_{cs}(T) + C_s(T)]\frac{dT_p}{dt} \qquad (2)$$

where $C_{cs}(T)$ and $C_s(T)$ are the heat capacity of the sample cell and the sample, respectively. In a similar manner, the rate of heat flow on the reference side is derived based on the condition that the heat resistance on the reference side is the same as that in the sample side

$$\frac{dq_r}{dt} = \frac{1}{R}(T_p - T_r) = [C_{cr}(T) + C_r(T)]\frac{dT_p}{dt} \qquad (3)$$

where $C_{cr}(T)$ and $C_r(T)$ are the heat capacity of the reference cell and reference, respectively. Combining equations, the following heat balance is obtained

$$\frac{dq_s}{dt} - \frac{dq_r}{dt} = -\frac{1}{R}(T_s - T_r) = \{[C_{cs}(T) - C_{cr}(T)] + [C_s(T) - C_r(T)]\}\frac{dT_p}{dt} \qquad (4)$$

In general, the heat capacity and the mass of the sample and reference cell are equal ($C_{cs}(T) = C_{cr}(T)$). Equation (4) is simplified and now depends only on the heat capacity of the sample and reference

$$\frac{dq_s}{dt} - \frac{dq_r}{dt} = \frac{1}{R}(T_s - T_r) = [C_s(T) - C_r(T)]\frac{dT_p}{dt} \qquad (5)$$

Quantitative measurements cannot be performed with DTA because the heat resistance R is undefined. Conversely, in heat flux DSC, heat transfer occurs via a well-defined path of heat resistance. Equation (5) demonstrates that the heat capacity difference between the sample and reference is obtained by measuring the differential temperature, T_s-T_r. In

power consumption DSC, power is supplied to the heaters in order to keep the same temperature at the sensors located under the sample and reference cell, and the energy supplied per unit time to the sample and the reference is measured to obtain $[C_s(T) - C_r(T)]\dfrac{dT_p}{dt}$. The primary output of a DSC instrument is a voltage as a function of time. The measured voltage is transformed to temperature or heat flow (J s^{-1})

$$\frac{d\Delta q}{dt} = K(T)\frac{dq_m}{dt} = [C_s(T) - C_r(T)]\frac{dT_p}{dt} \qquad (6)$$

where K(T) is a temperature-dependent factor and dΔq_m/dt is the measured signal.

A transition or reaction occurring on the sample surface or bulk yields a peak in the DSC curve. In general, an exothermic change is represented by a convex peak, whereas a concave peak represents and endothermic reaction. The initial peak temperature, T_i, is the temperature (at time t_i) where the measured curve deviates from the baseline while the final peak temperature, T_f is the temperature (at time t_f) where the curve reaches the final baseline. The interpolated baseline is a horizontal straight line between T_i and T_f (assuming $\Delta C_p \approx 0$), the extrapolated peak onset temperature, T_e, is the temperature (at time t_e) where the extrapolated ascending peak slope intersects the interpolated baseline. In general, T_e is read as the temperature representing the transition or reaction.

Differential scanning calorimetry was used in **Chapter 8** for the investigation of PVP removal from encapsulated Pt particles.

3.1.5 *Temperature programmed oxidation (TPO) and desorption (TPD)*

Temperature programmed desorption (TPD) measurements are generally conducted in two types of experimental regimes: studies of materials having low surface

areas at ultra-high vacuum (UHV) conditions and studies of porous catalysts at ambient pressures [16]. The primary difference in analysis of these experiments is that readsorption during desorption must be addressed on high surface area materials. Desorption is always endothermic and therefore requires energy. The desorption energy, E_d is at least equivalent to the heat of adsorption (ΔH_{ads}) and can have an activation barrier associated with it. For simplicity, a TPD experiment in the absence of readsorption is considered first. The desorption of species A according to the reaction: $A^* \rightarrow A(g) + {}^*$, where * denotes a surface atom. It follows that the rate of desorption, r_d is given by

$$r_d = -\frac{d\rho_A}{dt} = \nu_A \exp\left(-\frac{E_d}{RT}\right)\rho_A \qquad (7)$$

where ν_A and E_d are the pre-exponential factor and the activation energy for desorption, ρ_A is the surface concentration of species A and T is the absolute temperature, respectively. Temperature programmed desorption experiments are conducted by increasing the temperature linearly with time, $T = T_0 + \beta t$, where T_0 is the initial temperature and β is the heating rate. The rate of desorption now becomes

$$\frac{d r_A}{dt} = -\frac{u_A}{b}\exp\left(-\frac{E_d}{RT}\right)r_A \qquad (8)$$

The TPD process is monitored by measuring the rate of desorption versus temperature. In general, a plot of r_d versus T passes through a maximum. At low temperatures, the rate of desorption is negligible because of the exponential dependence of the rate constant for desorption rate on temperature, and the rate of desorption becomes small at high temperatures because the surface concentration (or coverage) approaches zero near

completion of the TPD experiment. The shape of the TPD spectrum can be used to determine the order of desorption (zero, first or second). For first order desorption, the TPD peak is asymmetric, starting with a gradual increased in r_d at lower temperatures followed by a sharper decrease in r_d at higher temperatures. In contrast, TPD peaks for second order desorption processes are symmetric [17]. A typical first order desorption trace is shown in Figure 11.
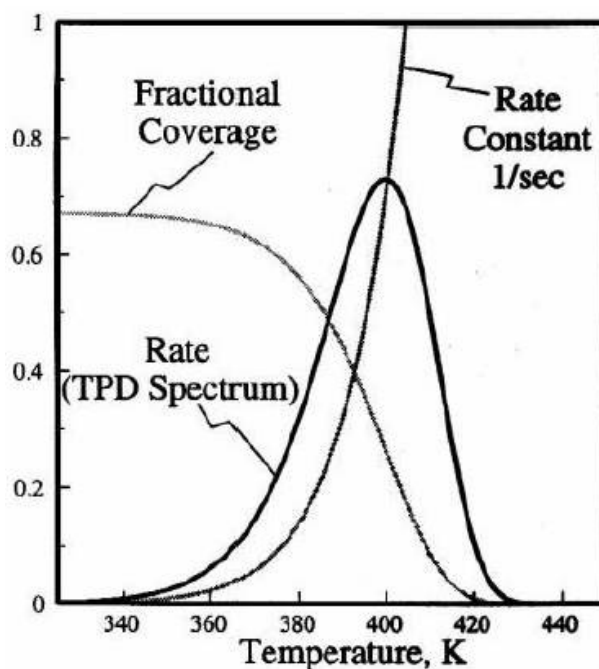
Figure 3.11. Typical UHV first order TPD experiment where readsorption effects are negligible. The coverage decreases with temperature while the first order rate constant increases with temperature. From ref. [18].

TPD studies of porous catalysts are generally carried out in reactors designed to minimize concentration gradients. The design equation for the nonsteady state continuous flow stirred tank reactor (CSTR) is appropriate for TPD analyses

$$\frac{dF_{si}}{dt} = \left(F_{si}^0 - F_{si} + O_i\right)\frac{F_s}{N_s} + \frac{F_{si}}{F_s}\left(\frac{dF_s}{dt}\right) - \frac{F_{si}}{N_s}\left(\frac{dN_s}{dt}\right) \qquad (9)$$

where F_{si} and F_{si}^0 are the outlet and inlet molecular site velocities of species i,

respectively; Ω_i is the turnover frequency of formation of species i; F_s is the total

molecular site velocity for all species leaving the reactor; and N_s is the number of gas-

phase molecules per site. If a large amount of inert material is present such that F_s is

constant and equal to the total molecular site velocity entering the reactor, F_s^0, and the

heating rate is sufficient such that β/T is much less than F_s/N_s, then the last two terms on

the right hand side can be ignored to give

$$\frac{dF_{si}}{dt} = \left(F_{si}^0 - F_{si} + \Omega_i\right)\frac{F_s^0}{N_s} \tag{10}$$

The TPD experiment is usually monitored by measuring the pressure of the desorbing

species, P_A, while the temperature of the catalyst is increased at a linear rate. The

pressure is related to $F_{s,A}$ by the relation, $P_A = \dfrac{F_{s,A}}{F_s^0} P^0$, where P^0 is the ambient pressure.

Because the feed to the reactor is typically a pure carrier gas that does not contain species

A, $F_{As}^0 = 0$, enabling the TPD design equation to be further modified

$$\frac{dP_A}{dT} = \left(-P_A F_s^0 + P^0 \Omega_d\right)\frac{1}{N_s \boldsymbol{b}} \tag{11}$$

where Ω_d is the net rate of desorption (in units of s^{-1}). For TPD experiments where

readsorption must be considered, the expression for Ω_d becomes

$$\Omega_d = -\frac{d\boldsymbol{q}_A}{dt} = \boldsymbol{u}_A \exp\left(-\frac{E_a}{RT}\right)\boldsymbol{q}_A - k_a P_A\left(1 - \boldsymbol{q}_A\right) \tag{12}$$

where θ_A is the fractional surface coverage by species A and k_a is the adsorption rate constant. If it assumed for simplicity that k_a is independent of temperature, the TPD design equation once again becomes

$$\frac{dP_A}{dT} = \left[-P_A F_s^0 + P^0 \boldsymbol{u}_A \exp\left(\frac{-E_d}{RT}\right)\boldsymbol{q}_A - P^0 k_a P_A (1-\boldsymbol{q}_A)\right]\frac{1}{N_s \boldsymbol{b}} \qquad (13)$$

Analysis of the TPD process at maximum pressure of desorption of species A give the following result for the temperature at which the pressure of the desorbing species a maximum, T_m

$$\frac{E_d}{RT_m^2} = \frac{\boldsymbol{u}_A}{\boldsymbol{b}} \exp\left(\frac{-E_d}{RT_m}\right)\frac{F_s^0 \left(F_s^0 + k_a P^0\right)}{\left[F_s^0 + k_a P^0 (1-\boldsymbol{q}_{Am})\right]^2} \qquad (14)$$

where θ_{Am} is the surface coverage at the peak maximum, approximately equal to half the initial peak coverage. Clearly, the peak temperature depends on the carrier gas flowrate and the adsorption rate constant. In the limiting case in which readsorption is fast, eqn. (14) becomes

$$\frac{E_d}{RT_m^2} = \frac{\boldsymbol{u}_A}{\boldsymbol{b}} \exp\left(\frac{-E_d}{RT_m}\right)\frac{F_s^0}{\left[k_a P^0 (1-\boldsymbol{q}_{Am})\right]^2} \qquad (15)$$

The TPD experiment is sensitive to v_A/k_a, and this sensitivity indicates that the desorption preexponential factor cannot be determined with independent information about the adsorption rate constant. More generally, in this case the TPD experiment provides information about the equilibrium constant for adsorption, k_a/k_d, in contrast to UHV experiments, in which information about the desorption rate constant, k_d is obtained.

The TPD experiments found in this thesis were conducted by Dr. T. J. Toops of Oak Ridge National Laboratory. The primary purpose of the TPD experiments used in this work was to determine the temperature at which PVP decomposes from the Pt

surface and which species are evolved under an oxidizing atmosphere. The set-up used for TPD experiments is shown below in Figure 12.
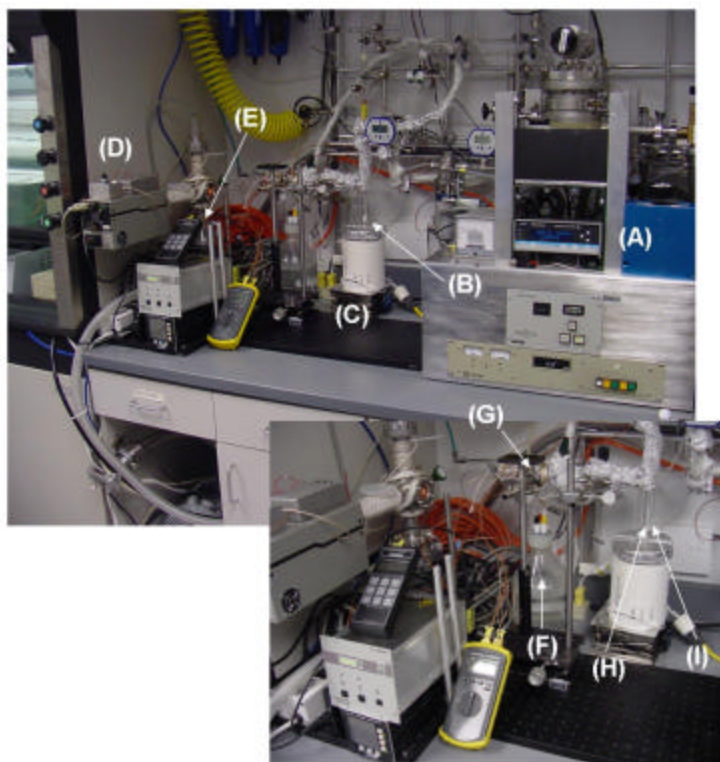
Figure 3.12. Temperature programmed desorption set-up. (A) temperature controller, (B) reactor with catalyst, (C) furnace, (D) SRS residual gas analyzer, (E) turbo pump, (F) condenser, (G) mass spec sampling port, thermocouple in (H) catalyst bed and (I) on reactor wall. Images courtesy of Dr. T. J. Toops of Oak Ridge National Laboratory.

The above TPD apparatus allowed for the detection of volatile decomposition products such as CO_2, CO, H_2O, H_2, light alkanes and NO_x products.

Temperature programmed desorption/decomposition methods were used in **Chapter 8** for the investigation of PVP removal from encapsulated Pt particles.

3.1.6 *Physical Adsorption*

The adsorption of gases on a solid surface can be used to determine the total surface area of a material. The experimental method widely used for the determination of surface area for porous materials is know as the BET method, which depends on the

porosity of the solid and the relative value of the heat of adsorption and the heat of liquefaction. Applying the kinetic theory of gas to molecular collisions on a surface, the number of molecules colliding with a surface per unit time, υ_{coll} is given by

$$\upsilon_{coll} = n\left(\frac{RT}{2\pmb{p}M}\right)^{1/2}$$

where n is number density of gas molecules, M is the molecular weight, R is ideal gas constant and T is the temperature. A molecule colliding with the surface may be adsorbed with probability α. Therefore the rate of adsorption becomes

$$\upsilon_{ads} = \alpha n\left(\frac{RT}{2\pmb{p}M}\right)^{1/2}$$

where n is the number density of gas molecules. The monolayer coverage for molecules adsorbed to a surface would require knowledge of the number of atoms available for bonding on the surface. Extending the adsorption to multilayers, the number density of molecules adsorbed in multilayer, σ is $s = s_m \sum_{i=1}^{\infty} i\theta_i$ where σ_m is the number density the number density of adsorbed molecules in one monolayer, θ_i is the fraction of the solid surface covered by layers of i molecules. Therefore, the surface coverage must be $1 = \theta_o + \sum_{i=1}^{\infty} \theta_i$ where θ_0 is the fraction of uncovered surface. Each layer which begins to pile up is subject to a dynamic equilibrium of adsorption and desorption. The rate of adsorption on the uncovered surface (*i.e.* first layer) is given by gas kinetic theory and is proportional to θ_0, $\pmb{u}_{ads} = a_0 n\left(\frac{RT}{2\pmb{p}M}\right)^{1/2}\theta_0$ which must be balanced by the rate of desorption of molecules from the first layer, $\pmb{u}_{des} = k_1 s_m \theta_1$. At

equilibrium, $a_0 n\left(\dfrac{RT}{2pM}\right)^{1/2}\theta_0 = k_1 s_m \theta_1$. The equilibrium maintained between the gas

phase and the first monolayer is shown schematically in Figure 13.
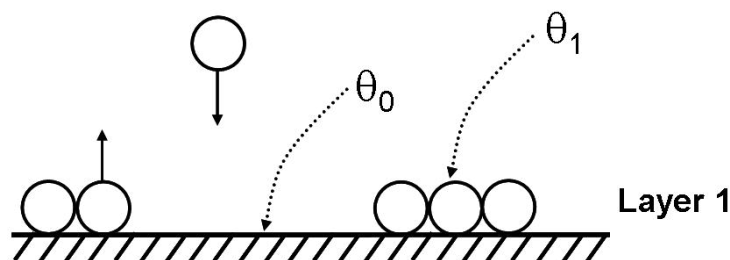
Figure 3.13. Thermodynamic equilibrium of the first layer during physisorption. From ref. [6].

The same analysis applies for the second layer to yield $a_1 n\left(\dfrac{RT}{2pM}\right)^{1/2}\theta_1 = k_2 s_m \theta_2$.

Figure 14 demonstrates the adsorption-equilibrium between the first and second layers.
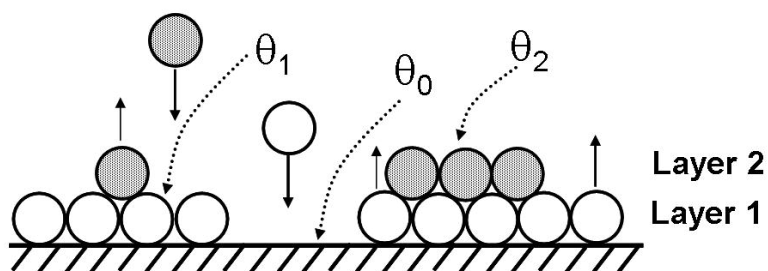
Figure 3.14. Thermodynamic equilibrium of the second layer during physisorption. From ref. [6]

This equilibrium will apply up to the ∞ layer. The multilayer can be assimilated to a

liquid in equilibrium with its saturated vapor. The dynamic equilibrium rates of

condensation and evaporation gives $a_\infty n_s\left(\dfrac{RT}{2pM}\right)^{1/2}\theta_\infty = k_\infty s_m \theta_\infty$ where θ_∞ is unity. To

acknowledge the difference in thermodynamic and kinetic properties between a molecule

directly adsorbed on the surface and a molecule adsorbed on top of another, it must

assumed that $\alpha = \alpha_1 = \alpha_2 \cdots = \alpha_\infty \neq \alpha_0$ and $k = k_1 = k_2 \cdots = k_\infty \neq k_0$. Assuming ideal gas

law is applicable n proportional to the pressure. After determining a relationship between

θ_0 and θ_i, which when performed, the equality is $\theta_i = Cx^i\theta_0$. This leads to the well known

BET expression (in a linearized form) [19]

$$\frac{P}{V_{ads}(P_0 - P)} = \frac{1}{CV_m} + \frac{C-1}{CV_m}\frac{P}{P_0} \qquad (16)$$

where it was noted that $\sigma/\sigma_m = V_{ads}/V_m$. Experimentally, V_{ads} and V_m are volume at NTP

conditions. The constant, C to a good approximation is

$$C = \exp\left(\frac{q_1 - q_L}{RT}\right) \qquad (17)$$

where q_1 is the heat of adsorption in the 1st monolayer and q_L is the heat of liquefaction

(condensation) of the adsorbate. Based on values of C and q_L, heats of physisorption are

< 10 kcal mol^{-1} [20]. The relative pressure range for the calculation of the total surface

area of the solid by eqn. 16 is known empirically to between 0.05 and 0.35 [21]. A plot

of the left hand side versus the relative pressure (P/P_0) should yield a linear plot with

slope, $(C-1)/V_mC$ and intercept, $1/V_mC$, from which V_m and C can be determined. With

N_2 and many other adsorbates $C \gg 1$, thus to a good approximation the slope equals

$1/V_m$. The total surface area is easily calculated from V_m values using 16.2 Å^2 for the

cross sectional area of N_2 [22].

The porosity of a solid material can be characterized from the shape of the

physical adsorption isotherm. Pores are divided into three categories based on their size.

These IUPAC approved size ranges are micropores (diameters = 20 Å), mesopores (20 Å

= d = 500 Å), while pores with diameters greater than 500 Å are referred to as

macropores [23]. In the case of this study, pores in SBA-15 are ~ 60-110 Å in diameter

and therefore classified as mesopores. The surface area and porosity of an adsorbent can be achieved by the construction of an isotherm, a procedure in which the quantity of adsorbate on a surface is measured over a wide range of relative pressures at a constant temperature. The procedure is done under equilibrium and desorption isotherms are required in the reverse procedure, where the relative pressure is decreased and the quantity of gas removed from the surface is measured. Isotherms on porous/nonporous materials are divided into five types (only type I and II are described here). The most common types are Type I, Langmuir isotherms which are concave to the P/P_0 axis and the amount of adsorbate approaches a limiting value and Type II is the isotherm form obtained from the SBA-15 materials in this work. This type of isotherm represents unrestricted monolayer-multilayer adsorption and the start of the linear central section of the isotherm is usually taken to indicate the relative pressure at which monolayer coverage is complete. Mesoporous materials generally exhibit hysteresis between the adsorption and desorption isotherms. Five types of hysteresis loops have been identified and correlated with various pore shapes. The most common type, Type A hysteresis is attributed to cylindrical pores. Hysteresis loops type B-E represent pores which are slit-shaped, wedge-shaped, and ink bottle shaped. If microporosity is absent from the adsorbent, the hysteresis loops close before reaching a relative pressure of 0.3 in the desorption process. The methods developed for determination of adsorbent porosity depend on the type of porosity (often a sample with have different types of porosity) present in the sample [24]. The primary hexagonally packed pores of SBA-15 are mesoporous, while the walls of these pores demonstrate microporosity. Two methods have for the determination of the pore size and its distribution has been developed. A

pore size distribution is the distribution of pore volume with respect to pore size. The desorption isotherm is more appropriate than the adsorption isotherm for evaluating the pore size distribution of an adsorbent because for the same volume of gas, the desorption branch exhibits a lower relative pressure resulting in a lower free energy state [24].

The total pore volume is derived from the amount of vapor adsorbed at a relative pressure close to unity, by assuming that the pores are filled entirely with liquid adsorbate. For mesoporous materials, the isotherm remains nearly horizontal over a range of P/P_0 approaching unity and therefore the pore volume is well defined. The volume of nitrogen adsorbed, V_{ads} can be converted to the volume of liquid nitrogen (V_{liq}) in the pores using the following relationship

$$V_{liq} = \frac{P_a V_{ads} V_m}{RT} \qquad (18)$$

where P_a and T are ambient pressure and absolute temperature, respectively, V_m is the molar volume of the adsorbate in its liquid state, and R is the ideal gas constant. The average pore radius or the Kelvin radius can simply be calculated from the Kelvin equation (assumes a cylindrical pore geometry)

$$r_K = \frac{-2gV_m}{RT \ln\left(\dfrac{P}{P_0}\right)} \qquad (19)$$

where γ is the surface tension of the adsorbate at its boiling point, V_m is the molar volume of the adsorbate in its liquid state, R is the ideal gas constant, T is the boiling point temperature of the adsorbate and P/P_0 is the relative pressure. The Kelvin radius doesn't represent the actual pore radius and must be corrected for the adsorption on the pore wall

prior to condensation. The thickness of the adsorbed layer is denoted by t and a method for its estimation is has been proposed by de Boer (t-method) [25].

A method for determination of the pore size distribution of mesopores has been developed by Barrett-Joyner-Halenda (BJH) [26]. At a relative pressure (P/P$_0$) close to unity, all pores are filled with liquid. The largest pore of radius, r_{p1} has a physically adsorbed layer of nitrogen molecules of thickness t. Inside this thickness is an inner capillary with radius r_K from which evaporation occurs as P/P$_0$ is lowered. The relationship between the pore volume, V_{p1} and the inner capillary volume V_K is

$$V_{p1} = V_{K1} \frac{r_{p1}^2}{r_{K1}^2} \tag{20}$$

Lowering the relative pressure from (P/P$_0$)$_1$ to (P/P$_0$)$_2$, a volume V_l will desorb from the surface. This liquid volume V_1 represents the emptying of the largest pore of its condensate and a reduction in the thickness of its physically adsorbed layer by an amount Δt_1. The average change in thickness across this relative pressure decrement is $\Delta t_1/2$. The pore volume of the largest pore is now expressed as

$$V_{p1} = V_1 \left(\frac{r_{p1}}{r_{K1} + \Delta t_1/2} \right)^2 \tag{21}$$

Upon decreasing the relative pressure a third time, (P/P$_0$)$_3$, the volume of liquid desorbing includes not only the condensate from the next larger size pores but also the volume from a second thinning of the physically adsorbed layer left behind in the pores of the largest size. The volume, V_{p2} desorbed from pores of the smaller size is

$$V_{p2} = V_1 \left(\frac{r_{p2}}{r_{K2} + \Delta t_2/2} \right)^2 \left(V_2 - V_{\Delta t_2} \right) \tag{22}$$

where $V_{\Delta t_2} = \Delta t_2 Ac_1$. The product Ac_1 is the area exposed by the previously emptied pores from which the physically adsorbed gas is desorbed. Any step, n of stepwise desorption, $V_{\Delta t_n}$ can be written as

$$V_{\Delta t_n} = \Delta t_n \sum_{j=1}^{n-1} Ac_j \qquad (23)$$

The summation in equation (23) is the sum of the average area in unfilled pores down to, but not including the pore that was emptied in the desorption. Substituting the value for $V_{\Delta t_2}$ into equation (22) results in an exact expression for calculating pore volumes at various relative pressures.

$$V_{pn} = V_1 \left(\frac{r_{pn}}{r_{Kn} + \Delta t_n /2} \right)^2 \left(\Delta V_n - \Delta t_n \sum_{j=1}^{n-1} Ac_j \right) \qquad (24)$$

Since the area *Ac* for any one size empty pore is not a constant but varies with each decrement of P/P_0, this term must be evaluated. The area of each pore, A_p is a constant and can be calculated from the pore volume, assuming cylindrical pore geometry, $A_p = 2V_p/r_p$. This enables the pore areas to be cumulatively summed so that for any step in the desorption process A_p is known.

The BJH method offers a means of computing $\sum Ac_j$ from A_p for each P/P_0 decrement by the following procedure. It is assumed that all pores emptied of their condensate during a relative pressure decrement have an average radius, r_K calculated from the Kelvin equation (eqn. 19) radii at the upper and lower values of P/P_0 in the desorption step. The average capillary radius is expressed as $r_{c,ave} = r_K - t_r$ where t_r is the thickness of the adsorbed layer as the average radius in the interval in the current pressure decrement and is calculated from equation (24). The term c is equation (24) is given by

$$c = \frac{r_{c,ave}}{r_K} = \frac{r_K - t_r}{r_K} \qquad (25)$$

Finally, equation (24) is used in conjunction with equation (25) to obtain an exact expression for the computation of pore size distributions.

Physical adsorption measurements were used in **Chapter 4, Chapter 5, and Chapter 9** for determination of the total surface, pore volume and pore size distribution for supported Pt/SBA-15 catalysts.

3.1.7 *Selective gas adsorption or chemisorption*

The above discussion of the formation of multilayers of adsorbents of atoms at or near their critical temperature is standard method to determine the total surface area of a solid. In most catalytic materials, only a very small fraction of the surface is actually catalytically active and methods to selectively determine this fraction or the catalytic surface area are based upon the adsorption of a gas which forms a single monolayer and interacts with metal surface atoms by a known reaction stoichiometry. This method is known as chemisorption or selective gas adsorption and differs significantly from physical adsorption. Chemisorption results in relatively strong, mostly irreversible chemical bonding between the adsorbate and metal surface with significantly higher heats of adsorption than observed in physisorption. Heats of chemical adsorption are $=$ 20 kcal mol^{-1} and can vary significantly with coverage due to intermolecular repulsive forces [10]. In some cases, chemical adsorption may even by activated.

In a chemisorption experiment, the total number of accessible surface atoms is measured, which is not necessarily equal to the number of active sites for a given reaction. The primary result of a chemisorption experiment is the determination of the metal dispersion, which is the ratio of surface atoms to the total number of atoms. Therefore as

the surface to volume ratio of the particle decreases, the dispersion increases. Dispersion

is synonymous with percentage exposed, although IUPAC recommends the latter [27].

Calculation of dispersion requires experimental determination of the monolayer uptake of

the adsorbate, the number of surface atoms covered by each chemisorbed gas molecule

(ratio is the adsorption stoichiometry) and the metal content of the catalyst. Therefore,

the dispersion (D) is calculated from the following formula

$$D = \frac{N_m \times S \times M}{100 \times W} \qquad (26)$$

where N_m is the number of adsorbed moles, S is the adsorption stoichiometry, M is the

molecular weight and W is the percent loading of the supported metal. Knowledge of the

dispersion allows the calculation of a hemispherical particle size, d (nm) $=c/D$ where

$c = \dfrac{f \times S \times M}{? \times N_A}$ where f is a shape factor (= 6 for spheres), S is the site (atom) density

(1.25×10^{19} m^{-2} for Pt) [28], M is the molecular weight, ρ is the mass density and N_a is

Avogardo's number. Insertion of all values into the equation for c leads to a constant of

1.13 for Pt. For all metal, the constant c is within 15% of unity. Surface area is

determined by the following relationship $SA_{Pt} = \dfrac{N_m \times S \times A_m}{N_A}$ where A_m is the cross

sectional area occupied by each active surface atom (8 Å^2 for Pt atom) [24, 28].

A number of methods have been suggested for measurement of the surface area of

supported metal catalysts. The most common selective gas adsorbates are hydrogen,

oxygen and carbon monoxide. Both H_2 and O_2 dissociate at room temperature and

require a pair of adjacent Pt atoms, *i.e.* $H_2 + 2Pt_s \rightleftharpoons 2H\text{-}Pt_s$ and $O_2 + 2Pt_s \rightleftharpoons 2O\text{-}Pt_s$,

where Pt_s represents a single surface atom. From these balanced chemical reactions, it is

apparent that the one H atom per Pt_s is the appropriate stoichiometry for counting the number of Pt surface sites. In some cases, the stoichiometry may change as the particle size decreases. The stoichiometry of the hydrogen platinum reaction may involve more than on H per Pt_s when the particle size becomes very small (= 1.5 nm) [29-31]. Similarly, in the case of oxygen, stoichiometries of $O:Pt_s = \frac{1}{2}$ have been proposed on small particles [31, 32].

The reaction between CO and Pt_s has also been used as measure of Pt surface area according to the following reaction, $Pt_s + CO \rightleftharpoons CO\text{-}Pt_s$. The stoichiometry in this case is 1:1 and is applicable over most particle sizes as long as the pressure is sufficiently high enough (Torr range) [6]. At low pressures, CO will populate 3-fold and bridge sites, which have 1:3 and 1:2 stoichiometries, respectively. By a few torr CO, bridge and 3-fold hollow CO have been displaced to atop bonding positions. Comparison of H_2, O_2 and CO chemisorption demonstrates from an experimental point of view (volumetric determination of number of surface atoms), CO is the most sensitive probe because the pressure is reduced by a factor of two compared with H_2 and O_2 adsorption. The fourth type of selective gas adsorption reaction which is 3 times more sensitive than H_2 adsorption is H_2-O_2 titration [33-36], in which (1) oxygen atoms are adsorbed on the Pt catalyst and (2) titrated with H_2 to form H_2O and Pt_s-H. The two surface reactions are written as: (1) $2Pt_s + O_2 \rightleftharpoons 2Pt_s\text{-}O$ and (2) $Pt_s\text{-}O + 3/2\ H_2 \rightleftharpoons Pt_s\text{-}H + H_2O$. As described above, the 1:1 stoichiometries may fail at very small particle sizes, but there is compensation as more hydrogen and less oxygen seems to chemisorb on the small particles. In general, the method yields dispersion values which are in excellent agreement with those obtained by other measurements.

Experimentally, adsorption of probe gases will occur on the metal and on the support. In some cases, the amount adsorbed on the support can make up a significant fraction of the total uptake; the total uptake consists of irreversibly bound adsorbate to the metal and reversibly bound adsorbate to both metal and support. The dual isotherm method of Boudart and Benson is utilized to determine the irreversible uptake on the metal only [34]. The first isotherm collected amounts to adsorption on metal and support, both irreversible and reversible adsorption. An evacuation step at the adsorption temperature removes adsorbate reversibly bound to the metal and support. A second isotherm which follows the evacuation is a measure of the reversibly bound adsorbate and is referred to as the weak isotherm. The difference between the two isotherms extrapolated to zero pressure is representative of irreversible or strong chemisorption. It is assumed and has been confirmed for a number of systems that the evacuation step doesn't remove the irreversibly bound adsorbate.

The measurements were conducted in a static equilibrium mode on a glass system pumped to ~3 × 10^{-6} Torr vacuum by a liquid nitrogen cooled diffusion pump (Varian MS2). The equilibrated system pressure was monitored by an MKS pressure transducer (Model PDR-D). The system is shown in Figure 20. Typical sample sizes for chemisorption ranged from 100 – 500 mg depending upon the type of sample analyzed and metal content. All adsorption measurements were conducted at room temperature which varied from 293–296 K, depending on the time of year. After pretreatment of the catalyst sample and evacuation at 623 K, the first isotherm was collected over a pressure range of 20–200 Torr with each point increasing in ~25 Torr increments. For all samples, the first point was given eight to ten minutes to equilibrate, and each subsequent point

was equilibrated for five minutes. Following completion of the first isotherm consisting of six to eight data points, the sample was pumped out with the diffusion at the adsorption temperature for 1 h. Following evacuation, a second isotherm was collected in an analogous fashion. In all cases but hydrogen, the irreversible adsorption was used to calculate the surface average metal particle size. H_2, CO and O_2 adsorption experiments on Pt were measured on each sample in the order listed. Following completion of the second O_2 isotherm and evacuation, adsorbed oxygen was titrated with hydrogen according to the H_2–O_2 titration method of Benson and Boudart [34].

Selective gas adsorption measurements were used in **Chapter 4** and **Chapter 5** for determination of catalyst dispersion, particle size of Pt/SBA-15 catalysts and **Chapter 6** to study competitive adsorption between carbon monoxide and ethylene.

3.1.8 Infrared spectroscopy: Theory of molecular vibrations

The most common application of infrared spectroscopy in catalysis is to identify adsorbed species and study the way in which these species chemisorb to a surface. These studies are often conducted on supported catalysts with different particle size distributions to determine the influence of surface structure on adsorption kinetics and dynamics and adsorbate-surface complex. The bonding of adsorbates to extended metal surfaces (both nanoparticles and single crystals) is analogous to ligand bonding in organometallic compounds [37]. The primary technique for characterization of catalysts and the adsorption of small probe molecules to their surfaces is diffuse reflectance Fourier transform infrared spectroscopy (DRIFTS). The details of this technique will be explained in section 2.2.9. The following section will introduce the fundamentals of

vibrational spectroscopy with emphasis on the theory of molecular vibrations of adsorbed species.

Vibrations in free molecules (gas or liquid) or molecules adsorbed to a solid surface are excited by the absorption of photons. The activity of a particular vibration is subject to strict selection rules; dependent upon of the type of spectroscopy being applied. The activity of particular vibrations on metal surfaces is subject to additional rules, so called metal surface selection rules (MSSR) [38]. Mid IR is the most common wavelength employed for the study of adsorbate-catalyst systems because molecular vibrations are active in this spectral region. Mid IR photons have wavelengths ranging from $50 - 2.5$ μm, which corresponds to energies of 200-4000 cm^{-1} (25-496 meV) [39].

Transitions between vibrational levels occur by absorption of photons with frequency, ν in the mid infrared region. These transitions represent the way in which a system translates from one stationary state (defined quantum mechanically as states that do not change with time) to another when a perturbation, such as electromagnetic radiation is applied. This requires the time dependent Schrödinger equation and solved using the principles of time dependent perturbation theory. The derivation and solution of this problem has been published elsewhere [39]. The outcome of this derivation demonstrates that two conditions are necessary for a transition to occur in a molecular system under the influence of a perturbation by electromagnetic radiation. First, the radiation must possess the proper energy, or frequency, corresponding to the energy difference between the molecular states. The second condition that must be fulfilled is that the transition moment must be nonzero, and in infrared spectroscopy, this transition moment is the expectation value of the dipole operator. The existence of a transition

moment for a vibrational transition depends on the geometry of the molecule and the polarity of the atoms. Certain vibrations that have a zero transition moment and cannot be observed in the infrared absorption spectrum are termed infrared inactive. In some cases, adsorption on a metal surface can perturbed the symmetry of a molecule enough to enable a particular vibration to become infrared active.

The potential energy of a molecule subjected to a small pertubation in its bond length from its equilibrium distance, r_{eq} in a molecule due to incident IR photons can be approximated by that of the harmonic oscillator. Therefore, the potential energy, V(r) is written as

$$V(r) = \frac{1}{2} k \left(r - r_{eq} \right)^2 \tag{27}$$

where k is the force constant of the vibrating bond and is analogous to Hook's law force constant, r is the distance between vibrating atoms. Substituting this form of V(r) into Schrödinger equation, the corresponding vibrational energy levels (eigenvalues of the vibrational Schrödinger equation) are equidistant and equivalent to

$$E_n = \left(n + \frac{1}{2} \right) h\nu \quad \text{where} \quad \nu = \frac{1}{2p} \sqrt{\frac{k}{m}} \tag{28}$$

The symbols in eqn (28) are E_n, the energy of the nth vibrational level, n is an integer, h is Planck's constant, μ is the reduced mass, ν is the frequency of the vibration, and k is same as defined above (eqn. 27). The harmonic oscillator wavefunctions and energy eigenvalues are shown in Figure 15.
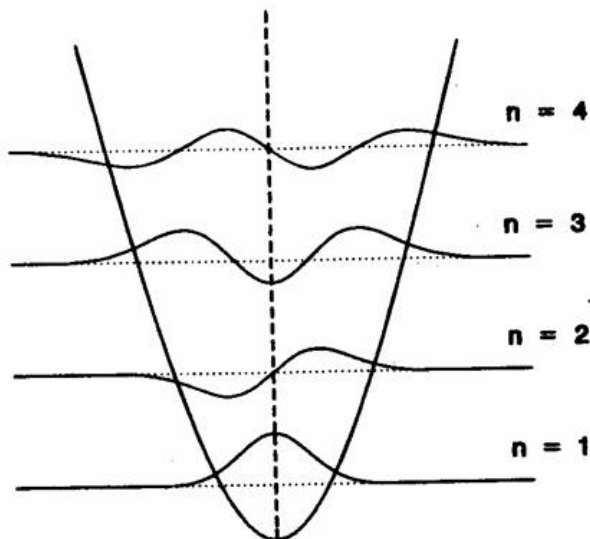
Figure 3.15. Vibrational wavefunctions for a harmonic oscillator. From ref. [39].

Equation (28) demonstrates that vibrational frequencies increase as the bond strength increases and decreases as the mass of the vibrating atoms increases. For example, the frequency (in cm^{-1}) of the CO stretch for different isotopic combinations are 2143 for $^{12}C^{16}O$, 2096 for $^{13}C^{16}O$, 2091 for $^{12}C^{18}O$ and 2042 for $^{13}C^{18}O$ [1]. The simple harmonic oscillator picture of a vibrating molecule has important implications. Knowledge of the frequency allows calculation of the bond force constant, which is related to the curvature of the interatomic potential.

The number of different vibrations that a molecule possesses is dependent upon the number of atoms in the molecule and the final geometry of the molecule. A molecule consisting of N atoms has 3N degrees of freedom. Three are translational and three are rotations of the molecule along the three principle axes of inertia. Linear molecules have only two rotational degrees of freedom, as no energy change is involved in the rotation along the main axis. The number of fundamental vibrations is 3N-6 for a nonlinear

molecule and 3N-5 for a linear molecule.   In addition, there are overtones and combinations of fundamental vibrations.   There are four types of allowed vibrations; stretching vibrations denoted by the symbol ν result in a change in the length of a bond from its equilibrium length (both reduction and expansion), bending vibrations in one plane denoted by the symbol δ result in changing bond angles while the bond lengths are unaltered.   In large molecules, bending vibrations can be further divided into rock, twist and wag vibrations.   The third type of vibration are out of plane bending vibrations identified by the symbol γ, in which one atom oscillates through a plane defined by at least three neighboring atoms.   The fourth vibration result from the changing the angle between two planes through atoms and are referred to as torsional vibrations.   They are indicated by the symbol τ.   Generally, the frequencies of these vibrations decrease in the order $\nu > \delta > \gamma > \tau$.   Vibrations are often further divided into symmetric, ν_s and asymmetric vibrations, ν_{as}.   Asymmetric stretching vibrations are higher in energy than their symmetric counterparts.   Absorption of an infrared photon occurs only if the dipole moment changes during the vibration.   The molecule need not possess a permanent dipole moment but the dipole moment must change during a vibration.   The intensity of an infrared band is related to magnitude of change in the dipole moment (*i.e.* the square of the transition moment).   Therefore, molecules like CO, NO and OH undergo large changes dipole moments and exhibit intense infrared bands, while covalent C-C bonds absorb infrared light very weakly and diatomic molecules such as N_2 and H_2 are infrared inactive.   Allowed transitions in the harmonic approximation (eqn. 28) are those for which the vibrational quantum number changes by unity ($\Delta n = \pm 1$).   Overtones or the

absorption of light at integer products of the fundamental frequency are not possible in the harmonic oscillator model but can be accounted for by the Morse potential.

In addition, to the required change in the vibrational quantum by $\Delta n = \pm 1$, surface metal selection rules for adsorbates on metal surfaces exist which require that the change in dipole due to perturbation by electromagnetic radiation is perpendicular to the surface. It has been confirmed by that only molecular vibrations which give dipole changes perpendicular to the metal surface will absorb radiation strongly. The unique property of metals is the freedom of the conduction electrons to respond to an electrical stimulus. This concept can be extended to the "perfect metal" which is described as being "perfectly polarizable." Therefore, a charge above the surface of a conducting medium (*i.e.* metal) produces lines of force as expected (Figure 16a) as if there was a negative charge at an equal distance below the surface of the conductor [40]. Dipoles parallel or perpendicular to the surface of the conductor will in the same manner produce virtual image dipoles as shown in Figure 16b and 16c, respectively. The bond stretching vibration which will give rise to a dipole change parallel to the surface will also, for a "perfect" metal, produce dipole changes in the opposite direction in the "image dipole." Because the separation between the original dipole and its image is of the order of molecular dimensions (a few angstroms) which is much less than the wavelength of the emitted infrared ration (a few μm), it is seen that in effect the image dipole change precisely cancels out the effect of the dipole change originating in the vibrating molecule. On the other hand, the oscillating dipole perpendicular to the surface will be reinforced by the oscillating image dipole (Figure 16c). This is one explanation for the origin of the "metal-surface selection rule." It seems reasonable to suppose that to a considerable
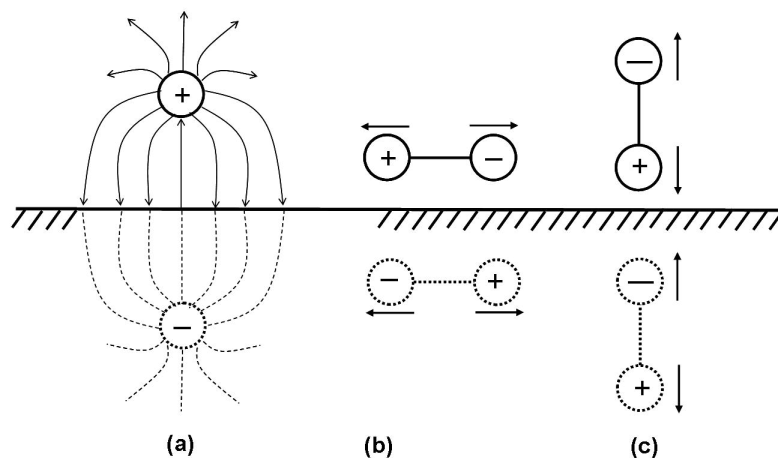
Figure 3.16. (a) The lines of force and the electrical "image" resulting from a positive charge over the surface of a conductor (the metal surface is the upper line above the hatched area). (b) The changes during the vibration of a dipole parallel to the surface of the metal; the "image" dipole change is in the opposite direction to the original. (c) The changes during the vibration of a dipole perpendicular to the surface; the "image" dipole change is in the same direction as the original. Reproduced from ref. [38].

extent the same effects operate for adsorbed molecules, even though in these cases the electrical "images" have to be formed by the polarizability of metal atoms close to the surface. On the scale of molecular dimensions, the model of a smooth planar metal surface is an oversimplification (see Figure 16a), but the general concept of an electrical image seems likely to apply to the curved surfaces of relatively small particles. Pearce and Sheppard [38] have also shown that the surface metal selection rule may be applicable to molecules adsorbed to single metal atoms (such as organometallic complexes and metal exchanged zeolites). Greenler and coworkers [41] have shown theoretically that the metal surface selection rule should apply to adsorption on metal particles larger than 2 nm in diameter, while the rule is weakened on smaller particles. The metal surface selection rule is considered during the adsorption of ethylene and carbon monoxide on small Pt crystallites, as examined in Chapter 6 of this thesis.

3.1.9   Diffuse Reflectance Infrared Spectroscopy

The primary infrared spectroscopy technique utilized in this study was diffuse reflectance Fourier transform infrared spectroscopy (DRIFTS) which ideally suited for the study of adsorption on porous catalysts. In reflectance spectroscopy, an infrared beam is bounced off the sample instead of passing through it (*i.e.* transmission). During a diffuse reflectance experiment, the angle of incidence (*i.e.* the angle at which the infrared beam hits the surface relative to the surface normal is fixed, but angles of reflection vary from 0 to 360º. This type of reflectance is common to rough surfaces and differs from specular reflectance which occurs from smooth, mirror like surfaces [42]. There are many advantages to using reflectance based spectroscopy over transmission spectroscopy in supported catalyst research. One major advantage is there no attenuation problem due to sample thickness, a problem often occurred in transmission spectroscopy where the pellet has to be thick enough to support itself and remain intact, but thin enough to allow transmission of the infrared beam. Sample preparation is trivial at this point because no grinding, crushing or diluting is necessary, although one must be careful when preparing a sample for diffuse reflectance spectroscopy. Sample purity and integrity is maintained allowing it to be reused because there is no requirement for dilution because the requirement that the sample be in the form of a pellet. The disadvantages of reflectance spectroscopy are numerous, which have proven difficult to overcome but don't inhibit utility of the technique. One of the primary problems in penetration depth of the incident infrared beam is unknown. The depth of penetration is determined by properties of the sample and its surface and the angle of incidence of the incoming photons. These factors make it extremely difficult to determine the pathlength in a reflectance experiment, making quantification difficult since pathlength is an important variable in determining a

sample's absorbance. This is manifested in Beers law, which states that the absorbance, A is proportional to the pathlength, A= $\varepsilon c l$, where ε is the extinction coefficient, c is concentration and l is the aforementioned pathlength. The range of penetration depth is 1 – 10 μ, thereby confining it primarily to the "surface" region of the sample, which is in stark contrast to transmission techniques whose signal will be dominated by the bulk. Capturing all the light reflected off a sample during a diffuse reflectance experiment is difficult to accomplish, so reflection spectra are generally noisier than transmission spectra for a given number of scans and resolution.

The specific reflectance spectroscopy used in this laboratory is diffuse reflectance which became faster and more sensitive with the advent of Fourier transform infrared (FTIR) spectroscopy, giving its well-known name of diffuse reflectance Fourier transform infrared spectroscopy (DRIFTS). The application of DRIFTS for the characterization of the structural and chemical properties of catalytic materials as well as DRIFTS *in-situ* identification of surface species during reaction has been reviewed [43]. One advantage of the DRIFTS technique is its applicability to carbon supported catalysts because absorption of the incident beam due to transmission through the sample is eliminated because of the reflectance nature of the technique.

DRIFTS is an excellent technique for qualitative analysis. In many cases, this technique is used to confirm or deny the existence of a particular chemical species. Quantitative analysis using DRIFTS is possible but requires the use of Kubelka-Munk (KM) units, similar to the requirement of using absorbance units in quantitative transmission spectroscopy. The equation used to relate concentrations to peak heights (or areas) is referred to as the Kubelka-Munk equation [44]. The form of the KM equation is

$$KM = \frac{k}{s} = \frac{(1-R_\infty)^2}{2R_\infty} \qquad (29)$$

where k is absorption coefficient, s is the scattering coefficient, R_∞ is the reflectance from an infinitely thick slab. The absorption coefficient, k can be further defined as

$$k = 2.303ac \qquad (30)$$

where a is the absorptivity and c is the concentration. This allows the KM units to be rewritten in terms of a and c as

$$KM = \frac{2.303ac}{s} \qquad (31)$$

The Kubelka-Munk equation assumes that the sample is infinitely thick compared to the depth of the sample. This is generally true for samples contained in standard diffuse reflectance cups (1/8" deep) because the penetration depth is 1-10 μ. The difficult variable to determine in equations (29) and (30) is the scattering factor, s, which depends on the particle size and shape distribution, and the packing density of the material. These parameters are difficult to control and for this reason it is critical that the samples are packed identically each time. Quantitative analysis using DRIFTS is more accurate if ratios are used rather than absolute quantities and internal standards are employed.

Diffuse reflectance Fourier transform infrared spectroscopy (DRIFTS) was used in **Chapter 5** and **Chapter 6** to study the influence of particle size on CO and ethylene adsorption and **Chapter 8** to follow the decomposition of PVP infrared bands during oxidation-reduction cycles of the as-synthesized catalysts.

3.2   Catalytic reaction studies.

Determination of catalytic rates free of heat and mass transfer artifacts is essential for assessing the catalytic efficiency of a particular catalysts. A number of valuable references have been published on the measurement of rates in laboratory reactors. Three references are highly recommended [45 – 47]. This section introduces the mass balance for a plug flow reactor and the methods for determination of reaction rate as well as the reactor system that were built and used to acquire the kinetic data presented in the proceeding chapters of this thesis.

3.2.1   *Measurement of reaction rates and kinetic parameters*

All reactions in this thesis were carried out in plug flow reactors. A plug flow reactor (PFR) is an open system in which an identical amount of material enters and leaves the reactor under steady state conditions. A plug flow reactor is considered ideally and can be modeled mathematically if the following assumptions are made: 1) mixing is infinitely rapid so that each plug of fluid is uniform in temperature and pressure, 2) no axial mixing as plug moves through reactor, and 3) all volume elements have identical residence times in the reactor [10]. A model of a PFR is shown in Figure 17.
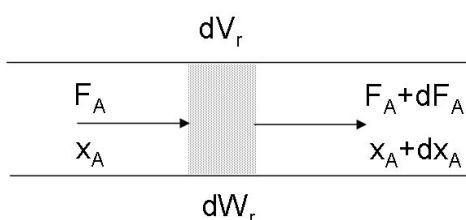
Figure 3.17. A differential volume element (dV$_r$) in a plug flow reactor with F and X being the flowrate and fractional conversion, respectively, of the limiting reactant, A. For a catalytic plug flow reactor, a differential catalyst amount (dW$_r$) is considered.

A mass balance on limiting reactant, A around the volume element, dV of Figure 17 is [Flow rate of A in] = [Flow rate of A out] + [Rate of disappearance of A by chemical reaction] [10, 48]. If the fractional conversion through the volume element is

defined as X, then a mass balance for species A in volume element, dV_r can be rewritten as follows

$$F_A = (F + dF_A) + (-r_A)dV_r \qquad (31)$$

where $-r_A$ is the rate of disappearance of A, and dF_A is the change in molal flowrate of A through volume element, dV_r. Substituting $F_A = F_{A0}(1-X)$, where F_{A0} is the initial flowrate of A and X is the fractional conversion, eqn. (31) rearranges to

$$\frac{dV}{F_{A0}} = \frac{dX}{(-r_A)} \qquad (32)$$

Integrating over the entire reactor volume, the ratio V/F_{A0} is given by

$$\frac{V}{F_{A0}} = \int_{X_{in}=0}^{X_{out}} \frac{dX}{(-r_A)} \qquad (33)$$

where X_{in} is generally zero. The utility of this design equation is it enables the required volume needed to achieve a conversion of A at the outlet of the reactor if the rate expression is known for the disappearance of A.

Within a differential reactor, the reactant concentration through the reactor is essentially constant and approximately equal to the inlet concentration. The reactor is gradientless, or the reaction rate is identical in all parts of the catalyst bed (*i.e.* spatially uniform). In a catalytic reactor, differential operation is maintained at low conversions and is therefore considered isothermal. Ideally, this is achieved with small catalyst beds or low residence time (high volumetric flowrates). Operation of a plug flow reactor as a differential reactor rather than an integral reactor simplifies the reactor design equation. Derivation of the reactor design equation for a differential catalytic reactor is as follows

$$[F_{A0}] - [F_{Ae}] + \left[\left(\frac{\text{rate of reaction}}{\text{mass of catalyst}} \right)(\text{mass of catalyst}) \right] = 0 \qquad (34)$$

where the rate per mass catalyst is given the symbol, r_A (rate based upon disappearance of

A). Therefore, eqn. 34 becomes

$$F_{A0} - F_{Ae} + (r_A)(W) = 0 \qquad (35)$$

where subscript e refers to the exit of the reactor. Solving for $-r_A$, the rate equation for a

differential reactor becomes

$$-r_A = \frac{F_{A0} - F_{Ae}}{W} = \frac{?_0 C_{A0} - ?C_{Ae}}{W} \qquad (36)$$

where the quotient after the second equality is the rate equation written in terms of

concentration and volumetric flowrate. Finally, rewriting eqn. (36) in terms of

conversion

$$-r_A = \frac{F_{A0} X}{W} \qquad (37)$$

It is evident by inspection of eqn. (33) and (37), the integral plug flow equation becomes

a simple algebraic equation. The advantages of a differential reactor are obvious, ease of

sampling and analysis, reactor isothermality and simple reactor construction. One of the

main disadvantages of differential reactors is that are not suitable for studies of catalyst

deactivation.

All rates are reported as turnover frequencies (TOF), defined as the number of

turnovers per site per second. The number of sites is difficult to define and is generally

measured by selective chemisorption (see section 2.2.7). In most cases, the number of

sites determined by chemisorption does not necessarily correspond to the active sites

under reaction conditions on a one to one basis. The exact atom or grouping of atoms

(ensemble) constituting an active site is typically not known for any heterogeneous

reaction, and it is very likely that a variety of active sites exists, each with it own rate. Therefore, the measured TOF is a *nominal* turnover rate [49].

3.2.2   Analysis of catalytic reaction data for transport artifacts

In commercial reactors, heat and mass transfer effects frequently impact upon the overall performance of the reactor because rates are maintained as high as possible [10]. In the case of laboratory experimental kinetic studies, kinetic data is required and the researcher must ensure that kinetic experiments are conducted under conditions which guarantee the rate data are acquired in a regime of kinetic control. A simplified version of a catalyst particle is shown in Figure 18 [50]. Before a reactant molecule can react, it must be transported from the well-mixed homogeneous bulk phase to the surface of the catalyst particle and then for porous materials containing active sites distributed within their structure, it must further diffuse into the pores. Interphase gradients can exist between bulk and solid phases, i.e. diffusive-convective transport processes link the source of reactants (bulk phase) to the sink of reaction (catalyst particle surface). Consequently, here diffusion and convection occur in series with the reaction. Intraphase gradients are confined within the particle to the local reaction zone; therefore pore diffusion occurs simultaneously with the reaction. While interphase transport limitations are important and quantified with the Damköhler number, these have been verified eliminated from our catalytic data.

A number of approaches have been proposed to evaluate the influence of pore diffusion on a catalytic reaction, including the Thiele modulus [51], Weisz-Prater criterion [52, 53], Koros-Nowak test [54] and the Madon-Boudart test [55]. In this discussion, we will concentrate on the Madon-Boudart test as this was applied to
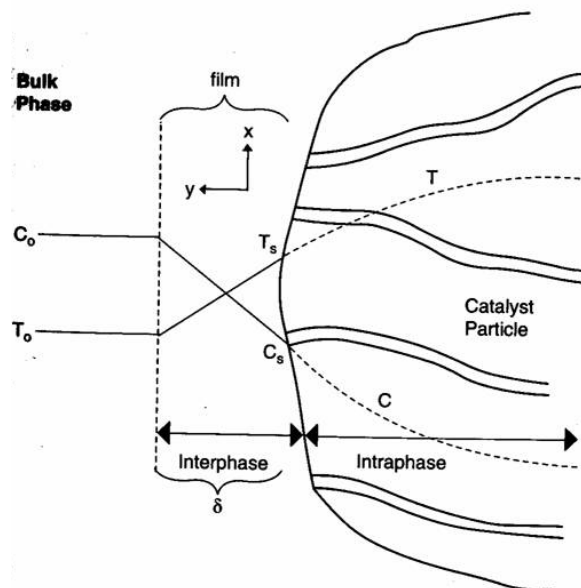
Figure 3.18. A diagram depicting concentration and temperature changes from the bulk phase through a stagnant film of thickness, δ to a particle surface and then through the catalyst particle, assuming an exothermic reaction occurs. From refs. [10] and [50].

reactions studied in this thesis. In a purely kinetic regime, the rate is directly proportional to the concentration of active sites, L. In the regime of internal (pore) diffusion control, the rate becomes proportional to $L^{1/2}$, and when external diffusion controls the rate there is no influence of L. This observation led to the proposal by Koros and Nowak to test for mass transfer limitations by varying L [54]. This concept was developed further by Madon and Boudart to provide a test that could verify the absence of any heat and mass transfer effects [55]. The Madon-Boudart test requires that the rate is measured as the number of active sites is varied by changing the metal loading or, for structure-insensitive reactions, by altering the metal dispersion. For structure sensitive reactions, the metal dispersion should be maintained constant while the active site concentration is changed. A slope of unity from a plot of ln (rate) versus L, *i.e.* a constant turnover rate verifies the absence of any mass transfer limitations (interphase and intraphase). An example of the

application of the Madon-Boudart test to the liquid phase hydrogenation of cyclohexene

is shown in Figure 19.
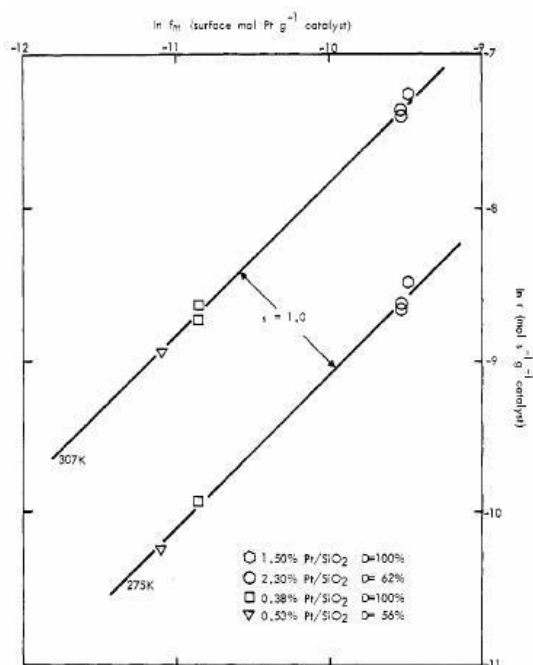
Figure 3.19. The Madon-Boudart criterion applied to the liquid phase hydrogenation of cyclohexene on Pt/SiO$_2$ catalysts. From reference [55].

The Madon-Boudart test can also be used to verify the absence of heat transfer artifacts.

As Figure 19 demonstrates measurement of the Madon-Boudart test at two temperatures

should yield plots of ln (rate) vs. L which are unity at both temperatures.

3.2.3   Laboratory catalytic reactors

Catalytic reactions were conducted in two separate reactors. One reactor system

was equipped with five mass flow controllers which allowed simultaneous metering of up

to five gases into the reactor feedstream. The flow loop and reactor was composed

entirely of pyrex glass and could be operated in flow or batch mode. In order to circulate

the gases efficiently during batch or continuous stirred tank reactor (CSTR) mode, a

bellows MB–2100 was used. During CSTR and batch operation, the recirculation rate of

1400 cm^3 min^{-1} (Figure 20). The second reactor setup was conducted entirely of 1/8"
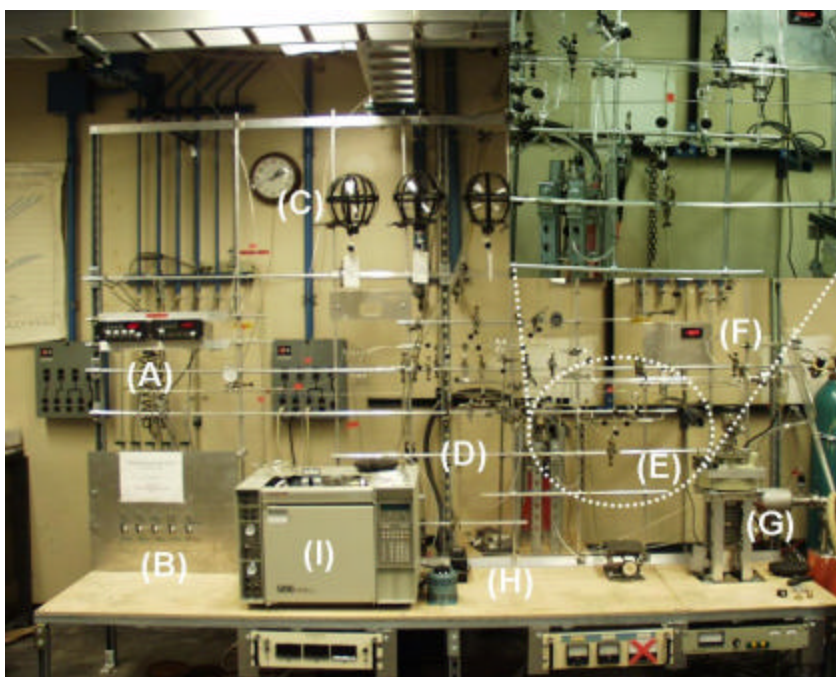
Figure 3.20. High surface area (HSA) combined reactor – chemisorption apparatus. (A) Gas manifold, (B) mass flow controller bank, (C) 5 L holding bulbs for physisorption/chemisorption adsorbates, (D) reactor section of rig, (E) chemisorption section of rig (enlarged area in upper right hand corner), (F) digital pressure gauge for pressure measurement during adsorption experiments, (G) liquid nitrogen cool diffusion pump, (H) recirculation pump for CSTR and batch reactor operation and (I) gas chromatograph.

stainless steel tubing in which all lines were heat traced to prevent the condensation of all

reactants in products. Gases were delivered to the reactor by a set of mass flow

controllers. The system was also equipped with a syringe pump (Cole–Parmer) which

allowed the controlled metering of liquids in the gas stream. This system could only be

run as a plug flow reactor (PFR). The composition of the product gas was measured

online with a Hewlett Packard (HP) 5890 Series II gas chromatogram equipped with a

flame ionization detector (FID) and a thermal conductivity detector (TCD). Equipped

with a ten way valve, separate samples could be analyzed by the TCD and FID

simultaneously. For most reactions, packed columns were used for organic and H_2 analysis, while a 50 m capillary column was used for *n*-hexane reforming studies (not included in this thesis). A schematic of the reactor setup with syringe pump is shown in Figure 21.
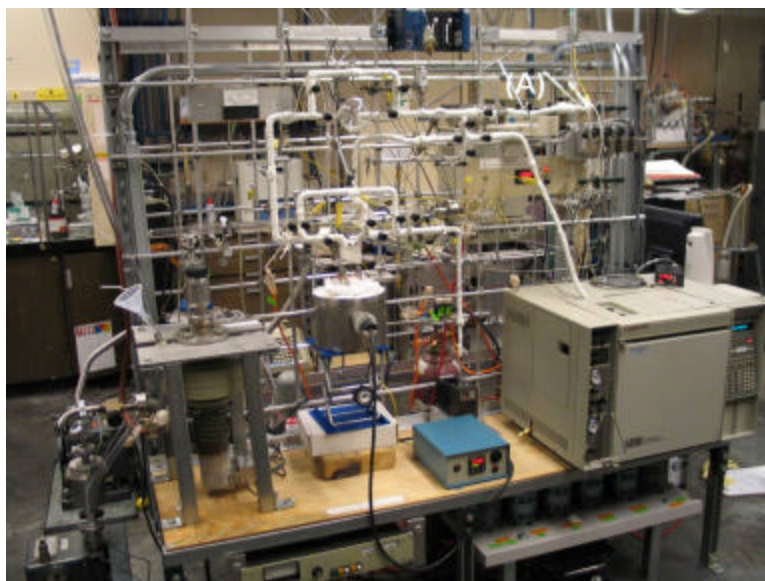
Figure 3.21. Reactor built for *n*-hexane reforming. All reactor lines are wrapped in insulation and heated to 403 K. All components the same as Figure 20 except for the (A) syringe pump used for metering of *n*-hexane into reactor.

All catalysts were diluted in low surface area acid washed white quartz (Sigma-Aldrich, 50-70 mesh) in a 5:1 quartz to catalyst ratio by weight. Dilution with a low surface area, high thermal conductivity diluent ensured that local hot spots were not created in the catalyst bed due to reaction exothermicity by effectively dispersing the catalyst particles in the quartz. Reactor operation under differential conditions required small catalyst quantities leading to small catalyst beds even when diluted with quartz. In order to increase the catalyst bed length and decrease chances for channeling, a triple bed dilution scheme was used. Pure acid washed quartz (~ 200 mg) was placed on top of the glass frit, followed by the diluted catalyst sample and another layer of pure acid washed quartz (~

200 mg) was placed on top of the diluted catalyst layer. A photograph of a typical

catalyst bed is shown in Figure 22.
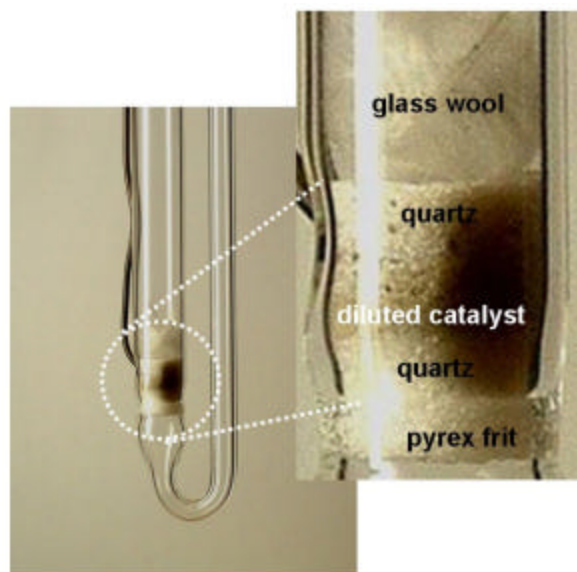
Figure 3.22. View of U‑tube plug flow catalytic reactor made of pyrex. Closeup shows the catalyst packing used for all flow reactors.

All catalysts were packed according to Figure 22 and verified free of mass and heat

transfer effects using the Madon‑Boudart test and in some cases, the Weisz‑Prater criteria

[52, 53].

3.3   References and Notes

1. J. W. H. Niemantsverdriet, *Spectroscopy in Catalysis*. VCH, Weinheim, 1993.

2. (a) D. B. Williams, C. B. Carter, *Transmission Electron Microscopy I Basics*. Plenum Press, New York, 1996. (b) D. B. Williams, C. B. Carter, *Transmission Electron Microscopy II Diffraction.* Plenum Press, New York, 1996. (c) D. B. Williams, C. B. Carter, *Transmission Electron Microscopy III Imaging*. Plenum Press, New York, 1996. (d) D. B. Williams, C. B. Carter, *Transmission Electron Microscopy IV Spectrometry*. Plenum Press, New York, 1996.

3. P. L. Gai, E. D. Boyes, *Electron Microscopy in Heterogeneous Catalysis.* Institute of Physics Series in Microscopy in Materials Science, Philadelphia, 2003.

4. A. K. Datye, *J. Catal*. 216 (2003) 144.

5. R. J. Matyi, L H. Schwartz, J.B. Butt, *Catal. Rev. –Sci. Eng*. 29 (1987) 41.

6. M. Boudart, G. Djéga-Mariadassou, *Kinetics of Heterogeneous Catalytic Reactions*. Princeton University Press, Princeton, New Jersey, 1984.

7. B. D. Cullity, *Elements of X-Ray Diffraction*. 2nd edition, Addison Welsey, Reading, 1978.

8. H. P. Klug, L. E. Alexander, *X-Ray Diffraction Procedures*. Wiley, New York, 1954.

9. B. E. Warren, J. Biscoe, *J. Am. Ceram. Soc*. 21 (1938) 49.

10. M. A. Vannice, *Kinetics of Catalytic Reactions*. Springer, New York, 2005.

11. R. M. Rioux, H. Song, J. D. Hoefelmeyer, P. Yang, G. A. Somorjai, *J. Phys. Chem. B* 109 (2005) 2192.

12. N. Koga, in *Comprehensive Handbook of Calorimetry and Thermal Analysis.* Ed.: Michio Sorai, John Wiley & Sons, Hoboken, 2004.

13. (a) Chapter 5 of this thesis (b) H. Song, R. M. Rioux, J. D. Hoefelmeyer, R. Komor, K. Niesz, M. Grass, P. Yang, G. A. Somorjai, Submitted to *J. Am. Chem. Soc.* (2005).

14. N. Koga, J. M. Criado, *J. Am. Ceram. Soc.* 81 (1988) 2901.

15. R. Ozao, in *Comprehensive Handbook of Calorimetry and Thermal Analysis.* Ed.: Michio Sorai, John Wiley & Sons, Hoboken, 2004.

16. J. A. Dumesic, D. F. Rudd, L. M. Aparicio, J. E. Rekoske, A. A Treviño, The Microkinetics of Heterogeneous Catalysis. American Chemical Society, Washington D.C., 1993.

17. P. A. Redhead, *Vacuum* 12 (1962) 203.

18. C. R. Tewell, PhD Dissertation. University of California, Berkeley, 2002.

19. S. Brunauer, P. Emmett, E. Teller, *J. Amer. Chem. Soc.* 60 (1938) 309.

20. D. O. Hayward, B. M. W. Trapnell, *Chemisorption.* Buttersworth, London, 1964.

21. S. J. Gregg, K. S. W. Sing, *Adsorption, Surface Area and Porosity,* 2nd ed., Academic Press, London, 1991.

22. P. H. Emmett, in *Catalysis* Vol. 1, Ed.: P. H. Emmett, Reinhold, New York, 1954.

23. J. Rouquérol, D. Avnir, C. W. Fairbridge, D. H. Everett, J. H. Haynes, N. Pericone, J. D. F. Ramsay, K. S. W. Sing, K. K. Unger, *Pure Appl. Chem.* 66 (1994) 1739.

24. Quantachrome 1-C instructional/operation manual, Quantachrome Instruments. Boynton Beach, FL., www.quantachrome.com.

25. J. H. de Boer, *The Structure and Properties of Porous Materials.* Butterworths, London, 1958.

26. E. P. Barrett, L. G. Joyner, P. P. Halenda, *J. Amer. Chem. Soc.* 73 (1951) 373.

27. R. L. Burwell, *Pure Appl. Chem.* 46 (1976) 71.

28. J. R. Anderson, *Structure of Metallic Catalysts.* Academic Press, New York, 1975.

29. J. H. Sinfelt, D. J. C. Yates, *J. Catal.* 10 (1968) 362.

30. D. E. Mears, R. C. Hansford, *J. Catal.* 9 (1967) 125.

31. G. R. Wilson, W. K. Hall, *J. Catal.* 17 (1970) 190.

32. R. Dalla Betta, M. Boudart, *Proc. 5th Intl. Cong. Catalysis*, Ed.: R. Hightower, Elsevier, Holland, 1973.

33. H. L. Gruber, *J. Phys. Chem.* 66 (1962) 48.

34. J. E. Benson, M. Boudart, *J. Catal.* 4 (1965) 704.

35. Y. Barbaux, B. Roger, J. P. Beaufils, J. Germain, *J. Chim Phys.* 67 (1970) 1035.

36. M. A. Vannice, J. E. Benson, M. Boudart, *J. Catal.* 16 (1970) 348.

37. M. R. Albert, J. T. Yates, Jr. *The Surface Scientist's Guide to Organometallic Chemistry.* American Chemical Society, Washington, DC, 1987.

38. H. A. Pearce, N. Sheppard, *Surf. Sci.* 59 (1976) 205.

39. M. Diem, *Introduction to Modern Vibrational Spectroscopy.* John Wiley & Sons, New York, 1993.

40. B. I. Bleaney, B. Bleaney, *Electricity and Magnetism.* 2nd ed., Oxford Univ. Press, London, 1965.

41. R. G. Greenler, D. R. Snider, D. Witt, R. S. Sorbello. *Surf. Sci.* 118 (1982) 415.

42. B. C. Smith, *Fundamentals of Fourier Transform Infrared Spectroscopy*. CRC Press, New York, 1996.

43. M. L. Hair, *Infrared Spectroscopy in Surface Chemistry*. Marcel Dekker, INC., New York, 1967.

44. P. Kubelka, F. Munk, *Z. Tech. Phys*. 12 (1931) 593.

45. V. W. Weekman, Jr. *AIChE J*. 20 (1974) 833.

46. R. B. Anderson, in Experimental Methods in Catalytic Research, Vol.1, Ed. R. B. Anderson, Academic Press, New York, 1968.

47. F. M. Dautzenberg, in Characterization and Catalyst Development, Eds.: S. A. Bradley, M. J. Gattuso, R. J. Bertolacini, ACS Symposium Series #411, Washington DC, 1989.

48. H. S. Fogler, *Elements of Chemical Reaction Engineering*. 2nd ed. Prentice Hall, New Jersey, 1992.

49. F. H. Ribeiro, A. E. S. von Witteneau, C. H. Bartholomew, G. A. Somorjai, *Catal. Rev. –Sci. Eng* 39 (1997) 77.

50. J. J. Carberry, *Chemical and Catalytic Reaction Engineering*. McGraw-Hill, New York, 1976.

51. E. W. Thiele, *Ind. Eng. Chem*. 31 (1939) 916.

52. P. B. Weisz, *Z. Physik. Chem. NF* 11 (1957) 1.

53. P. B. Weisz, C. D. Prater, *Adv. Catal*. 6 (1954) 143.

54. R. M. Koros, E. J. Nowak, *Chem. Eng. Sci*. 22 (1967) 470.

55. R. J. Madon, M. Boudart, *Ind. & Eng. Chem. Fund*. 21 (1982) 438.

Chapter 4

High Surface Area Catalyst Design: Synthesis, Characterization, and Reaction Studies of Platinum Nanoparticles in Mesoporous SBA-15 Silica

4.1   Introduction

One of the goals of catalysis research is to design and fabricate a catalyst system that produces only one desired product out of many other possible products (100% selectivity) at high turnover rates. Such a "green chemistry" process eliminates the production of undesirable waste. To design a catalyst for the "green chemistry" era, an understanding of the molecular ingredients that influence selectivity must be incorporated into catalyst synthesis. Using model catalysts possessing low surface area (1 cm^2 metal single crystals) and 2-D transition metal/metal oxide array catalysts, many of the molecular features that control activity and selectivity have been uncovered. These include the surface structure [1], metal particle size [2], site blocking (i.e., selective poisoning of the catalyst surface) [3], bifunctional catalytic systems [4], and certain metal-oxide interfaces [5] capable of performing unique chemistry. One of the most mature areas of selectivity control in heterogeneous catalysis is shape selective zeolite

catalysis [6]. Reaction selectivity is imparted by restricting the entry channel to the internal zeolite structure to molecular diameters which are smaller than the diameter of some potential reactants and products, requiring product formation to occur in a shape-selective manner. We have recently initiated research to design high-surface area catalysts [7, 8] whose properties can be controlled systematically and ultimately allow us to determine the role of various parameters on reaction activity and selectivity. Departing from the traditional catalytic synthetic techniques (*i.e.*, incipient wetness, ion exchange), we have developed a synthetic method which allows precise control of the metal particle size and tuning of the mesoporous SBA-15 silica support pore diameter (Figure 1).
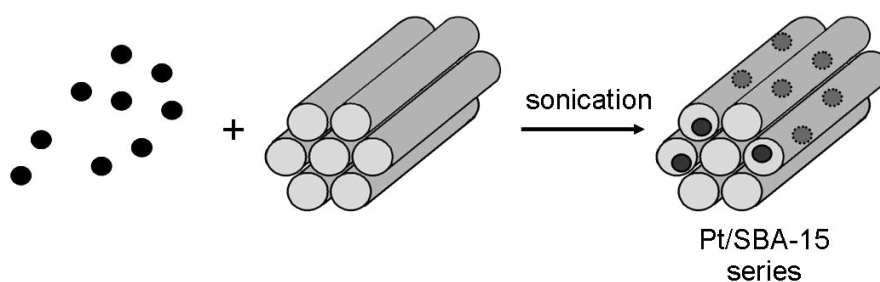
Figure 4.1. Synthetic scheme for the inclusion method.

Control of the Pt particle size is achieved with solution based alcohol reduction methods. Platinum nanoparticles in the 1.7-7.1-nm range have been synthesized and incorporated into a mesoporous silicate support using low-power sonication that facilitates Pt particle entry into the SBA-15 channels by capillary inclusion (CI). After synthesis, the catalysts were characterized by both physical and chemical techniques, such as transmission electron microscopy (TEM), X-ray diffraction (XRD), low-angle XRD, physical adsorption, and chemisorption of probe gases to determine metal surface area. Chemisorption of probe gases demonstrated that the stabilizing polymer used during

nanoparticle synthesis could be removed after appropriate thermal treatment. These Pt/SBA-15 materials are active for two hydrocarbon test reactions, C_2H_4 hydrogenation and C_2H_6 hydrogenolysis. Reaction kinetics are compared with results obtained using two-dimensional single crystals, nanoparticle arrays deposited on silica, and with classical high-surface-area supported platinum catalysts. This study represents a new strategy in catalyst design that utilizes nanoscience to fabricate active catalyst sites, which are deposited on a support to produce a model heterogeneous catalyst. The precise control obtained in these catalytic systems may enable very accurate structure-activity or more importantly structure-selectivity correlations to be established, which will be the direction of future research.

4.2   Experimental Section

4.2.1   Pt Nanoparticle Synthesis.

Hexachloroplatinic acid, $H_2PtCl_6 \cdot 6H_2O$ (99.9%, metals basis) was purchased from Alfa Aesar. Poly(vinylpyrrolidone) (PVP, M_w = 29 000 and 55 000) was obtained from Aldrich. Methanol, ethanol, and ethylene glycol were used without further purification. Platinum particles from 1.7 to 3.6 nm were synthesized according to literature methods [9, 10]. The synthesis of Pt nanoparticles in the size range 1.7-7.1 nm is briefly summarized.

1.7-nm Pt Particles. NaOH (12.5 mL, 0.5 M) in ethylene glycol was added to a solution of $H_2PtCl_6 \cdot 6H_2O$ (0.25 g, 0.48 mmol) in 12.5 mL of ethylene glycol. The mixture was heated at 433 K for 3 h accompanied by N_2 bubbling. A 6-mL aliquot of the resulting solution was transferred to a vial. The particles were precipitated by adding 1

mL of 2 M HCl, and dispersed in ethanol containing 12.2 mg of PVP (M_w = 29 000). The solvent was evaporated and the residue was redispersed in water.

2.6-nm Pt Particles. PVP (133 mg) was dissolved in a mixture of 20 mL of 6.0 mM $H_2PtCl_6 \cdot 6H_2O$ aqueous solution and 180 mL of ethanol. The mixture was refluxed for 3 h. The solvent was evaporated, and the residue was redispersed in water.

2.9-nm Pt Particles. PVP (133 mg) was dissolved in a mixture of 20 mL of 6.0 mM $H_2PtCl_6 \cdot 6H_2O$ aqueous solution and 180 mL of methanol. The reaction condition was the same as that for 2.6-nm particles.

3.6-nm Pt Particles. Freshly prepared 2.9-nm Pt colloidal solution (100 mL) in a water/methanol (1:9) mixture was mixed with 10 mL of 6.0 mM $H_2PtCl_6 \cdot 6H_2O$ solution and 90 mL of methanol. The reaction condition was the same as those for 2.6- and 2.9-nm particles.

7.1-nm Pt Particles. A total 3 mL of 0.375 M PVP (M_w = 55 000) and 1.5 mL of 0.0625 M $H_2PtCl_6 \cdot 6H_2O$ (PVP/Pt salt = 12:1) solutions in ethylene glycol were alternatively added to 2.5 mL of boiling ethylene glycol every 30 s over 16 min. The reaction mixture was refluxed for additional 5 min. The particles were precipitated by adding triple volume of acetone, and redispersed in water. All Pt colloidal solutions were adjusted to 3×10^{-3} M based on the Pt salt concentration by adding appropriate amount of deionized water.

4.2.2 Synthesis of Mesoporous SBA-15 Silica

Silica SBA-15 was prepared according to the method reported in the literature.[11] Pluronic P123 (BASF, $EO_{20}PO_{70}EO_{20}$, EO = ethylene oxide, PO = propylene oxide) and tetraethoxysilane (TEOS, 99+%, Alfa Aesar) were used as received. Pluronic P123 (6 g)

was dissolved in 45 g of water and 180 g of 2 M HCl solution with stirring at 308 K for 30 min. TEOS (12.75 g) was added to the solution with stirring at 308 K for 20 h. The mixture was aged at 373 K for 24 h. The white powder was recovered through filtration, washed with water and ethanol thoroughly, and dried in air. The product was calcined at 823 K for 12 h to produce SBA-15 with a pore diameter of 9 nm. The final calcined material had a surface area of 765 m^2 g^{-1} and a pore volume of 1.16 cm^3 g^{-1}.

4.2.3   Preparation of Pt/SBA-15

Pt colloidal aqueous solution (25.6 mL, 3×10^{-3} M) was mixed with 74.4 mL of water and 100 mL of ethanol. The mixture was quickly added to 1.5 g of SBA-15, and the slurry was sonicated for 3 h at room temperature by a commercial ultrasonic cleaner (Branson, 1510R-MT, 70 W, 42 kHz). The brown precipitates were separated by centrifugation, thoroughly washed with water and ethanol, and dried in an oven at 373 K. Pt (1.7 nm)/SBA-15 was calcined at 623 K for 12 h, Pt (7.1 nm)/SBA-15 was calcined at 723 K for 24 h, and all other catalysts were calcined at 723 K for 12 h with O_2 flow.

4.2.4   Catalyst Characterization

TEM experiments were made on a Topcon EM002B microscope operated at 200 kV at the National Center for Electron Microscopy at Lawrence Berkeley National Laboratory. Aqueous Pt colloidal solutions were dropped and dried on carbon-film-coated copper grids (Ted Pella). Dried SBA-15 and Pt/SBA-15 powders were sonicated in acetone for several seconds, dropped on the TEM grids, and dried in air. A minimum of two hundred particles were counted for determination of a number-average particle size. XRD patterns were measured on a Bruker D8 GADDS diffractometer using Co Kα radiation (1.79 Å). Low-angle XRD patterns were recorded on a Siemens D5000

diffractometer using Cu Kα radiation (1.54 Å). Nitrogen porosimetry data were collected on a Quantachrome Autosorb-1 analyzer at 77 K. Elemental analyses were conducted at Galbraith Laboratories, Inc. Selective gas adsorption measurements were measured in a volumetric apparatus constructed of Pyrex that obtained a pressure below 5×10^{-6} Torr in the sample cell by use of a liquid nitrogen trapped diffusion pump (Varian M2). The amount of adsorbed gas was monitored using a digital pressure gauge (MKS, model PDR-D). Total and reversible isotherms were measured with an interim 1-h evacuation between isotherms. The amount of adsorbed gas was extrapolated to zero pressure for all adsorbates. Catalysts were reduced at 673 K for 75 min and evacuated at 623 K for 1 h prior to any chemisorption measurement at 295-300 K. H_2 (Matheson, UHP), O_2 (Airgas, UHP), and CO (Matheson, UHP, Al cylinder) were all used without further purification for chemisorption measurements.

4.2.5   Reaction Studies

The hydrogenation of ethylene was conducted at 273-313 K in a plug flow reactor (PFR) constructed of Pyrex. Gas flow rates were controlled by mass flow controllers (Unit instruments) connected to a central manifold of 1/4-in. stainless steel tubing. Ethylene (Airgas CP grade), H_2 (Matheson, UHP), and He (Matheson, UHP) were used without further purification. Gas-phase concentrations were determined by gas chromatography (HP 5890) using an FID detector and isothermal temperature program with a homemade alumina column (6 ft. × 1/8-in. o.d.). The total conversion of ethylene was <10% for all temperatures studied. Typically, catalysts were diluted with low-surface-area (2.5 m^2 g^{-1}) acidwashed quartz in a 1:3 catalyst-to-quartz ratio. Room-temperature ethylene hydrogenation required 1-3 mg of catalyst. The effect of dilution

on catalyst performance was tested [12] and it was verified that dilution ratios less than 10 had no effect on catalyst activity. Lack of heat and mass transfer limitations were confirmed by use of the Madon-Boudart test [13] at 273 and 298 K for Pt (3.6 nm)/SBA-15 with three different Pt loadings.

Kinetic parameters on the reduced catalysts were measured as well as reaction orders in ethylene and hydrogen at various temperatures. Turnover rates in this paper are reported at standard conditions of 10 Torr C_2H_4, 100 Torr H_2, and 298 K. During all kinetic measurements, the last point was duplicated to verify that deactivation had not occurred during the course of the experiment. Hydrogenolysis of ethane (Airgas, UHP) was studied from 613 to 653 K in a differentially operated plug flow reactor (PFR). At standard conditions of 20 Torr C_2H_6 and 200 Torr H_2, all conversions were <5% for the entire temperature range examined. Reaction orders in ethane and hydrogen were collected for Pt (X)/SBA-15 catalysts at 643 K with particle sizes (X) ranging from 1.7 to 7.1 nm.

4.3 Results and Discussion

4.3.1 Synthesis and Characterization of Pt Particles

Monodisperse Pt particles of 1.7-3.6 nm were synthesized by modified alcohol reduction methods according to the literature [9, 10]. Methanol, ethanol, and ethylene glycol served as solvents for dissolving Pt salts and PVP, and as a reducing agent of Pt according to the following reaction:

$$H_2PtCl_6 + 2\ RCH_2OH\ ?\ \ Pt^0 + 2RCHO + 6HCl$$
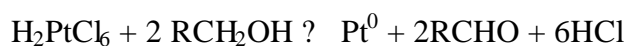
Pt particle size increases from 1.7 to 2.9 nm as the reaction temperature decreases from 433 K in ethylene glycol to 338 K in boiling methanol. This indicates that reduction of the Pt salts at high temperature produces more Pt nuclei in a short period and eventually affords smaller Pt particles. The 3.6-nm Pt particles were successfully obtained by addition of 2.9-nm particles as a seed for stepwise growth. 7.1-nm Pt particles were generated by slow and continuous addition of the Pt salt and PVP to boiling ethylene glycol, described elsewhere in detail [14]. All aqueous Pt colloidal solutions with PVP are stable for more than two weeks. Pt particle sizes were measured by XRD and TEM. Figure 2 shows that the particles are uniform and have a narrow size distribution.
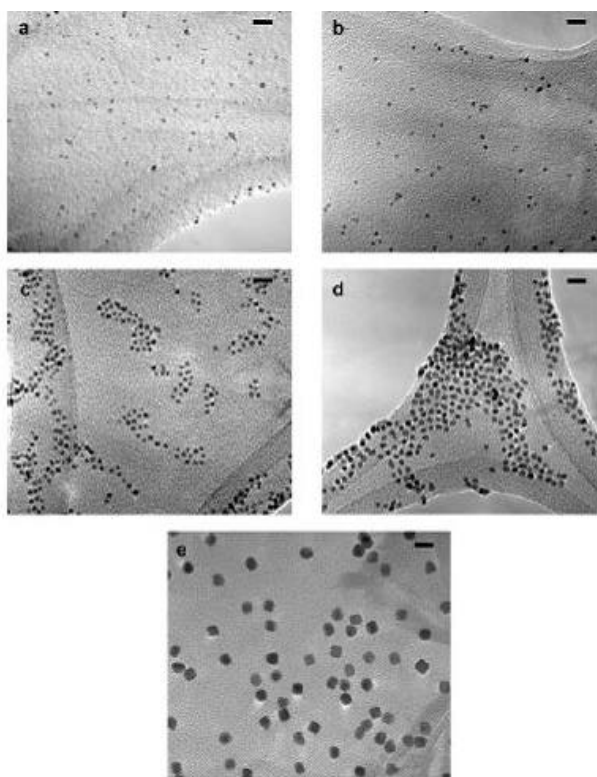
Figure 4.2. TEM images of the Pt particles of (a) 1.7 nm, (b) 2.6 nm, (c) 2.9 nm, (d) 3.6 nm, and (e) 7.1 nm. The scale bars represent 10 nm.

An example of the particle size distribution for freestanding 2.9-nm particles is shown in Figure 3.
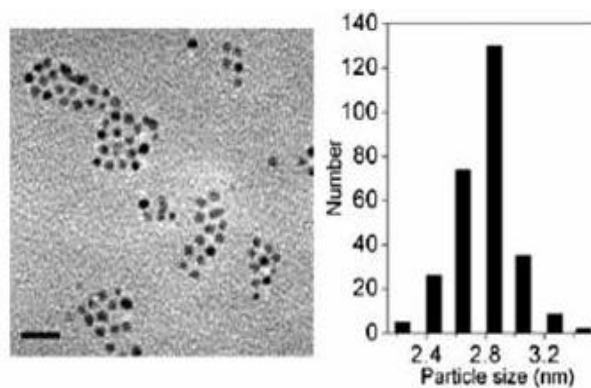
Figure 4.3. TEM image and particle size histogram for free-standing 2.9 nm Pt particles. The number-average Pt particle size was obtained by counting 281 particles.

Average Pt particle sizes estimated by XRD (Figure 4) are 1.7, 2.6, 2.9, 3.6, and 7.1 nm, and match very well with TEM results (1.73 ± 0.26, 2.48 ± 0.22, 2.80 ± 0.21, 3.39 ± 0.26, and 7.16 ± 0.37 nm).
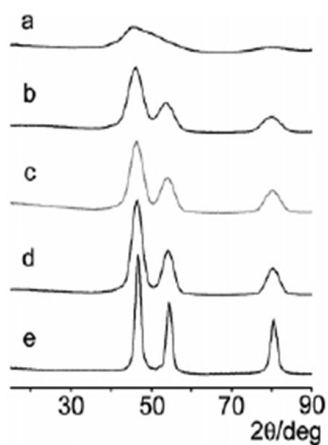
Figure 4.4. XRD data for free-standing Pt particles of (a) 1.7 nm, (b) 2.6 nm, (c) 2.9 nm, (d) 3.6 nm, and (e) 7.1 nm.

4.3.2   Synthesis and Characterization of Pt/SBA-15 Catalysts

Incorporation of the Pt Particles in SBA-15 Structure.

SBA-15 with a pore diameter of 9.0 nm was used as a catalyst support due to its high surface area (700-800 m^2 g^{-1}) and ordered mesoporous structure [11].   Platinum

particles of different sizes were dispersed in a 1:1 mixture of water and ethanol, and mixed with SBA-15 under sonication for 3 h at room temperature. After calcination at 723 K with O_2 flow, *ca.* 1 wt. % Pt(*X*)/SBA-15 catalysts (*X*) 1.7, 2.6, 2.9, 3.6, and 7.1 nm) were obtained as pale brown powders. These materials were characterized by XRD, TEM, and physisorption measurements. TEM images of Pt/SBA-15 samples (Figure 5) show that the particles are well-dispersed in the entire channel structures even for the largest Pt particles (7.1 nm).
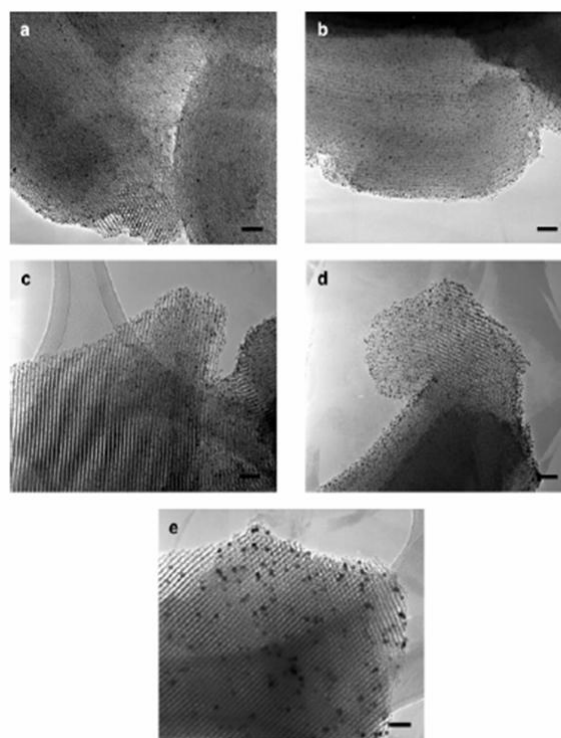
Figure 4.5. TEM images of the Pt(X)/SBA-15 catalysts: X = (a) 1.7 nm, (b) 2.6 nm, (c) 2.9 nm, (d) 3.6 nm, and (e) 7.1 nm. The scale bars represent 20 nm.

Three Pt reflections are seen in the XRD patterns of SBA-15 catalysts (Figure 6). These peaks are observed at $2\theta = 45.9°$, $54.0°$, and $80.1°$ assignable to (111), (200), and (220)

reflections of the fcc Pt lattice, respectively, as well as a very broad signal at 2θ =

27.4° for amorphous SiO_2. As the particle size increases, characteristic reflections of the
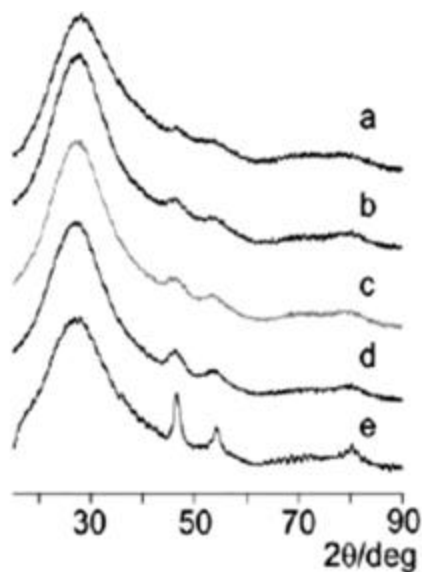
Figure 4.6. XRD data of the Pt(X)/SBA-15 catalysts: X = (a) 1.7 nm, (b) 2.6 nm, (c) 2.9 nm, (d) 3.6 nm, and (e) 7.1 nm.

Pt lattice become sharper as expected. The particle sizes for Pt incorporated into the

support were calculated from the full width at half-maximum (fwhm) of the Pt(111) peak

after baseline subtraction of pristine SBA-15. Particle sizes are almost identical to those

of the free-standing Pt particles in solution. Low-angle XRD patterns (Figure 7) for all

Pt/SBA-15 catalysts exhibit three characteristic peaks indexed as (100), (110), and (200)

of the two-dimensional *p6mm* hexagonal mesostructure with d_{100} spacing of 10.1 nm,

similar to pristine SBA-15 [11]. Measured BET surface areas of the catalysts are 690 -

830 m^2 g^{-1}, while pore volumes are 1.08-1.31 cm^3 g^{-1}. BET isotherms of the samples

before and after inclusion of 2.9-nm Pt particles on SBA-15 are shown in Figure 8, and

demonstrate that the inclusion process does not disrupt the SBA-15 mesostructure.
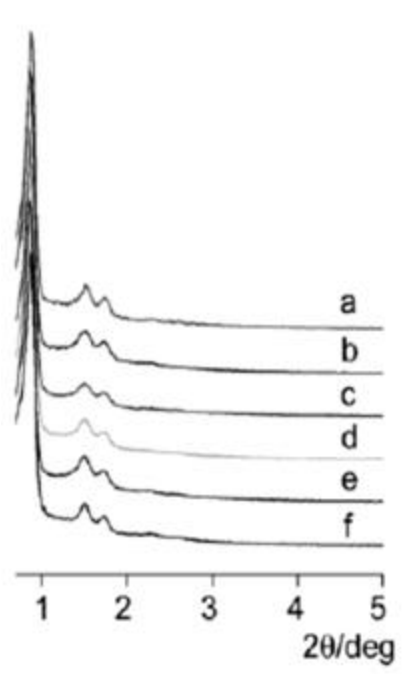
Figure 4.7. Low-angle XRD patterns of (a) pristine SBA-15, and ~1% Pt(X)/SBA-15: X = (b) 1.7 nm, (c) 2.6 nm, (d) 2.9 nm, (e) 3.6 nm, and (f) 7.1 nm.
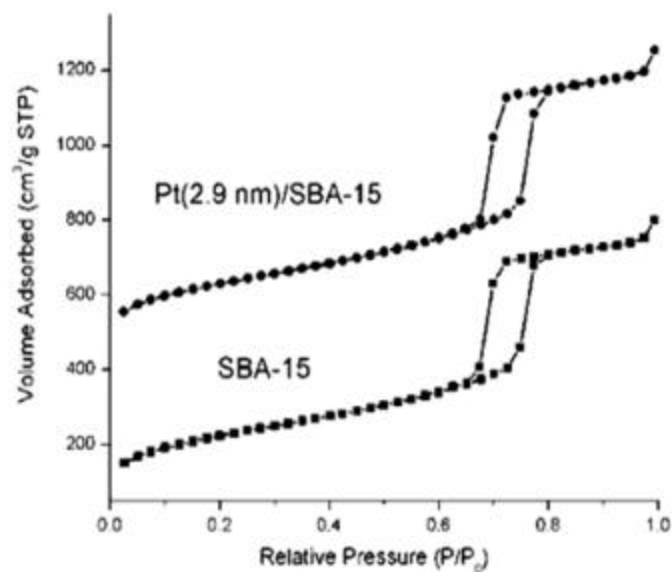
Figure 4.8. Nitrogen adsorption isotherm of SBA-15 and Pt(2.9 nm)/SBA-15. The isotherm for Pt(2.9 nm)/SBA-15 is shifted by 400 cm^3 (STP) g^{-1}.

Low-angle XRD data and TEM images indicate that the hexagonal wall structure of

SBA-15 is robust under the conditions of catalyst synthesis. The minimal change in

SBA-15 physical parameters after incorporation of Pt into the silica reveals that there is no significant blocking of the SBA-15 channel by Pt particles.

Efficient Incorporation of Pt Nanoparticles in SBA-15.

For homogeneous dispersion of the Pt particles within the silica channels, sonication of the reaction mixture is required. Without sonication, particles are primarily attached on the external surface of SBA-15 and become large aggregates after high temperature treatment. The extent of Pt dispersion with the SBA-15 framework was followed with time by TEM (Figure 9). Pt particles were rapidly adsorbed on the external surface of
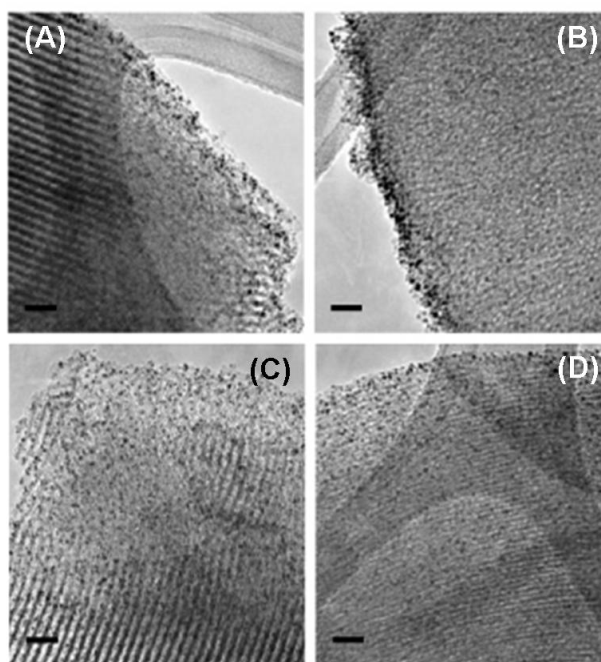
Figure 4.9. TEM images of Pt/SBA-15 sonicated for various times at room temperature in water/ethanol (1:1) mixture: (A) for 3 min., (B) for 10 min., (C) for 30 min., (D) for 90 min. The scale bars represent 20 nm.

SBA-15 within 3 min, followed by diffusion of the Pt particles into the channels over 1.5 h, and finally dispersed throughout the entire SBA-15 channel. Sonication effectively

prevents Pt particles from blocking the pore entrance, promoting homogeneous inclusion. A proper choice of the inclusion solvent should also be considered. In pure water rather than a water/ethanol (1:1) mixture, Pt particles were mainly deposited on the outer surface of SBA-15 after sonication for 3 h, eventually leading to large aggregates after calcination. Huang et al. reported similar phenomenon for Ag nanowire formation within SBA-15 channels [15], and suggested that it is attributed to the different surface tensions of H_2O (71.99 mN m^{-1}) and ethanol (21.97 mN m^{-1}).

The location of nanoparticles is an important issue in these metal/mesoporous silica catalysts. Janssen *et al*. imaged three dimensional structures of metal and metal oxide particles in SBA-15 by bright-field electron tomography, but the results were difficult to interpret due to diffraction contrast [16]. The ordering of Pt nanoparticles within the silica channels was visualized by synthesizing a Pt (2.9 nm)/SBA-15 with a high metal content (14.4 wt %). Figure 10a shows that the silica channels are filled with a significant number of small particles appearing as black stripes. After treatment at 673 K for 75 min with H_2 flow (Figure 10b), nearest neighbor particles aggregated to form nanorods in conformation with the geometry of the SBA-15 channel. This confirms that most of the Pt particles in Pt/SBA-15 are located inside the mesopores. It appears that the Pt particles in 0.95% Pt (2.9 nm)/SBA-15 are primarily located inside the channels, although the possibility of Pt particles located on the external surface cannot be ruled out.

Particle Size Determination by Chemisorption Measurement.

Particle size determinations by TEM and XRD are in excellent agreement. While these techniques are bulk measures of particle size, we have measured the particle size of
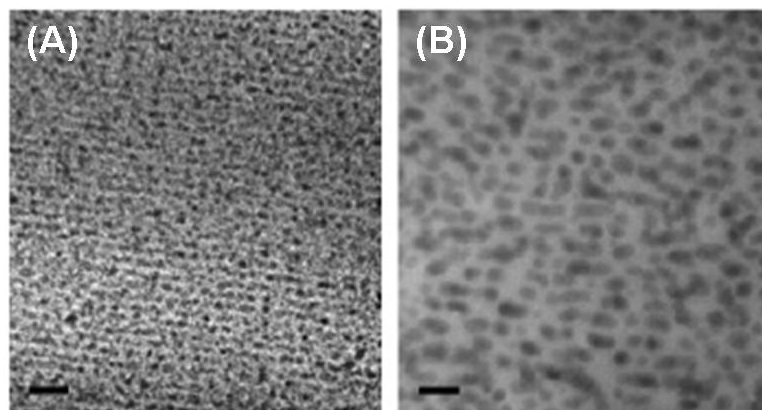
Figure 4.10. TEM images of 14.4 wt % Pt(2.9 nm)/SBA-15: (A) before H_2 treatment, and (B) after treatment with H_2 at 673 K for 75 min. The scale bars represent 20 nm.

the supported Pt crystallites using selective chemisorption measurements. Boudart [17] has suggested that the most pertinent normalization of catalytic activity to a turnover frequency basis should be done with chemisorption measurements rather than electron microscopy or XRD. The dispersion or ratio of surface atoms to the total number of atoms was determined for all ~1% Pt/SBA-15 catalysts. A summary of the chemisorption data for all catalysts is compiled in Table 1. Monolayer values were obtained by extrapolating isotherms to zero pressure. Dispersions for all catalysts were determined using four separate methods: H_2 chemisorption, CO chemisorption, O_2 chemisorption, and H_2-O_2 titration (Pt_s-O + 3/2H_2 ? Pt_s-H + H_2O) [18]. The well accepted 1:1 surface hydrogen metal atom stoichiometry was used to count the number of surface atoms by H_2 [19]. The reported dispersion based on H_2 chemisorption and H_2-O_2 titration for the Pt/SBA-15 series was based on the total, rather the irreversible (strong) uptakes. Boudart [20] has suggested that the total rather than the irreversible uptake is a better measurement of Pt surface area when Pt is not highly dispersed. For CO

Table 4.1. Probe gas uptake and average particle size for Pt/SBA-15 catalysts

catalyst[a]	TEM Particle size[b]	probe gas uptake[c] (μmol g^{-1})					dispersion, D	Particle size, d (nm)		
		H$_2$ total	CO total	CO irrev	O$_2$ irrev	H$_2$-O$_2$ total	H$_2$-O$_{2,total}$	chemisorption[d] H$_2$	H$_2$-O$_2$	XRD[e]
Pt powder	--	12.3	7.1	6.9	4.0	17.2	0.0022	235	505	> 100
3.2% Pt/SiO$_2$-IE	--	133.1	166.7	152.2	24.2	262.0	1[f]	< 1	< 1	--
0.73% Pt/SBA-15	1.7	7.4	13.3	12.2	4.3	17.4	0.311	2.9	3.6	--
0.90% Pt/SBA-15	2.6	3.9	9.4	9.4	3.2	22.2	0.321	6.6	3.5	2.5
0.95% Pt/SBA-15	2.9	6.8	7.8	7.8	2.6	18.1	0.248	4.1	4.6	3.0
0.46% Pt/SBA-15	3.6	3.7	5.0	3.9	1.6	12.9	0.364	3.5	3.1	3.8
1.0% Pt/SBA-15	3.6	4.0	9.6	9.3	2.6	15.6	0.203	7.1	5.6	3.8
1.01% Pt/SBA-15	7.1	2.1	5.0	4.6	2.2	10.1	0.131	8.7	8.7	7.8

[a]Elemental analysis determined by ICP-AES.
[b]Number average particle size. Determined by counting a minimum of 200 free-standing particles.
[c]Conducted at 295 K.
[d]Determined by $1.13/(Pt_s/Pt_T)$.
[e]Based on the Scherrer equation after subtracting SBA-15 baseline.
[f]Dispersion, $D = 1$, if $Pt_s/Pt_T > 1$.

chemisorption, the surface reaction was assumed to occur with a 1:1 stoichiometry. Carbon monoxide adsorbs predominantly in the linear form on Pt at ambient temperatures and high pressures of CO [21]. Oxygen was assumed to adsorb dissociatively at room temperature. Fractional dispersions for the Pt/SBA-15 series range from 0.13 to 0.31 based on total H_2-O_2 titration uptakes for supported as-synthesized Pt particles ranging from 1.7 to 7.1 nm. The four separate measurements are in good agreement when compared for the same sample. A 3.2% Pt/SiO$_2$ catalyst prepared by ion exchange (Pt/SiO$_2$-IE) [22] used as a standard had an irreversible measured uptake corresponding to a dispersion greater than unity. Spenadel and Boudart [23] have suggested it is unlikely that Pt is truly atomically dispersed because it would be difficult to account for the rapid uptake of one hydrogen atom per platinum atom. The lack of any Pt reflections in the X-ray diffraction pattern confirms that the Pt particles are very small (<2.5 nm). A value of unity for metallic dispersion was used for the 3.2% Pt/SiO$_2$-IE in calculations of turnover frequency for ethane or methane formation in ethylene hydrogenation and ethane hydrogenolysis, respectively.

The Pt particle size based on chemisorption was calculated according to the equation d (nm) = 1.13/D, where D is the metallic dispersion. The above equation assumes spherical particles and a Pt atom density of 1.25×10^{19} atoms m^{-2} [24]. From Table 1, it can be seen that the Pt particle size calculated from chemisorption trends with the TEM particle size of the free-standing particles. XRD measurements on the supported Pt/SBA-15 particles indicated that the Pt particles were not agglomerated by sonication or the pretreatment procedure; however, as shown in Table 1, there is a significant difference in the measured particle size between the two techniques

(chemisorption and XRD). While the two techniques measure average particle size, their averages (surface versus volume) are different, but often good agreement between the two is found when the Pt particle size is in the range in which the line-broadening technique is applicable [23]. Two possible explanations exist to explain this large discrepancy in particle size. Synthesis of the Pt nanoparticles requires the use of a template polymer that prevents particles from agglomerating while in solution. Consequently, this polymer (PVP in our synthesis) bonds very strongly to the Pt surface and is difficult to remove after the particles have been dispersed within the SBA-15 matrix. A polymer removal method based on thermal calcination that leads to no particle agglomeration has been developed. Although the calcination procedure has been optimized, a possible explanation for the discrepancy between chemisorption and XRD particle size is a reduced exposed surface area due to the existence of remaining polymer on the Pt surface. XRD would be insensitive to this circumstance, while chemisorption would directly probe this loss of surface area. Spectroscopic data (both infrared and Raman) show no absorption bands attributable to PVP, although it cannot be ruled out that the Pt surface is covered with carbon. There is no apparent advantage of using calcination times longer than 12 h (7.1 nm as an exception).

An important consequence to note about comparison of the free-standing TEM particle and that determined by selective chemisorption is that some portion of the supported Pt nanoparticle is involved in bonding with the silica surface and will be unable to chemisorb gas. With the construction of the appropriate geometrical picture of the metal-support interface, the difference in particle size between XRD and

chemisorption measurements could potentially be used to calculate the interfacial area between the Pt nanoparticle and mesoporous SBA-15 silica.

4.3.3 Ethylene Hydrogenation on Pt/SBA-15 Catalysts.

Comparison of Activity and Kinetic Parameters with Other Model Systems

Ethylene hydrogenation was chosen as a test reaction to compare the activity of Pt/SBA-15 materials with kinetic measurements made on supported Pt catalysts prepared by standard preparation techniques (*i.e.*, incipient wetness, ion exchange) and other model systems such as single crystals and nanoparticle arrays. Table 2 is a compilation of the turnover rates (at standard conditions) measured on a number of catalysts used in this study including a Pt powder (Alfa Aesar, 99.9%, 1 μm particle size). Turnover frequencies at standard conditions (10 Torr C_2H_4, 100 Torr H_2, 298 K) for the Pt/SBA-15 catalysts are ~0.7 s^{-1}. Pristine SBA-15 and the quartz diluent had no activity for ethylene hydrogenation over the entire temperature range of this study (273-313 K). The apparent activation energy for this reaction is low (~6-7 kcal mol^{-1}). Turnover frequencies for all catalysts with particle sizes ranging from 1.7 to 7.1 nm were the same, confirming the well-known structure insensitivity of this reaction. Table 3 is a compilation of turnover frequencies for ethylene hydrogenation over selected classical high-surface area supported catalysts and model systems. A complete compilation of ethylene hydrogenation kinetics on metallic catalysts can be found elsewhere [25]. Both the Pt(111) single crystal and Pt nanoparticle arrays are more active than the Pt/SBA-15 catalysts by an order of magnitude. Rates measured on our monodispersed nanocatalysts (Pt/SBA-15 series) are in very good agreement with measurements on classical high

Table 4.2. Reaction rate and kinetic data for ethylene hydrogenation on Pt/SBA-15 catalysts

catalyst[a]	TEM particle size[b] (nm)	activity[c] (μmol g^{-1} s^{-1})	TOF[c,d] (s^{-1})	E_a[e] (kcal mol^{-1})	reaction orders C_2H_4[f]	H_2[g]
3.2% Pt/SiO$_2$-IE	--	123.3[h]	0.75	7.1	-0.2	0.86
0.73% Pt/SBA-15	1.7	8.3	0.71	6.9	0.1	0.75
0.90% Pt/SBA-15	2.6	9.8	0.66	7.4	0.08	0.72
0.95% Pt/SBA-15	2.9	8.5	0.70	7.9	0.05	0.77
0.46% Pt/SBA-15	3.6	5.9	0.68	7.6	0.08	0.7
1.0% Pt/SBA-15	3.6	6.7	0.64	6.9	0.11	0.69

[a]Elemental analysis determined by ICP-AES.
[b]Number average particle size. Determined by counting a minimum of 200 free-standing particles.
[c]Reaction conditions were 10 Torr C_2H_4, 100 Torr H_2, and 298 K.
[d]Surface Pt (Pt_s) determined from total H_2-O_2 titration amount.
[e]Reaction conditions were 10 Torr C_2H_4, 100 Torr H_2, and 273–313 K.
[f]Reaction conditions were 6–40 Torr C_2H_4, 150 Torr H_2, and 298 K.
[g]Reaction conditions were 10 Torr C_2H_4, 100 –500 Torr H_2, and 298 K.
[h]Rate extrapolated from 227 K assuming E_a = 7 kcal mol^{-1} and temperature independent reaction orders.

surface-area supported catalysts.

The Madon-Boudart (MB) test [13] was used to verify the absence of heat and mass transfer effects during the room temperature hydrogenation of ethylene in a differential PFR. The MB test requires measurement of the reaction rate (on per gram basis) for catalysts with varying surface concentrations of metal but with similar dispersion. A log-log plot of rate versus surface concentration should yield a straight line with a slope equal to one, if heat and mass transfer effects are absent. For an exothermic reaction, the test should be repeated at a second temperature. In accordance with the criteria of the MB test, the rate was measured using catalysts with different metal loading but similar dispersion (determined by H_2-O_2 titration) at two different temperatures. The slope of the line (not shown) at both temperatures is ~1 verifying that the measured rate is independent of the influence of transport effects. Table 3 also contains a compilation of apparent activation energies for a number of model systems and some selected examples of classically prepared (*i.e.*, incipient wetness, ion exchange) heterogeneous catalysts. It is well-known that ethylene hydrogenation occurs at room temperature and below, which suggests that the true activation energy for the reaction is quite low. For all catalysts used in this study, the apparent activation energy was ca. 7 kcal mol^{-1}, which is slightly lower than previously reported values on low loaded Pt/SiO$_2$ catalysts (9 kcal mol^{-1}) [26], electron beam lithography Pt nanoparticle arrays (10.2 kcal mol^{-1}),27 and a Pt(111) single crystal (10.8 kcal mol^{-1}) [28]. Reaction orders in hydrogen are ~0.6 at 298 K. These are higher than the H_2 order (0.5) predicted based on the Horiuti-Polanyi mechanism [29], which assumes gas-phase hydrogen and surface H atoms are in equilibrium. The apparent H_2 reaction order is temperature-dependent, as shown in Figure 11. As the

Table 4.3. Compilation of turnover frequencies for ethylene hydrogenation on model catalysts and selected classical high surface area supported catalysts

catalyst	Turnover frequency[a,b] (s^{-1})	E_a $(kcal\ mol^{-1})$	reference
Pt/SBA-15	~0.7	~7	this work
Pt(111)	9.3	10.8	25
Pt nanoparticle array	14.3	10.2	26
0.04% Pt/SiO$_2$	4.4	8.6	27
Pt wire	2.7	8.6	27
Pt wire	3.5	10.0	28
0.05% Pt/SiO$_2$	3.7×10^{-3}	16.0	29
0.05% Pt/SiO$_2$	2.9×10^{-3}	17.0	30
2.45% Pt/SiO$_2$	9.3	10.5	31
evaporated Pt film	50.5	10.7	32
0.05% Pt/SiO$_2$	1.3	9.1	33
0.5% Pt/SiO$_2$	17.5	8.9	33
9.2% Pt/Al$_2$O$_3$	53.4	10.0	34

[a]Rates corrected to 10 Torr C$_2$H$_4$, 100 Torr H$_2$, and 298 K.
[b]Corrected assuming zero and first order dependencies on ethylene and hydrogen, respectively.
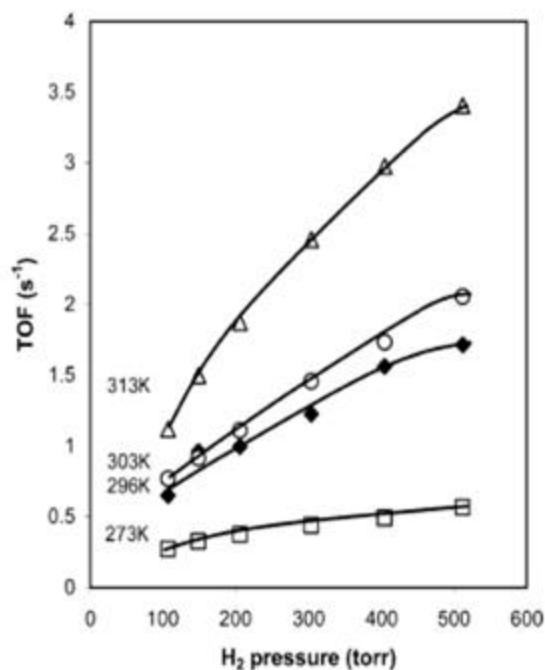
Figure 4.11. Temperature dependence (273–313 K) of H_2 partial pressure for ethylene hydrogenation on a 1.0% Pt(3.6 nm)/SBA-15. Reaction conditions were 10 Torr C_2H_4, 100-500 Torr H_2. Lines are drawn in for clarity.

temperature increases from 273 to 313 K, the reaction order in hydrogen increases from 0.45 to 0.7. Reaction orders in hydrogen on the same series of Pt/SBA-15 catalysts at 195 K are ~0.4. In a study of ethylene hydrogenation on Pt/SiO_2 catalysts, Cortright and co-workers30 have shown that the hydrogen order increased from 0.48 to 1.10 as the temperature was increased from 223 to 336 K, at 25 Torr C_2H_4 and hydrogen pressures ranging from 50 to 650 Torr. At low temperatures and high ethylene pressures, the observed reaction-order dependency for both ethylene and hydrogen can be explained by a Horiuti-Polanyi mechanism in which hydrogen is adsorbed noncompetitively on a surface essentially covered with adsorbed hydrocarbon species.

The olefin generally has an inhibiting effect on the overall reaction rate in olefin hydrogenation reactions [31]. The olefin displaces hydrogen from the metal surface,

negatively impacting the measured reaction rate as the olefin pressure is increased. At lower ethylene pressures and higher temperatures, more adsorption sites are available for hydrogen and a maximum in ethylene hydrogenation activity is seen on Pt catalysts. The apparent reaction order in ethylene is temperature-dependent (not shown). At room temperature, the dependence on ethylene is zero order or slightly positive, while at higher temperatures, the reaction order approaches -0.3. As the temperature is increased and total surface coverage decreases, the ethylene order becomes more negative, suggesting that the adsorption between ethylene and hydrogen becomes competitive. Cortright and co-workers [30] have measured a similar trend with temperature, and have separately assembled a microkinetic model [32]. Assuming a mechanism in which H_2 could adsorb dissociatively on a surface site in direct competition with ethylene or on a noncompetitive adsorption site, the microkinetic model is able to predict the experimentally observed reaction orders over a 100 K range [32]. El-Sayed and co-workers have shown that the reaction order in propylene during propylene hydrogenation is ~0.1 at 313 K [33]. In fact, a reaction order of ~0.2 for ethylene on the Pt/SBA-15 catalysts at 195 K has been measured. At these low temperatures, on the Pt/SBA-15 catalysts, it appears that ethylene is in direct competition with hydrogen for adsorption sites and ethylene hydrogenation is not occurring over the hydrocarbon-covered fraction of the surface.

Horiuti and Polanyi [29] proposed a reaction mechanism that involved the sequential hydrogenation of a surface olefin species, which involved the formation of a surface half-hydrogenated species (*i.e.*, ethyl in the case of ethylene hydrogenation). Zaera and Somorjai demonstrated that the hydrogenation of ethylene on Pt(111) occurs on a hydrocarbon-covered surface [28]. Ethylidyne ($\equiv$C-CH$_3$) was identified as a

spectator species that turns over orders of magnitude slower than the presumed reaction intermediate, π-bonded ethylene [34]. Somorjai and co-workers suggest that the ethylidyne layer covers the surface upon which ethylene adsorbs and H_2 is adsorbed dissociatively on the Pt surface [35]. Electron energy loss spectroscopy studies of ethylene hydrogenation on Pt(111) at 298 K demonstrated that the Pt(111) surface is covered with ethylidyne and ethyl radicals [36]. The ethyl radicals were easily hydrogenated, which suggests they are a reaction intermediate to ethane formation. Dumesic and coworkers have shown that the formation of ethylidyne is not necessary for the hydrogenation of ethylene on supported Pt particles [37]. Beebe and Yates [38] have shown that under hydrogen rich conditions, surface ethylidyne is not necessary for ethane formation over supported Pd catalysts. It appears that there is still much debate over the mechanism of ethylene hydrogenation, but it is clear that the mechanism changes with temperature and partial pressure of both ethylene and hydrogen, and our nanocatalysts display behavior similar to that of classical catalyst systems when ethylene and hydrogen pressures are varied.

4.3.4   *Ethane Hydrogenolysis*

The hydrogenolysis of ethane is one of the most fundamental reactions studied in heterogeneous catalysis. The importance of studying such a reaction is noted by considering that two of the most important processes in heterogeneous catalysis are occurring in one reaction: C-H and C-C bond activation. The high temperatures required for ethane hydrogenolysis signifies the strength of the C-C bond because it is well-known that H/D exchange on ethane occurs at temperatures significantly lower than those required for measurable hydrogenolysis activity [39]. Anderson and Kemball [40] have

shown that H/D exchange on Pt films occurs at ~430 K with an apparent activation energy of 22 kcal mol^{-1}. Zaera and Somorjai have shown that deuterium exchange rates were 3 orders of magnitude higher than the rate of ethane hydrogenolysis on Pt(111) at 550 K [41].

Comparison of Hydrogenolysis Activity and Kinetic Parameters with Classical Supported Catalyst.

The hydrogenolysis of ethane on the Pt/SBA-15 catalysts was studied in a PFR at temperatures of 613-653 K under high hydrogen partial pressures. Freshly reduced catalysts generally deactivated over a 1-2 h time period, after which a steady-state rate was achieved and measured rates were stable for the duration of an experiment. The temporal behavior of ethane hydrogenolysis for a 1% Pt (3.6 nm)/SBA-15 catalyst is shown in Figure 12. All rates reported represent measured rates after deactivation had subsided. Table 4 is a compilation of turnover frequencies (at standard conditions) and kinetic parameters for this reaction. Turnover frequencies for ethane hydrogenolysis range from 0.52 to 1.44×10^{-2} s^{-1} at 643 K. The turnover frequency for Pt powder was higher by about a factor of 3 for the most active SBA-15 sample, 0.73% Pt (1.7 nm)/SBA-15. The higher turnover frequency may be due to temperature gradients within the catalyst bed. The Pt powder was not diluted and heat transfer effects may influence the rate reported in Table 4. The absence of transport artifacts was confirmed with the MB test for the Pt/SBA-15 catalysts. Cortright and co-workers [42] reported a turnover frequency of 2.4×10^{-1} s^{-1} at 643 K for a 2.5% Pt/SiO$_2$ with a particle size of 1.3 nm, which is an order of magnitude higher than that measured on a Pt/SBA-15 catalyst with
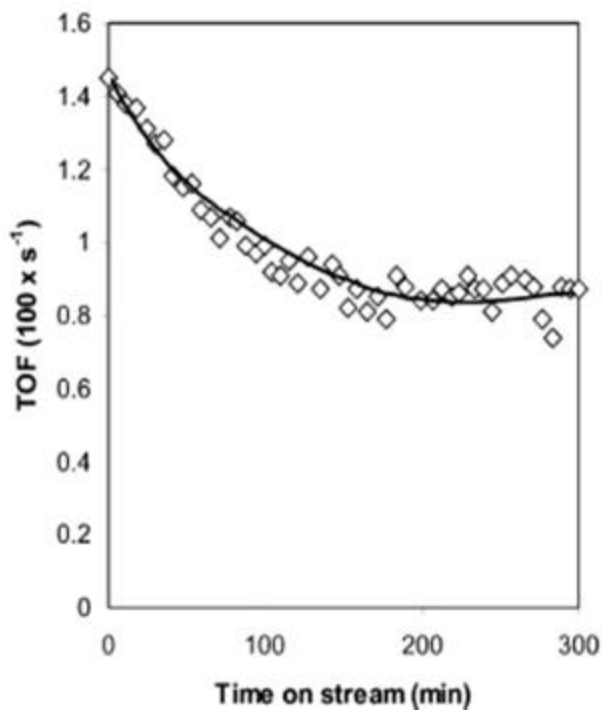
Figure 4.12. Time on stream behavior of 1% Pt(3.6 nm)/SBA-15 during ethane hydrogenolysis. Rates corrected to 20 Torr C_2H_6, 200 Torr H_2 and 643 K.

of 1×10^{-3} s^{-1} on a 10% Pt/SiO_2 catalyst with a particle size of 5 nm. On the Pt/SBA-15 catalysts, the rate is sensitive to the Pt particle size with smaller particles displaying higher activity. It appears from comparison with reported turnover frequencies on high-surface-area supported catalysts that rates differ with particle size. A discussion about the apparent structure sensitivity [44] of ethane hydrogenolysis will be presented later. The apparent activation energy over the temperature range studied (613-653 K) and a C_2H_6:H_2 ratio of ~5 varied from 48 to 65 kcal mol^{-1} with average activation energy of *ca.* 53 kcal mol^{-1} for the Pt/SBA-15 samples (Figure 13). Sinfelt and co-workers measured an apparent activation of 54 kcal mol^{-1} on a 0.6% and 10% Pt/SiO_2 catalyst at similar temperatures and partial pressures of ethane and hydrogen [43, 45]. Apparent activation energies for ethane hydrogenolysis have been shown to change due to catalyst

Table 4.4. Reaction rate and kinetic data for ethane hydrogenolysis on Pt/SBA-15 catalysts

catalyst[a]	TEM particle size[b] (nm)	activity[c] (μmol g^{-1} s^{-1})	TOF[c,d] $100 \times$ (s^{-1})	E_a[e] (kcal mol^{-1})	reaction orders C_2H_6[f]	H_2[g]
Pt powder	--	0.51	4.5	54	0.9	-2.2
3.2% Pt/SiO$_2$-IE	--	2.4	1.4	65	1	-2.6
0.73% Pt/SBA-15	1.7	0.16	1.4	49	0.7	-1.9
0.90% Pt/SBA-15	2.6	0.16	1.1	55	0.7	-1.8
0.95% Pt/SBA-15	2.9	0.11	0.9	54	0.7	-1.9
1.0% Pt/SBA-15	3.6	0.09	0.9	57	0.7	-1.9
1.01% Pt/SBA-15	7.1	0.04	0.5	49	0.8	-1.9

[a]Elemental analysis determined by ICP-AES.
[b]Number average particle size. Determined by counting a minimum of 200 free-standing particles.
[c]Reaction conditions were 20 Torr C_2H_6, 200 Torr H_2, and 643 K.
[d]Based on total H_2-O_2 titration amount.
[e]Reaction conditions were 20 Torr C_2H_6, 200 Torr H_2, and 613–653 K.
[f]Reaction conditions were 18–55 Torr C_2H_4, 200 Torr H_2, and 643 K.
[g]Reaction conditions were 32 Torr C_2H_4, 80 –300 Torr H_2, and 643 K.
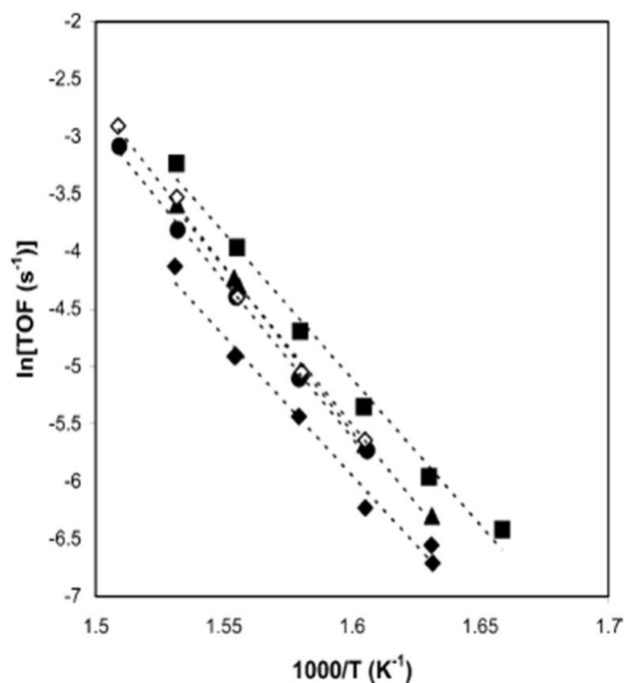
Figure 4.13. Arrhenius plot for ethane hydrogenolysis. Reaction conditions were 20 Torr C_2H_6, 200 Torr H_2 and 613–653 K: (■) 1.7 nm, (▲) 2.6 nm, (◇) 3.6 nm, (◆) 7.1 nm.

supports [43, 46], bimetallic composition [47, 48], and metal surface [43]. The change in activation energy with metal surface is attributed to a change in the rate determining step [49] and has been correlated with the % *d* character of the metal [50]. The amount of hydrogen has been shown to have a significant influence on the measured apparent activation energy, with the activation energy decreasing as the ratio of C_2H_6:H_2 becomes greater than unity. Gudov *et al.* [51] determined an apparent activation energy of 47 kcal mol^{-1} when H_2 was present in a 10-fold excess, and 23 kcal mol^{-1} when ethane was in 3-fold excess.

Reaction orders for ethane and hydrogen are ~0.7 and -1.9, respectively; on the Pt/SBA-15 catalysts at 643 K (see Table 4). The strong negative hydrogen dependence suggests an intense competitive adsorption between hydrogen and ethane on the catalyst surface. Cortright and co-workers have shown that the H_2 order becomes less negative as the temperature is increased (-1.6 at 673 K versus -2.2 at

573 K) or the H_2 partial pressure is decreased. A noticeable difference between the Pt/SBA-15 catalysts and both standard samples (Pt powder and Pt/SiO$_2$-IE) is the degree of hydrogen dependence on the overall rate. The hydrogen reaction order for the two standard catalysts are $\geq$ -2.2, while the H_2 order for the SBA-15 catalysts is $\sim$ -1.9. One possible explanation for the lower negative dependence on hydrogen is consistent with a previously proposed mechanism in which ethane is adsorbed on chemisorbed hydrogen [52-54]. The apparent reaction order in ethane is consistent with previous experimental observations [55] that for measured reaction orders less negative in H_2, the reaction order in ethane decreases to below one. The ethane reaction order was temperature-dependent, decreasing from 1 to 0 as the temperature was increased from 573 to 673 K at a H_2 partial pressure of 100 Torr, but remained unity when the hydrogen pressure was 350 Torr [42]. Gudkov *et al.* [51] have shown that the measured reaction order in hydrocarbon and hydrogen can be either positive or negative depending on the conditions, and Cimino *et al.* [56] have shown that the identity of the metal can influence whether the hydrogen reaction order is positive or negative. Observed partial pressure dependencies are consistent with previously reported values and suggest a mechanism where ethane adsorbs associatively to chemisorbed hydrogen.

Structure Sensitivity of Ethane Hydrogenolysis on Pt.

Turnover frequencies for ethane hydrogenolysis varied by a factor of 3 over 1.7-7.1-nm particles with smaller particles having higher activity for the Pt/SBA-15 catalysts (Figure 14). A limited number of studies of ethane hydrogenolysis have been conducted on Pt catalysts. Guczi and Gudkov [57] reported a monotonic decrease in ethane hydrogenolysis on supported Pt particles in the size range of 3-20 nm. Turnover frequency varied from 0.13 to 3 $\times$ 10^{-3} s^{-1} at 523 K with smaller
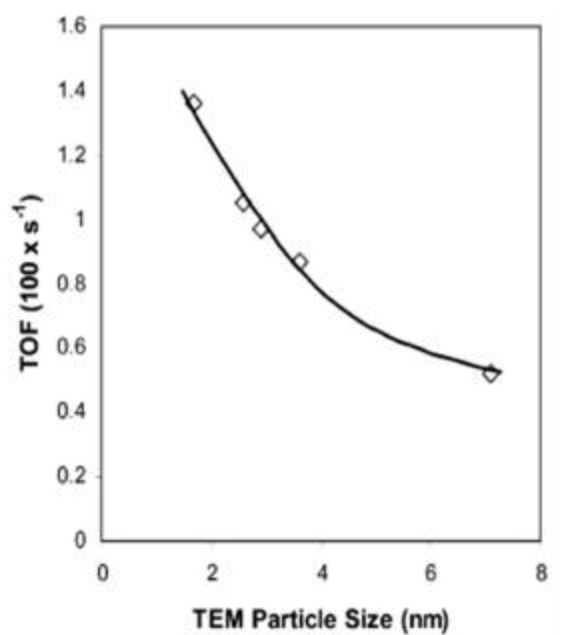
Figure 4.14. Structure sensitivity of ethane hydrogenolysis on ~1% Pt(X)/SBA-15 with Pt particle sizes ranging from X = 1.7 – 7.1 nm. Rates corrected to 20 Torr C_2H_6, 200 Torr H_2, and 643 K.

particles demonstrating higher activity. The authors suggest that the increase in rate with smaller particles is related to an increase in the number of corner and edge atoms. Sinfelt and co-workers have measured turnover rates on atomically dispersed Pt particles supported on both Al_2O_3 and SiO_2. Measured turnover frequencies are approximately an order of magnitude lower than those measured in this work [45]. Maximum rates as a function of particle size have also been observed on supported Pt catalysts. In a range of Pt particles of 1.7-5 nm, the specific activity had a clear maximum at 2.5 nm [58]. In fact, similar behavior was observed for propane hydrogenolysis on the same series of catalysts. Ethane hydrogenolysis over Pt/g-Al_2O_3 catalysts prepared by impregnation methods demonstrated a maximum in rate with particle size although a limited number of samples were studied [59]. Catalysts with atomically dispersed Pt (d_{Pt} < 1 nm by H_2 chemisorption) had a turnover frequency of 0.02 s^{-1} at 666 K in excess hydrogen, while the turnover frequency for a

catalyst with 1.4-nm particles increased by a factor of 2.5 (0.05 s-1), but decreased to 0.01 s^{-1} after the catalyst was intentionally sintered by thermal treatment.

Ethane Hydrogenolysis Reaction Mechanism and Its Relationship to Structure Sensitivity

A feature common to all proposed mechanisms for ethane hydrogenolysis is that the dehydrogenated C_2H_x species is bonded to more than one metal surface atom, which is dependent upon the degree of ethane dehydrogenation. Dumesic and co-workers have conducted a number of theoretical studies of ethane adsorption on Pt clusters [60, 61] and slabs [61] to investigate the interaction of possible C_2H_x intermediates with a Pt surface. Calculations of C_2H_x species adsorbed on a Pt surface suggest that primary pathways for C-C bond cleavage may take place through highly hydrogenated activated complexes, which is contrary to the mechanisms interpreted solely from kinetic measurements [62, 63]. For example, the barriers to C-C bond cleavage of the activated complexes of ethyl (C_2H_5) and ethylidene ($CHCH_3$) are 44 and 39 kcal mol^1, respectively, compared with 61 and 79 kcal mol^1 for vinyl ($CHCH_2$) and vinylidene (CCH_2) species. Microkinetic analysis [64] has also suggested that C-C bond cleavage takes place through an ethyl (C_2H_5) species, while a $CHCH_3$ species also contributes to C-C bond cleavage. The ethyl radical is the most reactive intermediate, but not the most abundant surface intermediate (*masi*). The highly dehydrogenated species, ethylidyne (C-CH$_3$), is stable on the surface and believed to be the *masi* after adsorbed H (θ_H = 0.55 at 623 K). Examining the hydrogenolysis of ethane over a wide range of experimental conditions, Gudkov suggested that the rate determining step changes with reaction conditions. At high ratios of hydrogen to ethane, the cleavage of the C-C bond occurs through the ethyl radical, while at low hydrogen-to-ethane ratios, C-C bond breakage occurs in a highly

dehydrogenated species [51]. The hydrogenolysis of ethane on Pt single crystals is currently under investigation in our laboratories using sum frequency generation to identify reaction intermediates under relevant turnover conditions [65].

Boudart has suggested that structure sensitivity/insensitivity may be related to the number of surface atoms to which the critical reactive intermediate is bound [66]. With this definition, a structure-insensitive reaction may be one where the critical intermediate binds through one or two surface atoms. Conversely, a reaction may be classified as structure-sensitive if the critical reactive intermediate is bound to multiple atoms. Single crystals are useful for studying the effect of surface structure on catalytic activity, and are useful analogues for comparison with metal particles in the range of 1-5 nm. A particle size change from 1 to 5 nm is similar to looking at different crystallographic planes on a macroscopic single crystal [66]. Surprisingly, outside of one study [41], no other kinetic data could be found for the hydrogenolysis of ethane on Pt single crystals.

To understand the role of surface structure on ethane hydrogenolysis, Dumesic and co-workers have studied the reactivity of various C_2H_x species on Pt(111) and Pt(211) slabs using density functional theory methods [61]. The (211) facet is composed of single atom steps of (001) orientation separated by two atom wide terraces of (111) orientation. The calculations show that the barrier from the stable C_2H_5 adsorbed species to the corresponding activated complex is 17 kcal mol^{-1} lower on Pt(211) than Pt(111), while the Pt(211) is more efficient at stabilizing the C_2H_5 adsorbed species by ~11 kcal mol^{-1} [60,61]. The stable adsorption of C_2H_5 to Pt(211) and Pt(111) occurs through a carbon atop a Pt atom, while the activated C_2H_5 complex is bonded to two Pt atoms on Pt(111). In the case of Pt(211), the activated C_2H_5 complex is bonded through two atoms on the (111) terrace adjacent to the step

edge. The binding energy in a 2-fold adsorption site is 28 kcal mol^{-1} stronger for Pt(211) than Pt(111). Small metal crystallites have a higher proportion of coordinatively unsaturated surface atoms, analogous to a stepped single crystal, while the surfaces of large particles primarily expose low index planes (*i.e.*, Pt(111)). It appears that reactions involving these C_2H_x and their activated complexes will occur on these defect sites because they provide more stable bonding. The theoretical calculation supports the observed structure sensitivity of ethane hydrogenolysis on smaller Pt crystallites. The presence of an adsorbed alkyl layer on the metal surface has been used to explain the structure insensitivity of olefin hydrogenation reactions [44, 66]. The presence of this organic layer on the metal surface effectively washes out the original metal surface. In the case of ethylene hydrogenation, Somorjai and co-workers [34] have shown that under reaction conditions, the surface is covered with ethylidyne, a spectator in the reaction because it turns over orders by magnitude slower than π-bonded ethylene. Theoretical calculations and microkinetic analyses of Dumesic and co-workers have shown that ethylidyne, vinylidene, and hydrogen are the most abundant intermediates on the surface during ethane hydrogenolysis. While ethylidyne and vinylidene are not involved in the primary reaction pathways, they affect the observed kinetic rates through site blocking. The presence of this metal-alkyl may be an additional factor contributing to the weak structure sensitivity for ethane hydrogenolysis on supported Pt nanoparticles.

4.3.5   Stability of the Pt/SBA-15 Catalysts After Reaction

Pt particles on the Pt/SBA-15 catalysts exhibited excellent thermal stability. There was no detectable agglomeration after ethylene hydrogenation at low temperature (195 K) and ethane hydrogenolysis at high temperature (643 K)

(Figure15).   Those observations indicate that this catalyst is a very good model for studying catalytic reactions at relevant turnover conditions.
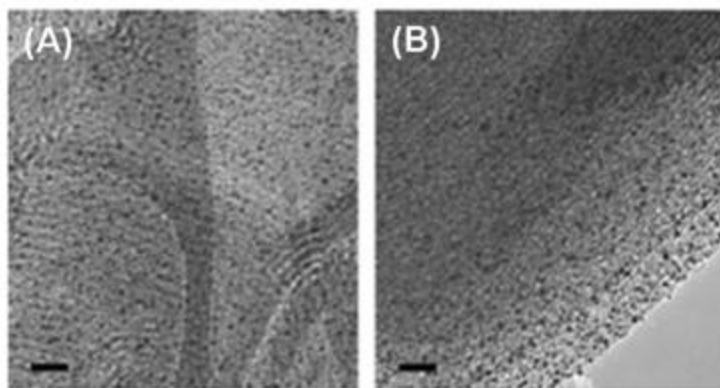
Figure 4.15.   TEM images of 0.95 wt % Pt(2.9 nm)/SBA-15 after reaction: (a) ethylene hydrogenation at 195 K, and (b) ethane hydrogenolysis at 643 K. The scale bars represent 20 nm.

4.3.6   Future Prospects for a High-Surface-Area Model Catalyst

Our understanding of heterogeneous catalysis has increased enormously due to studies using model systems. The development of theoretical tools has enabled us to understand experimental results and calculate heterogeneous catalysis phenomena from first principles. In most circumstances, the tools are complimentary and more is learned together rather than individually.   The development of a high-surface-area monodisperse metal nanocatalyst is a major development in heterogeneous catalysis research. These materials are model systems of the industrially used materials with the major advantage that they have several properties (*i.e.* metal particle size and surface structure, particle location within support) that can be rationally tuned.   This permits promising experimental studies of structure-activity and more importantly structure-selectivity relationships using multi-path catalyzed reactions such as alkane (*n*-hexane, *n*-heptane) reforming.

4.4   Summary

Pt nanoparticles with narrow size distributions (i.e., monodispersed) were produced by various solution-based reduction methods and mesoporous SBA-15 silica was produced by well established hydrothermal reactions. Pt nanoparticles were embedded into the mesoporous silica using low power sonication. The as-synthesized Pt/SBA-15 was calcined under specific conditions to remove the template polymer from the nanoparticle surface and subsequently reduced to remove oxygen from the Pt surface. The reduced Pt/SBA-15 catalysts were characterized by TEM, XRD, and selective chemisorption measurements. TEM and XRD measurements confirm that the as-synthesized Pt particle size is unaffected by sonication, calcination, or reduction, but particle sizes measured by selective chemisorption are larger on average. Ethylene hydrogenation and ethane hydrogenolysis were used as test reactions to compare the activity of our high-surface-area monodisperse metal nanocatalysts with classical high-surface-area catalysts. Turnover rates for room-temperature hydrogenation of ethylene were identical to a Pt/SiO_2 catalyst made by ion exchange and in good agreement with single-crystal measurements, confirming the structure insensitivity of this reaction. Ethane hydrogenolysis rates were comparable to rates on Pt powder and an ion-exchanged Pt/SiO_2 catalyst. The Pt/SBA-15 catalysts demonstrated weak structure sensitivity, with smaller particles demonstrating higher activity. These catalysts exhibited excellent thermal stability under relevant turnover conditions. The synthesis of these catalysts is a general procedure which enables numerous metal/support systems to be constructed for the study of structure-selectivity correlations in heterogeneous catalysis.

4.5   References and Notes

1. D. R. Strongin, J. Carrazza, S. R. Bare, G. A. Somorjai, *J. Catal.* 103 (1987) 213.

2. C. Mohr, H. Hofmeister, J. Radnik, P. Claus, *J. Am. Chem. Soc.* 125 (2003) 1905.

3. M. H. Farias, A. J. Gellman, G. A. Somorjai, R. R. Chianelli, K. S. Lang, *Surf. Sci.* 140 (1984) 181.

4. J. H. Sinfelt, H. Hurwitz, J. C. Rohrer, *J. Phys. Chem.* 64 (1960) 892.

5. K. Hayek, R. Kramer, Z. Paál, *Appl. Catal. A Gen.* 162 (1997) 1.

6. P. B. Weisz, *Pure Appl. Chem.* 52 (1980) 2091.

7. Z. Kónya, V. F. Puntes, I. Kiricsi, J. Zhu, A. P. Alivisatos, G. A. Somorjai, *Catal. Lett.* 81 (2002) 137.

8. Z. Kónya, V. F. Puntes, I. Kiricsi, J. Zhu, A. P. Alivisatos, G. A. Somorjai, *Nano Lett.* 2 (2002) 907.

9. T. Teranish, M. Hosoe, T. Tanaka, M. Miyake, *J. Phys. Chem. B* 103 (1998) 3818.

10. Y. Wang, J. Ren, K. Deng, L. Gui, Y. Tang, *Chem. Mater.* 12 (2000) 1622.

11. D. Zhao, Q. Huo, J. Feng, B. F. Chmelka, G. D. Stucky, *J. Am. Chem. Soc.* 120 (1998) 6024.

12. R. J. Berger, J. Pérez-Ramíréz, F. Kapteijn, J. A. Moulijn, *Chem. Eng. Sci.* 57 (2002) 4921.

13. R. J. Madon, M. Boudart. *Ind. Eng. Chem. Fundam.* 21 (1982) 438.

14. H. Song, F. Kim, S. Connor, G. A. Somorjai, P. Yang, *J. Phys. Chem. B* 109 (2005) 188.

15. M.H. Huang, A. Choudrey, P. Yang, *Chem. Commun.* (2000) 1063.

16. A. H. Janssen, C. –M. Yang, Y. Wang, F. Schüth, A. J. Koster, K. P. de Jong, *J. Phys. Chem. B* 107 (2003) 10552.

17. M. Boudart, G. Djéga-Maraidassou, Kinetics of Heterogeneous Catalytic Reactions. Princeton University Press, Princeton, 1984.

18. J. E. Benson, M. Boudart, *J. Catal*. 4 (1965) 704.

19. J. H. Sinfelt, D. J. C. Yates, *J. Catal.* 10 (1968) 362.

20. M. A. Vannice, J. E. Benson, M. Boudart, *J. Catal.* 16 (1970) 348.

21. D. J. C. Yates, J. H. Sinfelt, *J. Catal.* 8 (1967) 348.

22. U. K. Singh, M. A. Vannice, *J. Catal.* 191 (2000) 165.

23. L. Spenadel, M. Boudart, *J. Phys. Chem.* 64 (1960) 204.

24. J. R. Anderson, Structure of Metallic Catalysts. Academic Press, New York, 1975.

25. J. Horiuti, K. Miyahara, Hydrogenation of Ethylene on Metallic Catalysts, NSRDS-NBS 13; National Bureau of Standards; U. S. Government Printing Office: Washington, DC, 1968.

26. J. C. Schlatter, M. Boudart, *J. Catal.* 24 (1972) 482.

27. J. Grunes, J. Zhu, E. A. Anderson, G. A. Somorjai, *J. Phys. Chem. B* 106 (220) 11463.

28. F. Zaera, G. A. Somorjai, *J. Am. Chem. Soc.* 106 (1984) 2288.

29. I. Horiuti, M. Polanyi, *Trans. Faraday Soc.* 30 (1934) 1164.

30. R. D. Cortright, S. A. Goddard, J. E. Rekoske, J. A. Dumesic, *J. Catal.* 127 (1991) 342.

31. G. C. Bond, Heterogeneous Catalysis: Principles and Applications. 2nd ed., Oxford Science Publication, New York, 1987.

32. J. E. Rekoske, R. D. Cortright, S. A. Goddard, S. B. Sharma, J. A. Dumesic, *J. Phys. Chem.* 96 (1992) 1990.

33. J. W. Yoo, D. J. Hathcock, M. A. El-Sayed, *J. Catal.* 214 (2003) 1.

34. S. M. Davis, F. Zaera, B. E. Gordon, G. A. Somorjai, *J. Catal.* 92 (1985) 240.

35. P. S. Cremer, X. C. Su, Y. R. Shen, G. A. Somorjai, *J. Am. Chem. Soc.* 118 (1996) 2942.

36. A. L. Backman, R. I. Masel, *J. Vac. Sci. Technol. A* 9 (1991) 1989.

37. S. A. Goddard, R. D. Cortright, J. A. Dumesic, *J. Catal.* 137 (1992) 186.

38. T. P. Beebe, Yates, J. T., Jr. *J. Am. Chem. Soc.* 108 (1986) 663.

39. A. Loazia, M. D. Xu, F. Zaera, *J. Catal.* 159 (1996) 127.

40. J. R. Anderson, B. G. Baker, *Proc. Roy. Soc. (London) A* 271 (1963) 402.

41. F. Zaera, G. A. Somorjai, *J. Phys. Chem.* 89 (1985) 3211.

42. R. D. Cortright, R. M. Watwe, B. E. Spiewak, J. A. Dumesic, *Catal. Today* 53 (1999) 395.

43. J. H. Sinfelt, W. F. Taylor, D. J. C. Yates, *J. Phys. Chem.* 69 (1965) 95.

44. M. Boudart, *Adv. Catal. Relat. Subj.* 20 (1969) 152.

45. J. H. Sinfelt, *J. Phys. Chem.* 68 (1964) 344.

46. W. F. Taylor, D. J. C. Yates, J. H. Sinfelt, *J. Phys. Chem.* 68 (1964) 2962.

47. J. H. Sinfelt, J. L. Carter, D. J. C. Yates, *J. Catal.* 24 (1972) 283.

48. J. H. Sinfelt, *Acc. Chem. Res.* 10 (1977) 15.

49. J. R. Anderson, C. Kemball. *Proc. Roy. Soc. (London) A* 223 (1954) 361.

50. J. H. Sinfelt, D. J. C. Yates, *J. Catal.* 10 (1968) 362.

51. B. S. Gudkov, G. Guczi, P. Tétényi, *J. Catal.* 74 (1982) 207.

52. A. Frennet, In: Hydrogen Effects in Catalysis, Eds: Z. Paál, P. Menon, Marcel Dekker, New York, 1988, p. 399.

53.   A. Frennet, *Catal. Today* 12 (1992) 131.

54.   A. Frennet, G. Liénard, *J. Chim. Phys. PCB* 68 (1971) 1526.

55.   A. Frennet, G. Liénard, A. Crucq, L. Degols, *J. Catal.* 53 (1978) 150.

56.   A. Cimino, M. Boudart, H. Taylor, *J. Phys. Chem.* 58 (1954) 796.

57.   L. Guczi, B. S. Gudkov, *React. Kinet. Catal. Lett.* 9 (1978) 343.

58.   Y. A. Rhyndin, B. N. Kuznetsov, Y. I. Yermakov, *React. Kinet. Catal. Lett.* 7 (1977) 105.

59.   I. H. Cho, S. B. Park, S. J. Cho, R. Ryoo, *J. Catal.* 173 (1998) 295.

60.   R. M. Watwe, B. E. Spiewak, R. D. Cortright, J. A. Dumesic, *J. Catal.* 180 (1998) 184.

61.   R. M. Watwe, R. D. Cortright, J. K. Nørskov, J. A. Dumesic, *J. Phys. Chem. B* 104 (2000) 2299.

62.   J. H. Sinfelt, *J. Catal.* 27 (1972) 468.

63.   J. H. Sinfelt, *Catal. Lett.* 9 (1991) 159.

64.   R. D. Cortright, R. M. Watwe, J. A. Dumesic, *J. Mol. Catal. A* 163 (2000) 91.

65.   R. M. Rioux, A. L. Marsh, G. A. Somorjai, To be published (2005).

66.   M. Boudart, *J. Mol. Catal.* 30 (1985) 27.

Chapter 5

Hydrothermal growth of mesoporous SBA-15 silica in the presence of PVP-stabilized Pt nanoparticles: Synthesis, characterization and catalytic properties

5.1   Introduction

One of the goals of modern catalysis research is to design catalysts capable of near 100% selectivity for the desired product without sacrificing activity and energy consumption [1-2]. The role of each component in these catalysts [3] – *i.e.* metal particles [4], oxide supports [5], and their interface [6] must be understood requiring catalyst synthesis, but characterization and performance in designated catalytic reactions (reactivity studies). To this end, there is a drive towards developing new strategies to synthesize catalysts whose catalytic performance can be predicted in a defined and rational manner. Parameters to control in transition metal heterogeneous catalysts include particle composition, size, and shape; support composition and pore size distribution; and the organizational structure of the porous network. This multidimensional problem is complex, thus the synthetic control and design of catalysts is a serious technological challenge [7-9]. A logical approach to the problem is to isolate one of the parameters and learn how to control it in a systematic way and then test its effect on catalytic performance.

Several methods have been developed thus far to afford the effective immobilization of metal particles on high surface area support materials [10, 11]. The most prominent methods are incipient wetness and ion exchange, in which the porous oxide support is impregnated with metal precursors (simple salts) in solution phase, followed by thermal treatment and/or reduction with H_2 to form metal nanoparticles [6, 12, 13]. The process can be further refined by post-synthesis modification of the support; surface functionalization which directs the interaction of precursor with the surface [14]. Due to its simplicity and crude effectiveness, this method is successful for the large scale production of catalysts; however, metal nanoparticles generated on the support typically lack uniformity in size and shape.

The discovery of M41S-type ordered mesoporous materials opened a new class of periodic porous solids [15]. Mesoporous silica structures have been regarded as ideal supports for heterogeneous catalysts due to their high-surface area, tunable pore size and alignment. In particular, the SBA-15 framework synthesized by Stucky *et al.* [16] has a highly ordered hexagonal mesostructure with parallel channels and adjustable pore size in the range of 5 – 30 nm [17]. This size regime is relevant to catalysis, since the catalytically active component are metal particles in the 1 – 10 nm size range. SBA-15 is well suited as a structure that can contain individual metal particles within its mesopores, and the pores are wide enough to permit facile diffusion of reactants and products.

Using the periodic SBA-15 structure, a general approach for the design of high surface area catalysts is demonstrated. Departing from traditional catalyst preparation methods, well-defined Pt nanocrystals have been synthesized in the presence of surface-regulating agents by a solution-based technique. The size and shape of the nanoparticles are uniform, and tunable in the range of 1.7 – 7.1 nm. We have recently

reported the particle incorporation on SBA-15 structure by sonication [18]. The Pt particles were well-dispersed within the entire silica framework, and the resulting Pt/SBA-15 catalysts demonstrated reasonable reactivity during ethylene hydrogenation and ethane hydrogenolysis. A large fraction of the active Pt nanoparticles are potentially located on the SBA-15 outer surface as well as inside the channels, and the maximum Pt particle size incorporated in the mesopores is restricted by the channel diameter of SBA-15 (~ 9 nm). An alternative approach is the encapsulation of nanoparticles during *in-situ* growth of SBA-15 (Scheme I). Polymers are effective mediators for organizing nanoparticles into higher order composite structures [19]. Somorjai *et al.* recently demonstrated the growth of SBA-15 on the surface of Pt cubes [20, 21]. Hexagonal silica structures were formed by adding Pluronic P123 (triblock copolymer poly(ethylene oxide)-poly(propylene oxide)-poly(ethylene oxide), $EO_{20}PO_{70}EO_{20}$) and tetraethoxysilane (TEOS) to the Pt hydrosol in acidic condition. The final Pt/SBA-15 composite, however, exhibited no catalytic activity.
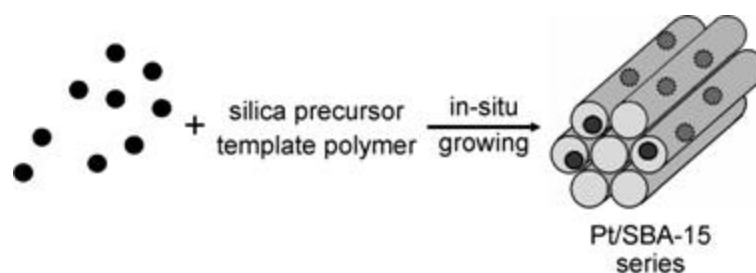
Scheme I. Schematic of nanoparticle encapsulation (NE) method for catalyst synthesis

The extremely low pH required for synthesis of SBA-15 disrupts the Pt colloid; however, the use of a pH neutral template would allow incorporation of the Pt sol. The MSU family of high surface area ordered mesoporous silica materials are synthesized at neutral pH, and utilize triblock polymers, which template SBA-15

synthesis, to obtain similar pore diameter [22]. Therefore, we introduce a synthetic procedure to generate hexagonal structures in neutral pH conditions in the presence of Pt nanoparticles. The resulting Pt nanocrystal/SBA-15 materials possess an ordered silica structure with improved dispersion of Pt nanoparticles in its channels. These nanocomposites exhibit comparable catalytic behavior to conventional catalysts after removal of the organic residues (silica template and surface pacifying agent of Pt sol) by heat treatment. Precise tuning of particle size and support structures will enable the elucidation of their contribution to the overall kinetic (activity and selectivity) behavior of a heterogeneous catalyst.

5.2   Experimental Section

5.2.1   Synthesis of Pt Nanoparticles

Dihydrogen hexachloroplatinate ($H_2PtCl_6 \cdot 6H_2O$, 99.9%, metals basis) was purchased from Alfa Aesar. Poly(vinylpyrrolidone) (PVP, M_w = 29,000 and 55,000) was obtained from Sigma-Aldrich. Methanol, ethanol, and ethylene glycol were of analytical grade and used without further purification.

Pt particles were synthesized according to literature methods [18, 23, 24]. Briefly, 1.7 nm Pt particles were made by adding NaOH solution (12.5 mL, 0.5 M) in ethylene glycol to a solution of $H_2PtCl_6 \cdot 6H_2O$ (250 mg) in 12.5 mL of ethylene glycol. The mixture was heated at 433 K for 3 h with N_2 bubbling. After reaction, particles were precipitated by adding 1 mL of 2 M HCl, and dispersed in ethanol containing 12.2 mg of PVP (M_w = 29,000). 2.9 nm Pt particles were synthesized by refluxing a mixture of PVP (26.6 mg) and $H_2PtCl_6 \cdot 6H_2O$ (124.3 mg) in water (40 mL)/methanol (360 mL) solution for 3 h. 3.6 nm Pt particles were formed by mixing the 2.9 nm Pt colloidal solution (100 mL) in a water/methanol (1:9) mixture with 10 mL of 6.0 mM

$H_2PtCl_6 \cdot 6H_2O$ aqueous solution and 90 mL of methanol. The mixture was refluxed for 3 h. 7.1 nm Pt particles were synthesized by adding a total 3 mL of 0.375 M PVP (M_w = 55,000) and 1.5 mL of 0.0625 M $H_2PtCl_6 \cdot 6H_2O$ solutions in refluxing ethylene glycol every 30 s over 16 min. The mixture was refluxed for an additional 5 min.

All Pt colloidal solutions were purified by sequential precipitation/redispersion, and eventually dispersed in an appropriate amount of deionized water necessary for a 3×10^{-3} M solution based on Pt salt concentration. The particle sizes were measured by transmission electron microscopy (TEM) and X-ray diffraction (XRD). Estimated particle sizes were 1.73 ± 0.26 (1.7), 2.80 ± 0.21 (2.9), 3.39 ± 0.26 (3.6), and 7.16 ± 0.37 (7.1) nm by TEM (XRD) respectively, indicating high uniformity and monodispersity of each particle less than $\sigma \sim 8\%$ [18].

5.2.2 Synthesis of Pt/SBA-15 Series by Nanoparticle Encapsulation Method

Pluronic P123 ($EO_{20}PO_{70}EO_{20}$, BASF), tetramethyl orthosilicate (TMOS, 98%, Aldrich), and sodium fluoride (99.99%, Aldrich) were used as received. 2.5 g of Pluronic P123 was completely dissolved in 50.5 mL of deionized water. The Pt colloidal aqueous solution (27.0 mL, 3×10^{-3} M) was mixed with the polymer solution and stirred for 1 h at 313 K. 0.375 mL of 0.5 M NaF aqueous solution was added, and 3.91 mL of TMOS was quickly added to the reaction mixture, followed by stirring for a day at 313 K. The resulting slurry was aged for an additional day at 373 K. The brown precipitates were separated by centrifugation, thoroughly washed with ethanol, and dried in an oven at 373 K. Pt(1.7 nm)/SBA-15 was calcined at 623 K for 24 h, Pt(7.1 nm)/SBA-15 was calcined at 723 K for 36 h, and other catalyst materials were calcined at 723 K for 24 h under O_2 flow.

A 3.2 % Pt/SiO_2 [25] and a 6.3% Pt/SiO_2 (EUROPT-1) catalyst prepared by an ion exchange method were used as reference materials. The EUROPT-1 sample has

been thoroughly characterized 26-30]. The Pt particle size distribution is 1-3.5 nm centered at 1.8 nm with 75% of the particles having a diameter of $\leq$ 2 nm [27]. Turnover frequencies of ethylene hydrogenation on the 3.2% Pt/SiO_2 have been previously reported [18]; these rates were a factor of five lower than those reported here. This discrepancy is attributed to errors in extrapolation from low temperature conditions used in the previous study to room temperature conditions. All turnover frequencies reported in this study were reproducible to $\pm$ 10 %.

5.2.3 *Characterization of Pt/SBA-15 Catalysts*

Physical and Chemical Characterization

TEM experiments were carried out on a Philips CM200 microscope operated at 200 kV at the National Center for Electron Microscopy at Lawrence Berkeley National Laboratory. Catalysts were sonicated in acetone for 10 s, dropped on lacey carbon film coated copper grids (Ted Pella), and dried in air. Water contact angle measurements were performed on a CAM 100 optical contact angle meter (KSY Instruments). Polymer and Pt nanoparticle solutions in ethanol were dropped on Si substrates, and dried under vacuum for 8 h. The preparation of Pt Langmuir-Blodgett (LB) monolayers for contact angle measurements has been described elsewhere [31].

XRD spectra were measured on a Bruker D8 GADDS diffractometer using Co Kα radiation (1.79 Å). Small angle X-ray scattering (SAXS) patterns were recorded on a Bruker Nanostar U diffractometer using Cu Kα radiation (1.54 Å) with a sample to detector distance of 107 cm. Nitrogen physisorption data was measured on a Quantachrome Autosorb-1 analyzer at 77 K. Thermogravimetric analysis (TGA) was performed using a Seiko Instruments SSC 5200 TG/DTA 220 under an O_2 flow. Elemental analyses by inductively coupled plasma–atomic emission spectroscopy (ICP–AES) were conducted at Galbraith Laboratories, Inc. (Knoxville, TN.).

Selective gas adsorption measurements were conducted in a pyrex volumetric apparatus pumped by a liquid nitrogen cooled diffusion pump to sample cell pressures of $\leq 3 \times 10^{-6}$ Torr. The amount of adsorbed gas was measured with a digital pressure gauge (MKS Instruments, PDR-D). Total and reversible isotherms were collected at room temperature with an interim 1 h evacuation between isotherms. Monolayer uptakes were determined by extrapolating adsorbate uptakes to zero pressure (P = 0). Catalysts were reduced for 75 min at 673 K in 50 cc (STP) H_2 min^{-1} (Praxair, UHP, 99.999%) followed by evacuation at 623 K before adsorption measurements. He (Praxair, UHP, 99.999%), O_2 (Airgas, UHP, 99.999%) and CO (Matheson, UHP, Al cylinder) were all used without further purification. Hemispherical particle sizes were determined from d (nm) = 1.13/D, where D is the metallic dispersion assuming a Pt surface atom density of 1.27×10^{15} cm^{-2} [32].

Diffuse reflectance infrared study of CO adsorption on Pt/SBA-15 catalysts

In-situ diffuse reflectance infrared Fourier transform spectroscopy (DRIFTS), using a Nicolet Nexus 670 spectrometer equipped with a Thermo Spectra-Tech controlled atmosphere-diffuse reflection cell was used to study the adsorption of CO on various silica supported Pt catalysts. A prereduced Pt/SiO$_2$ catalyst (*ca.* 10-40 mg) was loaded in the diffuse reflectance cell and given an abbreviated pretreatment identical to those used for chemisorption and catalytic studies. A single beam spectrum of the freshly reduced catalyst was obtained at 300 K under 30 cc (STP) He min^{-1} and used as the background for spectra of the same catalyst in the presence and absence of gas-phase CO at 300 K. Samples were exposed to a 30 cc (STP) min^{-1} flowing mixture of 10% CO/He for 30 min. at 300 K, followed by purging in 30 cc (STP) He min^{-1} at 300 K. Single beam scans with a resolution of 2 cm^{-1} and a scan number of 128 were measured in the presence and absence of gas phase CO. The

contribution of gas phase CO was subtracted out of each spectrum with a single beam spectrum of 10% CO/He measured over a Au mirror. Contribution of adsorbed CO associated with SBA-15 at room temperature was removed by spectral subtraction.

Catalytic Reaction measurements

Catalytic rate measurements were conducted in a plug flow reactor made of pyrex. Mass flow rates of ethylene (AirGas, CP grade), ethane (Praxair, 99%), hydrogen (Praxair, UHP, 99.999%) and He (Praxair, UHP, 99.999%) were controlled by mass flow controllers (Unit Instruments). Reaction temperatures were measured with a thermocouple extending into the catalyst bed. Reactants and products were detected by gas chromatography (Hewlett Packard 5890 Series II) and quantified using Dietz tables [33]. Rate measurements for both ethylene hydrogenation and ethane hydrogenolysis were conducted at differential conditions (all conversions, X < 10%). Typically, catalysts (2-300 mg) were diluted with low surface area acid washed quartz in a 1:3 (catalyst: quartz) ratio. Dilution ratios of up to 10 had no effect on the observed conversion. All rates were verified free of heat and mass transfer limitations.

5.3.   Results and Discussion

5.3.1   Encapsulation of Pt nanoparticles by SBA-15 and plausible mechanism for catalyst formation

It was determined that upon addition of PVP-capped Pt nanoparticles to the acidic conditions of SBA-15 synthesis, Pt nanoparticles aggregated and the silica matrices were disordered (see supporting information). For this reason, SBA-15 was synthesized under neutral conditions using sodium fluoride and a different organosilicon source, tetramethyl orthosilicate (TMOS). PVP-capped Pt particles with sizes of 1.7, 2.9, 3.6, and 7.1 nm were introduced into the neutral pH reaction

mixture. In a typical reaction, Pt colloidal solution was mixed with aqueous polymer solution at 313 K and stirred for 1 h to ensure complete dissolution of Pt particles. Brown precipitates were formed 5 min after the addition of NaF solution and TMOS. The supernatant was colorless and transparent, indicating that all Pt colloids were incorporated into the silica matrix. The slurry was aged for a day at 313 K, and placed in an oven at 373 K for an additional day. The product was washed with water and ethanol, and dried in air at 373 K. Pt/SBA-15 catalysts were obtained by calcination of the raw materials under optimal conditions (*vide infra*). Figure 1 shows that the Pt nanoparticles are encapsulated by ordered silica structures and the Pt particles are isolated and distributed throughout the entire silica framework without severe agglomeration.

Free PVP is very hydrophilic because of the polar pyrrolidone functionality attached to the main alkyl chain. It dissolves in water, ethanol, and chloroform, while PVP-capped Pt nanoparticles are poorly soluble in water. The addition of Pluronic P123 helps to form a stable colloidal solution of Pt nanoparticles in water. Water contact angles have been measured to check the hydrophilicity of materials used during catalyst synthesis (Table 1). A PVP layer on the Si substrate exhibits a contact angle of 15°, the lowest value in Table 1 and therefore the most hydrophilic. PVP-capped Pt nanoparticle layers made by drop casting and Langmuir-Blodgett techniques [31] are relatively hydrophobic with contact angles of 39° and 53°, respectively. The more hydrophobic nature of the PVP-capped Pt nanoparticle layers is due to the strong interaction between the pyrrolidone rings of PVP and Pt, resulting in the exposure of the hydrophobic main chain at the surface. Pluronic P123 is known to form spherical micelles in water at room temperature, with the hydrophobic

Table 5.1. Water contact angle of polymers (PVP and Pluronic P123) and Pt nanoparticles.

Si Substrate	q_{H2O} (^{o})
Bare Si substrate	52
PVP layer	15
PVP-capped Pt layer	39
PVP-capped Pt LB layer	53
Pluronic P123 layer	26
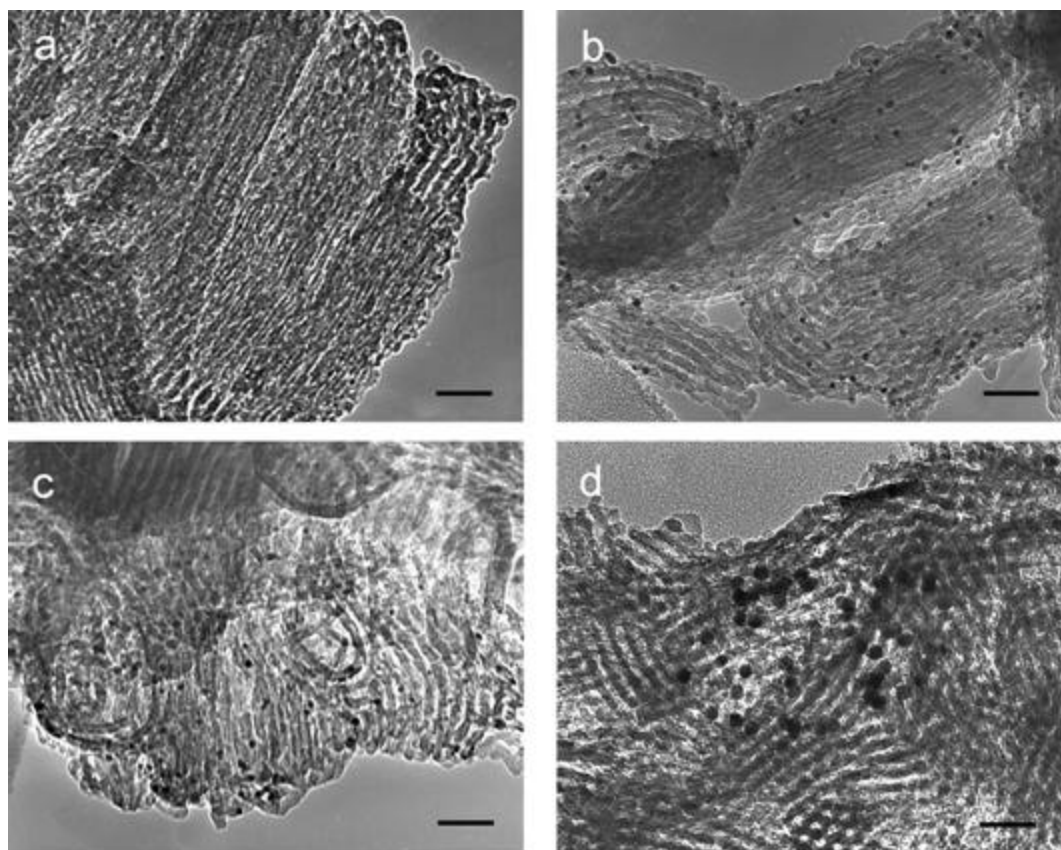
Figure 5.1. TEM images of Pt(X)/SBA-15 catalysts. X = (a) 1.7 nm, (b) 2.9 nm, (c) 3.6 nm, and (d) 7.1 nm. The scale bars represent 40 nm.

propylene oxide unit in the core and the hydrophilic ethylene oxide unit comprising the sphere surface [34]. Therefore, PVP-capped Pt nanoparticles are likely to be encapsulated within the core of Pluronic P123 micelles. After NaF and TMOS are added to the reaction mixture, silica species polymerize on the surface of Pluronic P123 micelles, and the final product contains Pt particles inside the mesoporous framework. The separate formation of SBA-15 with Pluronic P123 and adsorption of the Pt particles on its surface cannot be excluded but the enhanced stability of PVP-capped Pt nanoparticles in a Pluronic solution suggests that Pt quickly associates with the Pluronic upon its introduction to the solution.

5.3.2   Characterization of Pt/SBA-15 Catalysts

Physical Characterization of Pt/SBA-15 Catalysts

The resulting SBA-15 and Pt(X)/SBA-15 catalysts (X = 1.7, 2.9, 3.6, and 7.1 nm) were characterized by elemental analysis, XRD, and SAXS. Catalysts were prepared with a nominal weight loading of 1%; actual metal loadings determined by elemental analysis were between 0.6 and 0.8 wt. % (Table 2). Three characteristic peaks for Pt appear in the XRD spectra (Figure 2) at $2\theta = 45.9\,°$, $54.0°$, and $80.1°$ corresponding to (111), (200), and (220) reflections of the Pt fcc lattice, respectively, as well as a broad amorphous SiO_2 signal at $2\theta = 27.4°$. All three Pt peaks become sharper with an increase of the particle size from 1.7 to 7.1 nm. Estimation of the particle size based on XRD was not successful because of the low signal-to-noise ratio of the peaks. Only in the case of the Pt(7.1 nm)/SBA-15 catalyst was a particle size determined. SAXS data (Figure 2b) exhibit three peaks assignable to (100),
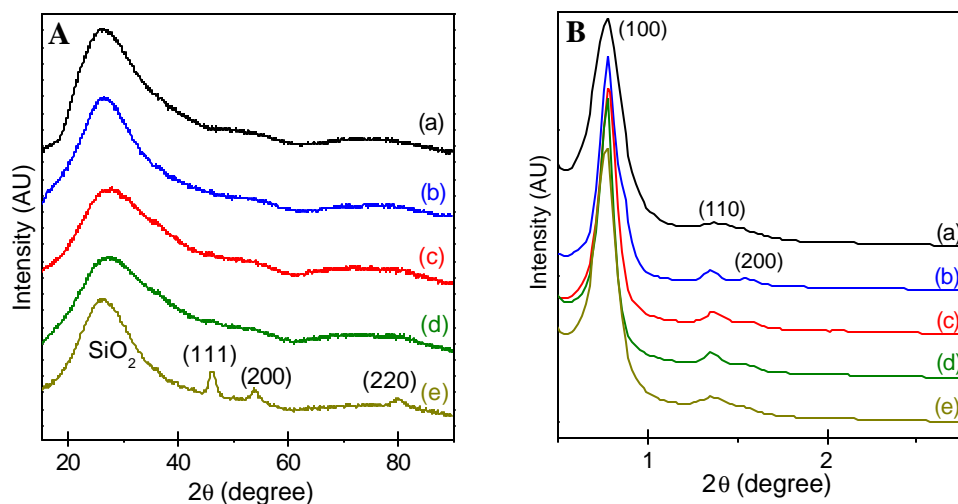
Figure 5.2. (A) XRD data for (a) SBA-15 and Pt(X)/SBA-15 catalysts. X = (b) 1.7 nm, (c) 2.9 nm, (d) 3.6 nm, and (e) 7.1 nm. The Pt(111), Pt(110), and Pt(200) peaks of the fcc lattice are indicated for Pt(7.1nm)/SBA-15. These peaks are visible in the other spectra at higher magnification, but have poor signal-to-noise. Spectra are offset for clarity. **(B)** SAXS data for (a) SBA-15 and Pt(X)/SBA-15 catalysts. X = (b) 1.7 nm, (c) 2.9 nm, (d) 3.6 nm, and (e) 7.1 nm. The SBA-15(100), (110), and (200) peaks are indicated, demonstrating the long range order of the channels. Spectra are offset for clarity.

Table 5.2. Elemental analysis and physisorption data on Pt loaded SBA-15

Support/Catalyst[a,b,c]	N_2 BET parameters		
	Surface Area $(m^2\ g^{-1})$	Pore volume $cc(STP)\ g^{-1}$	Pore diameter [d] (Å)
SBA-15 prepared in acidic conditions[e]	765	1.16	90
SBA-15 prepared in neutral conditions	619	2.05	113
0.6% Pt(1.7 nm)/SBA-15	661	1.58	112
0.77% Pt(2.9 nm)/SBA-15	567	1.50	113
0.6% Pt(3.6 nm)/SBA-15	523	1.42	113
0.62% Pt(7.1 nm)/SBA-15	545	1.65	113

[a]Actual metal loading determined by ICP-AES.
[b]Particle sizes measured from XRD data of freestanding Pt colloidal particles.
[c]SBA-15 synthesized in neutral conditions.
[d]Determined from adsorption branch of the N_2 isotherm.
[e]From ref. [18].

(110), and (200) of the hexagonal mesostructure with the same *p6mm* symmetry as observed in pristine SBA-15 [17]. Pt/SBA-15 catalysts exhibit relatively strong (110) and (200) peaks compared to those of SBA-15 in neutral conditions, suggesting that the presence of PVP-capped Pt nanoparticles enhances the ordering of the polymer's hexagonal structure during reaction. Lattice spacings of d_{100} are almost constant (~11 nm) with variation in particle size, in contrast to previous results of Somorjai *et al.* [20, 21], in which the lattice parameter of Au/SBA-15 increased with the incorporation of larger Au nanoparticles into the mesoporous structure. BET N_2 adsorption measurements were carried out on the Pt/SBA-15 catalysts (Figure 3). Surface areas of the catalysts ranged from $523 - 661$ m^2 g^{-1}; comparable to pristine SBA-15 (Table 2) [17]. Average pore diameters calculated from adsorption branches are ~ 11 nm, and pore volumes determined by the Kelvin equation at $P/P_0 = 0.975$ are ~$1.42 - 2.05$ cc(STP) g^{-1}, which are larger than the pore volume of SBA-15 synthesized in acidic conditions (see Table 2 and supporting information).
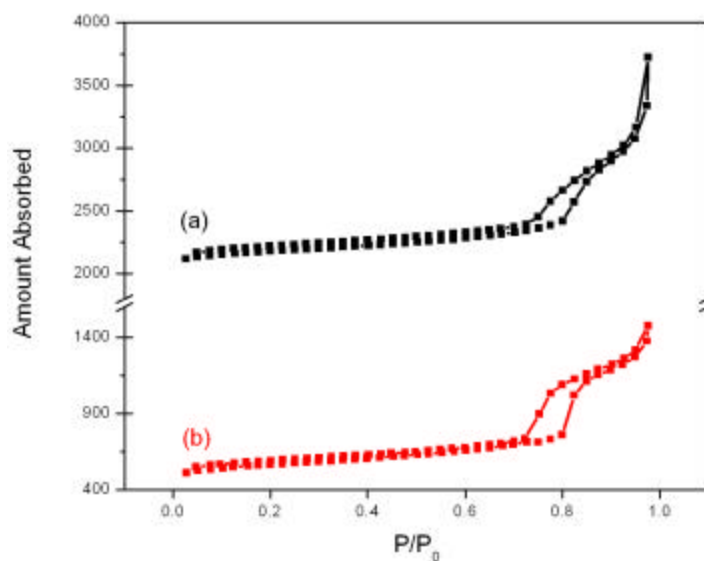
Figure 5.3. N_2 adsorption-desorption isotherms of (a) SBA-15 and (b) 0.77% Pt(2.9 nm)/SBA-15 catalysts. Isotherms for the other catalysts look similar and are therefore not included. The hysteresis loop observed is indicative of cylindrical pores. Isotherms are offset for clarity.

Removal of PVP while maintaining nanoparticle dispersion represents a significant challenge. Technical catalysts are typically activated by thermal treatment in an inert atmosphere or oxygen followed by reduction to produce a clean, reduced catalyst. Previous work demonstrated that Pt-PVP covered nanoparticles deposited into calcined SBA-15 by sonication required calcination times between 12 and 24 hours and temperatures $\geq$ 573 K for PVP removal [18]. In the case of nanoparticle encapsulation catalysts prepared here, three distinct weight loss regimes are evident from thermogravimetric analysis (TGA) of as-synthesized 0.77% Pt(2.9 nm)/SBA-15 sample (Figure 4). Water desorbed below 373 K, Pluronic P123 decomposed at 453 - 573 K, and PVP decomposed at 573 - 773 K under O_2. Based on this information,
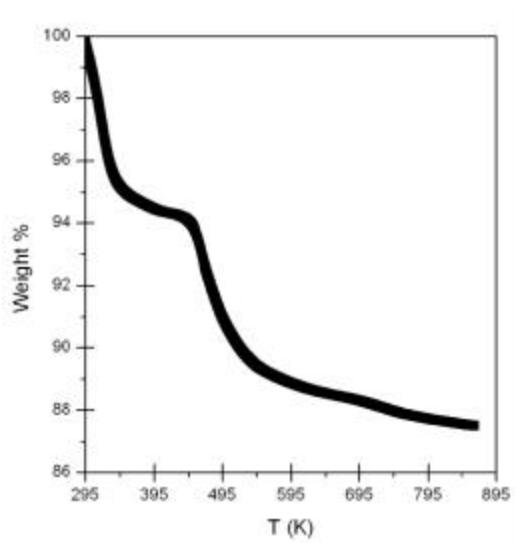
Figure 5.4. TGA data of the as-synthesized 0.77% Pt(2.9 nm)/SBA-15 under a continuous O_2 flow. Three weight loss regimes are observed. The first step is attributed to loss of water, the second to decomposition of Pluronic P123 and the third to decomposition of PVP.

Pt/SBA-15 catalysts were treated with 50 cc(STP) O_2 min^{-1} at 723 K for 24 - 36 h. The Pt(1.7 nm)/SBA-15 was treated at 623 K for 24 h in order to prevent severe agglomeration of the particles. Chandler and co-workers obtained similar results for dendrimer covered Pt nanoparticles; dendrimer was effectively removed for

nanoparticles deposited directly on a silica support [35], while the same calcination-reduction procedure was ineffective for dendrimer removal from nanoparticles encapsulated during synthesis of a microporous xerogel silica [36]. The stage at which the dendrimer covered nanoparticles were introduced into the xerogel synthesis had an influence on the degree of poisoning; addition of particles after sol formation were poisoned to a greater extent by dendrimer decomposition products than nanoparticles added before sol formation. Chandler and coworkers [36] suggest that the small pores (≤ 2 nm) of the xerogel inhibit transport of dendrimer decomposition products from the nanoparticle surface. In the case of the nanoparticle encapsulation method, nanoparticles are added before sol formation and it is proposed that some of the Pt may be occluded in silica capsules which can form during SBA-15 synthesis [37], although capsules have not been observed in our microscopy studies. Chemical titration of the metal surface area has proven that most of the nanoparticle surface area is accessible for adsorption and reaction.

Particle size determination by chemisorption

Particle size measurements by TEM and XRD verified that particle size was not perturbed during the nanoparticle encapsulation synthesis. Particle sizes obtained from these measurements are not a good measure of the catalytically relevant particle size. Before calcination, the nanoparticle surfaces contain the surface-regulating agent, PVP which bonds very strongly to the Pt surface. Removal of this polymer requires high temperature as shown by thermogravimetric analysis (TGA) (Figure 4) and care must be taken to ensure sufficient polymer removal without severe sintering. Selective adsorption of probe gases represents the most appropriate probe for determining Pt particle size and is used to normalize measured reaction rates to the exposed metal surface area [38]. Chemisorption is sensitive to the polymer presence

on the nanoparticle surface and any changes in particle size during pretreatment. Particle size was determined by chemisorption with three independent measurements, H_2, CO and H_2-O_2 titration. Adsorption uptakes and particle sizes calculated assuming hemispherical particle geometry are compiled in Table 3. The three independent techniques are in relatively good agreement and variance in particle size determined by the different adsorption techniques may be a consequence of changes in adsorbate stoichiometry with particle size or the influence of residual PVP on the nanoparticle surface. Regardless, the agreement with TEM measurements and XRD (except in the case of Pt(7.1 nm)/SBA-15) is very good. Measured dispersion for the two reference catalysts are in good agreement with previously reported results. Catalytic activities are normalized per surface atom based on total H_2-O_2 titration uptake.

Infrared spectroscopic measurements of CO adsorption

The adsorption of carbon monoxide has been used as a probe of local surface structure, both geometric and electronic [39, 40]. The geometry in which CO bonds to the surface, the position of such vibrations in the infrared region and the lineshape of the absorption band are qualitative probes of Pt surface structure. An example of the sensitivity of CO adsorption to surface site coordination is the adsorption of CO on low index surfaces (Pt(111)) and stepped Pt surfaces (Pt(211)). The stretching frequency of adsorbed CO on Pt(111) is 2090-2100 cm^{-1} at high coverages [41]. Upon the introduction of coordinatively unsaturated atoms onto Pt single crystal surfaces, atop adsorption of CO on terrace (~2090 cm^{-1}) and step (~2075 cm^{-1}) sites can be distinguished at low temperatures (~ 100 K), but at higher temperatures, as employed in this study, distinction between the two adsorbate-surface site interactions is more difficult, likely due to facile surface diffusion between the two sites [42].

Table 5.3. Selective gas uptakes and Pt particle sizes for supported Pt/silica catalysts

Catalyst[a]	Selective gas uptake (μmol g^{-1})[b]					Dispersion, D[c]	Particle size, d (nm)	
	$H_{2, total}$	CO_{total}	CO_{irr}	$O_{2,irr}$	H_2-$O_{2,total}$		Chemisorption[d]	XRD
3.2% Pt/SiO$_2$-IE	133.1	166.7	152.2	24.2	262.0	1[e]	1.0	--
6.3% Pt/SiO$_2$ (EUROPT-1)	151.2	182.0	175.0	94.6	334.0	0.69	1.6	1.8[f]
0.6% Pt(1.7 nm)/SBA-15	4.5	13.3	12.0	4.4	19.1	0.41	2.7	--
0.77% Pt(2.9 nm)/SBA-15	6.0	11.3	10.0	4.4	21.8	0.36	3.1	--
0.6% Pt(3.6 nm)/SBA-15	4.0	7.9	7.4	3.1	12.5	0.27	4.2	--
0.62% Pt(7.1 nm)/SBA-15	1.5	2.9	2.3	2.4	5.6	0.11	9.4	7.9[g]
Pt powder	16.7	15.1	13.7	8.6	30.3	0.004	287	>100

[a]Actual catalyst loading determined by ICP-AES.
[b]Monolayer uptakes (P = 0) determined at 295 K.
[c]Based on total H_2-O_2 titration uptake at P = 0.
[d]Based on d(nm) = 1.13/D.
[e]Dispersion greater than unity calculated, assumed 100% dispersion for calculation of turnover frequency.
[f]From Gnutzman, V.; Vogel, W. *J. Phys. Chem.* **1990**, *94*, 4991.
[g]After subtraction of pristine SBA-15 background.

The influence of particle size on CO adsorption was examined in this work. Infrared spectra (1900-2200 cm^{-1}) demonstrate that atop bonded CO is the dominant interaction between CO and the Pt surface. No bridge bonded CO was observed on any catalyst used in this study, though it has been previously observed on Pt/SiO$_2$. Figure 5 demonstrates the position of the atop frequency redshifted by ~15 cm^{-1} between the 1.7 and 7.1 nm particles. The clear distinction between particle sizes
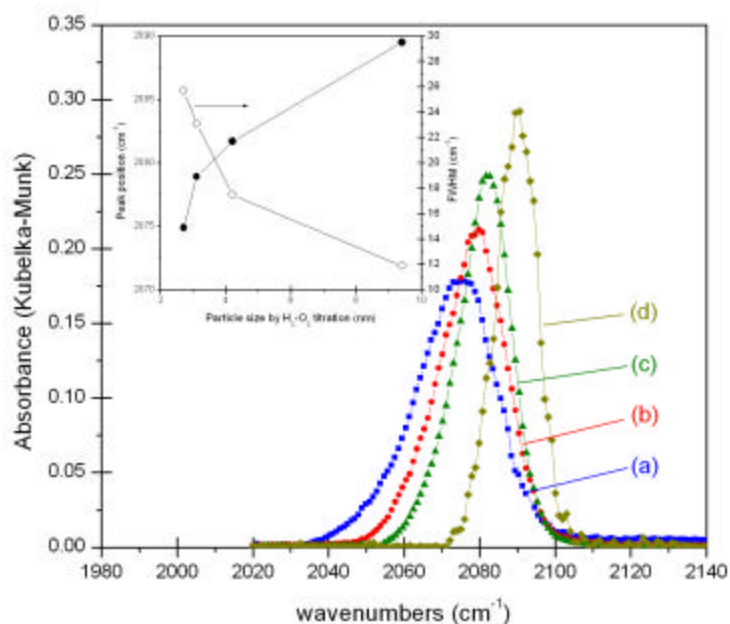
Figure 5.5. Infrared spectrum of CO adsorption at 295 K for Pt/SBA-15 catalyst series. (a) 2.33% Pt(1.7 nm)/SBA-15, (b) 2.69% Pt(2.9 nm)/SBA-15, (c) 2.62% Pt(3.6 nm)/SBA-15, and (d) 2.86% Pt(7.1 nm) /SBA-15. Inset is peak position and FWHM of atop CO stretching vibration as a function of particle size at room temperature. At saturation coverage, the peak position redshifts due to changes in the average coordination number as the particle decreases. Peak heights have been modified for clarity.

confirms that CO is a good probe molecule for assessing the state of the Pt surface. Cant and Donaldson [43] have shown a minor influence of particle size on the position of the atop CO vibration for two Pt/SiO$_2$ catalysts with surface average particle sizes as determined by H$_2$ chemisorption of 1.8 and 18 nm; the band position for the 1.8 nm was redshifted by 6 cm^{-1} relative to the 18 nm Pt particle silica catalyst

(2078 cm^{-1}). Bischoff and co-workers [44] have studied the effect of particle size on CO adsorption for Pt dispersed within a neutralized faujasite zeolite. The authors suggest that a clear particle size dependent shift of the atop adsorbed CO stretching vibration was observed due to the narrow Pt particle size distribution. At room temperature, the absorption of the atop CO stretching frequency was at ~2050 cm^{-1} for 1-2 nm particles and ~2100 cm^{-1} for 4-5 nm particles. Clearly, work on single crystals [41, 42] and supported catalysts [43, 44] suggest that the position of the atop CO vibration redshifts with increasing surface roughness and decreasing particle size. The stretching frequency of a single CO molecule on a Pt_{10} cluster as determined by DFT calculations is 2050 cm^{-1}, [45] while a single CO stretching vibrational frequency of 2020 cm^{-1} was reported for gas-phase CO saturated neutral $Pt_3(CO)_6$ clusters [46]. Vibrational frequencies for atop CO have been reported as low as 2000 cm^{-1} for $Pt(CO)_2$-type surface species [47]. The work presented here is in agreement with previous studies and suggests that the strength of π back donation of the CO chemisorption bond is stronger on a small particle with a larger fraction of low coordination metal sites relative to a single crystal or platinum particle with a large fraction of high coordination surface sites [47].

The inset of Figure 5 demonstrates that the full width at half maximum (FWHM) increases as the nanoparticle size decreases. Although these spectra have a narrower FWHM than conventional catalyst due to their monodisperse particles, within the series of Pt/SBA-15 catalysts, the decrease in FWHM as the particle size increases suggests that on the larger particles there is less surface heterogeneity because the surface is terminated by large terraces of identical surface atoms. As the nanoparticle size decreases, the surface heterogeneity increases due to changing surface atom statistics [48] and the infrared spectrum represents an ensemble average

of CO vibrations on all sites resulting in a broadened peak. In a similar study, Chandler and co-workers [35] demonstrated that FWHM for adsorbed CO on dendrimer templated nanoparticles supported on SiO_2 was much narrower as compared to a Pt catalyst synthesized by incipient wetness on the same silica because of a much narrower TEM particle size distribution for the dendrimer particles (σ = 20%) as compared to the standard Pt catalyst (σ = 50%). The infrared data on dendrimer derived Pt nanoparticles is similar to that determined in this study.

5.3.3 Reaction Studies

Ethylene hydrogenation

Ethylene hydrogenation was chosen as a probe reaction to assess the extent of polymer removal and to compare the activity of nanoparticle encapsulation catalysts with classically prepared supported catalysts and single crystals. The insensitivity of catalytic activity and kinetic parameters to Pt particle size and surface structure is well known for this reaction [49]. Specific activities and turnover frequencies at standard conditions of 10 Torr C_2H_4, 100 Torr H_2, and 298 K are reported in Table 4. At standard conditions, all catalysts have initial turnover frequencies of ~ 3.5 s^{-1}, in good agreement with the room temperature turnover frequency of 10 s^{-1} on a Pt(111) single crystal under similar pressure conditions [50]. At similar conditions, turnover frequencies as high as 20 s^{-1} [51] and as low as 3×10^3 s^{-1} [52] have been measured on SiO_2 supported Pt catalysts. Figure 6 demonstrates the influence of particle size on catalytic activity with time on stream. Initial rates (Table 4) are identical, but steady state rates (after 40 ks) decrease with increasing particle size. The reason for this behavior is unknown at the time but may be related to stronger adsorption of ethylidyne and its subsequent decomposition on the surface of larger particles. Comparison of the initial heats of adsorption of ethylene and identification of

Table 5.4. Ethylene hydrogenation turnover rates and kinetic parameters on Pt catalysts.

Catalyst[a]	Activity[b] (μmol g^{-1} s^{-1})	TOF[b,c] (s^{-1})	E_a[d] (kcal mol^1)	Reaction orders	
				C_2H_4[e]	H_2[f]
3.2% Pt/SiO$_2$-IE	623	3.8	8.0	-0.1	0.62
0.6% Pt(1.7 nm)/SBA-15	45	3.5	10.5	0	0.57
0.77% Pt(2.9 nm)/SBA-15	50	3.5	9.8	0	0.48
0.6% Pt(3.6 nm)/SBA-15	28	3.4	10.1	0.1	0.47
0.62% Pt(7.1 nm)/SBA-15	11	3.2	12.1	0.1	0.51
Pt powder	69	3.4	8.9	-0.1	0.4

[a]Actual catalyst loading determined by ICP-AES.
[b]Initial activity. Reaction conditions were 10 Torr C_2H_4, 100 Torr H_2, and 298 K.
[c]Normalized to number of surface atoms determined by total H_2-O_2 titration.
[d]Reaction conditions were 10 Torr C_2H_4, 200 Torr H_2, and 273-323 K.
[e]Reaction conditions were 10-40 Torr C_2H_4, 200 Torr H_2, and 298 K.
[f]Reaction conditions were 10 Torr C_2H_4, 200-600 Torr H_2, and 298 K.
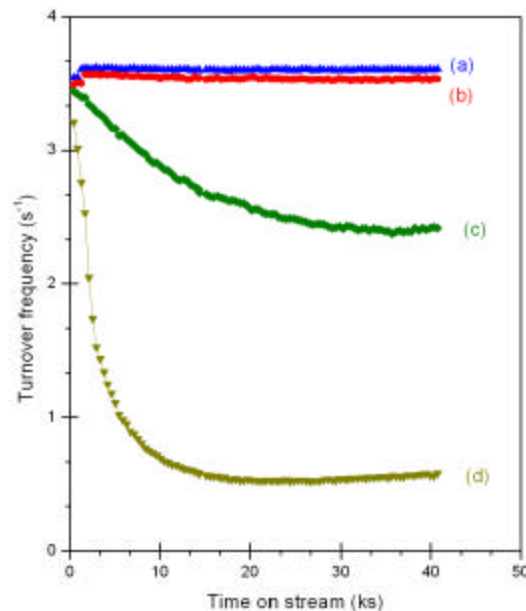
Figure 5.6. Time on stream behavior during ethylene hydrogenation on Pt(X)/SBA-15 catalyst. X = (a) 1.7 nm, (b) 2.9 nm, (c) 3.6 nm and (d) 7.1 nm. Reaction conditions were 10 Torr C_2H_4, 100 Torr H_2 and 298 K. Turnover frequencies were calculated from metal dispersions determined by H_2-O_2 titration. All catalysts have the same initial turnover frequency, but the catalysts with larger metal particles deactivate with time on stream.

adsorbed species by various surface spectroscopy suggests that the dehydrogenation of adsorbed ethylene is suppressed on small crystallites [53, 54]. Yates and coworkers [55] have shown by vibrational coupling that ethylidyne is produced on (111) facets of small Pt particles (d = 10-40 Å, ave. 20 Å) rather than on random trimer Pt sites and no ethylidyne was detected on highly dispersed Pt particles ($d \leq 10$ Å). Passos and Vannice [56] found that the initial heat of adsorption at 300 K was 10 kcal mol^{-1} higher on large (~20 nm) Pt particles as compared with small Pt particles (~ 1 nm); the higher heat of adsorption on large crystals is attributed to the exothermic dehydrogenation of ethylene to ethylidyne or ethylidene [57]. These surface reactions are not probed by UHV temperature programmed desorption (TPD) from Pt single crystal surfaces because only the evolution of reversibly adsorbed molecular C_2H_4 is measured. Correction of reported TPD data for the enthalpy of reaction for the

dehydrogenation of ethylene to ethylidyne yields ethylene heat of adsorption values on Pt single crystals which are similar to values measured on large (= 4 nm) Pt crystallites [56, 58].

The increased heat of adsorption of ethylene on larger crystallites suggests that the barrier for ethylidyne surface diffusion may be higher on larger crystallites, although extended Hückel calculations of C_2H_3 surface diffusion on Pt(111) suggest that the required activation energy is low (2.3 kcal mol^{-1}) [59]. Stronger heats of adsorption should hinder adsorbate mobility, critical for catalytic turnover [60], and the increased residence time of C-C species on the surface may lead to their decomposition and eventual poisoning until a steady state carbon coverage is obtained. A model of a supported ethylene hydrogenation catalyst under reaction conditions may be similar to the model proposed for a Pt reforming catalyst [61].

Hydrogenation of ethylene is easily catalyzed at room temperature, with apparent activation energies of ~10 kcal mol^{-1} for the Pt/SBA-15 catalyst series. One notable exception is the apparent activation energy of 12 kcal mol^{-1} for the 0.62% Pt(7.1 nm)/SBA-15 catalyst. Activation energies in this range have been attributed to a dirty or poisoned catalyst surface [51]. During the synthesis of 7.1 nm Pt nanoparticles, 12-fold molar excess of PVP is added relative to the Pt concentration. The larger excess of PVP was removed with a 723 K calcination time of 36 h (2.9 and 3.6 nm particles were calcined at 723 K for 24 h). It is possible that the higher apparent activation energy is due to the presence of residual polymer, although TGA of 7.1 nm particles suggests that PVP decomposes over the same temperature range as observed on the 2.9 nm particles [62]. The observed time on stream deactivation dependence of Pt(7.1 nm)/SBA-15 may be related to residual PVP on the surface. Partial pressure dependencies of ethylene hydrogenation over encapsulated

nanoparticles (Table 4) are in accord with classically prepared samples. Dependence on ethylene and hydrogen partial pressures are ~ 0.1 and 0.5, respectively for the Pt/SBA-15 catalysts. Similar to other SiO_2 supported Pt catalysts, the hydrogen reaction order approached unity as the temperature was increased and the ethylene order was zero order at temperatures around room temperature [63].

Ethane hydrogenolysis as probe of structure sensitivity

The hydrogenolysis of alkanes has been studied extensively because of the well-known sensitivity of hydrogenolysis rates on surface structure [64, 65]. As a test of particle surface structure, the hydrogenolysis of ethane was examined over the Pt/SBA-15 catalysts. Table 5 summarizes the kinetic results of ethane hydrogenolysis; as previously reported, ethane hydrogenolysis is very sensitive to particle size, with turnover frequencies varying by at least two orders of magnitude for catalysts containing Pt particles from 1-7 nm. Apparent reaction orders in ethane and hydrogen were 1 and ~ -3, respectively, for the Pt/SBA-15 series. The observed reaction orders are in agreement with measurements on other supported Pt catalysts [66]. Measured apparent activation energies increase with decreasing metal dispersion.

Ion-exchanged 3.2% Pt/SiO2-IE with particles of ~ 1 nm were the most active (6.4×10^{-2} s^{-1} at 658 K) and had an apparent activation energy of 54 kcal mol^{-1}. Apparent activation energies increased to ~ 75 kcal mol^{1} on the 0.6% Pt(3.6 nm)/SBA-15 catalyst. The apparent preexponential factors assuming a power rate law, $r_{CH_4} = k_{app}P_{C_2H_6}P_{H_2}^{-3}$ where $k_{app} = Ae^{-E_{app}/RT}$ varied by four orders of magnitude (10^{25}-10^{29} $Torr^2$ s^{-1}) over the particle size range studied. The influence of particle size on catalytic activity and the measured apparent activation energy are shown in Figure 7. As the particle size increases, a linear increase in the apparent activation energy is

Table 5.5. Ethane hydrogenolysis turnover rates and kinetic parameters on Pt catalysts

Catalyst[a]	Activity[b] (μmol g^{-1} s^{-1})	TOF[b,c] $100 \times$ (s^{-1})	E_a[d] (kcal mol^{-1})	Reaction orders C$_2$H$_6$[e]	H$_2$[f]
3.2% Pt/SiO$_2$-IE	10.6	6.5	54.5	0.99	-2.8
6.3% Pt/SiO$_2$ (EUROPT-1)	11.3	4.7	46.0	0.9	-1.8
0.6% Pt(1.7 nm)/SBA-15	0.16	1.2	63.4	0.97	-2.4
0.77% Pt(2.9 nm)/SBA-15	7.8×10^{-2}	0.6	68.7	1	-3.1
0.6% Pt(3.6 nm)/SBA-15	1.1×10^{-2}	0.1	75.8	1.1	-3.0
0.62% Pt(7.1 nm)/SBA-15	6.5×10^{-3}	0.08	74.5	0.97	-2.9
Pt powder	7×10^{-3}	0.04	70.5	0.99	-2.6

[a]Actual catalyst loading determined by ICP-AES.
[b]Reaction conditions were 20 Torr C$_2$H$_6$, 200 Torr H$_2$, and 658 K.
[c]Normalized to number of surface atoms determined by total H$_2$-O$_2$ titration.
[d]Reaction conditions were 20 Torr C$_2$H$_6$, 200 Torr H$_2$, and 593-673 K.
[e]Reaction conditions were 10-60 Torr C$_2$H$_6$, 200 Torr H$_2$, and 658 K.
[f]Reaction conditions were 20 Torr C$_2$H$_6$, 140-270 Torr H$_2$, and 658 K.
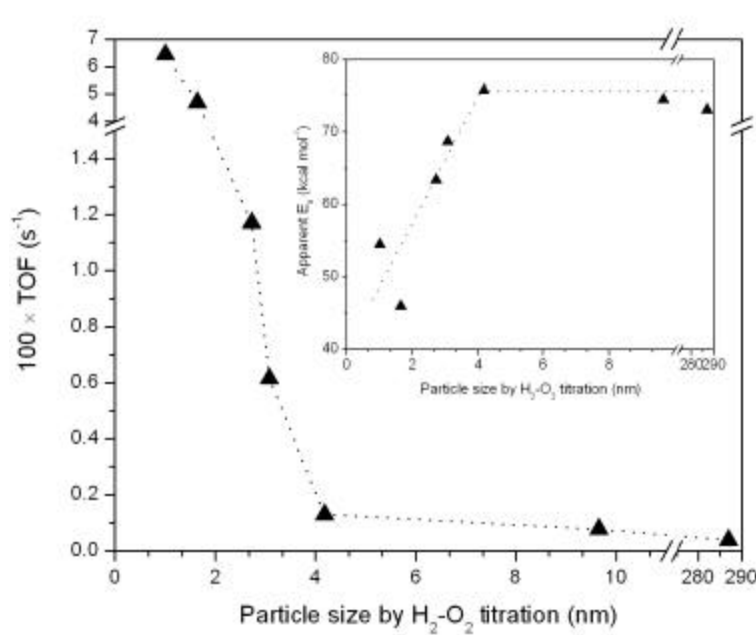
Figure 5.7. Dependence of ethane hydrogenolysis turnover frequency and apparent activation energy on Pt particle size. Turnover frequencies decrease by 2 orders of magnitude over the size range, while the apparent activation energy increases. Coordinatively unsaturated surface atoms in small particles have a higher reactivity and subsequently a smaller barrier for hydrogenolysis than highly coordinated surface atoms of larger particles. Turnover frequencies were measured at 20 Torr C_2H_6, 200 Torr H_2, and 658 K.

found, up to a particle size of 3.6 nm, after which the activation energy is unchanged

with larger particle size. Figure 7 demonstrates that the turnover frequency for

methane formation decreases as the particle size increases; similar trends have been

observed on supported Pt catalysts [67, 68]. A maximum in ethane hydrogenolysis

turnover frequency has been observed for Pt/Al_2O_3 catalysts with Pt particles ranging

from 1.7-5 nm [69]. These authors also observe a minimum in the apparent activation

energy with particle size, after ~4 nm there is no change in the apparent activation

energy. A compilation of reported ethane hydrogenolysis rates normalized to

standard conditions of 20 Torr C_2H_6, 200 Torr H_2 and 658 K is given (see supporting

information). Rates of ethane hydrogenolysis follow a trend of decreasing rate with

increasing metal particle size on the Pt/SBA-15 series, although significant

discrepancies do exist and these have been highlighted in a recent review [70]. For example, two independent studies of ethane hydrogenolysis on Pt(111) have determined similar turnover frequencies of ~ 0.3 s^{-1} at standard conditions, which is an order of magnitude higher than Pt(1.7 nm)/SBA-15 and three orders of magnitude higher than Pt(7.1 nm)/SBA-15.

It is believed that large ensembles of Pt atoms are necessary for ethane hydrogenolysis because the C_2 intermediate is most likely bonded to multiple Pt atoms and adjacent sites are needed for H adsorption. The necessity for a large Pt ensemble is most likely not the only requirement for an appropriate active site for ethane hydrogenolysis. Goodwin and coworkers suggest that these ensembles must also be properly oriented [71]. Comparison of ethane hydrogenolysis rates on Ni(111) and (100) has led Goodman to suggest that the spatial coordination of surface metal atoms is a decisive factor in determining reactivity; differences in spacing between surface atoms on the two surfaces could account for the differences in activity [72]. The number of atoms in the ensemble varies with metal most likely due to the stoichiometry of the C_2H_x species in which the C-C bond is broken. In the case of Ni, methane forms through surface carbide followed by hydrogen reduction; suggesting that a 12 atom ensemble is required [73]. On Pt, the proposed C_2 intermediate that undergoes C-C bond cleavage on Pt is the ethyl radical, C_2H_5 [74, 75]. In this case, the ensemble size may be significantly reduced but the orientation of the atoms composing that ensemble is still critical; most likely requiring a fraction of the ensemble to be composed of atomic steps, kinks, or other sources of surface roughness. Theoretical calculations of C_2H_x fragment stability on Pt slabs and clusters have shown that barriers to bond activation are lower on a stepped Pt(211) surface relative to a flat (111) surface [76, 77]. Correspondingly, the activated

complexes along the hydrogenolysis reaction coordinate are stabilized on the stepped surface relative to the flat surface. Small metal crystallites have a higher proportion of coordinatively unsaturated surface atoms, analogous to a stepped single crystal, while the surfaces of large Pt particle are terminated primarily by low index, high coordination surfaces. It appears that reactions involving C_2H_x and their activated complexes occur on these defect sites because they provide more stable bonding. Recent work has shown that methane activation rates increased with Pt dispersion suggesting that CH_x species are stabilized on coordinatively unsaturated atoms [78]. The identity of the active site for C-H and C-C bond activation is unknown, but particle size dependent catalytic behavior of ethane hydrogenolysis suggests that surface roughness is a primary component of the active site.

Structure sensitivity of ethane decomposition to surface carbon during hydrogenolysis

Methane is the only product observed in the gas phase, but consideration of the decomposition of ethane to surface carbon as a reaction pathway is an important parameter for the design of hydrogenolysis catalysts. For example, Besenbacher *et al*. [79] demonstrated that step sites on a Ni single crystal are significantly more reactive for C-C bond breaking than terrace atoms and the selective blocking of step sites with inert Au atoms led to a Ni surface capable only of C-H bond activation. In another study, two competing reaction pathways were found for methanol decomposition; C-H bond activation leading to the formation of CO_2 at terrace sites and C-O bond scission leading to carbon covered step sites [80]. In these elegant examples, the morphology and surface roughness of the surface not only influence activity, but play an important role in determining reaction selectivity.

The extent of carbon deposited on Pt/SBA-15 after hydrogenolysis has been determined by H_2-O_2 titration. It has been suggested that adsorption of probe

molecules can be used to determine the fraction of the surface covered with carbon [81, 82]. Table 6 demonstrates that the fraction of the Pt surface covered with carbon on catalysts used in this study varied from 10-30 % and was dependent on particle size. The significantly higher fractional carbon coverage after ethane hydrogenolysis on the Pt(2.9 nm)/SBA-15 catalysts is proposed to be due to the presence of a higher fraction of coordinatively unsaturated surface atoms which promote formation of irreversibly chemisorbed carbon. While this carbon was removed by oxidative treatment restoring the original surface area; it appears that under reducing conditions this carbon is irreversibly chemisorbed and most likely deposited during the first few turnovers on surface atoms with the highest coordinative unsaturation. On Pt(111), Rodriguez and Goodman have shown the amount of surface carbon after ethane hydrogenolysis in a 100 fold excess of hydrogen is temperature dependent, with the coverage increasing approximately linearly with temperature. Approximately 35% of the surface was covered with carbon as determined by Auger electron spectroscopy at 620 K [83]. At lower H_2:C_2H_6 ratios ($H_2/C_2H_6 = 10$), the coverage of the Pt(111) surface after ethane hydrogenolysis at 620 K is 60% [84]. The difference between the fraction of carbon coverage reported for single crystals and the Pt/SBA-15 catalysts is most likely due to the support serving as a sink for coke precursors as proposed by Parera [85]. Therefore, it is evident that reaction selectivity is structure sensitive due to competing reaction pathways occurring at different rates on distinct surface sites.

Comparison of the reactivity of Pt/SBA-15 catalysts prepared by different synthetic methods

Table 5.6. Exposed Pt surface area before and after ethane hydrogenolysis on selected Pt/SBA-15 catalysts determined by H_2-O_2 titration

Catalyst	Probe gas uptake (μmol g^{-1})[a]		H_2-O_2 titr.	Based on total H_2-O_2 titration uptake			Fraction of Pt surface area exposed
	CO			Dispersion, D	Pt surface area[b]	Pt particle size[c]	
	Total	Irrev.	Total		(m^2 g^{-1})	(nm)	
0.77% Pt(2.9 nm)/SBA-15 before rxn	11.3	10.0	21.8	0.37	14.2	3.1	--
0.77% Pt(2.9 nm)/SBA-15 after rxn[d]	8.9	8.9	16.5	0.28	10.7	4.1	0.68
0.77% Pt(2.9 nm)/SBA-15 after calcination[e]	9.4	8.5	21.7	0.37	14.1	3.1	--
0.6% Pt(3.6 nm)/SBA-15 before rxn	7.9	7.4	12.5	0.27	8.1	4.2	--
0.6% Pt(3.6 nm)/SBA-15 after rxn[d]	6.8	5.6	11.2	0.24	7.3	4.7	0.88
0.6% Pt(3.6 nm)/SBA-15 after calcination[e]	7.5	6.7	12.0	0.26	7.8	4.3	--

[a]Measured at 295 K. Monolayer values extrapolated to P = 0.
[b]H:Pt = 1 and cross setional area of H_2 molecule = 10.4 Å^2 were assumed.
[c]Determined by d(nm) = 1.13/D.
[d]Measured directly after ethane hydrogenolysis.
[e]Sample was calcined for 1 h in 20% O_2/He at 573 K followed by reduction at 673 K for 1 h.

The original method, capillary inclusion (CI) developed in our laboratory for the synthesis of Pt/SBA-15 catalysts involved the incorporation of PVP-capped Pt nanoparticles into calcined SBA-15 by sonication in aqueous ethanolic solution [18]. PVP was removed from the Pt nanoparticle surface by calcination in oxygen by a procedure similar to that described for the NE catalysts. Adsorption uptakes on CI-Pt/SBA-15 catalysts were significantly smaller than the NE series leading to larger calculated average particle sizes. Ethylene hydrogenation rates were within a factor of five on both sets of catalysts with similar kinetic parameters. Ethane hydrogenolysis rates were less than a factor of two different on the CI series, while the NE series demonstrated a much more pronounced particle size dependence (order of magnitude for NE catalysts). The more pronounced variation is consistent with previous measurements of ethane hydrogenolysis rates on supported Pt catalysts

This is most likely related to the larger variation in dispersion for the NE samples as determined by chemisorption. The calcination-reduction procedure was more effective removing PVP from the nanoparticle surface or the capillary inclusion method perturbed the mesoporous oxide in a way that could not be assessed by the conventional characterization tools (TEM, SAXS, nitrogen adsorption). The smaller monolayer uptakes on the CI samples suggest that the quantity of residual PVP is higher on these samples than the NE samples. One possible explanation may be related to condensation of volatile PVP precursors during calcination on the surface of PVP particles, which may be reduced in the NE silica having pores with a slightly larger diameter. A similar explanation has recently been proposed by Chandler *et al.* [35, 36] for differences in catalytic behavior between xerogel silica encapsulated dendrimer templated nanoparticles

and the same nanoparticles deposited on amorphous silica by impregnation. A second explanation for the effective removal of PVP from NE nanoparticle surface is the additional heat released by the combustion of the silica template polymer (Pluronic P123) may enhance the combustion of PVP. Pluronic P123 is removed from CI-SBA-15 by *ex-situ* calcination at 823 K for 12 h. Both studies demonstrate comparable reaction rates (turnover frequency) for both ethylene hydrogenation and ethane hydrogenolysis when normalized to the number of surface atoms determined by gas adsorption. Both studies exemplify the importance of PVP removal from the catalyst surface before accurate catalytic reaction rates can be measured.

The nanoparticle encapsulation method introduced in this manuscript enables the synthesis of catalytic structures with tunable properties such as metal particle size represents an advance in catalyst synthesis. Characterization of such materials confirms that particle size can be rationally controlled during synthesis, incorporated into oxide structures and are catalytically active after activation. Reactivity studies with these catalysts may enable the development of very accurate structure-activity and selectivity correlations in heterogeneous catalysis.

5.4   Summary

Platinum nanoparticle supported catalysts with narrow size distributions and a highly ordered mesoporous silica matrix were prepared by *in-situ* hydrothermal growth in stabilized nanoparticle aqueous solution. Resulting materials are calcined to remove stabilizing polymer from the nanoparticle surface and amphiphilic tri-block copolymers used to template the mesoporous structure. Reduction of the materials yields supported

metallic nanoparticles with a high fraction of the as-synthesized particle size chemically active as determined by selective gas adsorption and infrared investigations of CO adsorption. Hydrocarbon conversion reactions confirm catalysts are active. Initial ethylene hydrogenation rates were insensitive to particle sizes in the 1-7 nm range, while ethane hydrogenolysis rates varied by two orders of magnitude over Pt particles within the same size range. Smaller particles were more active for hydrogenolysis suggesting that coordinatively unsaturated surface atoms prevalent in small crystallites were more reactive for C-H and C-C bond activation. CO adsorption experiments qualitatively confirm that surface site heterogeneity (*i.e.* surface roughness) increases with decreasing particle size. The most reactive of these unsaturated sites are assumed responsible for ethane decomposition to surface carbon during hydrogenolysis. The degree of surface carbon deposition was structure sensitive, with smaller Pt nanoparticles demonstrating higher carbon coverage after reaction. Larger particles are more selective for methane formation; smaller particles are more active for methane formation and carbon deposition. Characterization of catalysts before and after hydrogenolysis confirms that surface carbon is irreversibly chemisorbed during reaction; the amount of which depends on particle size. Surface site heterogeneity affects reaction selectivity by enabling competing reaction pathways to exist. The most significant impact of nanoscience methods on heterogeneous catalysis is in catalyst synthesis; the ability to design and control catalytic structures during synthesis which enables production of catalysts capable of specific (*i.e.* selective) function. In the present example, the ability to synthesize monodisperse particles by solution phase reduction enables the study of intrinsic activity and selectivity

of particle size rather than ensemble (particle size) averaged values of these kinetic phenomena.

5.5   References and Notes

1.   G. A. Somorjai, Y. G. Borodko, *Catal. Lett*. 76 (2001) 1.

2.   A. T. Bell, *Science* 299 (2003) 1688.

3.   J. Grunes, J. Zhu, G. A. Somorjai, *Chem. Commun*. 18 (2003) 2257.

4.   M. Boudart, *J. Mol. Catal*. 30 (1985) 27.

5.   D. R. Rolison, *Science* 299 (2003) 1698.

6.   K. Hayek, R. Kramer, Z. Paál, *Appl. Catal. A. Gen.* 162 (1997) 1.

7.   H. H. Kung, M. C. Kung, *Appl. Catal. A Gen*. 246 (2003) 193.

8.   H. H. Kung, M. C. Kung, *Top. Catal*. 34 (2005) 77.

9.   R. Schlögl, S. B. A. Hamid, *Angew. Chem. Int. Ed*. 43 (2004) 1628.

10.   G. Ertl, H. Knözinger, J. Weitkamp, *Handbook of Heterogeneous Catalysis*; Wiley/VCH: New York/Weinheim, 1997.

11.   J. W.Geus, J. A. R. van Ween, Catalysis: An integrated approach to homogeneous, heterogeneous and industrial catalysis; Moulijn, J. A.; van Leeuwen, P. W. N. M.; van Santen, R. A. ed.; Elsevier: Amsterdam, 1993, chap 9.

12.   A. Fukuoka, N. Higashimoto, Y. Sakamoto, S. Inagaki, Y. Fukushima, M. Ichikawa, *Top. Catal*. 18 (2002) 73.

13.   C.-M. Yang, P.-H. Liu, C.-Y.Chiu, K.-J.Chao, *Chem. Mater*. 15 (2003) 275.

14.   A. Fukuoka, H. Araki, Y. Sakamoto, N. Sugimoto, H. Tsukada, Y. Kumai, Y. Akimoto, M. Ichikawa, *Nano Lett*. 2 (2002) 793.

15.   C. T. Kresge, M. E. Leonowicz, W. J. Roth, J. C. Vartuli, J. S. Beck, *Nature* 359 (1992) 710.

16. D. Zhao, J. Feng, Q. Huo. N. Melosh, G. H. Fredrickson, B. F. Chmelka, G. D. Stucky, *Science* 279 (1998) 548.

17. D. Zhao, D. Q. Huo, J. Feng, B. F. Chmelka, G. D. Stucky, *J. Am. Chem. Soc*. 120 (1998) 6024.

18. R. M. Rioux, H. Song, J. D. Hoefelmeyer, P. D. Yang, G. A. Somorjai, *J. Phys. Chem*. B 109 (2005) 2192.

19. R. Shenhar, T. B. Norsten, V. M. Rotello, *Adv. Mater*. 17 (2005) 657.

20. Z. Kónya, V. F. Puntes, I. Kiricsi, J. Zhu, A. P. Alivisatos, G. A. Somorjai, *Nano Lett*. 2 (2002) 907.

21. Zhu, J.; Kónya, Z.; Puntes, V. F.; Kiricsi, I.; Miao, C. X.; Ager, J. W.; Alivisatos, A. P.; Somorjai, G. A. *Langmuir* 19 (2003) 4396.

22. Bagshow, S. A.; Prouzet, E.; Pinnavaia, T. J. *Science*, 269 (1995) 1242.

23. Wang, Y.; Ren, J.; Deng, K.; Gui, L.; Tang, Y. *Chem. Mater*. 12 (2000) 1622.

24. Teranish, T.; Hosoe, M.; Tanaka, T.; Miyake, M. *J. Phys. Chem. B* 103 (1999) 3818.

25. Singh, U. K.; Vannice, M. A. *J. Catal*. 191 (2000) 165.

26. Bond, G. C.; Wells, P. B. *Appl. Catal*. 18 (1985) 221.

27. Bond, G. C.; Wells, P. B. *Appl. Catal*. 18 (1985) 225.

28. Geus, J. W.; Wells, P. B. *Appl. Catal*. 18 (1985) 231.

29. Frennet, A.; Wells, P. B. *Appl. Catal*. 18 (1985) 243.

30. P. B. Wells, P. B. *Appl. Catal*. 18 (1985) 259.

31. Song, H.; Kim, F.; Connor, S.; Somorjai, G. A.; Yang, P. *J. Phys. Chem. B* 109 (2005) 188.

32. Anderson, J. R. *Structure of Metallic Catalysts*, Academic Press: New York, 1975.

33. Dietz, W. A.; *J. Gas. Chrom*. 5 (1967) 68.

34. Alexandridis, P.; Holzwarth, J. F.; Hatton, T. A. *Macromolecules* 27 (1994) 2414.

35. Lang, H.; May, R. A.; Iverson, B. L.; Chandler, B. D. *J. Am. Chem. Soc*. 125 (2003) 14832.

36. Beakley, L. W.; Yost, S. E.; Cheng, R.; Chandler, B. D. *Appl. Catal. A Gen*. 292 (2005) 124.

37. Van Der Voort, P.; Ravikovitch, P. I.; De Jong, K.P.; Benjelloun, M.; Van Bavel, E.; Janssen, A. H.; Neimark, A. V.; Weckhuysen, B. M.; Vansant, E. F. *J. Phys. Chem. B* 106 (2002) 5873.

38. Boudart, M. *Adv. Catal*. 20 (1969) 153.

39. Little, L. H. *Infrared Spectra of Adsorbed Species*, Academic Press: New York, 1966.

40. Hair, M. L. *Infrared Spectroscopy in Surface Chemistry*, Dekker: New York, 1967.

41. McCrea, K. R.; Parker, J. S.; Chen, P. L.; Somorjai, G. A. *Surf. Sci.* 494 (2001) 238.

42. Mukerji, R. J.; Bolina, A. S.; Brown W. A. *Surf. Sci*. 527 (2003) 198.

43. Cant, N. W.; Donaldson, R. A. *J. Catal*. 78 (1982) 461.

44. Bischoff, H.; Jaeger, N. I.; Schulz-Ekloff, G., *Z. Phys. Chemie Leipzig* 271 (1990) S1093.

45. Watwe, R. M.; Spiewak, B. E.; Cortright, R. D.; Dumesic, J. A. *Catal. Lett*. 51 (1998) 139.

46. Schulze Icking-Konert, G.; Handschuh, H.; Ganteför, G.; Eberhardt, W. *Phys. Rev. Lett*. 76 (1996) 1047.

47. Härle, H.; Metka, W.; Volpp, H. –R.; Wolfrum, J. *Phys. Chem. Chem. Phys*. 1 (1999) 5059.

48. Van Hardeveld, R. V.; Hartog, F. *Surf. Sci*. 15 (1969) 189.

49. Dorling, T. A.; Eastlake, M. J.; Moss, R. L. *J. Catal*. 14 (1969) 23.

50. Zaera, F. and Somorjai, G. A. *J. Am. Chem. Soc*. 106 (1984) 2288.

51. Schlatter, J. C.; Boudart, M. *J. Catal*. 24 (1972) 482.

52. Sinfelt, J. H. *J. Phys. Chem*. 68 (1964) 856.

53. Gay, I. D. *J. Catal*. 108 (1987) 15.

54. Soma, Y. *J. Catal*. 75 (1982) 267.

55. Paul, D. K.; Beebe, T. P.; Uram, K. J.; Yates, J. T. *J. Am. Chem. Soc*. 114 (1992) 1949.

56. Passos, F. B.; Schmal, M.; Vannice, M. A. *J. Catal*. 160 (1996) 118.

57. Carter, E. A.; Koel, B. E. *Surf. Sci*. 226 (1990) 339.

58. Shen, J.; Hill, J. M.; Watwe, R. M.; Spiewak, B. E.; Dumesic, J. A. *J. Phys. Chem. B* 103 (1999) 3923.

59. Nomikou, Z.; Van Hove, M. A.; Somorjai, G. A. *Langmuir* 12 (1996) 1251.

60. Somorjai, G. A. *Nature* 430 (2004) 730.

61. Somorjai, G. A.; Zaera, F. *J. Phys. Chem*. 86 (1982) 3070.

62. Rioux, R. M.; Song, H.; Habas, S.; Grass, M.; Hoefelmeyer, J. D.; Niesz, K.; Yang, P. D.; Somorjai, G. A. *Top. Catal*. 2005, manuscript in revision.

63. Cortright, R. D.; Goddard, S. A.; Rekoske, J. E.; Dumesic, J. A. *J. Catal*. 127

(1991) 342.

64. Martin, G. A. *J. Catal*. 60 (1979) 452.

65. Carter, J. L.; Cusumano, J. A.; Sinfelt, J. H. *J. Phys. Chem*. 70 (1966) 2257.

66. Sinfelt, J. H.; Taylor, W. F.; Yates, D. J. C. *J. Phys. Chem*. 68 (1965) 95.

67. Guczi, L.; Gudkov, B. S. React. Kinet. *Catal. Lett*. 9 (1978) 343.

68. Barbier, J.; Morales, A.; Maurel, R. *Bull. Soc. Chim. Fr*. I31 (1978).

69. Nazimek, D.; Ryczkowski, J. *React. Kinet. Catal. Lett*. 40 (1989) 145.

70. Gunter, P. L. J.; Niemandsverdriet, J. W. H.; Ribeiro, F. H.; Somorjai, G. A. *Catal. Rev. Sci. Eng*. 39 (1997) 77.

71. Goodwin, J. G.; Kim, S.; Rhodes, W. D. in: Catalysis, Vol. 17, ed. J. J. Spivey (The Royal Society of Chemistry, 2004) ch. 8.

72. Goodman, D. W. *Surf. Sci*. 123 (1982) L679.

73. Martin, G. A. *Catal. Rev. Sci. Eng*. 30 (1988) 519.

74. Cortright, R. D.; Watwe, R. M.; Spiewak, B. E.; Dumesic, J. A. *Catal. Today* 53 (1999) 395.

75. Gudkov, B. S.; Guczi, L.; Tétényi, P. *J. Catal*. 74 (1982) 207.

76. Watwe, R. M.; Spiewak, B. E.; Cortright, R. D.; Dumesic, J. A. *J. Catal*. 180 (1998) 184.

77. Watwe, R. M.; Cortright, R. D.; Nørskov, J. K.; Dumesic, J. A. *J. Phys. Chem. B* 104 (2000) 2299.

78. Wei, J.; Iglesia, E. *J. Phys. Chem. B* 108 (2004) 4094.

79. Vang, R. T.; Honkala, K.; Dahl, S.; Vestergaard, E. K; Schnadt, J.; Lægsgaard, E.; Clausen, B. S.; Nørskov, J. K.; Besenbacher, F. *Nature Mater*. 4 (2005) 160.

80. Hoffman, J.; Meusel, I.; Hartmann, J.; Libuda, J.; Freund, H. J. *J. Catal*. 204 (2001) 378.

81. Rivera-Latas, F. J.; Dalla Betta, R. A.; Boudart, M. *AIChE J*. 38 (1992) 771.

82. Zaera, F.; Somorjai, G. A. *Langmuir*, 2 (1986) 686.

83. Rodriguez, J. A.; Goodman, D. W. *J. Phys. Chem*. 94 (1990) 5342.

84. Zaera, F.; Somorjai, G. A. *J. Am. Chem. Soc*. 89 (1985) 3211.

85. Parera, J. M.; Figoli, N. S.; Traffano, E. M.; Beltramini, J. N.; Martinelli, E. E. *Appl. Catal*. 5 (1983) 33.

Chapter 6

Influence of Pt particle size on the co-adsorption of ethylene and carbon monoxide: Volumetric adsorption and infrared studies

6.1. Introduction

The role of lateral interactions between like and different coadsorbates in adsorption and catalytic reactivity leads to kinetic phenomena which may deviate from conventional theory, *i.e.* Langmuir-Hinshelwood heterogeneous kinetics [1]. Interactions between adsorbates can lead to well-ordered surface structures, to disordered structures and even to surface adsorbate islanding [2]. These phenomena induced by adsorbate interactions can span large length scales, ranging from a few atomic diameters to mesoscale dimensions [3]. Many of these phenomena originate or terminate at defect sites and therefore the role of surface roughness (nanoparticle size) on adsorbate interactions is important. Conventional theories such as the Langmuir isotherm have been modified to account for these intermolecular interactions, such as the Temkin

isotherm [4] which differs from the previous isotherm in that it accounts for reduced adsorption (linearly) as a function of coverage. It has been shown that this model can accurately predict the thermodynamics of CO adsorption on many transition metal single crystals [5]. Non-uniform (spatially, energetically and temporally) interactions between adsorbates on surfaces have tremendous impact on observed heterogeneous reaction kinetics by influencing the stability of transition states, modifying adsorption geometries and changing the adsorbate-surface bonding. The influence of intermolecular interactions between same co-adsorbates on adsorption dynamics and kinetics has been studied extensively, while the influence of different co-adsorbates (*i.e.* reactants) has been studied to a lesser extent but important due to their role in heterogeneous catalysis at industrially relevant conditions. Most studies have been conducted on single crystal surfaces using methods and techniques unable to truly duplicate or function under high pressure, high coverage conditions. The influence of co-adsorbate interactions on small metal crystallites supported on oxides have received even less attention because of the enormous system complexity. The co-adsorption behavior of carbon monoxide and ethylene was chosen as a model system to study because the surface chemistry of both molecules on supported catalysts has been studied extensively [6]. The bonding of CO is extremely sensitive to the local environment, both underlying metal surface structure and neighboring adsorbates. The bonding of π-bonded ethylene [7], the presumed reaction intermediate in ethylene hydrogenation is similar to the bonding of CO in that it involves donation from a bonding orbital of the adsorbate and back donation from the metal into an anti-bonding orbital [8]. Therefore, the adsorption of these adsorbates should be influenced by the other and this has proven true on a number of metal surfaces. In fact,

the introduction of small pressures of CO to an ethylene hydrogenation catalyst leads to orders of magnitude change in reactivity.

In this paper, the influence of Pt particle dimension on the adsorption of carbon monoxide and ethylene was investigated. Infrared spectroscopy of CO adsorption demonstrate the atop CO stretching frequency redshifts as the particle size is decreased, due to a change in the average coordination of the Pt atom. The formation of ethylidyne was structure-sensitive; its formation was more facile on larger particles. Infrared investigations of sequential co-adsorption demonstrate that preadsorbed ethylene influences the band position of atop CO, while ethylene adsorption on CO covered surface had little influence on adsorbed CO due to minor adsorption of ethylene. The implication of particle size on the coadsorption of ethylene and carbon monoxide is extended to the hydrogenation of ethylene in low pressures of carbon monoxide in Chapter 7.

6.2.   Experimental

6.2.1   Catalyst Synthesis and Characterization

A series of ~ 3 % Pt/SBA-15 catalysts were used in these experiments. A detailed description of their synthesis and characterization can be found elsewhere [9]. Briefly, Pt nanoparticles between 1.7 and 7.1 nm were synthesized in the presence of a surface templating polymer, polyvinylpyrrolidone (PVP) by a modified alcohol/diol reduction method to yield nearly monodisperse Pt nanoparticles in solution [10–12]. Number averaged particle sizes determined from TEM images [13] with their standard deviation after counting ≥ 200 particles were 1.73±0.26 (1.7), 2.80±0.21 (2.9), 3.39±0.26 (3.6), and

7.16±0.37 (7.1) nm by TEM (XRD) respectively, indicating high uniformity and monodispersity of each particle less than $\sigma \sim 8\%$. After synthesis and purification of the nanoparticles, they are encapsulated in mesoporous silica (SBA-15) structure by direct participation in the hydrothermal reaction. Synthesis of SBA-15 [9] was conducted at neutral pH using NaF for hydrolysis of the silica precursor, tetramethyl orthosilicate (TMOS). The mechanism of nanoparticle encapsulation has been previously discussed [9]. Calcination in O_2 at 623 or 723 K for 24 to 36 hrs (sample dependent) was used to remove PVP from the particle surface; 1.7 nm particles are calcined at 623 K for 24 h to prevent particle sintering, while 36 h at 723 K is required for the catalyst containing 7.1 nm particles.

A 3.2% Pt/SiO$_2$ catalyst prepared by ion exchange of Pt(NH$_3$)$_4$(OH)$_2$•xH$_2$O [14] and an ultrahigh purity (UHP) Pt powder (Alfa Aesar, 1μm particle size) were used as standard samples for both chemisorption and infrared spectroscopy measurements. The ultrahigh purity Pt powder was cleaned by heating at 473 K for 30 minutes in 10% O$_2$/He to remove any surface contaminants before normal catalyst pretreatment. A 2% Pt/Al$_2$O$_3$ (Exxon Research and Engineering) was included to determine if the support influenced co-adsorption behavior. A thoroughly characterized 6.3% Pt/SiO$_2$ (EUROPT-1) catalyst was used; Pt particle size distribution is 1-3.5 nm centered at 1.8 nm with 75% of the platinum particles with a diameter of $\leq$ 2 nm [15-20]. All standard catalyst samples were reduced by the same procedure used for SBA-15 catalysts.

6.2.2   Volumetric gas adsorption measurements

Selective chemisorption measurements were conducted to determine the dispersion of each sample. An automated volumetric physisorption/chemisorption

analyzer (Quantachrome 1C) with *in-situ* pretreatment capabilities was utilized.

Catalysts were reduced with 50 cc (STP) H_2 min^{-1} at 673 K for 75 min after activation in

50 cc (STP) He min^{-1} at 473 K for 1h. Prior to chemisorption measurements, catalyst

samples were evacuated for 1h at 623 K and cooled to room temperature under vacuum.

H_2, CO and H_2-O_2 isotherms were collected on the same sample (*ca*. 300 mg). After the

initial reduction, catalysts were subsequently reduced with 50 cc (STP) H_2 min^{-1} at 673 K

for 30 min. Adsorption uptakes extrapolated to zero pressure (monolayer uptake) were

used to calculate metal dispersion (D). Spherical particle sizes were calculated from

dispersion measurements, d(nm) = 1.13/D, assuming a Pt atom density of 1.27×10^{19} m^{-2}

[21].

Co-adsorption experiments of CO and C_2H_4 were conducted at 298 and 403 K on

catalyst samples pretreated as previously described. Adsorption experiments were

sequential; CO adsorption followed by C_2H_4 adsorption and vice versa. After

pretreatment, total and reversible isotherms of one adsorbate with an interim 1 h

evacuation between isotherms were collected. After a 1 h evacuation following the

reversible isotherm of the first adsorbate, dual isotherms were measured for the second

adsorbate. Experiments at 298 and 403 K were conducted on the same sample (*ca*. 300

mg); the 298 K experiment followed by the 403 K. Samples were subjected to ½ h

oxidation at 573 K before beginning the 403 K isotherm set.

6.2.3 *Infrared measurements of CO and C_2H_4 adsorption*

In-situ diffuse reflectance infrared Fourier transform spectroscopy (DRIFTS),

using a Nicolet Nexus 670 spectrometer equipped with a Thermo Spectra-Tech controlled

atmosphere-diffuse reflection cell was used to study the adsorption of CO and C_2H_4 on

various silica supported Pt catalysts. A Pt/SiO$_2$ catalyst (*ca.* 50 mg for amorphous SiO$_2$, *ca.* 10 mg for SBA-15 samples) was loaded in the diffuse reflectance cell and given a pretreatment identical to those used for chemisorption and catalytic studies using a gas handling manifold equipped with mass flow controllers (Porter Instruments Company) and connected to the diffuse reflectance cell. He (99.999%, Praxair), 10% H$_2$/He (99.999% both gases, Praxair), CO (99.9%, Airgas) and C$_2$H$_4$ (99.9%, Praxair) were used without further purification. A single beam spectrum (128 scans, 2 cm^{-1} resolution) of the freshly reduced catalyst was obtained at 300 K under 30 cc (STP) He min^{-1} and used as the background for subtraction of silica features for all samples in the presence and absence of gas-phase CO and/or ethylene at 300 K. The sample was then exposed to a 30 cc (STP) min^{-1} flowing mixture of 10% CO/He or 10% C$_2$H$_4$/He for 30 min at 300 K, followed by purging in 30 cc (STP) He min^{-1} at 300 K. Spectra taken at temperatures above ambient were collected fifteen minutes after achieving the target temperature. Gas phase spectrum of CO and ethylene were taken in the DRIFTS cell using a Au mirror.

6.3   Results

6.3.1   Catalyst Characterization.

A brief summary of the characterization results for the ~3% Pt catalysts is given. Total surface area of the Pt loaded SBA-15 catalysts varied from 523-661 m^2 g^{-1} with a pore diameter of ~ 90 Å and pore volume of ~ 1.5 cc (STP) g^{-1} as determined from BET measurements. Long range order of the SBA-15 matrix was assessed by small angle x-ray scattering (SAXS). Three peaks assignable to (100), (110) and (200) of the hexagonal mesostructure with *p6mm* symmetry are observed in the pristine (no Pt

loading) SBA-15; confirming the SBA-15 was ordered, but to lower degree than SBA-15 synthesized under acidic conditions.

Metal particle sizes were determined by transmission electron microscopy (TEM), x-ray diffraction (XRD) and selective gas adsorption. Table 1 is a compilation of adsorption uptakes of H_2, CO and O_2, as well as the titration of O_{ad} by H_2 (Pt_s-O + 3/2H_2 $\rightarrow$ Pt_s-H + H_2O) [22]. Dispersion and particle size values based on H_2-O_2 total uptakes are included in Table 1. Three characteristic peaks for Pt appear in the XRD spectra at $2\theta = 45.9°$, $54.0°$, and $80.1°$ corresponding to (111), (200), and (220) reflections of the Pt fcc lattice. Line-broadening XRD techniques used to calculate Pt particle sizes from the full width at half maximum (FWHM) of the Pt(111) reflection are in good agreement with chemisorption measurements. Table 1 demonstrates that the particle size determined by chemisorption are always larger than TEM or XRD particle size which is believed to be due to the influence of residual PVP on the particle surface or the inclusion of a small fraction of nanoparticles in silica capsules during the hydrothermal synthesis of SBA-15 [9].

The H_T:CO_{Irr} ratio was greater than unity, as expected assuming a 2:1 adsorbate stoichiometry per surface platinum (Pt_s), but in the intermediate particle size range (2-4 nm), this ratio was between unity and ~ 1.3, while all other particles size have ratios close to ~1.75. Assuming the number of surface atoms, Pt_s counted by H_2-O_2 titration is the most accurate of the dispersion measurements by chemisorption, the ratio, CO_{Irr}:Pt_s were calculated. These ratios ranged from 0.6 to 1.5, yielding an average stoichiometry of ~1, consistent with atop adsorption of carbon monoxide. It was determined with infrared spectroscopy that carbon monoxide adsorbs on SBA-15 at room temperature and desorbs

Table 6.1. Adsorption uptake and particle size determined by chemisorption, TEM and XRD techniques.

Catalyst[a,b]	Probe gas uptakes[c] (μmol g^{-1})					Dispersion, D	Particle size, d(nm)		
	H$_2$	CO		O$_2$	H$_2$-O$_2$	H$_2$-O$_{2,total}$	chemisorption[d]		XRD[e]
	Total	Total	Irrev	Irrev	Total		H$_2$	H$_2$-O$_2$	
3.2% Pt/SiO$_2$-IE	133.1	166.7	152.2	24.2	262.0	1[f]	1	1	--
6.3% Pt/SiO$_2$ (EUROPT-1)	151.2	182.0	175.0	94.6	334.0	0.69	1.2	1.6	1.8[f]
2% Pt/Al$_2$O$_3$-Exxon	43.5	80.6	70.1	17.4	66.1	0.43	1.3	2.6	3.4
2.33% Pt(1.7 nm)/SBA-15	29.8	66.1	59.6	21.9	94.9	0.53	2.3	2.1	1.7
2.69% Pt(2.9 nm)/SBA-15	21.0	39.5	34.9	15.4	76.2	0.37	3.7	3.1	2.9
2.62% Pt(3.6 nm)/SBA-15	16.6	32.8	30.7	12.9	51.9	0.26	4.6	4.4	3.7
2.86% Pt(7.1 nm)/SBA-15	9.4	14.7	11.7	12.2	28.4	0.13	8.8	8.7	7.3
UHP Pt powder	16.7	15.1	13.7	8.6	30.3	0.004	173.5	286.5	>100

[a]Actual metal loading determined by ICP.

[b]Number average particle size. Determined by counting a minimum of 200 freestanding particles.

[c]Conducted at 295 K.

[d]determined by $1.13/(Pt_s/Pt_T)$.

[e]Based on the Scherrer-Debye equation after subtracting SBA-15 baseline.

[f]Ref. [19].
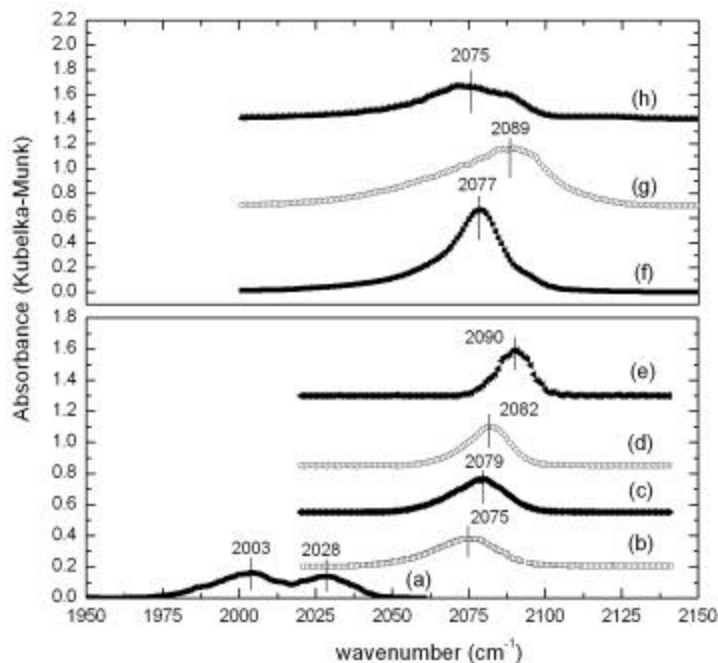
Figure 6.1. Diffuse reflectance infrared spectra of CO adsorbed at 300 K on Pt(X)/SBA-15; (a) SBA-15 support, (b) X = 1.7 nm, (c) X = 2.9 nm, (d) X = 3.6 nm, (e) X = 7.1 nm particles, (f) 3.2 % Pt/SiO$_2$, (g) 6.3 % Pt/SiO$_2$ (EUROPT-1) and (h) 2 % Pt/Al$_2$O$_3$. The peak position for the Pt/SBA-15 series decreases with increasing Pt dispersion, an outcome of the changing surface atom coordination of the bonding surface atoms.

slowly under vacuum or He purge. Peaks at ~2003 and 2028 cm^{-1} are associated with CO

adsorbed to SBA-15 (Figure 1a). Both peaks lose significant intensity upon heating and

at a temperature >353 K, both bands disappear. These peaks are significantly red-shifted

relative to bands at 2158 and 2140 cm^{-1} associated with CO hydrogen bonded to SiOH$^{\delta+}$

at low temperatures [23]. No reports of CO stretching frequencies reduced by this

amount on silica could be found in the literature and the analysis and origin of these

bands will be published separately [24]. Adsorption of CO on ultrapure SBA-15 [25]

produced the same bands observed on a standard preparation method for SBA-15 and

therefore the adsorption of CO is not attributed to transition metal contamination.

6.3.2 Volumetric adsorption and IR spectroscopy of CO and C_2H_4 adsorption on clean Pt/SBA-15

The volumetric adsorption uptakes of CO and C_2H_4 on clean Pt surfaces are compiled in Table 2. Carbon monoxide adsorption at room temperature on clean Pt surfaces is used as a measure of the Pt surface area because the adsorption stoichiometry is well known; $CO:Pt_s = 1$, as demonstrated in the preceding section. The fraction of bridge and 3-fold hollow bonded CO is small on clean Pt surfaces near saturation coverage. Both total and irreversible CO uptakes decreased at 403 K while the amount of reversibly adsorbed CO was similar at both adsorption temperatures. Comparison of irreversible uptakes at the two temperatures demonstrated that chemisorption decreased by 20-35 % on the Pt/SiO_2 catalysts, 20% on Pt powder and ~ 50 % on the Pt/Al_2O_3 catalyst at 403 K. There is no evidence for CO dissociation even at highest pressures used in this study, contrary to recent work on Pt single crystals [26, 27].

The infrared spectroscopy of carbon monoxide adsorbed to solid surfaces has long been used as a qualitative probe of surface structure; the peak position is especially sensitive to the coordination environment of bonding surface atoms and interaction with other adsorbates [28]. Figure 1 are stacked diffuse reflectance infrared spectra (1900-2100 cm^{-1}) of CO adsorbed on a series of SBA-15 supported Pt catalysts. Peaks at 2003 and 2028 cm^{-1} are identified as CO associated with SBA-15, which are completely removed after heating to 353 K even in a CO atmosphere. Spectra (b)-(e) are CO adsorbed on the Pt/SBA-15 catalyst series at room temperature after subtraction of the CO-SBA-15 interaction. Atop CO is the only surface CO species identified on all samples; bridge bonded CO was not detected. Spectra (f)-(h) demonstrate atop CO was

Table 6.2. Sequential co-adsorption uptakes of carbon monoxide and ethylene on supported Pt catalysts at 298 and 403 K

Catalyst	Uptake on clean Pt surface[a,b]							
	CO at 298 K		CO at 403 K		C_2H_4 at 298 K		C_2H_4 at 403 K	
	Total	Irreversible	Total	Irreversible	Total	Irreversible	Total	Irreversible
2% Pt/Al$_2$O$_3$ (Exxon)	80.6	70.1	44.6	34.5	30.5	16.0	29.2	24.6
3.2% Pt/SiO$_2$-IE	166.7	152.2	138.5	110.3	57.0	51.0	74.1	67.0
2.33% Pt(1.7 nm)/SBA-15	66.1	59.6	52.4	46.5	25.5	22.9	40.1	29.4
2.69% Pt(2.9 nm)/SBA-15	39.5	34.9	32.6	26.1	14.4	11.9	22.5	16.4
2.62% Pt(3.6 nm)/SBA-15	32.8	30.7	27.6	19.8	13.1	10.1	17.6	12.9
2.86% Pt(7.1 nm)/SBA-15	14.7	11.7	9.5	7.9	6.9	4.9	7.5	5.6
UHP Pt powder	14.2	12.8	12.9	10.2	3.6	2.9	5.0	4.2
	CO uptake on "C_2H_4 covered" Pt surface[a,b]				C_2H_4 uptake on "CO-covered" surface[a,b]			
	CO at 298 K		CO at 403 K		C_2H_4 at 298 K		C_2H_4 at 403 K	
	Total	Irreversible	Total	Irreversible	Total	Irreversible	Total	Irreversible
2% Pt/Al$_2$O$_3$ (Exxon)	17.2	12.1	32.6	22.1	18.7	0.4	12.4	5.5
3.2% Pt/SiO$_2$-IE	78.9	72.4	98.5	67.5	4.8	0.0	16.5	3.4
2.33% Pt(1.7 nm)/SBA-15	32.8	29.5	39.3	29.2	1.9	0.1	9.2	1.7
2.69% Pt(2.9 nm)/SBA-15	17.4	13.2	21.5	14.1	1.6	0.2	5.0	1.1
2.62% Pt(3.6 nm)/SBA-15	14.1	11.4	19.1	10.9	1.1	0.0	3.7	0.6
2.86% Pt(7.1 nm)/SBA-15	5.1	3.1	7.8	2.4	0.5	0.0	1.7	0.3
UHP Pt powder	8.5	7.9	7.2	4.8	0.2	0.07	1.4	0.4

[a]Uptakes extrapolated to zero pressure (monolayer uptake).
[b]Uptakes in μmol g^{-1}.

the only adsorbed species on the atomically dispersed 3.2% Pt/SiO$_2$, while the CO peak

position on the alumina support was blue-shifted by 10 cm^{-1} compared with a Pt/SiO$_2$

catalyst with a similar particle size. Figure 2 is the influence of temperature on the band

position of linear adsorbed CO for a 2.69 % Pt(2.9 nm)/SBA-15 catalyst; the inset of
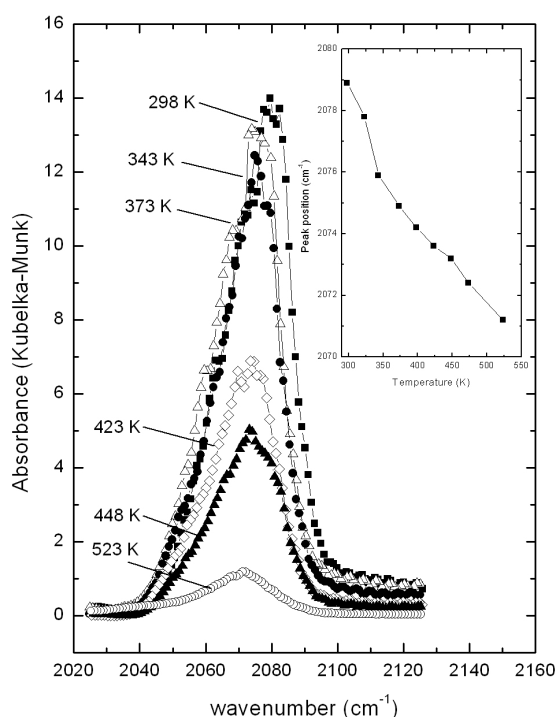
Figure 6.2. Temperature dependence of linear CO band position for 2.69% Pt(2.9 nm)/SBA-15. Inset is the linear bound CO peak position as a function of temperature. The decrease in frequency is due to anharmonic coupling of the C-O stretch and the frustrated parallel translational mode of adsorbed carbon monoxide. Significantly larger changes in CO frequency with temperature have been attributed to adsorbate induced surface reconstruction and roughening.

shows the influence of temperature on the peak position for atop bonded CO. The

decrease in frequency with temperature is due to vibrational dephasing due to anharmonic

coupling between the CO stretch and frustrated translational motion parallel to the

surface. This phenomenon has been observed on single crystals [29-31] and predicted

theoretically. If it is assumed that the intensity of the IR band is proportional to the

amount of CO species on the surface and the IR extinction coefficient is independent of

the adsorption temperature, the relative coverage is obtained by the ratio of the IR band

intensity at a temperature to the band intensity for CO adsorption after exposure to 76

Torr CO at room temperature [32-34]. Using this approach, the coverage of CO at 403 K

is estimated to be ~0.7 (Figure 3), and only above ~380 K does the coverage of CO begin

to decrease.
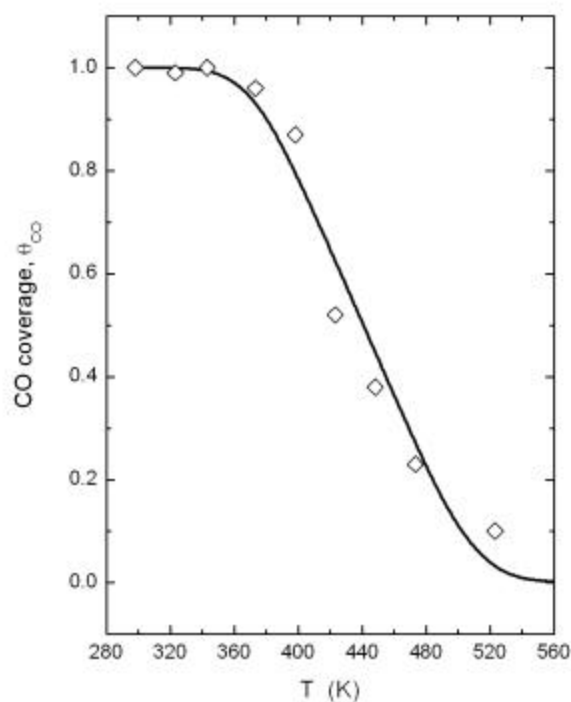
Figure 6.3. Temperature dependence of CO coverage on the 2.69% Pt(2.9 nm)/SBA-15 catalyst. The integrated intensity of the atop CO band was used to calculate relative coverages. Solid line represent fit of Temkin adsorption model assuming heats of adsorption of 40 kcal mol^{-1} ($\theta = 0$, initial) and 30 kcal mol^{-1} ($\theta = 1$, saturation). The raw data indicates CO desorption begins at ~380 K for adsorbed CO in equilibrium with the gas phase.

The volumetric (or gravimetric) adsorption of ethylene on supported Pt catalysts

has been studied to a lesser extent [35]. The adsorption of ethylene is complex yielding

multiple surface species with different coordination to the surface. In Table 2, at the

adsorption temperatures (298 K and 403 K) in the absence of H_2, most of the adsorbed ethylene is assumed converted to ethylidyne. The strong intermolecular repulsion between adjacent ethylidyne limits the coverage on Pt surfaces to ~¼ ML [36]. Total and irreversible uptakes are greater at 403 K than 298 K for all samples (except the total adsorption on Pt/Al_2O_3). The increased total adsorption is split between irreversible and reversible adsorption for most catalysts. Comparison of the amount of ethylene adsorption per mole of surface Pt (Pt_s) as determined by H_2-O_2 titration (Table 1), the C_2H_4:Pt_s adsorption stoichiometries are all < 1 and increase with temperature. The ratio, Pt_s:C_2H_4 is an indication of the average number of free sites available to convert each adsorbed C_2H_4 to ethylidyne. These ratios are particle size and temperature dependent; generally increasing with particle size and temperature. The Pt_s:C_2H_4 ratios are listed in Table 3. At 298 K, ~2-7 sites are available for adsorption and decomposition of ethylene with the number of atoms increasing with particle size. The available number of sites decreases to 2-5 at 403 K.

Infrared studies of ethylene adsorption on supported Pt catalysts have been performed in an attempt to determine the type and concentration of ethylene derived intermediates [6]. The influence of particle size on ethylene adsorption and decomposition has been investigated in this study. Only two studies examining the influence of particle size on ethylene surface chemistry have been found by the authors; the influence of particle size on the heat of adsorption of ethylene and the preferential formation of ethylidyne on larger particles [35]. Figure 4 is a stack spectrum of ethylene adsorbed on Pt catalysts at 298 K. No stable IR active surface species were identified on pure SBA-15 silica upon ethylene adsorption, but π-bonded, di-σ bonded and ethylidyne

Table 6.3. Available surface Pt (Pt_s)-C_2H_4 stoichiometry determined for a clean and CO covered Pt surface

Catalyst	Pt_s:C_2H_4 stoichiometry at 298 K[a]		Pt_s:C_2H_4 stoichiometry at 403 K[a]	
	Clean surface	"CO covered" surface[b]	Clean surface	"CO covered" surface[b]
2% Pt/Al$_2$O$_3$ (Exxon)	2.8	[c]	1.8	2
3.2% Pt/SiO$_2$-IE	3.2	--	2.4	16
2.33% Pt(1.7 nm)/SBA-15	2.8	37	2.2	10
2.69% Pt(2.9 nm)/SBA-15	4.3	81	3.1	23
2.62% Pt(3.6 nm)/SBA-15	3.5	--	2.7	25
2.86% Pt(7.1 nm)/SBA-15	3.9	--	3.4	37
UHP Pt powder	7.1	110	4.9	26

[a]Surface platinum based on total H_2-O_2 titration at 298 K.
[b]Corrected for surface atoms covered by CO (CO:Pt_s = 1) at either 298 or 403 K.
[c]Irreversible CO adsorption greater than Pt_s determined by total H_2-O_2 titration.
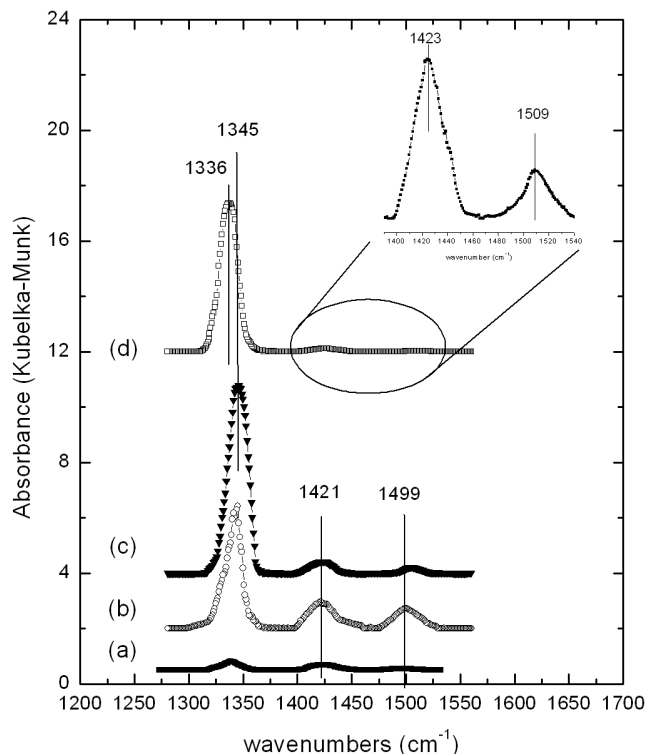
Figure 6.4. Diffuse reflectance infrared spectra of C_2H_4 adsorbed at 300 K on Pt(X)/SBA-15; (a) 1.7 nm, (b) 2.9 nm, (c) 3.6 nm, (d) 7.1 nm particles. Ethylidyne, π-bonded ethylene and di-σ bonded ethylene are the three surface species identified on all Pt surfaces.

were identified on all Pt nanoparticles. The ratio of surface species present was dependent upon particle size, on small particles ($\leq$ 2 nm) the amount of ethylidyne was comparable to π-bonded ethylene and very little ethylene in the di-σ form was identified. The infrared spectrum of the larger particles ($\geq$ 2.5 nm) were dominated by a stretch at ~ 1340 cm^{-1} which are assigned to the symmetric deformation ($\delta_s(CH_3)$) of the CH_3 group of adsorbed ethylidyne. Table 4 summarizes observed modes for adsorbed π-, di-σ bonded ethylene, ethylidyne as well as other C_2 species on supported Pt catalysts and various Pt single crystals, respectively. From Figure 4, it is evident that the support plays little role in bonding of ethylene to Pt nanoparticles. All spectra have a small peak at

Table 6.4. Assignment of vibrational bands upon adsorption of ethylene on supported Pt catalysts and Pt single crystals
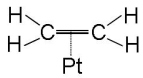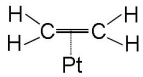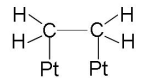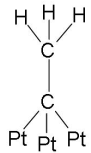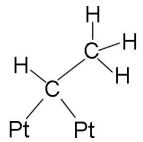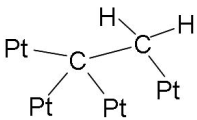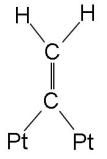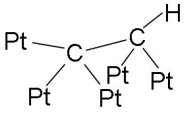
Surface species and structure	Surface	Wavenumber (cm^{-1}) and intensities	Temperature range (K)
π-bonded C_2H_4	Pt(210), Pt(110)-(1 × 1), Pt(110)-(2 × 1), Pt/SiO$_2$, Pt/Al$_2$O$_3$	3080-3020 (m), 1530-1500 (w), 1200 (mw), 950 (s)	≤ 100- 300
physisorbed π-bonded C_2H_4	H/Pt(110)	3060-3040 (m), 1620 (w), 1360 (m), 960 (s)	*ca.* 100
di-σ bonded ethylene	All Pt surfaces and supported Pt catalysts	*ca.* 2940 (ms), *ca.* 1420 (m), 1040/980 (s), 460 (s)	≤ 100- 300
Ethylidyne	Pt(111), Pt(100)-(5 × 20), supported catalysts	*ca.* 2890 (ms), *ca.* 1340 (s), *ca.* 1130 (s), *ca.* 450 (m)	≤ 100-450
Ethylidene	Pt(111)	2960 (s), 1390 (m), 1040 (w), 480 (s)	≤ 100- 300
Ethylylidyne	Pt(210), Pt(110)	*ca.* 2940 (s), 1420 (ms), *ca.* 980 (ms), *ca.* 470 (m)	290-350

Table 6.4. cont'd. Assignment of vibrational bands upon adsorption of ethylene on supported Pt catalysts and Pt single crystals

Surface species and structure		Surface	Wavenumber (cm^{-1}) and intensities	Temperature range (K)
Vinylidene		Pt(100)-(1 × 1)	*ca.* 2940 (m), 1585 (m), *ca.* 1040 (m), 440 (m)	270-350
Ethynyl		Pt(110)-(2 × 1)	*ca.* 3050 (mw), *ca.* 860 (s)	450-500
C≡C	--	Pt(110), Pt(210)	*ca.* 2200 (m)	> 600

1420 cm^{-1} due to the symmetric deformation (δ_s(CH$_2$)) of the methylene groups of di-σ bonded ethylene and a peak at 1500 cm^{-1} which is ascribed to the ν(C=C) and δ(CH$_2$) normal modes of π-bonded ethylene [37]. Peaks in the C-H region for all three species have been previously observed on Pt surfaces were not identified in this study because residual PVP peaks in the C-H stretching most likely obscure detection of these bands. The moderately weak C=C stretch in ethylidyne has been identified at 1126 cm^{-1} on Pt(111) [38], but it is not detectable on SBA-15 catalysts due to strong SiO$_2$ absorption bands obscuring this region. Upon introduction of 5 Torr H$_2$ to the evacuated DRIFTS cell at room temperature; all ethylene derived surface species are removed from the surface. Upon adsorption of C$_2$H$_4$ at 403 K (infrared spectrum not shown but very similar to Figure 4), ethylidyne is the only observed spectral feature. It is postulated that on a clean Pt surface at 403 K, π-bonded ethylene has desorbed or converted to di-σ ethylene which subsequently converts to ethylidyne, which may begin to decompose to carbon and hydrogen even though it is stable up to 450 K in vacuum [39].

6.3.3   Volumetric adsorption and IR spectroscopy of CO and C$_2$H$_4$ sequential co-adsorption on clean Pt/SBA-15

The sequential uptakes of C$_2$H$_4$ and CO on the Pt/SBA-15 catalysts and Pt powder are compiled in Table 2. Pt catalysts initially exposed to ethylene are referred to as C$_2$H$_4$ covered surfaces; due to the fact that adsorption of ethylene is primarily converted to ethylidyne on clean Pt surfaces. Examples of sequential CO and C$_2$H$_4$ adsorption isotherms at 298 and 403 K are given in Figure 5. Chemisorption of carbon monoxide on an ethylene covered surface results in substantial decrease in CO adsorption capacity. For example, irreversible CO uptake decreased ~63 and 46 % at 298 and 403 K upon
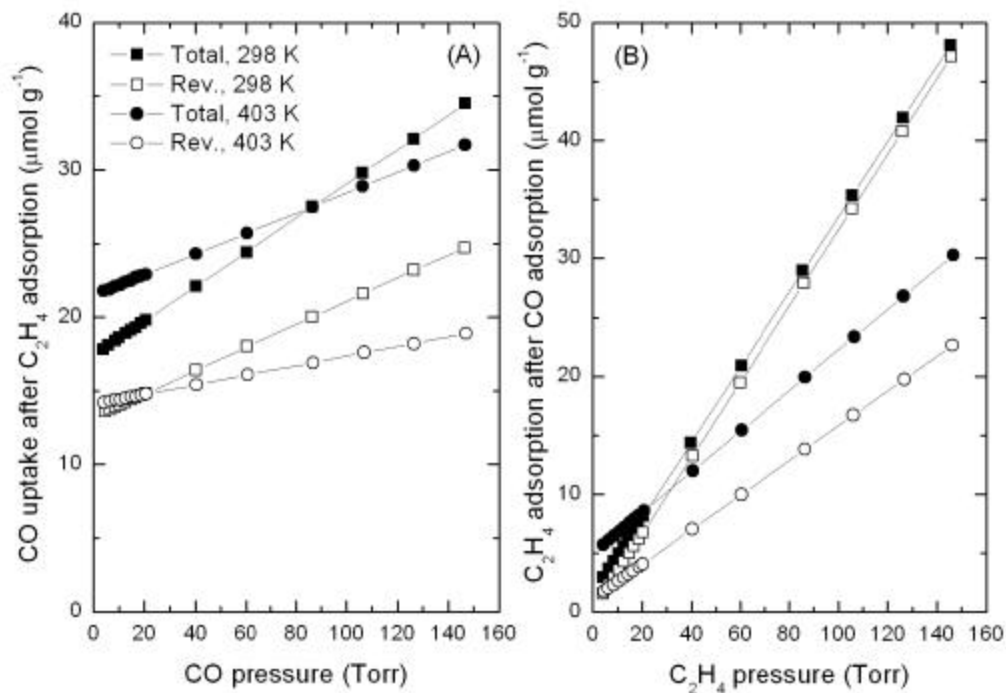
Figure 6.5. Sequential CO and C_2H_4 adsorption experiments on 2.69 % Pt(2.9 nm)/SBA-15. (A) CO adsorption on C_2H_4 covered surface at 298 and 403 K. (B) C_2H_4 adsorption on CO covered surface at 298 K and 403 K. C_2H_4 adsorption on a CO covered surface is significantly reduced relative to adsorption on a clean surface due to the formation of a dense unit cell under high coverage CO conditions, while CO is able to adsorb on an ethylidyne pre-covered surface due to its more open unit cell capable of accommodating at least one single CO per cell.

adsorption on a C_2H_4 covered surface for the 2.69% Pt(2.9 nm)/SBA-15 catalyst. On the

2.86% Pt(7.1 nm)/SBA-15, CO adsorption was reduced by 73 and 70% at 298 K and 403

K, respectively. The amount of reversibly adsorbed CO varied little on the ethylidyne

covered surface regardless of temperature. The presence of ethylidyne adlayer at either

adsorption temperature decreases the number of sites directly by adsorbing in a 3:1

Pt:CCH_3 ratio. Strong repulsive forces between adsorbed ethylidyne most likely lead to

empty sites around 3-fold hollow sites which allow CO to bond. Reversing the

adsorption sequence, it is evident that carbon monoxide is much more effective at

excluding C_2H_4 from the surface. There is no irreversible C_2H_4 adsorption on a CO

covered 2.69 % Pt(2.9 nm)/SBA-15 at 298 K, most likely due to the inability of ethylene to form ethylidyne because of the lack of threefold hollow sites which have been effectively diluted by adsorbed CO. At 403 K, preadsorbed CO reduces the adsorption of ethylene by ~ 92 %. In a similar fashion, if the adsorption uptakes are used to estimate the Pt_s:C_2H_4 ratio as done for the clean Pt surfaces, the number of Pt atoms available for bonding of a single C_2H_4 molecule after correcting for CO adsorption on atop sites (Pt_s-CO) vary from 40-80 sites at 298 K , while a surface temperature of 403 K available 10-40 sites for ethylene adsorption on a CO saturated surface. Assuming 0.68 ML coverage at 403 K, the number of sites available for ethylene bonding (in parentheses) increases as the particle size increases; 1.7 nm (35), 2.9 nm (105), 3.6 nm (160) and 7.1 nm (640).

The sequential co-adsorption of CO and C_2H_4 has been investigated at 298 and 403 K with diffuse reflectance infrared spectroscopy on a 2.69 % Pt(2.9 nm)/SBA-15 sample. Figure 6a is the vibrational spectra of Pt/SBA-15 catalysts after removal of ethylene from the gas phase by a He purge 298 K. The observed vibrational bands are assigned to π-bonded ethylene (1499 cm^{-1}), di-σ bonded ethylene (1421 cm^{-1}) and ethylidyne (1345 cm^{-1}). These vibrational assignments are in agreement with ethylene adsorption on clean Pt surface (see Table 4). Figure 6b is the influence of CO on the vibrational features of ethylene derived adsorbates after the He purge at 298 K. The band at ~1500 cm^{-1} attributed to π-bonded ethylene has lost significant intensity and the amount of di-σ bonded ethylene has also decreased. Also appearing in the spectrum is a band at 2050 cm^{-1} for adsorbed linear carbon monoxide, which is redshifted compared to a clean Pt surface (see Figure 1c). Upon heating to 403 K under a He purge, the ethylidyne band is slightly reduced in intensity and slightly blue-shifted to 1345 cm^{-1}
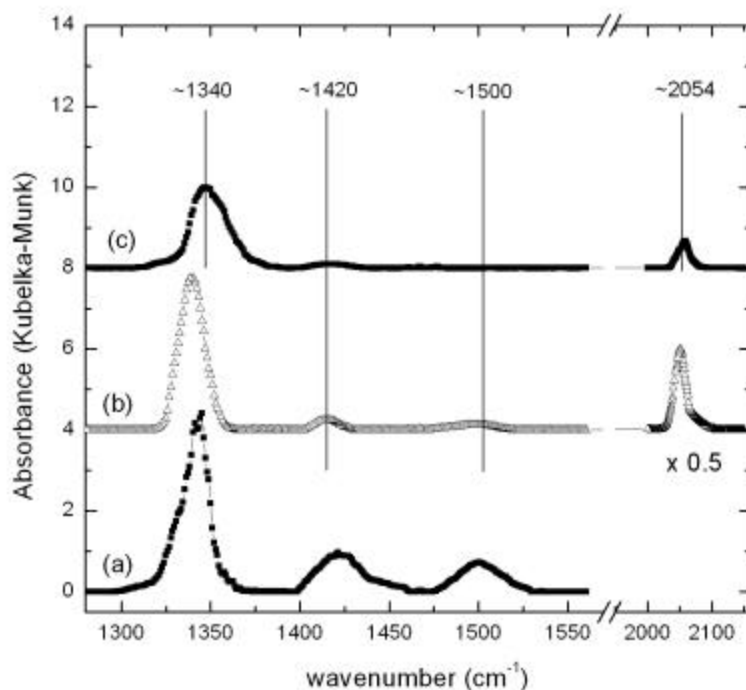
Figure 6.6. Diffuse reflectance infrared spectra of (a) adsorbed C_2H_4 on clean Pt surface after He purging, (b) Pt surface with co-adsorbed CO and C_2H_3 after He purge at 298 K, and (c) Pt surface with co-adsorbed CO and C_2H_3 after He purge at 403 K. Adsorption of CO at 298 K leads to elimination of π- and di-σ bonded ethylene. All adsorption experiments were conducted on a 2.69 % Pt(2.9 nm)/SBA-15 catalyst.

(Figure 6c). The most interesting observation is the very asymmetric lineshape of the methyl deformation mode of ethylidyne, which is usually very narrow on single crystal surfaces [40]. Minimal changes in the vibrational spectrum observed upon heating (compare 6b and c) are in agreement with ethylidyne formation near room temperature and stable up to 450 K on Pt. Additional heating to 500 K led to a decrease in the ethylidyne and CO vibrational bands due to decomposition and desorption, respectively.

6.4. Discussion

6.4.1 Catalyst Characterization

Catalysts were characterized by a number of physical techniques including TEM, XRD and SAXS [41]. Electron microscopy verified that Pt nanoparticles were incorporated into the SBA-15 mesostructure during synthesis, while XRD and SAXS confirmed the bulk Pt particle size and SBA-15 structural ordering, respectively. The primary means of chemical characterization were selective chemisorption measurements and infrared investigations of CO adsorption on Pt/SBA-15 catalysts. Table 1 demonstrates the particle sizes measured by chemisorption are in good agreement with those determined from TEM and XRD. Dispersion values determined by total H_2-O_2 titration uptake (at P = 0) range from 13 to 53 % on the SBA-15 series catalysts. Total H_2 and H_2-O_2 uptakes on the 3.2% Pt/SiO_2-IE were significantly higher than the assumed stoichiometry in either H_2 chemisorption or H_2-O_2 titration at room temperature causing dispersion values greater than 100% (d(nm) < 1) to be measured; suggesting that the Pt is atomically dispersed on the ion exchanged catalyst. Boudart has suggested that it would be extremely difficult for truly atomically dispersed Pt to dissociate H_2 [42]; particles were not observed by TEM or XRD. The Pt/Al_2O_3 catalyst had a dispersion of 43 % by H_2-O_2 titration which yields a Pt particle size of 2.6 nm. Adsorption values on a UHP Pt powder led to calculated particle sizes of ~285 nm. The particle size determined for the EUROPT-1 sample is in good agreement with previously published results [15-20].

6.4.2   Carbon monoxide adsorption on clean Pt surfaces

Carbon monoxide is an ideal probe of heterogeneous adsorption kinetics and dynamics because of its sensitivity to the local environment, *i.e.* underlying metal structure and neighboring adsorbates [43]. Carbon monoxide adsorbed on transition metal nanoparticles is complex due to extensive charge transfer between adsorbed CO molecules and surface, strong intermolecular adsorbate interactions (attractive and

repulsive) and structure (*i.e.* coordination number) specific CO interactions with the underlying metal surface. There is no evidence for carbon monoxide dissociation under the experimental conditions used in this study. Somorjai and co-workers have shown that CO dissociates on close packed surfaces of Pt at high temperatures and pressures (≥ 40 Torr) due to induced surface roughening, while Masel and co-workers have shown that high density stepped surfaces are capable of dissociating CO [44, 45].

Influence of temperature on CO adsorption

The influence of temperature on the peak position of atop bound CO is shown in the inset of Figure 2. The CO stretching frequency redshifts by only 9 cm^{-1} with increasing temperature (298–523 K) on the 2.69% Pt(2.9 nm)/SBA-15 catalyst. The change in CO frequency with increasing temperature is small compared to changes in frequency due to coverage effects [46]. For example, the change in peak position for atop on Pt(110) was 29 cm^{-1} [47], while values as high as 42 cm^{-1} have been reported for coverages ranging from 0.13 to unity. These large changes are often more substantial than changes in CO stretching frequency with surface structure. In the case of CO frequency change with temperature, it is associated with vibrational phase relaxation (dephasing contribution) caused by anharmonic coupling of the C-O stretch with lower frequency Pt-CO modes, which increase with temperature causing a decrease in the peak position for atop CO [29, 30]. The specific low frequency Pt-CO mode has been identified as the frustrated parallel translational mode [29]. The change in CO frequency with temperature ($\sim$30-220 K) was only $\sim$ 6 cm^{-1} on a Ni(111) surface [29]. In contrast to the rather modest changes in frequency with temperature reported above, large changes in CO frequency are observed on Pt single crystals of (111), (100) and (557) orientation at high CO pressures [48]. For example, on Pt(100), the atop CO frequency decreased by

35 cm^{-1} from 300–500 K. In addition, to vibrational phase relaxation, surface roughening (and therefore changing surface atom coordination which the CO molecules are bound to) contributed to the redshift in CO frequency.

Beyond coupling of high and low frequency modes, CO begins to desorb as the temperature is increased. From temperature dependent infrared data, the integrated area under the curve is proportional to the number of adsorbed CO molecules. Assuming that the surface was saturated under room temperature conditions, the corresponding change in the CO integrated area can be used to calculate the relative coverage. The outcome of this calculation is shown in Figure 3. The solid fit line to the data is a Temkin adsorption model assuming an initial heat of adsorption, $\Delta H_{ads}(\theta = 0)$ of 40 kcal mol^{-1} and a ΔH_{ads} at saturation of 30 kcal mol^{-1}. Previous work on close packed Pt single crystal surfaces have shown that CO adsorption isotherms can be described by the Temkin model [5]. As discussed below, these thermodynamic values are on the higher end of experimentally reported values, but adequately fit the data and demonstrate CO desorption from a 2.9 nm particle surface does not begin until ~380 K. An initial differential heat of adsorption of CO at 403 K has been measured on a 0.85% Pt/SiO$_2$ catalyst as 33 kcal mol^{-1}, which decreases to ~9.5 kcal mol^{-1} at saturation coverage [49]. CO saturates the Pt particle surface at a coverage of 0.68 ML on Pt(111) as determined by STM [50, 51] and a ΔH_{ads} of 10 kcal mol^{-1} has been determined by laser induced thermal desorption (LITD) [52] at these conditions.

Influence of Pt particle size on CO adsorption

The influence of Pt single crystal structure on CO adsorption has been studied extensively, while a relatively few number of studies have examined the influence of particle size on CO adsorption. The heat of adsorption of CO is dependent on the

supported Pt crystallite size with smaller particles showing slightly higher heats of adsorption [53]. The reported heats of adsorption from temperature programmed desorption studies of CO at low coverages was dependent upon Pt surface structure and varied from 28 kcal mol^{-1} for Pt(110)-(2 × 1) surface to 34 kcal mol^{-1} for the Pt(210) surface. The heats of adsorption from the three most stable surfaces of Pt (i.e. (100), (111), and (110)) were 27-29 kcal mol^{-1}, respectively. This suggests that the heat of adsorption doesn't vary significantly as a function of surface structure but does demonstrate that CO should bind to defect sites before terrace atoms. In fact, it has been shown that CO molecules adsorb at step edges first to form a 1D chain, only after which the step is saturated will CO molecules adsorb to terrace sites beginning with those adjacent to the step edge [54]. The adsorption sequence, step than terrace atoms was shown to be dominate on Pt(211) [55] but not on Pt(311) [56] suggesting that the CO-surface interaction is not controlled by thermodynamics alone.

The CO stretching frequency is sensitive to the surface structure and serves as a probe of the local environment around the adsorption site. The primary observations from both single crystal and nanoparticle surfaces is the CO stretching frequency for the atop species decreases relative to the gas phase frequency (2140 cm^{-1}) due to changes in surface atom coordination. Figure 7 demonstrates that the frequency for the atop band redshifts by ~15 cm^{-1}. Kappers and van der Maas [57] found a linear correlation between the Pt coordination number and the position of the atop CO frequency for a series of Pt
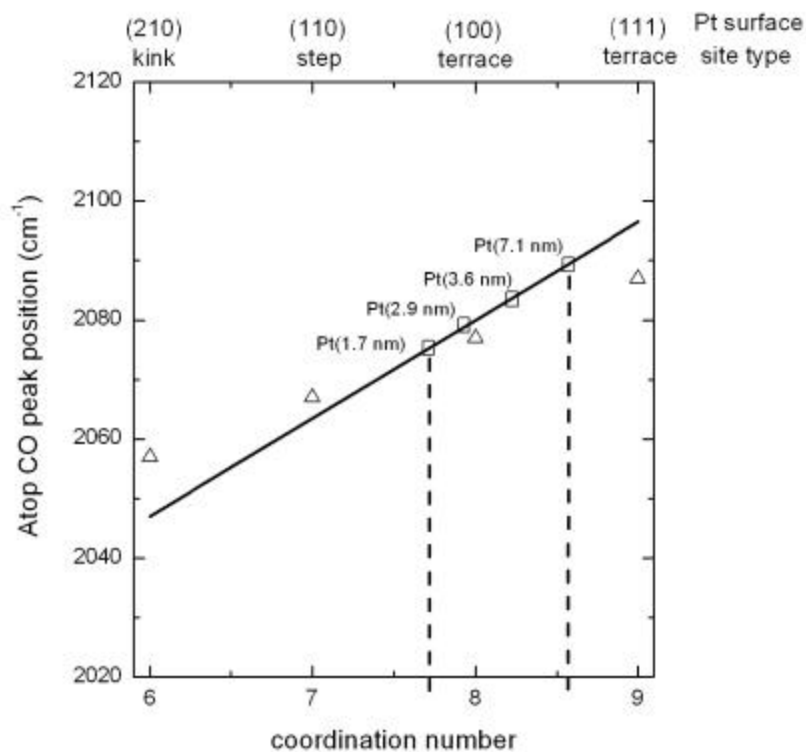
Figure 6.7. Influence of Pt coordination number on the peak position of atop CO. Linear trendline represent best fit to data from [57]. Triangles are singleton CO frequencies as a function Pt atom coordination from [58]. The Pt surface structure and site type is given as an example of entity with the corresponding coordination number. Fitting the data from the Pt/SBA-15 series, the average coordination number is 7 – 9 indicating adsorption on defect and terrace sites.

supported catalysts with varying particle sizes. Figure 7 demonstrates that if their data is

plotted (as the solid line in Figure 7) and the SBA-15 catalyst data forced to fit this line,

the change in coordination number of the atoms bonding CO is < 1 in this case. In both

cases, the CO coverage used to determine the line in Figure 7 is not known, and the

influence of dipole-dipole coupling between neighboring adsorbates may lead to

frequency positions which are not due to coordination effects only. At low coverages,

conditions in which co-adsorbed CO molecules do not interact (so-called singletons) [58],

the peak position for atop CO as a function of surface coordination number is given by

the open triangles (Figure 7). This line intersects the data of Kappers and van der Maas

[57] suggesting on smaller particles adsorbate-adsorbate interactions led to a redshift of the CO frequency, while on larger particles (> 3 nm), these same interactions cause the CO frequency to blueshift. A few other systematic studies of the influence of particle size on CO adsorption are known. Cant and Donaldson [59] have shown a minor influence of particle size on the position of the atop CO vibration for two Pt/SiO_2 catalysts with particle sizes determined by chemisorption of 1.8 and 18 nm; the band position for the 1.8 nm was redshifted by 6 cm^{-1} relative to the 18 nm Pt particle silica catalyst (2078 cm^{-1}). Bischoff and co-workers [60] have studied the effect of particle size on CO adsorption for Pt dispersed within a neutralized faujasite zeolite; a clear particle size dependent shift of the atop adsorbed CO stretching vibration was observed due to the narrow Pt particle size distribution. At room temperature, the absorption of the atop CO stretching frequency was at ~2050 cm^{-1} for 1-2 nm particles and ~2100 cm^{-1} for 4-5 nm particles. Clearly, work on single crystals [48, 61] and supported catalysts [59, 60] suggest that the position of the atop CO vibration redshifts with increasing surface roughness and decreasing particle size. The stretching frequency of a single CO molecule on a Pt_{10} cluster as determined by DFT calculations is 2050 cm^{-1} [62], while a single CO stretching vibrational frequency of 2020 cm^{-1} was reported for gas-phase CO saturated neutral $Pt_3(CO)_6$ clusters [63]. Vibrational frequencies for atop CO have been reported at 2000 cm^{-1} for $Pt(CO)_2$-type surface species [64] and frequencies as bw as 1990 cm^{-1} have been reported for CO molecules adsorbed on step sites of 6-8 Pt atom clusters inside zeolite L channels [65]. The shift is related to greater degree of backbonding from the 5d orbital of the Pt atom into the $2\pi^*$ orbital of CO; the greater the degree of charge transfer from the surface to the molecule than molecule to surface, the weaker the C-O bond becomes. The molecular orbital picture of CO bounding to

transition metal surfaces was proposed by Blyholder [8] and has been confirmed by density functional methods [62, 66-68] (see Appendix A). The work presented here is in agreement with previous studies and suggests that the strength of π back donation of the CO chemisorption bond is stronger on a small particle with a larger fraction of low coordination metal sites relative to a single crystal or platinum particle with a large fraction of high coordination surface sites [64]. This is in accord with the Blyholder model, the more unsaturated sites will have the lowest CO frequencies because highly coordinated metal atoms with their low electron density minimizes the backbonding into the π^* orbital of CO. Pt-carbonyl cluster studies have shown that the strength of π backbonding of the CO chemisorption bond to a small particle is stronger than to a surface [64].

One interesting observation is all CO spectra on the Pt/SBA-15 catalysts consist of a single resonance although some have a small shoulder to the red of the maximum (Figure 1). Previous experimental and modeling work on small Pt crystallites has produced complex CO spectra with multiple peaks, indicative of CO bonding to surface atoms with different coordination and complex phase interactions between neighboring adsorbates. For example, four CO species have been identified during the low temperature adsorption of CO on a stepped Pt single crystal (Pt(211)); bridge and atop adsorption on terrace sites as well as bridge and atop adsorption on step sites [69]. The situation is potentially more complex on a Pt nanoparticle due to the high probability that there may be a larger number of different types of surface sites capable of adsorbing CO. Infrared spectra of CO adsorbed on 39 Å particles were much more complex than spectra of 11 Å particles. Based on low coverage experimental studies and a coupled harmonic

oscillator model [70], CO vibrations at 2070, 2080 and 2090 cm^{-1} are due CO located at edges, terrace of (100) atoms and terrace of (111) atoms, respectively.

6.4.3 Ethylene adsorption on clean Pt catalysts: Influence of particle size

The proposed surface species on Pt surfaces after ethylene exposure (dependent upon surface temperature and dose) are π-bonded ethylene where the carbons are still sp^2 hybridized, di-σ bounded ethylene where the carbons of ethylene are now sp^3 hydridized and ethylidyne, a very stable dehydrogenated species. Due to its stability under UHV conditions, the surface chemistry of ethylidyne has been studied by a number surface science techniques including sum frequency generation (SFG), reflection absorption infrared spectroscopy (RAIRS), high resolution electron energy loss spectroscopy (HREELS), x-ray and ultraviolet photoelectron spectroscopy (XPS/UPS) and temperature programmed desorption (TPD). While most of these studies have been performed on Pt(111), the surface chemistry of ethylene has been studied on other Pt single crystals [6]. A brief summary of the results reported on single crystals is given and compared with results obtained in this and other studies on supported Pt catalysts. Table 4 demonstrates the infrared allowed bands of the three primary ethylene derived surface species; π-bonded and di-σ bonded ethylene as well as ethylidyne and other species which have been identified on Pt surfaces during ethylene decomposition.

Ethylene adsorbs molecularly on Pt(111) at low temperatures ($\leq$ 200 K) forming up to three species: π-, di-σ or physisorbed ethylene. In the π-bonded mode, it is believed from comparison with organometallic complexes, ethylene sits with it CC bond parallel to the surface bound to an atop site. The heat of adsorption of π-bonded ethylene on clean Pt(111) was measured as 9.6 kcal mol^{-1} [71]. Coadsorption of Bi atoms and

ethylene suggest that ensemble size of four atoms is necessary for ethylene adsorption on Pt(111) [72]. Di-σ ethylene bonds to the surface with its CC bond parallel to the surface through the formation of two metal-carbon bonds bridging two metal atoms. The type of ethylene bound species is dependent upon metal surface and temperature. Stuve and Madix [73] have introduced the πσ parameter, which is a measure of the degree of π- to di-σ character. It has been shown on Pt(111), di-σ ethylene is favored and has a corresponding πσ parameter of 0.92, while for Pd(100), the same parameter has a value of 0.37, favoring π-bonded ethylene and an intermediate value (0.78) suggests both modes are present on the Pd(100) surface [74]. The di-σ bonded ethylene dehydrogenates to form an intermediate with C_3 symmetry. The intermediate was first proposed to be ethylidene [75], but later was shown to be ethylidyne, which binds with its CC axis perpendicular to the surface. LEED studies have shown that ethylidyne species adsorb in fcc 3-fold hollow sites on a Pt(111) surface [76] and is stable up to 430-450 K. Above these temperatures, ethylidyne decomposes either to CH_x fragment or adsorbed carbon and hydrogen atoms and forms carbon particles of up to ~30-40 atoms [39].

The adsorption of ethylene has been studied extensively on Pt(111) surfaces, less so on other crystallographic faces of Pt. A study of the influence of surface structure has been undertaken by Masel and coworkers [77-83]. The activation energy for desorption of ethylene (θ = 0.1-0.25) from Pt surfaces with varying step atom density varied from 12-19 kcal mol^{-1}, although there was no correlation between these two parameters. A correlation between step atom density and self-hydrogenation was found, and correlated with the concentration of π-bonded ethylene on step sites. Surfaces with intermediate step atom densities converted ethylene to methane under UHV conditions [77]. The TPD

and HREELS work from Masel and co-workers has shown that although the thermodynamics of ethylene decomposition are similar on most Pt surfaces, the mechanism of ethylene decomposition on platinum is controlled by the symmetry of the surface. It was believed that ethylidyne would not form on surface lacking three-fold symmetry, but this has proven not to be the case [79].

The (1×1) Pt(110) [80] and (2×1) Pt(110) [81] surface was very active for carbon-carbon bond scission and coke formation. On the (1×1) Pt(110) surface, π-bonded ethylene forms at 93 K. This is contrary to previous results on Pt(111), (5×20) Pt(100) (pseudo-hexagonal) or (1×1) Pt(100) surfaces where di-σ bonded ethylene was identified at the same conditions, but in agreement with theory which predicts that (1×1) Pt(110) has one of the highest orbital availabilities for the formation of π-bound ethylene [82, 83]. The π-bonded form is converted to di-σ ethylene upon heating to 220 K and at 300 K; ethane and methane are detected. No formation of ethylidyne has been observed on (1×1) Pt(100) [80], rather a vinylidene intermediate has been proposed. Ethylidyne formation has been observed by HREELS on (2×1) Pt(110), and it is proposed to form in the valleys of the (2×1) structure by a mechanism identical to one proposed for Pt(111) [84]. By 400 K, H_2 TPD and HREELS spectra are complex and suggest a mixture of C_2 species, denoted as $[-C\equiv C-]_x$ accumulate on the surface with adsorbed atomic carbon. These species have also been observed on the (2×1) Pt(110) surface [81].

The formation and stability of π-bonded ethylene was the greatest on Pt(210) [83]. The π-bonded species is thought to be extremely stable on Pt(210) because it is a highly stepped surface enabling π-bonded ethylene to form on top of step sites, while di-σ formation is sterically hindered on this surface. Pt(210) has a $\pi\sigma$ parameter of 0.48

similar to Zeise's salt [85, 86], while Pt(111) is 0.92, the smaller number suggestive of more π-bonding character. The π-bonded species are stable up to 300 K on Pt(210), in contrast with the (1 × 1) Pt(110) surface where its intensity is attenuated after annealing to 160 K while the infrared bands associated with π-bonded ethylene are attenuated on (2 × 1) Pt(110) by 100 K. No ethylidyne has been observed on the Pt(210) upon heating due to lack of space and the highly strained nature of a CCH_3 species on this surface; there is not enough space for ethylidyne to stand up over the fcc 3-fold hollow site because the opposing step gets in the way. Rather, the authors suggest that an ethan-1-yl-2-ylidyne ($\eta^4 \equiv CCH_2$-) species forms. This species has been proposed to form on (1 × 1) Pt(110) and (2 × 1) Pt(110) during the decomposition of ethylene; Pt(210) and the (1 × 1) Pt(110) have a similar step geometry. This same species is thought to bond to three step atoms and one terrace atom on the reconstructed (1 × 2) Pt(311) surface [87].

Fewer studies on the influence of particle size on the formation and stability of ethylene derived species. In this study, ethylidyne forms upon adsorption on all particles, as do π-bonded and di-σ bonded ethylene, but in different proportions depending on crystallite size. Very little ethylidyne was formed on the 1.7 nm crystallites, while its formation on 3.6 and 7.1 nm crystallites was substantially larger. Both di-σ and π-bonded ethylene were found in high concentration on the 2.9 nm surface. Over a series of Pt/Al_2O_3 catalysts with varying dispersion, ethylidyne was favored relative to π-bonded ethylene as particle size increases, suggesting that coordinatively unsaturated sites are primarily responsible for the formation of π-bonded ethylene [88, 89] in agreement with the stability of π-bonded ethylene on step edges of Pt(210) [80]. Similar results were shown by vibrational coupling of adsorbed $^{13}C_2H_4$/$^{12}C_2H_4$ that ethylidyne is

produced on (111) facets of small Pt particles (d = 10-40 Å, ave. 20 Å) rather than on random trimer Pt sites [90]. No ethylidyne was detected on highly dispersed Pt particles ($d \leq$ 10 Å). Beebe and Yates [91] have even suggested that because ethylidyne doesn't form on surfaces lacking 3-fold symmetry, ethylidyne because of its site specificity can be used to determine the fraction of the (111) oriented surfaces. Ethylene adsorption at 300 K led to the formation of ethylidyne on Pt crystallites of 2.2 nm, which were thought to consist primarily of (111) facets with a small fraction of (100) surfaces [92]. The stability of the π-bonded ethylene on Pt catalysts prepared by chloride impregnation was greater than that found by Masel and coworkers on Pt(210) and with Pt/SiO_2 catalysts [93]. Passos and Vannice [35] found that the initial heat of adsorption at 300 K was 10 kcal mol^{-1} higher on large (~20 nm) Pt particles as compared with small Pt particles (~ 1 nm); the higher heat of adsorption on large crystals is attributed to the exothermic dehydrogenation of ethylene to ethylidyne [94]. These surface reactions are not probed by UHV temperature programmed measurements of ethylene desorption on Pt single crystal surfaces because desorption only measures reversibly adsorbed molecular C_2H_4. Correction of reported TPD data for the enthalpy of reaction for the dehydrogenation of ethylene to ethylidyne yields ethylene heat of adsorption values on Pt single crystals which are similar to values measured on large (= 4 nm) Pt crystallites [90, 94].

It is clear from our spectroscopic data that the fraction of π-bonded ethylene is vastly higher on the 1.7 nm Pt, and decreases sharply going to 7.1 nm Pt, which is well faceted. The increased surface abundance of π-bonded ethylene on small particle surfaces is consistent with the idea that these surfaces are rough. The surface of the 1.7 nm Pt particles have higher ratio of corner and edge surface atoms, which stabilize the π-

bonded ethylene, presumably in the same manner as Pt(210) step edges. [Just like the abundance of ethylidyne is a measure of the ratio of surface Pt(111) on a particle, the abundance of π-bonded ethylene seems to be a measure of corner and edge sites.

6.4.4   Coadsorption of carbon monoxide and ethylene on Pt catalysts.

Volumetric and infrared adsorption measurements of CO and C_2H_4 demonstrate that both adsorbates are influenced by the presence of the other. The results demonstrate that CO is an effective site blocker, while preadsorbed ethylidyne modifies the surface to a significant extent which is manifested in a large redshift in the atop CO peak relative to adsorption on a CO surface. This suggests significant interaction between CO and C_2H_3 directly or one mediated through the metal surface.

Numerous studies of the co-adsorption of CO and organics have been conducted on various metals in the surface science literature [95-100]. These studies are often conducted at low temperatures and UHV conditions, so the surface is not in equilibrium with the gas phase. Under these conditions, H atoms are formed on the surface quickly recombine and desorb as H_2 leaving the surface depleted of hydrogen. Carbon monoxide and hydrogen co-adsorption has been studied extensively [101-105] but not considered here due to the low H coverage under the experimental conditions of this study. These studies of ethylene and carbon monoxide co-adsorption demonstrate ordered structures are formed on the surface with most interactions cooperative because the structure are mixed. Co-adsorption of carbon monoxide and ethylene on single crystal surfaces have shown that CO stabilizes ethylidyne [106, 107] and even induce its formation on surfaces lacking 3-fold symmetry [99]. The adsorption of ethylene on clean Rh(100) led to the formation of "hydrocarbon fragments" while the preadsorption of 0.5 ML of CO led to the exclusive formation of ethylidyne [99]. The stability of ethylidyne to decomposition

is 50 K higher on a CO covered Ir(111) versus a clean surface, which the authors suggest is related to the strong interactions between the CO and C_2H_3 dipoles [106]. A similar increase was observed on Ru(001) [107]. C_xH_y fragments from ethylidyne decomposition were also more stable in the presence of adsorbed CO which suggests that CO inhibits C-C bond cleavage by a mechanism in which CO blocks highly reactive decomposition sites and a repulsive CO-C_2D_x interaction which reduces the M-C_2D_x binding strength [108]. These observations suggest that carbon monoxide may play a more complicated role in catalysis than merely site blocking but may also influence the binding strength of other surface species (reactants and intermediates) such that it is no longer optimal. Co-adsorption studies of ethylene and CO or NO on Rh(111) demonstrate that the small inorganic molecules adsorb on their favored sites, while ethylidyne is left to adsorb on less favored sites, which supports the thermal desorption behavior of carbon monoxide on mixed adsorbate surfaces; CO desorption from an ethylidyne covered was unchanged relative to CO adsorbed on the same clean surface [106-108]. However, it is difficult to explain the increased stability of ethylidyne if it is displaced from favored adsorption sites but the proposed mechanism for ethylidyne decomposition suggest that up to 6 atoms [72] are needed and the statistically probability of six vacant atoms coalescing near an adsorbed ethylidyne molecule is small.

An interesting result of sequential co-adsorption studies is the order in which CO and ethylene are adsorbed and the resulting interaction between them. Table 3 demonstrates that the adsorption of C_2H_4 is affected to a greater extent on a CO covered surface than CO is affected by preadsorbed ethylene. The interaction between co-adsorbates can be discussed in terms of three potentially competing effects [98]. They are (1) static dipole interactions (the Stark effect), (2) charge transfer processes mediated

through the surface or (3) a direction chemical interaction. CO is ideal probe molecule to understand the strength of the C-O bond (and therefore the CO stretching frequency) because they are sensitive to the chemical environment. In the case of dipole-dipole coupling through the Stark effect, this interaction between coadsorbed CO and C_2H_4 can be excluded since no vibrational modes of the two adsorbates are close in frequency [109, 110]. Conversely, Somorjai and coworkers have suggested that the magnitude of the CO frequency change, $\Delta(v(CO))$ on C_2H_3/Rh(111) versus CO/Rh(111) indicates a Stark effect [98].

A recent study by Tang *et al.* [95] using high pressure scanning tunneling microscopy (STM) suggests that the adsorbate structures formed by co-adsorption of mTorr pressures of CO and C_2H_4 at room temperature on Pt(111) is complex. When in equilibrium with the gas phase, a static densely packed mixed adsorbate overlayer of CO and ethylidyne form. The lack of adsorbate mobility on the surface suggested a surface sterically crowded. Regions of densely packed pure CO producing a unit cell of large dimensions ($\left(\sqrt{19} \times \sqrt{19}\right)R23.4° - 13CO$) (Figure 8b) [95] was formed, and upon addition of C_2H_4, the same overlayer structure in which C_2H_3 replaces CO in 3-fold fcc hollow sites (Figure 8d). The authors contend it is unlikely that ethylidyne replaces CO molecules while maintaining the same large unit ordered structures, suggesting that regimes of pure and mixed adlayers coexist but cannot be differentiated by STM. Sum frequency generation (SFG) surface vibrational spectroscopy studies of CO adsorption on an ethylidyne covered Pt(111) surface suggests that two different atop CO species exist, supporting the presence of a pure and mixed adsorbate overlayers [111]. A UHV study of the adsorption of carbon monoxide on an ethylidyne covered a Pd(111) surface has
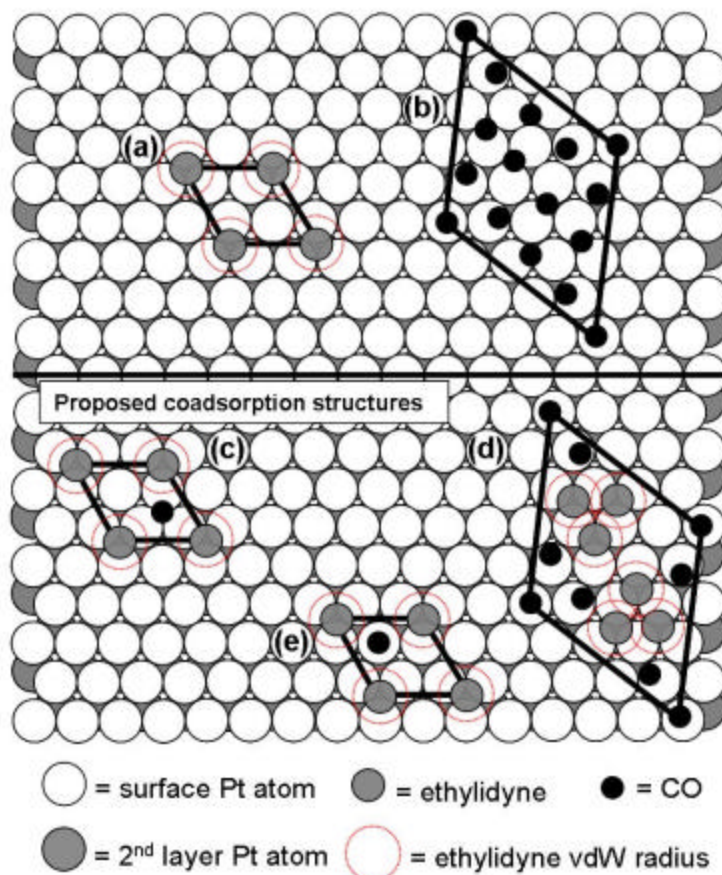
Figure 6.8. Proposed adsorption structure for (a) ethylidyne on clean Pt(111), (b) high coverage CO on clean Pt(111), (c) coadsorbed CO-C_2H_3 on Pd(111), (d) coadsorbed CO-C_2H_3 on Pt(111) and (d) variant of (c) adsorption structure on Pt(111). The van der Waals radius of ethylidyne is ~2 Å. The p(2 × 2) structure of ethylidyne is capable of accommodating a single atop CO molecule per unit cell (Fig. 8d), while the high CO coverage unit is dense and ethylene adsorption most likely requires CO desorption.

shown that the coverage of CO is 0.25 ML compared with 0.55 ML upon adsorption on

clean Pd(111) [112]; which is contrast to a vinylidene covered ($\theta = 1$) Pd(111) surface

where no CO is irreversibly adsorbed even up to 10 Torr CO [113]. No change in CO

coverage with pressure (10^{-2} – 5 Torr) was observed upon adsorption on the ethylidyne

covered surface and the initial sticking coefficient (S_0) decreased by ~25% on the

ethylidyne covered surface. A much simpler unit cell has been proposed by Tysoe *et al*.

compared with Somorjai *et al*. for the adsorption of CO on a C_2H_3 covered surface. In

both cases, the surfaces are prepared with a saturated coverage of ethylidyne. The ethylidyne unit cell on Pd(111) under ultra-high conditions consists of the well-known p(2 × 2) (Figure 8a) with CO adsorbed in a hexagonal close packed (hcp) hollow site (Figure 8c). The authors suggest that due to steric hindrance of the ethylidyne methyl group (van der Waals radius of ~2 Å [114]) on the remaining fcc hollow sites in the unit cell, CO adsorbs to the hcp hollow site. A structure of this type leads to an ethylidyne coverage of 0.25 and since there is one CO molecule per ethylidyne unit cell, its coverage is also 0.25. Within the $\left(\sqrt{19} \times \sqrt{19}\right)R23.4°$ unit cell, the ethylidyne coverage actually increases from 0.22 ML to 0.31 ML upon CO adsorption [95]. The structure of both mixed unit cells are shown in Figure 8 and a modified version of the Pd unit cell which accounts for CO adsorption primarily occurring on atop sites on Pt surfaces. Figure 8 demonstrates that the ethylidyne-ethylidyne interactions in the $\left(\sqrt{19} \times \sqrt{19}\right)R23.4°$ unit cell should be strongly repulsive due to their overlapping van der Waal radii. In this regard, a mixed unit cell like Figure 8e is preferred with areas of pure adsorbate overlayers. The unit cell proposed by Somorjai *et al*. may actually prevail at high pressure conditions to the high flux encountered by the surface and the ability of highly compressed adsorption structures to form under high pressure.

The coadsorption of ethylene and CO on Pt(111) and Pt/SiO$_2$ have been compared and the influence of CO on ethylidyne has been studied. On both the supported catalyst and the single crystal, di-σ and π-bonded ethylene are displaced by low pressures (10^{-5} Torr) of CO, which binds predominantly to atop sites; while ethylidyne is partially displaced on Pt(111), but remains on the Pt/SiO$_2$ catalyst. These authors also noted a significant redshift of 40 cm^{-1} for the CO band when coadsorbed with a saturation

coverage of ethylidyne and a corresponding blueshift of 9 cm^{-1} for the $\delta_s(CH_3)$ of ethylidyne. This implies that ethylidyne donates electron density to the adsorbed carbon monoxide mediated through the metal surface [115].

The adsorption of CO onto an C_2H_4 covered surfaces led to an adsorption capacity reduced by ~50% and large changes in the CO vibrational spectrum; the linear bound CO is located at ~2079 cm^{-1} on a clean surface which is redshifted to 2050 cm^{-1} on a saturated ethylidyne surface. If CO is adsorbed initially, the adsorption capacity of C_2H_4 is reduced by almost 100 % and very small changes in the CO spectrum are identified (not shown). Upon the addition of C_2H_4 to a CO covered surface, adsorption is totally reversible and the CO frequency redshifts by ~ 4 cm^{-1}. A study of sequential adsorption of CO and then ethylene on film thins showed olefins easily displace CO from nickel and cobalt, but not on platinum or rhodium. The linear CO frequency shifted by 5 cm^{-1} with ethylene addition, while for the Rh catalyst, a redshift of 20-30 cm^{-1} was observed relative to CO adsorption on a clean Rh surface. The different behavior observed when sequential adsorption is reversed can be explained by the uptake of the second adsorbate on the precovered surface. In the case of CO adsorption followed by C_2H_4, it is evident that ethylene inclusion on the surface is essentially prohibited and therefore the adsorbates do not interact on the surface. The high coverage CO structure has 13 CO molecules per unit cell on Pt(111) [95], while ethylene adsorption, isomerization to ethylidene and decomposition to ethylidyne on 3-fold hollow sites within the $\left(\sqrt{19} \times \sqrt{19}\right)R23.4°$ unit cell would greatly increase the total energy of the unit cell. Inclusion of the van der waals radius of the methyl group of ethylidyne, it is apparent that the high coverage CO unit cell is too crowded to allow ethylene adsorption and

conversion to ethylidyne. In fact, the formation of π-bonded ethylene may be inhibited entirely, or conversely it maybe stabilized if it is supported on an atop site on the CO unit cell. Unfortunately, infrared experiments in this study were performed simultaneously, that is CO and ethylene were exposed to a clean Pt surface at the same time, rather than CO adsorption on an ethylidyne covered surface. The ability for CO to adsorb on an ethylene covered surface may be related to sterics rather than adsorption affinity. Figure 8a demonstrates that the within the p(2 $\times$ 2) structure, one carbon monoxide molecule is free to bind in the 2 $\times$ 2 structure at either a hcp 3-fold hollow site or an atop site. Even though, the repulsion between ethylidyne and CO is greater when CO is adsorbed to an atop site, this unit cell (Figure 8e) is preferred over the unit cell with CO in the hcp hollow site (Figure 8b). CO is located between 3-fold and bridge sites as a result of delicate balance between substrate-adsorbate and adsorbate-adsorbate interactions. The structure actually rotates over a range of pressure. The incommensuration is one main argument why ethylidyne substitution at the off-bridge/off-3-fold site is unlikely in the coadsorption scenario.

The conversion of ethylene to ethylidyne doesn't demonstrate strict first order kinetics over a large range of C_2H_4 coverage. For C_2H_4 coverage greater than ~20% of saturation, two distinct regimes of "first-order" kinetics are observed. The transition between the kinetic regimes (defined by a critical time, t_{crit}) is dependent upon surface temperature and C_2H_4 coverage. At 17% of saturation coverage, ethylene decomposition to ethylidyne demonstrates only one regime of first order kinetics. Conversely, at 27% and above of ethylene saturation, the kinetics demonstrate two first order regimes. These regimes have similar temperature dependences (~ 18 kcal mol^{-1}), but the kinetics which are distinguished as slow and fast differ because of changes in the preexponential factor.

This change in kinetics is associated with a decrease in ethylene coverage and an increase in the number of atoms in free ensembles because upon the conversion of ethylene (di-σ type, bonded parallel to the surface) to ethylidyne (C-C bond axis perpendicular to the surface), a free surface of 6.3 $\AA^2$ in gained (based on van der Waals radii). This increase in vacant sites catalyzes the decomposition of ethylene to ethylidyne through a η^2-$CHCH_2$ (di-σ adsorbed vinyl) intermediate whose coverage is ~4% of a monolayer (The intermediate was not observed spectroscopically but proposed based on work by Koel and Carter [94]). The second significant finding from this work, which is in agreement with previous STM work from the same group, is the spatially non-uniform nature of ethylene adsorption and decomposition. It appears from STM measurements and Monte Carlo simulations, the reaction proceeds in patches due to adsorbed ethylene islanding and free ensemble effects. Monte Carlo simulations assuming ethylene molecules surrounded by four ethylidyne molecules enable sufficient free sites for ethylene conversion to ethylidyne predicted two "first order" kinetic regimes in agreement with experimental results [116].

6.4.5 Comparison of CO and C_2H_4 coadsorption on Pt nanoparticle catalyst with organometallic complexes containing both adsorbates.

The similarity between adsorbate bonding on metal surfaces and the bonding of ligands to organometallic metal centers have many similarities [117]. In the fact, the identification of ethylidyne on Pt surfaces was confirmed by comparison with an ethylidyne nonacarbonyl tricobalt complex [118]. To draw analogies between single molecule organometallic complexes and adsorbate species, we examine some relevant examples. Ethylene and carbon monoxide are ubiquitous ligands in platinum organometallic chemistry. The bonding of these ligands occurs through two interactions:

i) a filled ligand orbital participates as a σ-donor to an empty metal orbital and ii) donation of electron density from a metal d-orbital to empty π^* ligand orbitals to form M-L π-bonds. The oxidation state of platinum and the surrounding ligand set influence the metal-ligand bonding. The complex tris(ethylene)platinum(0) has been isolated, which consist of three co-planar side-on ethylene ligands [119, 120]. The C-C stretch (IR: 1501 cm^{-1}; Raman: 1617 cm^{-1}) indicates a weakened bond relative to gaseous ethylene (Raman: 1630 cm^{-1}) [121]. The Pt-C_2H_4 bonding is analogous to π-bonded ethylene on surfaces, where a single ethylene molecule binds to a single Pt surface atom. This model is in contrast to the di-sigma bonded ethylene in which each carbon atom is sp^3 hybridized, and the adsorbate bound to two surface Pt atoms. HREELS data of ethylene on Pt(111) exhibits ν_{C-C} = 1230 cm^{-1} indicating a di-sigma bonding mode [75]. The homoleptic platinum carbonyl $Pt(CO)_4$ is unstable and has not been isolated [122]; however it has been detected by condensation of Pt(0) atoms with CO in an Argon matrix at 10K [123]. Vibrational spectroscopic data indicated tetrahedral $Pt(CO)_4$ molecules (IR: ν_{CO} = 2048 cm^{-1} , 2055(sh) cm^{-1} ; Raman: ν_{CO} = 2049 cm^{-1} , 2119(w) cm^{-1}). Pt(0) carbonyl complexes can be isolated, however, as seen in the tris(carbene)pincer complex, [(CO)Pt{=C(Ph$_2$P=NCOSiMe$_3$)$_2$] [124]. The planar Fischer carbene ligand set saturates the π-acceptor capability at carbon, resulting in a mostly σ-donor tridentate ligand. The ν_{CO} data (2038 cm^{-1}) indicates significant metal-ligand bonding due to back-donation from the electron rich Pt(0). A number of platinum carbonyl clusters have been isolated. Positively charged clusters, might be expected to form weak bonds to CO due to reduced ability to back-donate electrons to the ligand. The $Pt(CO)_4^{2+}$ cation was isolated and vibrational spectroscopic data was obtained (IR: ν_{CO} = 2231 cm^{-1} , 2235(sh) cm^{-1} ;

Raman: ν_{CO} = 2257 cm^{-1} , 2281 cm^{-1}) [125]. The frequency of ν_{CO} exceeds that of gaseous CO (2243 cm^{-1}), indicating negligible π-backdonation from the Pt^{2+}. The homoleptic, cationic Pt-carbonyl Pt$_2$(CO)$_6^{2+}$ which contains Pt(I) was recently reported. The vibrational spectroscopic data IR: ν_{CO} = 2174 cm^{-1}, 2187 cm^{-1}, 2218 cm^{-1} ; Raman: ν_{CO} = 2173 cm^{-1}, 2194 cm^{-1} , 2209 cm^{-1}, 2219 cm^{-1}, 2233 cm^{-1}) indicates weak π-backdonation [126]. Negatively charged platinum carbonyl clusters have stronger metal-ligand bonding than the neutral and cationic counterparts due to the increased availability of electrons for π-backdonation. The cluster [Pt$_3$(CO)$_6$]$_n^{2-}$ (n = 1) can be formed by reductive carbonylation in strongly reducing conditions, while higher nuclearity (n = 2 – 10) clusters are formed under less reducing conditions, or assembly of Pt$_3$(CO)$_6^{2-}$ with the use of oxidizing agents [127]. Vibrational spectroscopic data indicates a progression of blue-shifting ν_{CO} with increasing nuclearity of the [Pt$_3$(CO)$_6$]$_n^{2-}$ clusters (IR, n=1: ν_{CO} = 1740 cm^{-1}, 1945 cm^{-1}; n = 6: ν_{CO} = 1840 cm^{-1}, 1855 cm^{-1}, 1875 cm^{-1}, 1900 cm^{-1}, 2065 cm^{-1}), consistent with the decreasing anionic charge density of the larger clusters.

Competition studies between cyclic alkenes and CO as a ligand on a Pt(II) complex indicate that bonding to CO is thermodynamically favored by about 30 kJ mol^{-1} [128]. IR data indicates red-shift of the ν_{CO} (2178 cm^{-1} and 2136 cm^{-1} in Cl$_2$Pt(CO)$_2$ to 2124/2117 cm^{-1} in Cl$_2$Pt(CO)(olefin); olefin = 1-octene/cyclohexene) upon substitution of CO with olefin. To date there are no known platinum alkylidyne molecules that have been isolated. Platinum alkylidene molecules are known; perhaps isolation of Pt-alkylidynes is likely in the future. Alkylidyne bonding to a metal can be regarded as analogous to metal-CO bonding, where rather than an empty π* orbital (CO) as an acceptor, the carbyne possess two lower lying carbon 2p orbitals having π symmetry with

respect to the metal, with one electron. On Pt surfaces exposed to ethylene, ethylidyne is formed in abundance.

6.5   Summary

The adsorption of carbon monoxide and ethylene as well as their sequential adsorption was studied over a series of Pt/SBA-15 catalysts with monodisperse particle sizes ranging from 1.7 – 7 nm. Volumetric adsorption of the two molecules demonstrated both species existed on the surface regardless of the order of adsorption but in substantially reduced amounts relative to adsorption on a clean surface. Ethylene was more sensitive to the presence of adsorbed carbon monoxide due to the rather dense unit cell CO forms at high coverages, while the adsorption of ethylene on a clean metal surface leads to ethylidyne formation with an open unit cell capable of accommodating CO molecules. Infrared investigations demonstrate that π-bonded, di-σ bonded ethylene and small amounts of ethylidyne form on small Pt crystallites ($\leq$ 2 nm), with the ratio of ethylidyne to π-bonded ethylene close to unity. On larger particles, ethylidyne was the dominant surface species. This suggests that the large ensemble of crystallographically identical surface atoms which terminate large particles are required for ethylidyne formation and stabilization. This stabilization is most likely due to the presence of 3-fold hollow sites. Adsorption of ethylene on a CO covered surface led to a substantial decrease in ethylene uptake and the only observable surface species were atop CO, whose position was slightly redshifted relative to CO adsorption on a clean Pt surface and ethylidyne whose position was slightly blue-shifted relative to the clean surface frequency. The weak perturbation of CO surface chemistry by adsorbed ethylene is due to the minor adsorption of hydrocarbon leading to a surface dominated by CO-CO and

CO-Pt interactions. Conversely, large changes in the CO stretching frequency were observed when CO was adsorbed on an ethylene covered surface. At 298 K, the CO adsorption capacity decreased by half the amount adsorbed on a clean surface and the peak position for the linear bond CO red-shifted considerably, suggesting donation of electron density from adsorbed ethylidyne to carbon monoxide most likely mediated through the metal substrate. The influence of surface defects (particularly surface atom coordination) is emphasized with regard to intermolecular interactions between like and different adsorbates. The interaction between adsorbed CO and C_2H_4 is dependent upon the metal surface structure due to structure sensitive changes in adsorbate surface chemistry for both carbon monoxide and ethylene on clean metal surfaces.

6.6   Appendix A. Bonding of CO to Pt surfaces – a molecular orbital description

The arrangement of atoms in the Pt crystal is described as an fcc lattice, or as an ABCABC layer by layer structure (cubic close packed). Any bulk Pt atom has 12 neighbors, and has D_{3d} symmetry. Using group theory, the metal d-orbitals can be assigned to symmetry adapted irreducible representations. The metal group orbitals are shown.
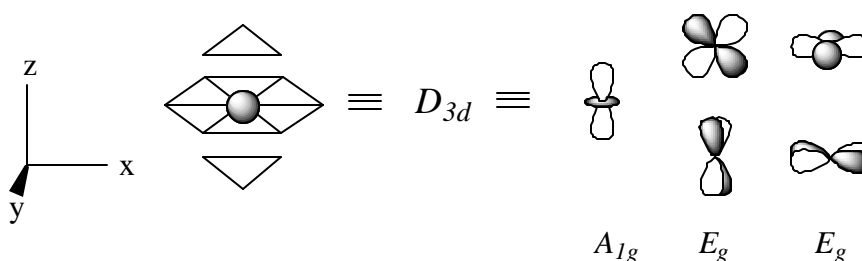
Figure 6.A1. Schematic representation of metal group orbitals

At the 111 surface, the local symmetry is C_{3v}. The group orbitals at the metal atom, are thus:
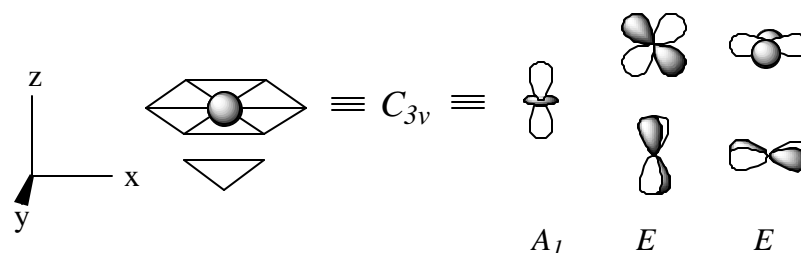
Figure 6.A2. Group orbitals of Pt metal atoms on a (111) surface.

CO can bind atop, bridging, or in 3-fold hollow sites. Experimentally, only atop CO is observed at 1 torr CO and 300-400 K. The bonding between surface Pt and CO(atop) is described in the Blyholder model, in which CO donates a lone pair via its 5σ to a vacant sp hybrid metal orbital, and accepts electrons into the $2\pi^*$ orbitals from a filled metal d-orbital (back-donation).
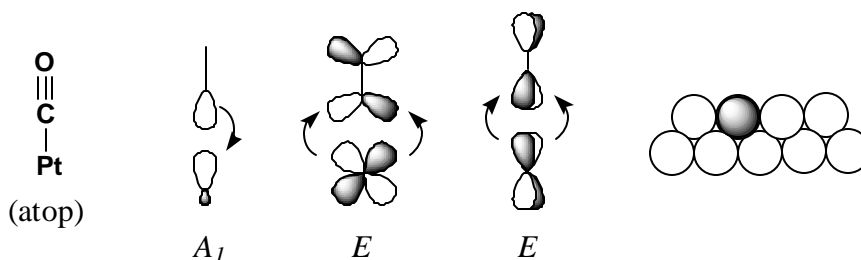
Figure 6.A3. Conventional Blyholder model [ref].

The 5σ orbital of CO has A_1 symmetry and the $2\pi^*$ orbitals have E symmetry. Edge atoms on the surfaces of the Pt crystal exhibit open coordination spheres that enable bonding of multiple CO molecules. If we use the 110 edge of a crystal as a model, the local symmetry is C_{2v}. The group orbitals at the metal atom are:
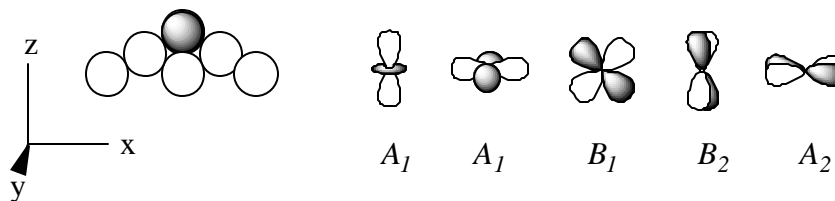
Figure 6.A4. Group orbitals for a 110 edge atom on the surface. Z-axis is coincident with 110.

If we suppose that this edge atom can simultaneously bond to two CO molecules, C_{2v} symmetry holds, and one can construct the following symmetry adapted linear combinations (SALCs) for CO:

COσ: $A_1 + B_1$
COπ: $A_1 + A_2 + B_1 + B_2$
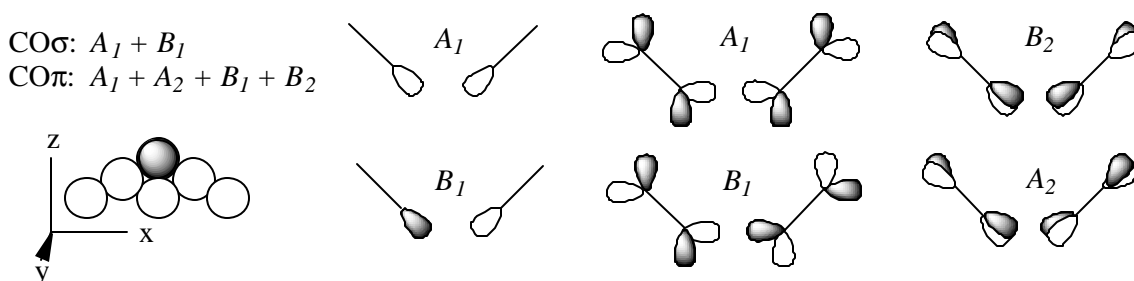
Figure 6.A5. Symmetry adapted linear combination (SALCs) for CO to Pt dicarbonyl formation on on a single edge atom.

Two types of interactions result, those where the ligand participates as an electron donor (Figure A6), and those where the metal participates as the electron donor (Figure A7). The empty s and p orbitals on the metal are the acceptor orbitals.
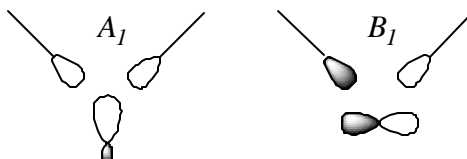
Figure 6.A6. Interactions where the ligand donates electron density to the metal.

A_1 A_2 B_1 B_2
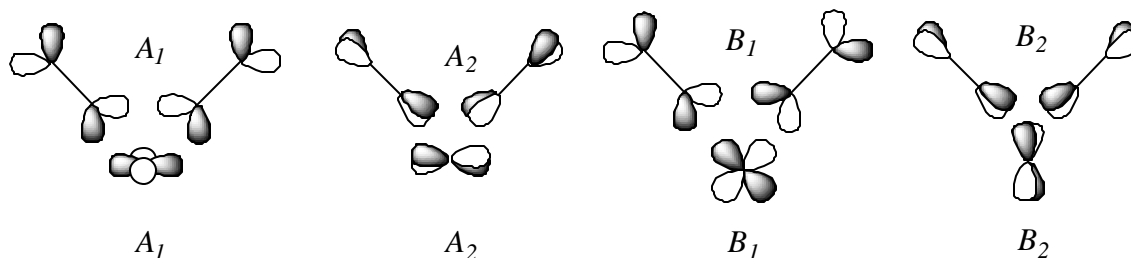
Figure 6.A7. Bonding interactions where the metal donates electron density to empty ligand orbitals.

However, there is no reason to separate the σ interactions from the π^*-d interactions. The only requirement is that orbitals of like symmetry can be combined. This gives rise to mixing of σ and π^* into common molecular orbitals (MOs). The net effect is partial redistribution of 5σ electron density to MOs with significant C-O π^* character. For a 111 corner atom on a surface, the local symmetry at the metal is C_{3v}, so the group orbitals again are $A_1 + E$ as already shown in Figure A2. The coordination sphere at the corner site is highly exposed, and can allow three CO molecules to simultaneously bind the metal atom.
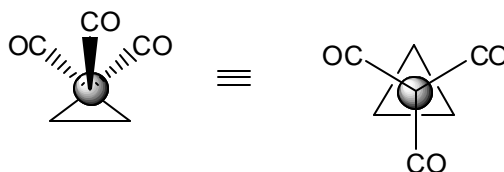
Figure 6.A8. Three-fold CO bonding to metal corner atoms. Left: view parallel to the surface, right: view normal to the 111 surface (coincident with 111).

The ligand SALCs for the σ donor orbitals are:
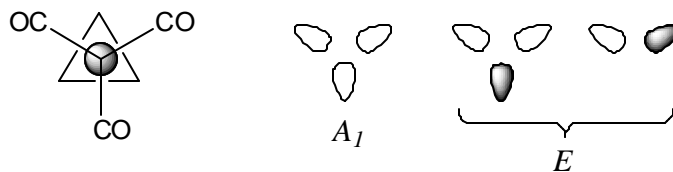
Figure 6.A9. Ligand SALCs for σ donor orbitals in the case of three-fold bonding to metal corner atoms.

The ligand SALCs for the π* acceptor orbitals are:
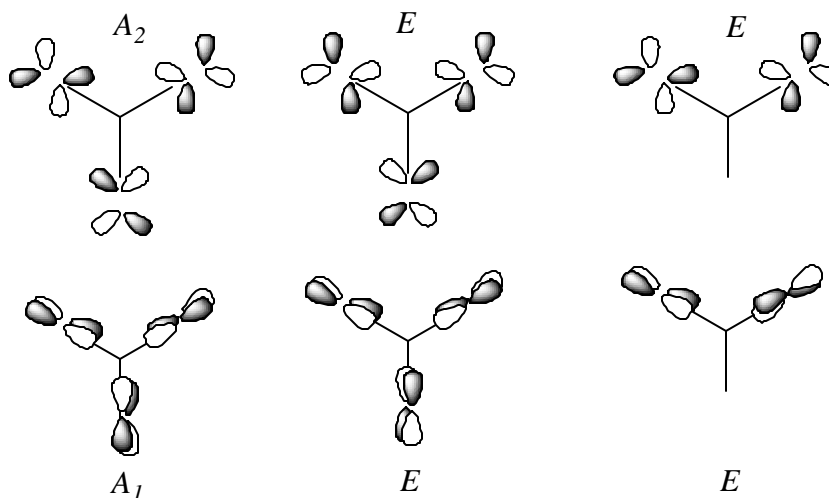
Figure 6.A10. Ligand SALCs for π* acceptor orbitals in the case of three-fold bonding to metal corner atoms.

The bonding combinations are as follows (note that the A_2 orbital has no symmetry match):

ligand donor interactions   back-bonding to pi*
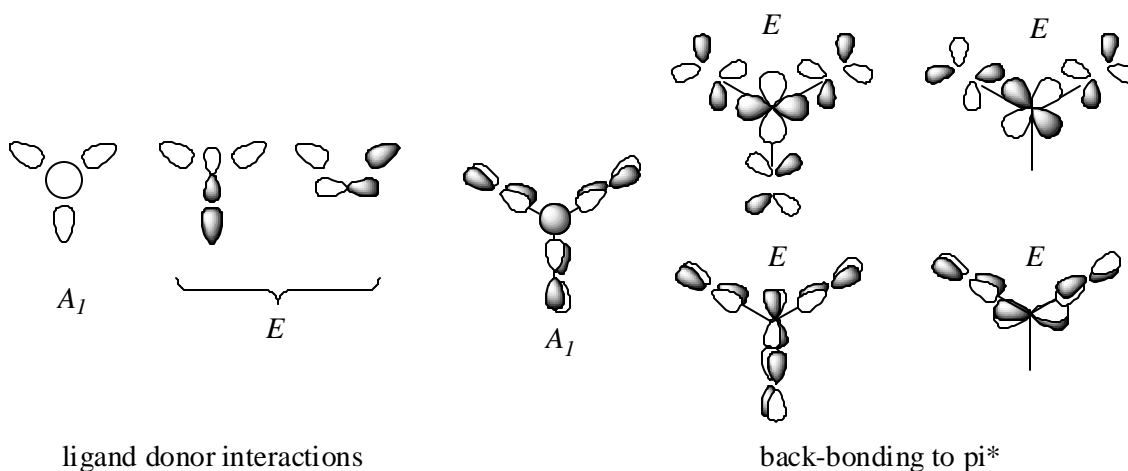
Figure 6.A11. Symmetry adapted bonding representations for surface corner atom with C_{3v} symmetry.

In summary, this appendix shows that in the single CO case, the σ and π ligand orbitals cannot mix, but in the multiple CO cases, there are σ and π ligand orbitals with the same representations, so there can be orbital mixing. The net effect is a decrease in

electron density in the 5σ orbital at carbon with an increase of electron density in orbitals with some CO π* character.

General references:

1.   F. A. Cotton, *Chemical Applications of Group Theory*. 3rd ed., John Wiley & Sons, New York, 1990.

2.   R. Hoffman, *Solids and Surfaces: A Chemist's View of Bonding in Extended Surfaces*. VCH Publishers, Germany, 1988.

3.   M. R. Albert, J. T. Yates, Jr. *The Surface Scientist's Guide to Organometallic Chemistry*. American Chemical Society, Washington D. C., 1987.

6.7   References and Notes

1.   F. Zaera, *Acc. Chem. Res*. 35 (2002) 129.

2.   M. A. Natal-Santiago, S. G. Podkolzin, R. D. Cortright, J. A. Dumesic, *Catal. Lett*. 45 (1997) 155.

3.   M. J. Weaver, *Langmuir* 14 (1998) 3140.

4.   R. Deng, E. Herceg, M. Trenary, *Surf. Sci*. 560 (2004) L195.

5.   R. W. McCabe, L. D. Schmidt, *Surf. Sci*. 66 (1977) 101.

6.   (a) G. A. Somorjai, *Introduction to Surface Chemistry and Catalysis*, Wiley Interscience, New York, 1994, p. 400. (b) R. I. Masel, *Principles of Adsorption and Reaction on Solid Surfaces*, Wiley Interscience, New York, 1996.

7.   (a) M. J. S. Dewar, *Bull. Soc. Chim. Fr.* 18 (1951) C79. (b) J. Chatt, L. A. Duncanson, *J. Chem. Soc*. (1953) 2939.

8.   G. Blyholder, *J. Phys. Chem*. 68 (1964) 2772.

9.   H. Song, R. M. Rioux, J. D. Hoefelmeyer, R. Komor, K. Niesz, M. Grass, P. D. Yang, G. A. Somorjai, Submitted to *J. Am. Chem. Soc*. (2005)

10.   Wang, Y.; Ren, J.; Deng, K.; Gui, L.; Tang, Y. *Chem. Mater*. 12 (2000) 1622

11.   Teranish, T.; Hosoe, M.; Tanaka, T.; Miyake, M. *J. Phys. Chem. B* 103 (1999) 3818.

12.   H. Song, F. Kim, S. Connor, G. A. Somorjai, *J. Phys. Chem. B* 109 (2005) 188.

13.   R. M. Rioux, H. Song, J. D. Hoefelmeyer, P. D. Yang, G. A. Somorjai, *J. Phys. Chem. B* 109 (2005) 2192.

14.   U. K. Singh, M. A. Vannice, *J. Catal*. 191 (2000) 165.

15.   G. C. Bond, P. B. Wells, *Appl. Catal*. 18 (1985) 221.

16.   G. C. Bond, P. B. Wells, *Appl. Catal*. 18 (1985) 225.

17.   J. W. Geus, P. B. Wells, *Appl. Catal*. 18 (1985) 231.

18.   A. Frennet, P. B. Wells, *Appl. Catal*. 18 (1985) 243.

19.   P. B. Wells, *Appl. Catal*. 18 (1985) 259.

20.   V. Gnutzman, W. Vogel, *J. Phys. Chem*. 94 (1990) 4991.

21.   J. R. Anderson, *Structure of Metallic Catalysts.* Academic Press, New York 1975, p. 25.

22.   J. E. Benson, M. Boudart, *J. Catal*. 4 (1965) 704.

23.   T. P. Beebe, P. Gelin, J. T. Yates, Jr., *Surf. Sci*. 148 (1984) 526.

24.   R. M. Rioux, J. D. Hoefelmeyer, T. D. Tilley, G. A. Somorjai. Unpublished results.

25.   Ultrapure SBA-15 was synthesize according to the literature [10], but the reagents used were 99.999% TEOS, 20% doubly distilled HCl and ultrapure H_2O.

26.   P. Chen, K. Y. Kung, Y. R. Shen, G. A. Somorjai, *Surf. Sci*. 494 (2001) 289.

27.   K. Y. Kung, P. Chen, F. Wei, Y. R. Shen, G. A. Somorjai, *Surf. Sci*. 463 (2000) L627.

28.   Y. Xu, B. T. Heaton, C. Jacob, K. Mogi, Y. Ichihashi, Y. Souma, K. Kanamori, T. Eguchi, *J. Am. Chem. Soc*. 122 (2000) 6862.

29.   B. N. J. Persson, R. Ryberg, *Phys. Rev. B* 40 (1989) 10273.

30.   B. N. J. Persson, R. Ryberg, *Phys. Rev. B* 32 (1985) 3586.

31.   A. M. Lahee, J. P. Toennies, Ch. Wöll, *Surf. Sci*. 177 (1986) 371.

32.   A. Bourane, O. Dulaurent, K. Chandes, D. Bianchi, *Appl. Catal. A Gen.* 214
       (2001) 193.

33.   A. Bourane, O. Dulaurent, D. Bianchi, *J. Catal.* 196 (2000) 115.

34.   T. Chafik, O. Dulaurent, J.L. Gass, D. Bianchi, *J. Catal.* 179 (1998) 503.

35.   F. Passos, M. Schmal, M. A. Vannice, *J. Catal.* 160 (1996) 118.

36.   C. T. Campbell, J. M. Campbell, P. J. Dalton, F. C. Henn, J. A. Rodriguez, S.
       G. Seimanides, *J. Phys. Chem.* 93 (1989) 806.

37.   B. E. Spiewak, R. D. Cortright, J. A. Dumesic, *J. Catal.* 176 (1998) 405.

38.   Sheppard Pt(111)

39.   T. A. Land, T. Michely, R. J. Behm, J. C. Hemminger, G. Comsa, *J. Phys.
       Chem.* 97 (1992) 6774.

40.   I. J. Malik, V. K. Agraval, M. Trenary, *J. Chem. Phys.* 89 (1988) 3861.

41.   R. M. Rioux, Ph. D Thesis, University of California, Berkeley, Chapter 5.

42.   L. Spenadel, M. Boudart, *J. Phys. Chem.* 64 (1960) 204.

43.   D. A. Hensley, L. L. Kesmodel, *Surf. Sci.* 231 (1990) 361.

44.   W. F. Banholzer, R. E. Parise, R. I. Masel, *Surf. Sci.* 155 (1985) 653.

45.   Y. O. Park, W. F. Banholzer, R. I. Masel, *Surf. Sci.* 155 (1985) 341.

46.   R. P. Eischens, S. A. Francis, W. A. Pliskin, *J. Phys. Chem.* 60 (1956) 194.

47.   C. Klünker, M. Balden, S. Lehwald, W. Daum, *Surf. Sci.* 360 (1996) 104.

48.   K. McCrea, J. S. Parker, P. Chen, G. A. Somorjai, *Surf. Sci.* 494 (2001) 238.

49.   R. M. Watwe, B. E. Spiewak, R. D. Cortright, J. A. Dumesic, *Catal. Lett.* 51
       (1998) 139.

50.   E. Kruse Vestergaard, P. Thostrup, T. An, E. Lægsgaard, I. Stensgaard, B.
       Hammer, F. Besenbacher, *Phys. Rev. Lett.* 88 (2002) 259601.

51. S. R. Longwitz, J. Schnadt, E. K. Vestergaard, R. T. Vang, E. Lægsgaard, I. Stensgaard, H. Brune, F. Besenbacher, *J. Phys. Chem. B* 108 (2004) 14497.

52. E. G. Seebauer, A. C. F. Kong, L. D. Schmidt, *Surf. Sci.* 176 (1986) 134.

53. J. Rogozik, V. Dose, *Surf. Sci.* 176 (1986) L847.

54. D. K. Lambert, *Phys. Rev. Lett.* 50 (1983) 2106.

55. W. A. Brown, P. Kose, D. A. King, *Surf. Sci.* 440 (1999) 271.

56. R. Kose, D. A. King, *Chem. Phys. Lett.* 313 (1999) 1.

57. M. J. Kappers, J. H. van der Maas, *Catal. Lett.* 10 (1991) 365.

58. R. K. Brandt, M. R. Hughes, L. P. Bourget, K. Truszkowska, R. G. Greenler, *Surf. Sci.* 286 (1993) 15.

59. N. W. Cant, R. A. Donaldson, *J. Catal.* 78 (1982) 461.

60. H. Bischoff, N. I. Jaeger, G. Schulz-Ekloff, *Z. Phys. Chemie. Liepzig* 271 (1990) 1093.

61. Mukerji, R. J.; Bolina, A. S.; Brown W. A. *Surf. Sci.* 527 (2003) 198.

62. Watwe, R. M.; Spiewak, B. E.; Cortright, R. D.; Dumesic, J. A. *Catal. Lett.* 51 (1998) 139.

63. Schulze Icking-Konert, G.; Handschuh, H.; Ganteför, G.; Eberhardt, W. *Phys. Rev. Lett.* 76 (1996) 1047.

64. Härle, H.; Metka, W.; Volpp, H. –R.; Wolfrum, J. *Phys. Chem. Chem. Phys.* 1 (1999) 5059.

65. G. S. Lane, J. T. Miller, F. S. Modica, M. K. Barr, *J. Catal.* 141 (1993) 465.

66. I. Grinberg, Y. Yourdshahyan, A. M. Rappe, *J. Chem. Phys.* 117 (2002) 2264.

67. R. A. Olsen, P. H. T. Philipsen, E. J. Baerends, *J. Chem. Phys.* 119 (2003) 4522.

68. P. J. Feibelman, B. Hammer, J. K. Nørskov, F. Wagner, M. Scheffler, R. Stumpf, R. Watwe, J. Dumesic, *J. Phys. Chem. B* 105 (2001) 4018.

69. R. Kose, D. A. King, *Chem. Phys. Lett*. 313 (1999) 1.

70. R. K. Brandt, R. S. Sorbello, *Surf. Sci*. 271 (1992) 605.

71. J. Kubota, S. Ichihara, J. N. Kondo, K. Domen, C. Hirose, *Surf. Sci*. 357-358 (1996) 634.

72. R. G. Windham, B. E. Koel, M. T. Paffet, *Langmuir*, 4 (1988) 1113.

73. E. M. Stuve, R. J. Madix, *J. Phys. Chem*. 89 (1995) 3183.

74. E. M. Stuve, R. J. Madix, *J. Phys. Chem*. 89 (1985) 105.

75. H. Ibach, S. Lehwald, *J. Vac. Sci. Technol*. 15 (1978) 407.

76. U. Starke, A. Barbieri, N. Materer, M. A. Van Hove, G. A. Somorjai, *Surf. Sci.* 286 (1993) 1.

77. E. Yagasaki, R. I. Masel, *Surf. Sci*. 222 (1989) 430.

78. W. T. Lee, L. Ford, P. Blowers, H. L. Nig, R. I. Masel, *Surf. Sci*. 416 (1998) 141.

79. E. Yagasaki, R. I. Masel, *Surf. Sci*. 226 (1990) 51.

80. G. H. Hatzikos, R. I. Masel, *Surf. Sci*. 185 (1997) 479.

81. E. Yagasaki, A. L. Backman, R. I. Masel, *J. Phys. Chem*. 94 (1990) 1066.

82. G. H. Hatzikos, R. I Masel, In Catalysis 1987 Ed.: J. W. Ward, Elsevier: New York 1988. p. 883.

83. A. L. Backman, R. I. Masel, *J. Phys. Chem*. 94 (1990) 5300.

84. F. Zaera, *J. Am. Chem. Soc*. 111 (1989) 4240.

85. J. Hiraishi, *Spectrochim. Acta* 25A (1969) 749.

86.   D. B. Powell, J. G. V. Scott, N. Sheppard, *Spectrochim. Acta A* 28 (1972) 327.

       W. A. Brown, R. Kose, D. A. King, *Surf. Sci.* 440 (1990) 271.

87.   S. B. Mohsin, M. Trenary, H. J. Robota, *Chem. Phys. Lett.* 154 (1989) 511.

88.   S. B. Mohsin, M. Trenary, H. J. Robota, *J. Phys. Chem.* 92 (1988) 5229.

89.   D. K. Paul, T.P. Beebe, Jr., K. J.Uram, J.T. Yates, Jr., *J. Am. Chem. Soc.* 114
       (1992) 1949.

90.   T. P. Beebe, Jr., J. T. Yates, Jr. *Surf. Sci.* 173 (1986) L606.

91.   P. –K. Wang, C. P. Slichter, J. H. Sinfelt, *J. Phys. Chem.* 89 (1985) 3606.

92.   J. D. Prentice, A. Lesinas, N. Sheppard, *J. Chem. Soc. Chem. Comm.* (1976)
       76.

93.   E. A. Carter, B. E. Koel, *Surf. Sci.* 226 (1990) 339.

94.   D. C. Tang, K. S. Hwang, M. Salmeron, G. A. Somorjai, *J. Phys. Chem. B*
       108 (2004) 13300.

95.   G. S. Blackman, C. T. Kao, B. E. Bent, C. M. Mate, M. A. Van Hove, G. A.
       Somorjai, *Surf. Sci.* 207 (1988) 66.

96.   M. A. van Hove, R. F. Lin, D. F. Ogletree, G. S. Blackman, C. M. Mate, G. A.
       Somorjai, *J. Vac. Sci. Technol. A* 5 (1987) 69.

97.   C. M. Mate, C. –T. Kao, G. A. Somorjai, *Surf. Sci.* 206 (1988) 145.

98.   A. J. Slavin, B. E. Bent, C. –T. Kao, G. A. Somorjai, *Surf. Sci.* 202 (1988) 388.

99.   C. M. Mate, B. E. Bent, G. A. Somorjai, *J. Elect. Rel. Spect.* 39 (19886) 205.

100.   H. Wang, R. G. Tobin, D. K. Lambert, G. B. Fisher, C. L. DiMaggio, *J. Chem.
       Phys.* 103 (1995) 2711.

101.   J. L. Gland, D. A. Fischer, D. H. Parker, S. Shen, *Langmuir* 7 (1991) 2574.

102. H. Wang, R. G. Tobin, D. K. Lambert, G. B. Fisher, C. L. J. DiMaggio, *J. Chem. Phys*. 103 (1995) 2711.

103. H. Wang, R. G. Tobin, D. K. Lambert, G. B. Fisher, C. L. J. DiMaggio, *Surf. Sci*. 330 (1995) 173.

104. D. H. Parker, D. A. Fischer, J. Colbert, B. E. Koel, *Surf. Sci*. 258 (1991) 75.

105. D. V. Chakarov, Ts. Marinova, *Surf. Sci*. 227 (1990) 297.

106. M. A. Henderson, G. E. Mitchell, J. M. White, *Surf. Sci*. 203 (1988) 378.

107. S. Akhter, J. M. White, *Surf. Sci*. 180 (1987) 19.

108. M. Morkel, G. Rupprechter, H. –J. Freund, *Surf. Sci*. 588 (2005) L209.

109. M. Frank, M. Bäumer, R. Kühnemuth, H. –J. Freund, *J. Vac. Sci. Technol. A* 19 (2001) 1497.

110. D. Hoge, M. Tüshaus, A. M. Bradshaw, *Surf. Sci*. 207 (1988) L935.

111. D. Stacchiola, M. Kaltchev, G. Wu, W. T. Tysoe, *Surf. Sci*. 470 (2000) L32.

112. D. Stacchiola, G. Wu, M. Kaltchev, W. T. Tysoe, *J. Chem. Phys*. 115 (2001) 3315.

113. M. Kawai, J. Yoshinobu, *Surf. Sci*. 368 (1996) 239.

114. M. K. Ainsworth, M. R. S. McCoustra, M. A. Chesters, N. Sheppard, C. De La Cruz, *Surf. Sci*. 437 (1999) 9.

115. W. Erley, Y. Li, D. P. Land, J. C. Hemminger, *Surf. Sci*. 103 (1994) 177.

116. M. R. Albert, J. T. Yates, Jr., *The Surface Scientist's Guide to Organometallic Chemistry*, ACS, Washington DC, 1987. p. 58.

117. P. Skinner, M. W. Howard, I. A. Oxton, S. F. A. Kettle, D. B. Powell, N. Sheppard, *J. Chem. Soc., Faraday Trans*. 2 77 (1981) 1203.

118. M. Green, J. A. K. Howard, J. L. Spencer, F. G. A. Stone *J. Chem. Soc., Dalton Trans*. (1977) 271.

119. J. A. K. Howard, J. L. Spencer, S. A. Mason, *Proc. Royal Soc. Lond. A* 386 (1983) 145.

120. P. Csaszar, P. L. Goggin, J. Mink, J. L. Spencer, *J. Organomet. Chem*. 379 (1989) 337.

121. J. P. Collman, L. S. Hegedus, J. R. Norton, R. G. Finke, *Principles and Applications of Organotransition Metal Chemistry*, University Science Books, Mill Valley, 1987, p. 71.

122. G. Longoni, P. Chini, *J. Am. Chem. Soc*. 98 (1976) 7225

123. G. Lin, N. D. Jones, R. A. Gossage, R. McDonald, R. G. Cavell, *Angew. Chem. Int. Ed*. 42 (2003) 4054.

124. G. Hwang, M. Bodenbinder, H. Willner, F. Aubke, *Inorg. Chem*. 32 (1993) 4667.

125. Q. Xu, B. T. Heaton, C. Jacob, K. Mogi, Y. Ichihashi, Y. Souma, K. Kanamori, T. Eguchi, *J. Am. Chem. Soc*. 122 (2000) 6862.

126. G. Longoni, P. Chini, *J. Am. Chem. Soc*. 98 (1976) 7225.

127. D. B. Dell'Amico, R. Bini, F. Calderazzo, L. Carbonaro, L. Labella, A. Vitullo, *Organomet*. 24 (2005) 4427.

128. L. Manceron, B. Tremblay, M. E. Alikhani, *J. Phys. Chem. A* 104 (2000) 3750.

Chapter 7

Influence of Pt particle size on poisoning of ethylene hydrogenation by carbon monoxide: Kinetic study and dual site reaction mechanism

7.1   Introduction

Designing heterogeneous catalysts that are capable of the highest possible selectivity at relevant conversions under environmental benign conditions is the aim of research in our laboratory [1–4]. To that end, the design and synthesis of high surface area Pt catalysts with tunable parameters (*i.e.* particle size and/or shape) has been pursued [1–3]. Monodisperse platinum nanoparticles are synthesized by solution based reduction methods [1, 5–6], followed by encapsulation of the nanoparticles in the pores of a mesoporous SBA-15 silica matrix [2]. These catalysts possess properties that can be tuned systematically to understand the influence of catalyst structure on catalytic activity [1–3] and selectivity [4]. Detailed control of catalyst morphology enables structure-function (activity and selectivity) relationships; it also enables the influence of structure (*i.e.* particle size) on poison/deactivation resistance to be investigated.

The mechanism by which an adsorbate poisons a catalytic reaction is either one of site blocking, perturbation of the surface electronic structure by either charge screening or surface reconstruction or a combination of both. The mechanistic complexity of poisoning is tractable when the influence of a poison is examined during a well-studied reaction. An example is the influence of carbon monoxide poisoning on olefin conversion reactions which has been previously studied [7–10]. Suppression of turnover rates is severe in some cases; while other catalysts appear to be resistant to poisoning by CO [9 ,10] and imaging studies suggest that limited adsorbate mobility may lead to poisoning [11]. Carbon monoxide is one of the most studied reaction inhibiting adsorbates because it serves as an indicator of local surface structure [12, 13] making it an ideal probe molecule (poison) to understand the influence of structure (*i.e.* particle size) on poison resistance. The CO stretching frequency is sensitive to the identity of neighboring adsorbates [14] and may allow insight into the interaction between poison and reactant molecules on the catalyst surface. CO adsorption perturbs the electronic structure of the surface Pt atoms by significant donation from the 2p orbital into the metal d-orbital and back donation to the anti-bonding $2\pi^*$ orbital of adsorbed carbon monoxide, which determines the stability of the metal carbon bond [15]. The properties of adsorbed CO predispose it to compete for sites and inhibit turnover during olefin conversion reactions. The co-adsorption of carbon monoxide and ethylene on the same monodisperse Pt(X)/SBA-15 (X = 1.7, 2.9, 3.6 and 7.1 nm) catalysts has been studied by volumetric adsorption measurements and infrared spectroscopy [16].

In this chapter, the hydrogenation of ethylene in the presence of CO in the torr pressure range has been examined on Pt/SBA-15 catalysts. Kinetic measurements demonstrate that the ethylene hydrogenation rate decreases by ~ 4-5 orders of magnitude

upon the addition of 0.5 Torr CO at 403 K. Kinetic parameters were also influenced by the presence of CO, the most notably change was a doubling of the apparent activation energy in the presence of CO. The sequence of elementary steps proposed for the uncompetitive Horiuti-Polanyi mechanism [17] with the inclusion of an equilibrated CO adsorption step allows the formulation of a rate expression which captures the experimental kinetics. This work demonstrates the rate of olefin hydrogenation which is insensitive to the size of the metal nanoparticles in the absence of CO remains structure insensitive although the adsorption of carbon monoxide is sensitive to the catalyst structure.

7.2   Experimental

7.2.1   Catalyst Synthesis and Characterization

The synthesis and characterization of catalysts used in this study have been described previously [1, 2] but is briefly described here. Pt particles were synthesized according to literature methods [5, 6]. 1.7 nm Pt particles were made by adding NaOH solution (12.5 mL, 0.5 M) in ethylene glycol (EG) to a solution of dihydrogen hexachloroplatinate ($H_2PtCl_6 \cdot 6H_2O$, Alfa Aesar 250 mg) in 12.5 mL of EG. The mixture was heated at 433 K for 3 h with N_2 bubbling. After reaction, particles were precipitated by the addition of 2 M HCl (1 mL), and dispersed in ethanol containing 12.2 mg of poly(vinylpyrrolidone) (PVP, M_w = 29,000, Sigma-Aldrich). 2.9 nm particles were synthesized by refluxing a mixture of PVP (26.6 mg) and $H_2PtCl_6 \cdot 6H_2O$ (124.3 mg) in water (40 mL)/methanol (360 mL) solution for 3 h. 3.6 nm Pt particles were formed by mixing the 2.9 nm Pt colloidal solution (100 mL) in a water/methanol (1:9) mixture with 10 mL of 6.0 mM $H_2PtCl_6 \cdot 6H_2O$ aqueous solution and 90 mL of methanol, followed by

refluxing for 3 h. 7.1 nm Pt particles were synthesized by adding 3 mL of 0.375 M PVP

(M_w = 55,000, Sigma-Aldrich) and 1.5 mL of 0.0625 M $H_2PtCl_6 \cdot 6H_2O$ solutions in

refluxing EG every 30 s over 16 min followed by an additional 5 min reflux. Pt colloidal

solutions were purified by sequential precipitation/redispersion, and dispersed in an

appropriate amount of deionized water necessary for a 3×10^{-3} M solution based on Pt salt

concentration. Estimated particle sizes were 1.73±0.26 (1.7), 2.80±0.21 (2.9), 3.39±0.26

(3.6), and 7.16±0.37 (7.1) nm by transmission electron microscopy (TEM) and (X-ray

diffraction, XRD), respectively, indicating high uniformity and monodispersity of each

particle less than $\sigma \sim 8$ %.

The synthesis of Pt/SBA-15 catalysts by the nanoparticle encapsulation method

has been published [2]. 2.5 g of Pluronic P123 ($EO_{20}PO_{70}EO_{20}$, BASF) was completely

dissolved in deionized water (50.5 mL). Pt colloidal aqueous solution (27.0 mL, 3×10^{-3}

M) was mixed with the polymer solution and stirred for 1 h at 313 K. 0.375 mL of 0.5 M

NaF aqueous solution was added, and 3.91 mL of tetramethyl orthosilicate (TMOS, 98%,

Aldrich) was quickly added to the reaction mixture, followed by stirring for a day at 313

K. The resulting slurry was aged for an additional day at 373 K. The brown precipitates

were separated by centrifugation, thoroughly washed with ethanol, and dried in an oven

at 373 K. Pt(1.7 nm)/SBA-15 was calcined at 623 K for 24 h, Pt(7.1 nm)/SBA-15 was

calcined at 723 K for 36 h, and 2.9/3.6 nm catalysts were calcined at 723 K for 24 h.

A 3.2% Pt/SiO_2 catalyst prepared by ion exchange of $Pt(NH_3)_4(OH)_2 \cdot xH_2O$ [18]

and an ultrahigh purity (UHP) Pt powder (Alfa Aesar, 1μm particle size) were used as

standard samples for reaction studies. The ultrahigh purity Pt powder was cleaned by

heating at 473 K for 30 minutes in 10% O_2/He to remove any surface contaminants

before normal catalyst pretreatment. A 2% Pt/Al_2O_3 (Exxon Research and Engineering)

was also included in this study to determine if the support influenced CO poisoning of ethylene hydrogenation. All standard catalyst samples were reduced at 673 K by the same procedure used for the SBA-15 catalysts [1–3].

TEM experiments were carried out on a Philips CM200 microscope operated at 200 kV at the National Center for Electron Microscopy at Lawrence Berkeley National Laboratory. XRD spectra were measured on a Bruker D8 GADDS diffractometer using Co Kα radiation (1.79 Å). Selective gas adsorption measurements were conducted in a pyrex volumetric apparatus pumped by a liquid nitrogen cooled diffusion pump to sample cell pressures of $\leq 3 \times 10^{-6}$ Torr. Total and reversible isotherms were collected at room temperature with an interim 1 h evacuation between isotherms. Monolayer uptakes were determined by extrapolating adsorbate uptakes to zero pressure (P = 0). Catalysts were reduced for 75 min at 673 K in 50 cc (STP) H_2 min^{-1} (Praxair, UHP, 99.999%) followed by evacuation at 623 K before adsorption measurements.

7.2.2 *Kinetic measurements of C_2H_4 hydrogenation in the presence and absence of CO*

Kinetic measurements were conducted in a quartz plug flow reactor (PFR) operating under differential conditions. Conversions were maintained below 5 % for most catalysts. Pt/SBA-15 catalysts (10-50 mg) diluted in acid washed low surface area quartz (~50-250 mg) (Aldrich) were reduced by the same pretreatment protocol used for the chemisorption samples. He (Praxair, UHP, 99.999%), H_2 (Praxair, UHP, 99.999%), C_2H_4 (AirGas, CP grade) and CO (Matheson, UHP, Al cylinder) were delivered to the reactor with mass flow controllers (Unit Instruments Corporation, Model UFC 1200) at a total flow rate of 90 cc (STP) min^{-1}. Turnover rates were corrected to standard conditions of 10 Torr C_2H_4, 100 Torr H_2, 0.5 Torr CO and 403 K. Ample amount of catalyst (5-90 mg) was used for each sample to allow kinetic measurements from 373-433 K. Reactant

and product concentrations were measured by gas chromatography (Hewlett Packard 5890 Series II) equipped with a 10 way-sampling valve allowing simultaneous monitoring of C_2H_4 and C_2H_6 with the flame ionization detector (FID) and CO and H_2 with the thermal conductivity detector (TCD). All turnover frequencies were reproducible to $\pm$ 10% as determined by multiple measurements. No conversion of CO to methane through a CO/H_2 reaction was detected. All turnover frequency values were calculated using the dispersion calculated from the total H_2-O_2 uptake [19].

7.2.3 *In-situ infrared spectroscopy measurements of ethylene hydrogenation in the absence and presence of carbon monoxide*

In-situ diffuse reflectance infrared Fourier transform spectroscopy (DRIFTS), using a Nicolet Nexus 670 spectrometer equipped with a Thermo Spectra-Tech controlled atmosphere-diffuse reflection cell was used to study the reaction between ethylene and hydrogen in the presence of carbon monoxide at 403 K. The IR cell was operated as a plug flow reactor at conditions similar to those used for microreactor studies. Typically, a Pt/SiO_2 catalyst (*ca.* 50 mg amorphous SiO_2, *ca.* 20-30 mg SBA-15 samples) was loaded in the cell and given a pretreatment identical to that used for the catalytic studies with a gas handling manifold equipped with mass flow controllers (Porter Instruments Company) connected to the diffuse reflection cell. He (99.999%, Praxair), H_2 (99.999%, Praxair), CO (99.9%, Airgas) and C_2H_4 (99.9%, Praxair) were used without further purification. Single beam spectra (128 scans, 2 cm^{-1} resolution) of the freshly reduced catalyst were obtained at 300 K or 403 K under 30 cc (STP) He min^{-1} and used as the background for subtraction of silica features for all samples. Samples were heated to reaction temperature (300 or 403 K) in He and then exposed to a 90 cc (STP) min^{-1} mixture of 10 Torr C_2H_4, 100 Torr H_2 and 1 Torr CO (because of experimental

constraints, this was the lowest obtainable CO pressure). Separately, a spectrum of gas phase CO (1 Torr) and ethylene (10 Torr) taken in the DRIFTS cell using a Au mirror was subtracted from each spectrum under reaction conditions. The only results presented are for a 2.69% Pt(2.9 nm)/SBA-15 catalyst.

7.3. Results

7.3.1 Catalyst characterization

The characterization of the Pt(X)/SBA-15 series catalysts has been previously reported [1, 2]. Briefly, monodisperse Pt particles of 1.7–7.1 nm were synthesized by modified alcohol reduction methods according to the literature [5, 6]. Reduction of Pt salts at high temperature produces more Pt nuclei in a short period and eventually affords smaller Pt particles. The 3.6 nm Pt particles were successfully obtained by addition of 2.9 nm particles as a seed for stepwise growth. The 7.1 nm Pt particles were generated by slow and continuous addition of the Pt salt and PVP to boiling ethylene glycol, described elsewhere in detail [20]. Colloidal PVP-capped Pt particles with sizes of 1.7, 2.9, 3.6, and 7.1 nm were introduced into a neutral pH aqueous polymer solution at 313 K and stirred for 1 h to ensure complete dissolution of Pt particles. Brown precipitates were formed 5 min. following the addition of NaF solution and TMOS. The supernatant was colorless and transparent, indicating Pt colloids were incorporated into the silica matrix. The slurry was aged for a day at 313 K, and placed in an oven at 373 K for an additional day. The product was washed with water and ethanol, and dried in air at 373 K. Figure 1 demonstrates that the Pt nanoparticles are encapsulated by ordered silica structures, isolated and randomly distributed throughout the silica framework without severe agglomeration.

Catalysts were prepared with a nominal weight loading of 1%; actual metal loadings determined by elemental analysis were between 0.6 and 0.8 wt. %. Estimation of the particle size based on XRD was not successful because of the low signal-to-noise ratio of the Pt Bragg reflections. Only in the case of the Pt(7.1 nm)/SBA-15 catalyst was a particle size determined (Table 1). Removal of PVP from encapsulated nanoparticle surfaces is achieved by sample dependent long calcination times (24–36 h) at relatively high temperatures (623–673 K). Thermogravimetric analysis (TGA) of the 0.77% Pt(2.9 nm)/SBA-15 sample demonstrated that Pluronic P123 decomposed at 453 - 573 K and PVP decomposed at 573 - 773 K under O_2 [2]. Selective gas adsorption (H_2–O_2 chemisorption) measurements of the exposed Pt surface area are shown in Table 1 and demonstrate that the residual PVP may still be present on the nanoparticle surface.
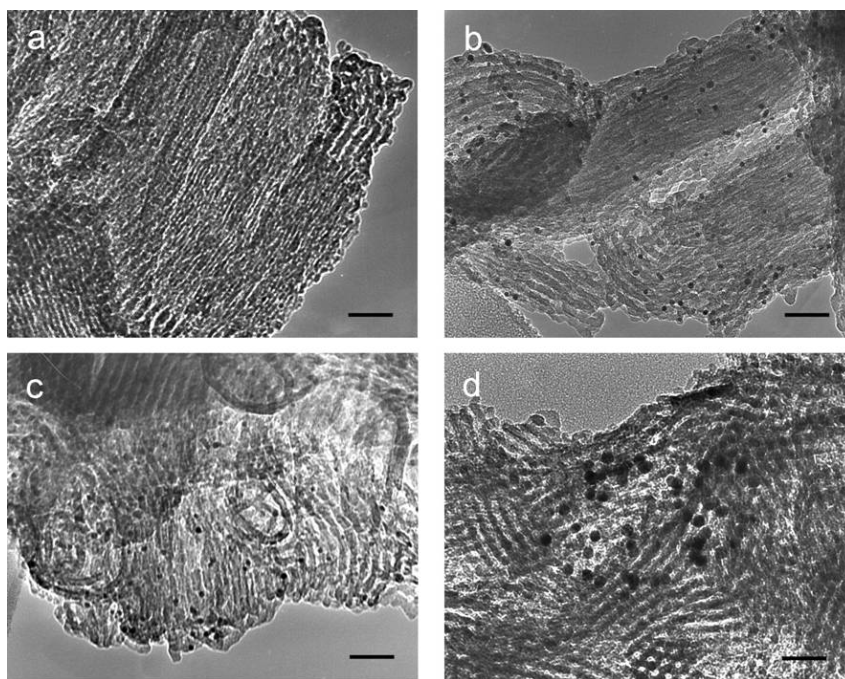
Figure 7.1. TEM micrographs of Pt(X)/SBA-15 catalysts. (a) X = 1.7 nm, (b) X = 2.9 nm, (c) X = 3.6 nm, and (d) X = 7.1 nm. The scale bars represent 40 nm.

7.3.2   Kinetics of CO poisoned C_2H_4 hydrogenation on Pt/SBA-15 catalysts

The kinetics of C_2H_4 hydrogenation in the presence of CO (0.2-0.9 Torr) was studied over a series of SBA-15 supported Pt catalysts. The influence of particle size on poisoning and the overall kinetics were examined. In the absence of CO, the turnover frequency (TOF) for ethylene hydrogenation is ~ 10^2 s^{-1} at 403 K, while the catalytic activity varied from 1.7-3.5 $\times$ 10^{-2} s^{-1} at 10 Torr C_2H_4, 100 Torr H_2, 0.5 Torr CO and 403 K. Activity (per gram catalyst) and turnover frequencies are reported in Table 2. Turnover frequencies were always reproducibly higher on the Pt(1.7 nm)/SBA-15 and 2% Pt/Al_2O_3, two samples with the same particle size (~2.7 nm). The difference in TOF varied by only a factor of two over the entire particle size range studied (1 – ~300 nm) and ethylene hydrogenation in the presence of CO is still structure insensitive. Reporting turnover rates for ethylene hydrogenation poisoned by CO, the CO pressure must be stated, because a change in this pressure has a substantial influence on the measured rate.

The influence of temperature on the overall reaction rate was measured at 10 Torr C_2H_4, 100 Torr H_2, 0.2 Torr CO and 373-423 K. At these conditions, all conversions (X) were $\leq$ 10 % and verified free of mass and heat transfer artifacts by the Madon-Boudart test [21]. Apparent activation energy measured at similar pressure conditions (but slightly lower temperatures) in the absence of carbon monoxide on Pt/SiO_2 catalysts have been reported at 8–12 kcal mol^{-1} [22]. The apparent activation energy for the CO poisoned ethylene hydrogenation was ~ 20 kcal mol^{-1} for supported catalysts, while the Pt powder activation energy was ~ 14 kcal mol^{-1}. The Al_2O_3 supported and 0.62% Pt(7.1 nm)/SBA-15 catalyst had apparent activation energies of 22 kcal mol^{-1}. Arrhenius plots for catalysts are shown in Figure 2 and compiled in Table 2. The same catalysts had apparent activation energies ranging from 8-12 kcal mol^{-1} in the absence of CO at 273–323 K [2].

Table 7.1. Pt particle sizes by chemisorption and XRD for supported Pt/SiO_2 and Al_2O_3 catalysts

Catalyst[a]	Selective gas uptake (μmol g^{-1})[b] H_2-$O_{2,total}$	Dispersion, D[c]	Particle size, d (nm)	
			Chemisorption[d]	XRD
3.2% Pt/SiO$_2$-IE	262.0	1[e]	~1	--
2% Pt/Al$_2$O$_3$	66.1	0.43	2.6	2.9
0.6% Pt(1.7 nm)/SBA-15	19.1	0.41	2.7	--
0.77% Pt(2.9 nm)/SBA-15	21.8	0.36	3.1	--
0.6% Pt(3.6 nm)/SBA-15	12.5	0.27	4.2	--
0.62% Pt(7.1 nm)/SBA-15	5.6	0.11	9.4	7.9[f]
Pt powder	30.3	0.004	287	>100

[a]Actual catalyst loading determined by ICP-AES.

[b]Monolayer uptakes (P = 0) determined at 295 K.

[c]Based on total H_2-O_2 titration uptake at P = 0.

[d]Based on d(nm) = 1.13/D.

[e]Dispersion greater than unity calculated, assumed 100% dispersion for calculation of turnover frequency.

[f]After subtraction of pristine SBA-15 background.
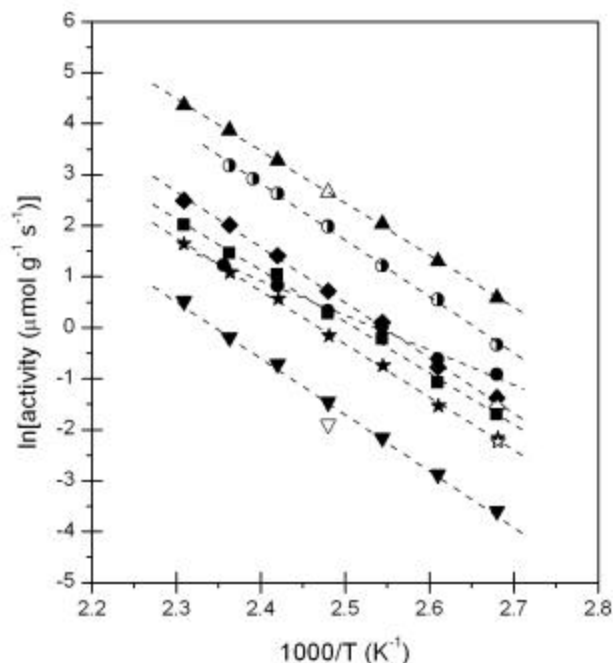
Figure 7.2. Arrhenius plot for hydrogenation of ethylene in the presence of CO. Reaction conditions were 10 Torr C_2H_4, 200 Torr H_2, 0.2 Torr CO and 373-433 K. Apparent activation energies of 20 kcal mol^{-1} are measured in the presence of CO pressures up to 1 Torr. (▲) 3.2% Pt/SiO$_2$; (●) Pt powder; (◆) Pt(1.7 nm)/SBA-15; (■) Pt(2.9 nm)/SBA-15; (★) Pt(3.6 nm)/SBA-15; (▼) Pt(7.1 nm)/SBA-15; (◐) Pt/Al$_2$O$_3$

Apparent reaction orders in ethylene, hydrogen and CO have been measured for all catalysts and are compiled in Table 2. Reaction orders in ethylene, hydrogen and CO at 403 K are shown in Figure 3. Reaction orders were ~1st order in ethylene, ~ ½ order in H_2 and –1 in CO for all catalysts, regardless of particle size. The inverse first order dependence of CO (Figure 3c) suggests that adsorbed CO is the most abundant surface intermediate (*masi*). Comparison of reaction kinetics in the presence and absence of CO suggest that both ethylene and hydrogen surface chemistry are influenced by adsorbed CO. H_2 dependencies on the overall reaction were ½ in all pressures of carbon monoxide while in the absence of CO at slightly lower temperatures; the hydrogen order is reported as unity [23]. The first order dependence on H_2 in the absence of CO is related to

Table 7.2. Ethylene hydrogenation reaction kinetics on supported Pt catalysts in the presence of CO

Catalyst[a]	Activity[b] (μmol g^{-1} s^{-1})	TOF[b,c] ($100 \times$ s^{-1})	E_a[d] (kcal mol^{-1})	reaction orders C_2H_4[e]	H_2[f]	CO[g]
3.2% Pt/SiO$_2$-IE	3.2	2.0	20.3	0.89	0.67	-1.1
2% Pt/Al$_2$O$_3$-Exxon	1.5	3.5	22.1	0.88	0.62	-1.1
0.6% Pt(1.7 nm)/SBA-15	0.43	3.4	21.6	0.97	0.60	-1.2
0.77% Pt(2.9 nm)/SBA-15	0.38	2.7	20.1	0.96	0.52	-1.1
0.6% Pt(3.6 nm)/SBA-15	0.19	2.3	20.7	0.99	0.44	-1.1
0.62% Pt(7.1 nm)/SBA-15	0.06	1.7	22.0	0.98	0.46	-1.0
UHP Pt powder	0.39	2.0	13.6	1	0.44	-1.1

The table header spans: "Kinetic Parameters in the presence of CO" over E_a and reaction orders columns.

[a]Actual Pt weight loading determined by ICP.
[b]Rates corrected to 10 Torr C$_2$H$_4$, 100 Torr H$_2$, 0.5 Torr CO and 403 K.
[c]Based on number of surface atoms determined by total H$_2$-O$_2$ titration.
[d]Conditions were 10 Torr C$_2$H$_4$, 200 Torr H$_2$, 0.2 Torr CO and 373-433 K.
[e]Reaction conditions were 5-40 Torr C$_2$H$_4$, 200 Torr H$_2$, 0.2 Torr CO and 403 K.
[f]Reaction conditions were 10 Torr C$_2$H$_4$, 140-540 Torr H$_2$, 0.2 Torr CO and 403 K.
[g]Reaction conditions were 10 Torr C$_2$H$_4$, 200 Torr H$_2$, 0.2-0.9 Torr CO and 403 K.
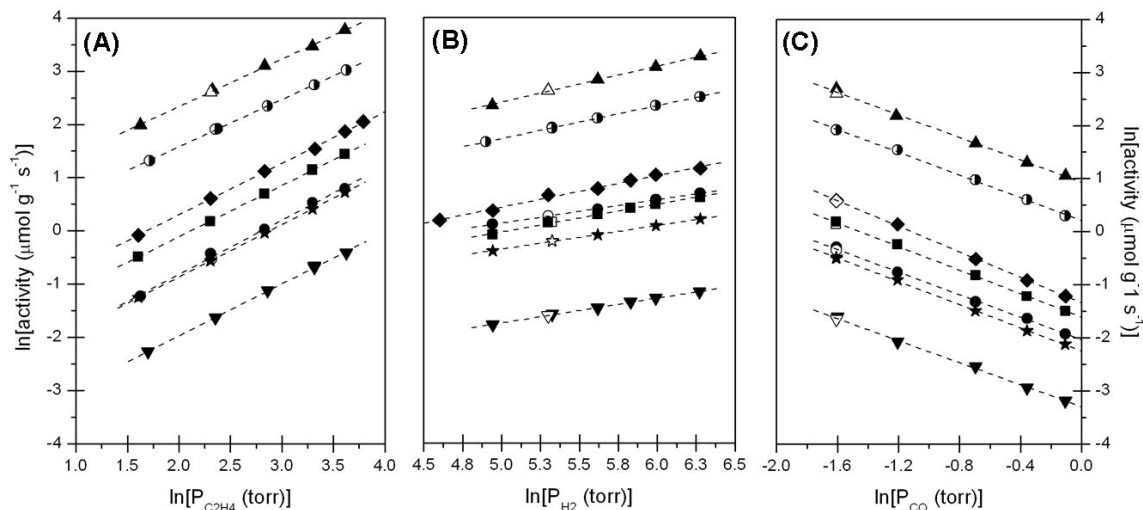
Figure 7.3. Reaction orders in (A) C_2H_4, (B) H_2 and (C) CO during C_2H_4 hydrogenation in the presence of CO. Reaction conditions were (A) 10 Torr C_2H_4, 140-540 Torr H_2, 0.2 Torr CO and 403 K; (B) 5-40 Torr C_2H_4, 200 Torr H_2, 0.2 Torr CO and 403 K and (C) 10 Torr C_2H_4, 200 Torr H_2, 0.2-0.9 Torr CO and 403 K. (▲) 3.2% Pt/SiO$_2$; (●) Pt powder; (◆) Pt(1.7 nm)/SBA-15; (■) Pt(2.9 nm)/SBA-15; (★) Pt(3.6 nm)/SBA-15; (▼) Pt(7.1 nm)/SBA-15; (◑) Pt/Al$_2$O$_3$

competitive adsorption between C_2H_4 and H_2, which is insignificant in the presence of CO because adsorbed CO displaces H_2 to surface sites inaccessible to ethylene. In the case of CO and C_2H_4, adsorption of these two species is competitive. The reaction order in ethylene is zero order in the absence of CO near 273 K [24–26] and becomes more negative at higher temperatures [23], but increases to 1st order when CO is present at 403 K. Under the reaction conditions of this study, the coverage of ethylene is low [27] and the surface is dominated by atop adsorbed CO. The pressure dependence in ethylene hydrogenation remains first order for gas phase pressures of CO ≥ 0.2 Torr (Figure 4) suggesting that the surface chemistry of ethylene at high temperatures in the presence of CO completely changes from inhibition to a dependence directly proportional to the gas phase ethylene pressure.
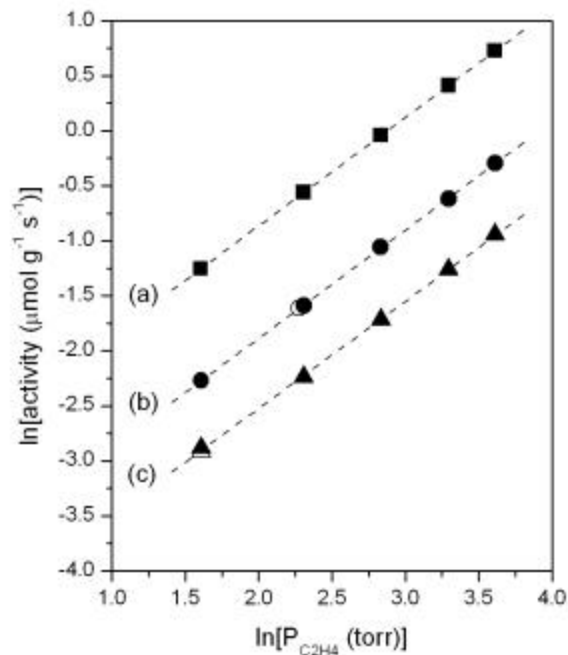
Figure 7.4. Reaction orders in C_2H_4 during C_2H_4 hydrogenation in (a) 0.2 Torr, (b) 0.5 Torr and (c) 0.9 Torr CO on 0.6 % Pt(3.6 nm)/SBA-15. Reaction conditions were 10 Torr C_2H_4, 200 Torr H_2, stated CO pressure and 403 K.

7.3.2   *In-situ diffuse reflectance spectroscopy under reaction conditions*

The hydrogenation of ethylene under reaction conditions (10 Torr C_2H_4, 100 Torr H_2, 1 Torr CO) was measured in the diffuse reflectance cell to probe the surface under reaction conditions. Figure 5 is a DRIFTS spectrum of a 2.69% Pt(2.9 nm)/SBA-15 catalyst under reaction conditions at 403 K. The rate determined in the DRIFTS cell under these conditions was $\sim 1 \times 10^{-2}$ s^{-1}. Assuming differential operation using 10 mg of catalyst, the estimated conversion in this DRIFTS cell is 0.001 %. The only adsorbed species under reaction conditions is linear bonded CO; the band position is redshifted relative to CO adsorbed on a clean surface at the same temperature [16]. No surface species are observable under reaction conditions at 300 and 403 K for the unpoisoned
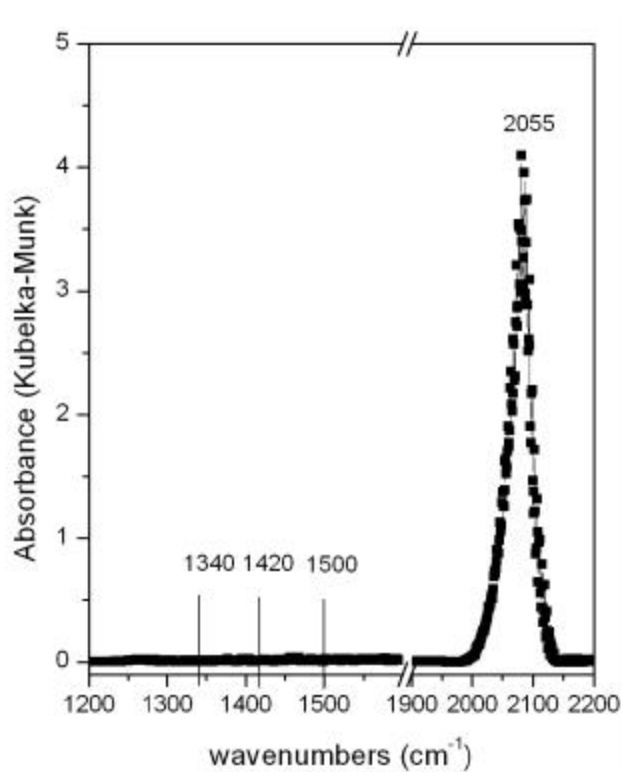
Figure 7.5. *In-situ* DRIFTS spectra of C_2H_4 hydrogenation (10 Torr C_2H_4, 100 Torr H_2) at 403 K in the presence of 1 Torr CO on 2.69 % Pt(2.9 nm)/SBA-15. The frequency for linear (atop) bound CO is 2055 cm^{-1}, peaks associated with ethylidyne (~1340 cm^{-1}), di-σ bonded ethylene and π-bonded ethylene (~1500 cm^{-1}) are absent from the surface during catalytic turnover.

reaction (spectra not shown), in agreement with previous results from a Pt/cabosil catalyst [23]. The reason for no ethylidyne identification is most likely due to the high H_2: ethylene ratio (=10) used and the low ethylene coverage expected at this temperature.

7.4   Discussion

7.4.1   Comparison of unpoisoned and CO poisoned ethylene hydrogenation kinetics

Steady state activities and turnover frequencies for the hydrogenation of ethylene in the presence of 0.5 Torr CO are compiled in Table 2. Activities (per gram catalyst) and turnover frequencies are reported at standard conditions of 10 Torr C_2H_4, 100 Torr

H_2, 0.5 Torr CO and 403 K. Ethylene hydrogenation rates ranged from $1.7\text{-}3.5 \times 10^{-2}$ s^{-1} at standard conditions. Extrapolated rates at standard pressure conditions in the absence of CO to 403 K, are ~ 200 s^{-1}. Previous work has shown that only ppm quantities of carbon monoxide are necessary to completely deactivate a Pd/charcoal catalyst for ethylene hydrogenation [28]. Chen *et al*. [29, 30] have shown that the addition of 10 Torr CO to benzene hydrogenation at 298 K on a Pt/SiO_2 catalyst reduced the hydrogenation by only a factor of four; CO is significantly less influential on benzene hydrogenation than ethylene. Interestingly, the authors found that CO pressures up to 20 Torr were insufficient to eliminate benzene hydrogenation activity and only at pressures $\geq$ 30 Torr CO was hydrogenation eliminated. These results differ considerable compared to ethylene hydrogenation in the presence of CO, catalysts were not active until the temperature was $\geq$ 353 K and low CO pressures ($\gtrsim$ 1 Torr) was sufficient to complete deactivate low temperature hydrogenation. It is possible that very low CO coverage may promote the hydrogenation of ethylene which has been observed with sulfur on polycrystalline Pt due to a "positive" electronic effect of adsorbed sulfur on neighboring atoms [31]. Above a critical coverage, the promotional effect of sulfur became a poisonous one. A similar phenomenon has been found in $H_2\text{-}D_2$ exchange, in which the exchange rate was maximized at a sulfur coverage of 1/9 [32]. Scanning tunneling microscopy studies have shown that presence of adsorbed CO on Pt(111) leads to the formation of static structures which completely eliminates $H_2\text{-}D_2$ exchange at room temperature [33]. A plausible mechanism for CO poisoning is hindrance of adsorbate mobility, a critical component for catalytic turnover [11]. The influence of CO on ethylene hydrogenation is complex, one in which adsorbate segregation may play a key

role and different types of active sites are apparently available on the surface. These issues are discussed in the proceeding sections.

7.4.2   Effect of CO addition on the apparent reaction energy

The second consequence of CO addition was a doubling of the apparent activation energy. Apparent activation energies increased from ~ 10 to ~ 20 kcal mol^{-1} in the presence of 0.2 Torr CO. This doubling of the apparent activation energy was also observed on a Pt(111) single crystal in the presence of 1 Torr CO [11, 12]. The gas phase pressure of CO had little influence on the measured value of the apparent activation energy. In 0.3, 0.5 and 0.9 Torr CO, apparent activation energies of 20.6, 20.1 and 20.8 kcal mol^{-1}, respectively, were measured. Similarly, the apparent activation energy for cyclohexene hydrogenation on Pt(111) doubled in the presence of 0.015 Torr CO [34]. Butt and co-workers found that the apparent activation energy for methylcyclopropane hydrogenolysis increased with CO coverage ranging from 0 to 0.6 on a Pt/Al$_2$O$_3$ catalyst [35], which the authors suggest reflects the increasing influence of CO in progressively displacing the reaction to less favorable sites. In a separate study of the same reaction on Pd/SiO$_2$ [36, 37], the authors found the opposite trend; the apparent activation energy decreases with the addition of CO ($\theta \leq 0.5$). In the case of Pd, the authors suggest that small levels of CO immediately remove a population of high activation energy sites from the reaction, although the turnover frequency for n-butane formation at $\theta = 0.5$ is an order of magnitude lower than the rate on a clean surface. In these experiments, CO was preadsorbed by pulse chemisorption before reaction, a method which may lead to different poisoning results than found in these steady state measurements where a constant coverage is maintained.

7.4.3   Carbon monoxide dominates surface chemistry: C_2H_4-CO competitive adsorption

and H_2 surface site distinction

Reaction orders in C_2H_4 and H_2 in hydrogen are $\sim$ 0 and ½, respectively in the absence of CO at low temperatures (<300 K) [2, 23], suggesting that the surface is saturated with ethylene and gas phase hydrogen is in equilibrium with surface H atoms adsorbed to sites not accessible ethylene. At higher temperatures (>340 K), the reaction order in hydrogen approaches unity and the ethylene coverage decreases as both species begin to adsorb to the same type of site. In the presence of CO, the reaction order in hydrogen remains $\sim$ ½ while the ethylene dependence becomes 1st order, suggesting that C_2H_4 and CO compete for the same adsorption sites. H_2 is able to adsorb and dissociate on a CO covered surface most likely because of the availability of adsorption sites that cannot be accessed by CO or ethylene due to steric reasons or potentially due to more complicated co-adsorption phenomena. Vacuum and high pressure studies of CO-H_2 coadsorption have suggested that both adsorbates segregate into islands, in which the local coverage within CO islands is near saturation coverage (θ = 0.68 ML). These locally high coverage CO regions causes a substantial lowering of the CO desorption energy ($\sim$30 kcal mol^{-1} at low coverage to $\sim$10 kcal mol^{-1} at saturation) due to repulsive interactions. Gland and co-workers [38] have shown that the hydrogen (0.2 Torr) induced displacement of CO is first order with an apparent activation energy of $\sim$11 kcal mol^{-1} above room temperature (313-348 K), in agreement with desorption from a highly compressed CO adlayer. If the heat of adsorption of H_2 is greater than the CO desorption energy at saturation, then hydrogen will displace the more weakly bound CO [38]. In fact, the differential heat of adsorption of H_2 at saturation on Pt powder was measured by microcalorimetry as 13 kcal mol^{-1} [39], which agrees well with zero coverage heat of H_2

adsorption on various Pt single crystal surfaces (in kcal mol^{-1}, 15 for (100) [40], 13 for (110) [41], and 18 for (111) [42], 20 for stepped (997) [43]). Values as high as 30 kcal mol^{-1} have been measured on Pt/SiO$_2$ catalysts with Pt particles of varying size [44]. Regardless, the values are all higher than the reported ΔH_{ads} for CO near saturation and in the present case with hydrogen in 1000 fold excess (relative to CO), hydrogen may displace CO from the surface. From kinetic and infrared spectroscopy measurements, rather than displacing CO, H$_2$ adsorbs on sites available on a CO covered surface which additional CO are unable to adsorb upon due to steric hindrance of adjacent CO. The formation of CO islands which presumably would open up small ensembles of clean Pt atoms for H$_2$ dissociation is discounted because the measured ethylene reaction order is unity for the Pt/SBA-15 series and these small clean ensembles would represent a small fraction of surface capable of high temperature ethylene hydrogenation behavior, *i.e.* ethylene and hydrogen adsorption would be competitive and both the ethylene and hydrogen partial pressure dependencies would differ from what is experimentally observed. Island formation and dissociation of H$_2$ on clean Pt ensembles is possible if the adsorption and intermixing of pure adsorbates is faster than the timescale of C$_2$H$_4$ adsorption.

The influence of carbon monoxide on ethylene adsorption on Pt has been studied to a lesser extent, but observed ethylene adsorption kinetics suggest that CO is competing with ethylene for surface sites and kinetic studies (at these temperatures and ethylene pressures) on clean Pt/SiO$_2$ catalysts demonstrate different kinetics (ethylene inhibits H$_2$ adsorption). A recent scanning tunneling microscopy study of CO adsorption on a Pt(111) surface precovered with C$_2$H$_4$ and H$_2$ at room temperature demonstrates that densely packed (θ = 0.68 ML [45]), large mixed C$_2$H$_4$-CO unit cells exist with H atoms

apparently capable of diffusing within the unit cell [46]. The authors suggest that the H_2 diffusion rate in the densely packed adlayer is inhibited but not eliminated, suggesting that turnover will occur when hydrogen and ethylene are located on adjacent sites. The integrity of this adlayer maybe diminished or less defined at the high temperature reaction conditions used in this study where diffusion should be more facile. Sum frequency generation (SFG) surface vibrational spectroscopy studies of C_2H_4/CO coadsorption on Pt(111) under hydrogenation conditions demonstrate that atop CO and ethylidyne are present on the surface, and their maybe significant interaction between neighboring ethylidyne and CO molecules as evidenced by the red-shift of the atop CO vibration [8]. This interaction between CO and ethylidyne suggests that they form a mixed adlayer with the same unit cell dimension as the pure CO regions; requiring CO to occupy atop and near-atop sites and ethylidyne to be located in 3-fold hollow sites. Additional SFG studies have shown that two different atop CO species are present upon CO adsorption on Pt(111) precovered with ethylidyne suggesting CO is adsorbed on sites with different neighboring adsorbates [7]. There was no indication that pure ethylidyne phases are present on the surface, which is responsible in promoting the formation of π-bonded ethylene, the proposed reactive intermediate for hydrogenation [47]. Infrared investigations of ethylene hydrogenation on Pt/SiO$_2$ catalysts have shown that ethylidyne is not necessary for π-bonded ethylene formation [24]. The most plausible explanation for the increased in ethylene pressure dependence is a direct competition between CO and ethylene for surface sites and only as the pressure is increased can ethylene displace CO from the compressed, mixed adlayer and adsorb and turnover to ethane which is aided at high temperatures due to the desorption of CO. No hydrogenation activity was measured on Pt(X)/SBA-15 catalysts at temperatures below 353 K. Therefore, the state of the

adsorbate covered surface maybe very complex with islands of pure CO and a mixed

C_2H_4-CO adlayer, which are open enough to enable dissociative hydrogen adsorption and

diffusion of H atoms in the adlayers. It is not believed pure H adlayers exist on the

surface because the reaction order in hydrogen is ~ ½ and if patches of a H covered

surface existed, competitive adsorption between ethylene and hydrogen would occur on

this fraction of the surface. This situation would be reflected in a H_2 reaction order

higher than ½. Table 2 shows that the reaction order in H_2 is > ½ on the small Pt

particles (1 – 2.7 nm) which may suggest a small percentage of ethane formed occurring

through a competitive mechanism or a smaller fraction of three-fold hollow sites, the

preferred adsorption site of H_2 [48]. In fact, H_2 dependencies at room temperature on the

same catalyst are > ½, while the H_2 reaction orders on the larger particles are ~ ½ [2].

Chen and co-workers [29, 30] have identified three types of hydrogen adsorption sites on

a Pt/SiO_2 catalyst with Pt particles having a mean diameter of 8 nm. Sites for hydrogen

adsorption are still available after 20 Torr benzene and 10 Torr CO are exposed to a

Pt/SiO_2 surface at 298 K and the authors have identified the site as close packed terrace

sites and lower coordination edge sites. They suggest that the lower benzene

hydrogenation activity of a supported Pt catalyst in the presence of CO is related to the

elimination of the most reactive low coordination sites for H_2 activation due to CO

adsorption at these sites [29].

7.4.4 *Non-competitive ethylene hydrogenation mechanism in the presence of carbon monoxide can explain doubling of apparent activation energy and partial pressure dependencies*

A mechanism in presence of carbon monoxide is proposed and the corresponding

rate expression is derived. Appendix A demonstrates that a noncompetitive mechanism

with the incorporation of an equilibrated CO adsorption-desorption step is sufficient to describe the kinetics of ethylene hydrogenation in the presence of carbon monoxide. Noncompetitive mechanisms are possible when adsorption of a reactant requires multiple sites and maximum surface coverage of the reactant is reached before all sites are occupied; but does not preclude adsorption of smaller molecules on the remaining isolated vacant sites. The effect of noncompetitive adsorption on the hydrogenation of propylene and isobutylene has been previously documented [49]. The competition between carbon monoxide and ethylene for the same type of active site leads to the observed kinetic dependency. Atop sites represent the preferential adsorption site for π-bonded ethylene [50–52] and on Pt, carbon monoxide prefers to bind at an atop site, rather than in bridge or 3-fold hollow sites [16]. This competition for the same type of active site has been confirmed by transient pulse methods; the introduction of additional hydrocarbon led to an increase in the CO desorption rate, known as cross desorption, where the rate of desorption of an adsorbate is influenced by the gas phase pressure of another molecule [53, 54]. The same phenomena was observed for the reverse process, a pulse of CO led to an increased desorption of ethylene.

Diffuse reflectance infrared measurements of ethylene hydrogenation at standard conditions (Figure 5), shows the surface is dominated by atop CO species with no evidence for π-bonded C_2H_4, ethylidyne or the half-hydrogenated ethyl species. The Pt surface under ethylene hydrogenation conditions is covered with carbonaceous materials, primarily ethylidyne, but it has been shown that this overlayer is not crucial for catalytic turnover. Radioisotope ^{14}C ethylene studies [55] demonstrate that ethylidyne turnovers to ethane six orders of magnitude slower than π-bonded C_2H_4. Ethylidyne was found to be stable up to 450 K on Pt(111) upon which it dehydrogenated to C_2H and CH species [56].

Recent work by Trenary and coworkers [57] has shown that the formation of ethane through the intermediate, ethylidene may be significant at room temperature. In the presence of carbon monoxide and high H_2:C_2H_4 ratios used in this study, the coverage of all potential ethylene derived intermediates is low. The proposed reactive intermediate, π-bonded ethylene is present as only 4% of a monolayer under reaction conditions (35 Torr C_2H_4, 100 Torr H_2, 295 K) [58]. The coverage of such species is significantly lower when coadsorbed with CO as has recently been determined [16]. The coverage of CO is determined by the equilibrium between gas phase and adsorbed CO. At these conditions (0.2-0.9 Torr CO), CO saturates the Pt particle surface and a heat of adsorption of 10 kcal mol^{-1} at saturation coverage on Pt(111) has been measured by laser induced thermal desorption (LITD) [59]. An initial differential heat of adsorption of CO at 403 K has been measured on a 0.85% Pt/SiO_2 catalyst as 33 kcal mol^{-1}, which decreases to ~9.5 kcal mol^{-1} at saturation coverage [60]. The heat of adsorption will most likely decrease due to the presence of adsorbed carbonaceous species, for example, Dumesic and co-workers measured a 10-30 % decrease in the initial heat of adsorption of C_2H_4 and H_2 on an ethylidyne-saturated surface when compared to a clean Pt surface [39]. No reported heat of adsorption values under C_2H_4/CO co-adsorption conditions could be found in the literature. CO influences the overall reaction rate by inhibiting ethylene adsorption and/or displacing adsorbed ethylene from the surface. The rate-determining step (the addition of hydrogen to the half-hydrogenated intermediate (C_2H_5)) is unchanged by the presence of CO in the gas phase, although the kinetic dependency on ethylene changes due a change in the *masi*. Kinetic (Figures 3 and 4) and spectroscopic (Figure 5) measurements suggest CO is the *masi*, and therefore CO must desorb to allow ethylene adsorption and hydrogenation to occur. The particle size insensitivity to poisoning by

CO suggests that the rate-determining step requires only one or two site to turnover, since the ethylene to ethyl to ethane conversion can occur on a single site adjacent to a H atom source, namely S-H (see Appendix A). Ethylene and ethyl stability is maximized on atop sites [61] and H atom diffusion on the surface is facile at these temperatures. The penalty paid for CO removal is ~ 10 kcal mol^{-1}. The doubling of the apparent activation energy can be explained in terms of an equilibrium between gas phase CO and a CO-saturated Pt surface (Appendix A, eqn. 5). The true activation energy (E_{true}) for ethylene hydrogenation remains the same as the rate determining step doesn't change and only the *apparent* activation energy increases. The apparent activation energy in the absence of CO, E_{app} depends on E_{true} and the enthalpy of adsorption of ethylene and hydrogen, respectively, while in the presence of CO, $E_{app,CO}$ is equal E_{app} plus the contribution of the enthalpy of adsorption of carbon monoxide ($\Delta H_{ads,CO}$). The apparent activation energy for the hydrogenation of ethylene on clean Pt ranges from 8-12 kcal mol^{-1} [2, 22]; including the heat of adsorption of CO at saturation coverage, $E_{app,CO}$ increases to ~ 20 kcal mol^{-1}, in agreement with experimental observations. A mechanism based on competitive H_2 adsorption could not reproduce the observed pressure dependencies and predict a doubling of the apparent activation energy.

7.4.6 *Influence of particle size on poisoning of ethylene hydrogenation by CO*

Kinetic studies have shown that the rate of ethylene hydrogenation is independent of the arrangement of the underlying metal atoms and therefore considered a structure insensitive reaction [62, 63]. One proposal for this insensitivity is the formation of an alkyl-metal "complex" [63] which effectively eliminates the surface's identity, and the resultant, ethylidyne becomes the active site for hydrogenation of ethylene, weakly binding incoming ethylene in a π-bonded form and shuttling H atoms from the Pt surface

to the weakly bound ethylene species. An explanation for the structure insensitivity of reactions has been proposed by Boudart; the critical intermediate requires only one surface atom or perhaps two adjacent ones [63]. This scenario can envisioned for the reaction of π-bonded ethylene with adsorbed hydrogen in the absence and presence of ethylidyne. DFT calculations by Neurock and van Santen [64] have shown that H is added to ethylene via a "slip mechanism" [65] requiring three metal atoms to stabilize a transition state that has H bonded in a bridge site on Pd(111). It is possible that H may add to π-bonded ethylene on an atop Pt site, followed by the addition of hydrogen on an adjacent atop site would lead to a two site mechanism. In the presence of ethylidyne, Cremer and Somorjai [61] suggest that ethylidyne moves out of the way for ethylene to physisorb on a single platinum atom in π-bonded form because of steric hindrance and H_2 dissociatively adsorbs on clean Pt sites. This scenario again requires 1-2 sites.

A significant amount of literature suggests that the ethylidyne formation is favored on larger Pt particles and has been identified on close-packed single crystal surfaces by a number of researchers, but whose formation has not been detected on more open Pt single crystals whose surface atoms have coordination numbers similar to small Pt crystallites (1-2.5 nm) [66, 67]. The formation of this ethylidyne layer is structure sensitive [68], but its presence is not critical for catalysis on smaller particles [24, 69] but it is not known if this is true for larger particles. This may be of particular important if ethylidyne is necessary for ethylene turnover because ethylidyne is believed to require the 3-fold symmetry of (111) facets rather than random trimer assemblies of Pt atoms [70] and the presence of adsorbed CO would have a greater affect on catalysts composed of larger crystallites ($\geq$ 5 nm) because adsorbed CO would inhibit ethylidyne formation by

breaking up 3-fold hollow sites. It has been proposed that ethylidyne can be used as a quantitative probe to detect for the presence of (111) facets on the surface of nanoparticles [71]. The presence of CO on the surface limits ethylidyne mobility and static ethylidyne-CO adlayers [46] may not enable the adsorption of π-bonded ethylene due to the inability of ethylidyne to move on the surface to accommodate ethylidyne, which Cremer and Somorjai [61] have proposed must occur for ethylene adsorption.

Adsorbed carbon monoxide may have a diminished effect during ethylene hydrogenation on smaller Pt crystallites because of the inability of ethylidyne to form on such small crystallites. Results are not conclusive (although a significant amount of single crystal work supports the claim); but the hydrogenation of ethylene of larger crystallites may *require* the ethylidyne adlayer whose formation would be suppressed in the presence of adsorbed CO due to site blocking and dilution of favored 3-fold hollow sites for C_2H_3 adsorption, while this layer is not necessary on small Pt nanoparticles because of their high concentration of atop sites, the preferred adsorption site for π-bonded ethylene. This would lead one to suggest that smaller crystallites maybe less affected by the presence of carbon monoxide because the rate is inhibited by site blocking rather than a combined site blocking and a disruption of the formation of the catalytic active surface. In fact, the influence of particle size on the ethylene hydrogenation turnover frequency poisoned by the addition of 0.5 Torr CO is shown in Figure 6 and the rate follows a trend in which larger particles are influenced to a greater extent by the presence of CO, although the difference in rate on small and large particles is only a factor of two. Rates of the poisoned ethylene hydrogenation reaction on large Pt particle catalysts, *i.e.* Pt(7.1 nm)/SBA-15 and Pt powder are in agreement with the rate measured on Pt(111) [7–9] confirming that ethylene hydrogenation rates are slightly more sensitive

to CO poisoning on large particles. Ethylene hydrogenation rates at room temperature in the absence of carbon monoxide are included in Figure 6 and are ~ 3.5 regardless of particle size.
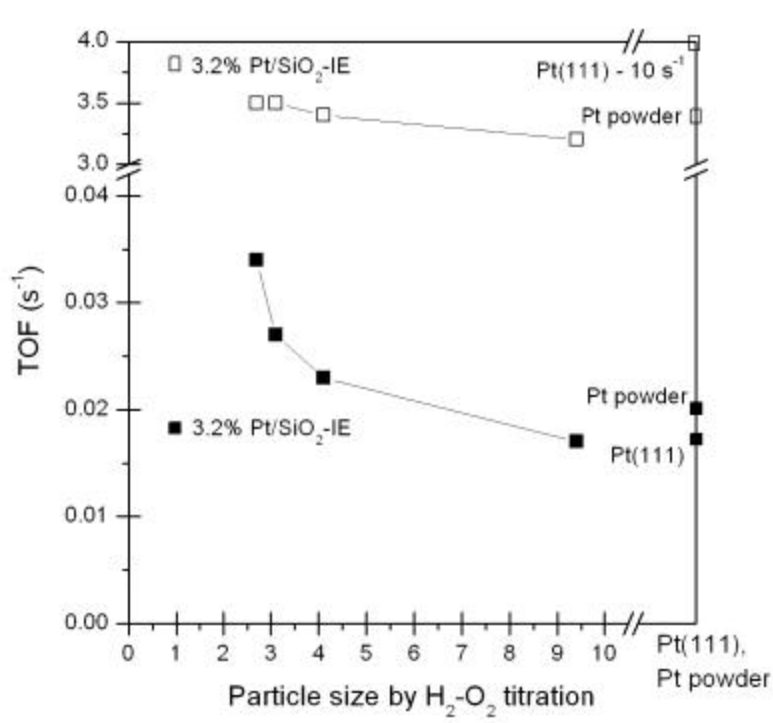
Figure 7.6. Influence of Pt particle size on turnover frequency for ethylene hydrogenation in the absence or presence of CO. ($\square$) Reaction conditions were 10 Torr C_2H_4, 100 Torr H_2, 0 Torr CO and 298 K. ($\blacksquare$) Reaction conditions were 10 Torr C_2H_4, 100 Torr H_2, 0.5 Torr CO and 403 K.

The rate of the smallest particles (~ 1 nm) on the ion exchanged Pt/SiO_2 spectrum has been excluded from this interpretation. If considered, the rate appears to proceed through a maximum at ~2.5–3 nm, again the change in rate with particle size no greater than a factor of two. One explanation for the sympathetic-antipathetic behavior [72] leading a maximum in turnover frequency has been related to the role of low coordination sites, distribution of crystal faces and/or a maximum in special ensemble (*i.e.* B_5 sites [73]) concentration. Butt and co-workers [35–37] found that poisoning of methylcyclopropane

MCP) hydrogenolysis, a structure sensitive reaction by CO was strongly dependent upon Pd and Pt particle size; a maximum in turnover frequency was observed, which the authors suggest is due to an optimal distribution of low index planes and defects. The apparent structure insensitivity of ethylene hydrogenation is upheld in the presence of CO, even though infrared measurements suggest that the nature of CO adsorption changes with Pt particle sizes. The particle size insensitivity to poisoning by CO suggests that the rate-determining step requires only one or two site to turnover.

7.4.7   *Comparison of CO poisoned ethylene hydrogenation rates with previously reported Pt catalytic structures.*

The poisoning of ethylene hydrogenation by carbon monoxide on a number of different Pt based catalysts has been studied by Somorjai *et al* [7–10]. Turnover rates corrected to standard conditions are compiled in Table 3. Rates vary by three orders of magnitude at identical poisoning conditions. The reported ethylene hydrogenation rate in the presence of ~0.5 Torr CO at 403 K on a Pt(111) single crystal is 1.7×10^{-2} s^{-1}, which is ~5 orders of magnitude lower than the rate in the case of the unpoisoned reaction [74]. The presence of CO in the feed leads to a doubling of the apparent activation energy on Pt(111) when 1 Torr was introduced to the reactor chamber [7–9]. Rates on SiO_2 and Al_2O_3 supported Pt nanowire arrays were an order of magnitude more active than Pt/SBA-15 and the Pt single crystal. In the case of the nanowire arrays, the apparent activation energy in the absence and presence of 0.3 Torr CO was ~13 and ~21 kcal mol^{-1}, respectively, in good agreement with the ΔE_{app} measured on the Pt/SBA-15 catalysts suggesting that preexponential factor is influenced to a less extent on the nanowire arrays. In the case of Pt nanoparticle arrays on SiO_2 and Al_2O_3 supports, the turnover frequencies were three orders of magnitude higher than the Pt/SBA-15 catalysts. The authors suggest

that increased activity of these nanoparticle arrays is due to sites at the metal oxide interface which are not poisoned by CO. Correction of the nominal turnover rate by using simple geometric arguments which only account for the sites located at this metal oxide interface; the turnover frequency based only on perimeter sites (7.1 s^{-1}) is similar to the unpoisoned catalyst (7.3 s^{-1}) [10]. Interestingly, apparent activation energies on the nanoparticle catalyst only increased by ~ 2 kcal mol^{-1} upon the addition of CO. It has been suggested that the enhanced activity of the nanoparticle arrays is due to the rapid hydrogenation of carbon monoxide adsorbed to these sites [75]. While it has been shown that the rate of CO hydrogenation is enhanced at the metal oxide interface [76], no such enhancement was observed for CO hydrogenation on Pt/SiO_2 [77, 78] and extrapolation of methane formation rate to conditions relevant for C_2H_4 hydrogenation in the presence of CO (1 Torr CO, 100 Torr H_2, and 473 K), a nominal turnover frequency of ~ 10^{-5} s^{-1} is estimated. Calculating the CO hydrogenation turnover frequency based only on metal oxide interface sites (assuming no structure sensitivity or enhanced reactivity at the interface), the rate is ~10^{-3} s^{-1}, significantly lower than the olefin hydrogenation rate (~ 7 s^{-1}) in the presence of CO confirming that the enhanced activity of the Pt nanoparticle array catalysts can not be due to rapid CO hydrogenation.

Beyond the work reported on Pt, very few studies have been found demonstrating the influence of carbon monoxide on ethylene hydrogenation. A study of ethylene hydrogenation poisoned by ppm levels of CO has been studied on Pd/charcoal catalysts; the resistance to poisoning by CO was dependent upon the Pd crystallite size distribution and their location in the carbon particles [28]. Catalysts with very uniform crystallite distribution and no Pd crystallites located at the carbon edges were the most resistant to poisoning while catalysts consisting of Pd particles mainly located on the external edge

Table 7.3. Compilation of C_2H_4 ethylene hydrogenation kinetics in the presence of CO

Catalyst	C_2H_4 hydrogenation with CO at standard conditions[a] TOF (s^{-1})	Reference
Pt powder	3.3×10^{-2}	this work
3.2% Pt/SiO$_2$	3.3×10^{-2}	this work
2% Pt/Al$_2$O$_3$	6×10^{-2}	this work
0.6% Pt(1.7nm)/SBA-15	6.2×10^{-2}	this work
0.77% Pt(2.9nm)/SBA-15	4.7×10^{-2}	this work
0.6% Pt(3.6 nm)/SBA-15	4×10^{-2}	this work
0.62% Pt(7.1 nm)/SBA-15	2.8×10^{-2}	this work
Pt(111) single crystal[b]	2.8×10^{-2}	[9, 75]
28nm Pt nanoparticle array on Al$_2$O$_3$	9	[9, 75]
28 nm Pt nanoparticle array on SiO$_2$	33	[10]
22 nm Pt nanowire array on Al$_2$O$_3$	0.5	[10]
25 nm Pt nanowire array on SiO$_2$	0.2	[10]
64 nm Pt nanowire array on SiO$_2$	0.4	[10]

[a]Standard conditions are 10 Torr C_2H_4, 100 Torr H_2, 0.3 Torr CO and 403 K.
[b]Pt single crystal rate extrapolated from 10 Torr C_2H_4, 100 Torr H_2, 1 Torr CO and 403 K assuming inverse first order dependence in CO.

of the carbon particles were the most susceptible to poisoning. Similarly, Pease and co-workers have found that the addition of small amounts of CO [79] and NO [80] to the ethylene hydrogenation over Cu catalysts leads to severe inhibition even at amounts significantly smaller than the hydrogen capacity of the catalyst.

7.5   Summary

Kinetics for the CO poisoned hydrogenation of ethylene were measured and differed substantially (~ 4-5 orders of magnitude) from the unpoisoned reaction. The apparent activation energy, ethylene and hydrogen order changed in the presence of low pressure CO (0.2-1 Torr). In the absence of CO at temperatures greater than 340 K and low ethylene partial pressures, ethylene inhibits the reaction by occupying sites suitable for H_2 dissociation and correspondingly the dependence on H_2 is ~1st order. In the presence of CO, the reaction rate is first order in ethylene and ½ order in H_2. Kinetic measurements demonstrate that C_2H_4 dependence is invariant with CO pressures greater than 0.2 Torr, suggesting that the surface is saturated with CO, leading to the inverse first order dependence on CO pressure. Measured apparent activation energies double for all samples regardless of particle size and do not change with CO pressure. This increase is a consequence of the adsorption equilibrium maintained between adsorbed and gas phase CO and not a change in the rate-determining step. The only surface species observed by *in-situ* diffuse reflectance spectroscopy during the hydrogenation of ethylene in the presence of CO was linear bound CO whose frequency position was redshifted relative to CO adsorption on a clean surface of the same catalyst, suggesting that ethylene derived species are present on the surface and influence the electronic structure of adsorbed CO.

Inclusion of a CO adsorption-desorption equilibrium to the noncompetitive Horiuti-Polanyi mechanism for ethylene hydrogenation reproduces the experimentally measured kinetics. The hydrogenation of ethylene on clean Pt catalysts is structure insensitive and remains as such in the presence of CO. Larger Pt particles are influenced by CO to a greater extent, although the difference in the poisoned rate for catalysts with particle size ranging from 1.7–7.1 nm is only a factor of two.

7.6 Appendix A: Incorporating carbon monoxide into a noncompetitive ethylene hydrogenation mechanism.

Horiuti and Polanyi proposed a mechanism for the hydrogenation of ethylene over Ni catalysts, in which the ethylene is hydrogenated to ethane through a half-hydrogenated intermediate [17]. In this mechanism, ethylene and hydrogen compete for the same type of site. This mechanism does not capture the low temperature macroscopic reaction kinetics. A noncompetitive variant of the Horiuti-Polanyi has been proposed in which hydrogen and ethylene adsorb on separate types of active sites, but this mechanism is incapable of reproducing high temperature kinetics. Both mechanisms are unable to reproduce the experimental kinetics over a range of conditions (ethylene: H_2 ratios and temperature). At the high temperatures (403 K) and low ethylene pressures (5-40 Torr) used in this work, Dumesic *et al.* have shown by combining results from steady state kinetic and temperature programmed measurements, deuterium tracing experiments, and microkinetic modeling, a H_2 activated noncompetitive-competitive mechanism can reproduce experimental kinetic data [27]. In this appendix, a rate expression which accounts for the observed kinetics in the presence of carbon monoxide is derived by only

the addition of a CO adsorption-desorption equilibrium step to the noncompetitive mechanism is derived.

The noncompetitive Horiuti-Polanyi ethylene hydrogenation mechanism consists of four elementary steps:

1. Non-competitive hydrogen adsorption: $H_2 + 2S \rightleftharpoons 2H\text{-}S$

2. Ethylene adsorption: $C_2H_4 + * \rightleftharpoons C_2H_4*$

3. First surface hydrogenation reaction: $C_2H_4* + H\text{-}S \rightleftharpoons C_2H_5* + S$

4. Surface reaction of half hydrogenated intermediate: $C_2H_5* + H\text{-}S \rightarrow C_2H_6 + * + S$

where steps (1)-(3) are quasi-equilibrated ($\rightleftharpoons$) and step (4) is rate determining. Steps (1)-(4) constitute a catalytic cycle; a single turnover of ethylene to ethane and regeneration of both the * site and S site pair, respectively. Surface sites denoted by * are adsorption sites for hydrocarbons only, while sites denoted by S are for hydrogen adsorption. In the absence of carbon monoxide, the surface coverage of carbonaceous species is high at low temperatures but decreases at higher temperatures (> 340 K) due to poor adsorption thermodynamics. Adsorption in a π-bonded or di-σ configuration requires at least a single site (*) or pair(*-*) and potentially more due to steric considerations [27]. Hydrogen atoms adsorb in threefold hollow sites on Pt(111) [48], and if ethylene adsorbs randomly on the surface, hydrogen adsorption sites exist on the ethylene covered surface because pairs of threefold sites near ethylene are sterically blocked from adsorbing another ethylene molecule [27].

Formulation of rate expression assuming the above sequence of elementary steps with adsorbed carboneacous species as the most abundant * species and adsorbed hydrogen saturating the S sites, a mechanism consistent with low temperature kinetics is

obtained; zero order ethylene and reversible, ½ order hydrogen kinetics. The coverage of

hydrogen (θ_{H-S}) is determined by step (1) and dependent upon the square of the H_2

pressure: $\theta_{H-S} = K_{H-S}^{1/2} P_{H_2}^{1/2} \theta_S$ and independent of the pressure of ethylene (due to the two

site mechanism). A competitive (*i.e.* single site) mechanism assuming the site in step (1),

S is *, leads to a rate expression which is unable to capture the experimentally observed

kinetics at low temperature.

   The introduction of carbon monoxide leads to experimental kinetics different than

those observed in the hydrogenation of ethylene in the absence of adsorbed carbon

monoxide. As shown in Table 2, the reaction order in C_2H_4 is unity, ½ in H_2 and -1 in

carbon monoxide, respectively. Figure 4 also demonstrates that the reaction order in

ethylene is first order regardless of CO pressure. The hydrogen reaction order remains

~½, regardless of CO or ethylene pressure (not shown). This leads to the formulation that

adsorption between H_2 and C_2H_4 is noncompetitive at high temperatures in the presence

of CO, in contrast with the competitive nature of C_2H_4 and H_2 adsorption in the absence

of CO at similar temperatures. For example, at 336 K, Cortright *et al.* measures a -0.43

order dependence on C_2H_4 in the absence of CO on a Pt/SiO_2 catalyst [23]. Adsorption

between CO and ethylene is competitive with the rate of hydrogenation directly

proportional to the ethylene pressure and adsorbed CO dominating the surface under

reaction conditions (see Figures 4 and 5). The adsorption of CO on the surface is

governed by the following equilibrium

   5. CO adsorption: $CO + * \rightleftharpoons CO*$
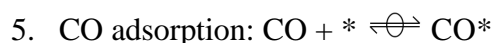
and the coverage of CO is defined as $\theta_{CO} = K_{CO} P_{CO} \theta_*$, where K_{CO} is the equilibrium

adsorption constant, and θ_* is the fraction of empty * sites. Retaining the uncompetitive

mechanism with the addition of a CO adsorption-desorption equilibrium step leads to the

½ order H_2 dependency, inverse first order CO dependency if CO is the most abundant

surface species on * type sites (as suggested by infrared measurements, Figure 5). The

rate of formation of C_2H_6 is determined by the rate determining addition of adsorbed

hydrogen to the half-hydrogenated intermediate, $r = k_{app} q_{C_2H_5*} q_{H-S}$, and the complete

mechanism (steps 1-5) can be used to derive a power rate law $r = k_{app} P_{C_2H_4} P_{H_2}^{1/2} P_{CO}^{-1}$

assuming [CO*] and [H-S] are the most abundant species on their respective types of

sites, respectively. The observed rate expression correctly predicts the experimentally

observed pressure dependencies and a doubling of the apparent activation energy (as

explained in Section 4.4).

7.7   References and Notes

1.   R. M. Rioux, H. Song, J. D. Hoefelmeyer, P. D. Yang, G. A Somorjai, *J. Phys. Chem. B* 109 (2005) 2192.

2.   H. Song, R. M. Rioux, J. D. Hoefelmeyer, R. Komor, K. Niesz, M. Grass, P. Yang, G. A. Somorjai, Submitted to *J. Am. Chem. Soc*. (2005).

3.   R. M. Rioux, H. Song, S. Habas, M. Grass, J. D. Hoefelmeyer, K. Niesz, P. D. Yang, G. A. Somorjai, Accepted in *Top. Catal*. (2005).

4.   R. M. Rioux, B. Hsu, H. Song, P. D. Yang, G. A. Somorjai, To be submitted to *J. Phys. Chem. B* (2005).

5.   T. Teranish, M. Hosoe, T. Tanaka, M. Miyake, *J. Phys. Chem. B* 103 (1999) 3818.

6.   Y. Wang, J. Ren, K. Deng, L. Gui, Y. Tang, *Chem. Mater*. 12 (2000) 1622.

7.   P. Chen, K. Y. Kung, Y. R. Shen, G. A. Somorjai, *Surf. Sci*. 494 (2001) 289.

8.   P. Chen, S. Westerberg, K. Y. Kung, J. Zhu, J. Grunes, G. A. Somorjai, *Appl. Catal. A Gen.* 229 (2002) 147.

9.   J. Grunes, J. Zhu, M. Yang, G. A. Somorjai, *Catal. Lett*. 86 (2003) 157.

10.   A. M. Contreras, J. Grunes, X. –M. Yan, A. Liddle, G. A. Somorjai, *Catal. Lett*. 100 (2005) 115.

11.   G. A. Somorjai, *Nature* 430 (2004) 730.

12.   L. H. Little, *Infrared Spectra of Adsorbed Species*, Academic Press, New York, 1966.

13.   M. L. Hair, *Infrared Spectroscopy in Surface Chemistry*, Dekker, New York, 1967.

14. M. Frank, M. Bäumer, R Kühnemuth, H. –J. Freund, *J. Vac. Sci. Technol. A* 19 (2001) 1497.

15. G. Blyholder, *J. Phys. Chem.* 68 (1964) 2772.

16. R. M. Rioux, J. D. Hoefelmeyer, M. Grass, H. Song, K. Niesz, P. D. Yang, G. A. Somorjai, To be submitted to *J. Catal*. (2005).

17. I. Horiuti, M. Polanyi, *Trans. Faraday Soc*. 30 (1934) 1164.

18. U. K. Singh, M. A. Vannice, *J. Catal*. 191 (2000) 165.

19. J. E. Benson, M. Boudart, *J. Catal*. 4 (1965) 704.

20. H. Song, F. Kim, S. Connor, G. A. Somorjai, *J. Phys. Chem. B* 109 (2005) 188.

21. R. J. Madon, M. Boudart, *Ind. Eng. Chem. Fundam*. 21 (1982) 438.

22. J. Horiuti, K. Miyahara, "Hydrogenation of Ethylene on Metallic Catalysts." NBS-NSRDS 13, U. S. Government Printing Office, Washington, DC, 1968.

23. R. D. Cortright, S. A. Goddard, J. E. Rekoske, J. A. Dumesic, *J. Catal*. 127 (1991) 342.

24. J. E. Rekoske, R. D. Cortright, S. A. Goddard, S. B. Sharma, J. A. Dumesic, *J. Phys. Chem*. 96 (1992) 1880.

25. J. C. Schlatter, M. Boudart, *J. Catal*. 24 (1972) 482.

26. G. C. Bond, J. J. Phillipson, P. B. Wells, J. M. Winterbottom, *Trans. Faraday Soc*. 60 (1964) 1847.

27. J. A. Dumesic, D. F. Rudd, L. M. Aparicio, J. E. Rekoske, A. A. Treviño, *The Microkinetics of Heterogeneous Catalysis*, ACS Professional Reference Book, Washington D. C., 1993, p. 113.

28. D. Pope, D. S. Walker, R. L. Moss, *J. Catal*. 28 (1973) 46.

29. C. –S. Chen, J. –H Lin, H. –W. Chen, C. –Y. Wang, *Catal. Lett*. 105 (2005) 149.

30. C. –S. Chen, J. –H Lin, H. –W. Chen, *Appl. Catal. A Gen.* 298 (2006) 161.

31. N. Barbouth, M. Salame, *J. Catal*. 104 (1987) 240.

32. C. –M. Pradier, E. Margot, Y. Berthier, J. Oudar, *C. R. Acad. Sci. Paris* 294 (1982) 1321.

33. D. C. Tang, PhD Thesis, University of California, Berkeley (2005).

34. M. Yang, R. M. Rioux, G. A. Somorjai, Accepted in *J. Catal*. (2005).

35. J. B. Butt, C. L. M. Joyal, *J. Chem. Soc., Faraday Trans*. 86 (1990) 2911.

36. D. E. Damiani, J. B. Butt, *J. Catal*. 94 (1985) 203.

37. I. Önal, J. B. Butt, *J. Chem. Soc., Faraday Trans*. 1 78 (1982) 1887.

38. J. L. Gland, D. A. Fischer, D. H. Parker, S. Shen, *Langmuir* 7 (1991) 2574.

39. B. E. Spiewak, R. D. Cortright, J. A. Dumesic, *J. Catal*. 176 (1998) 405.

40. F. P. Netzer, G. Kneringer, *Surf. Sci*. 51 (1975) 526.

41. R. W. McCabe, L. D. Schmidt, *Surf. Sci*. 56 (1977) 189.

42. K. Christmann, *Surf. Sci. Rep*. 9 (1988) 1.

43. B. Poelsema, G. Mechtersheimer, G. Comsa, *Surf. Sci*. 111 (1981) 519.

44. B. Sen, M. A. Vannice, *J. Catal*. 130 (1991) 9.

45. E. Kruse Vestergaard, P. Thostrup, T. An, E. Lægsgaard, I. Stensgaard, B. Hammer, F. Besenbacher, *Phys. Rev. Lett*. 88 (2002) 259601.

46. D. C. Tang, K. S. Hwang, M. Salmeron, G. A. Somorjai, *J. Phys. Chem. B*, 108 (2004) 13300.

47. P. S. Cremer, G. A. Somorjai, *J. Chem. Soc., Faraday Trans*. 91 (1993) 3671.

48. K. Christmann, *Surf. Sci. Rep*. 9 (1988) 1.

49.   G. B. Rogers, M. M. Lih, O. A. Hougen, *AIChE J*. 12 (1966) 369.

50.   J. Evans, G. McNulty, *J. Chem. Soc., Dalton Trans*. 1 (1984) 79.

51.   M. Grogan, K. J. Nakamoto, *J. Am. Chem. Soc*. 88 (1966) 5454.

52.   C. Anson, N. Sheppard, D. Powell, B. Bender, J. Norton, *J. Chem. Soc., Faraday Trans*. 90 (1994) 1449.

53.   L. Cider, N. –H. Schöön, *Appl. Catal*. 60 (1991) 191.

54.   L. Cider, N. –H. Schöön, *Appl. Catal*. 60 (1991) 207.

55.   S. M. Davis, F. Zaera, B. E. Gordon, G. A. Somorjai, *J. Catal*. 92 (1985) 240.

56.   T. Land, T. Michely, R. Behm, J. Hemminger, G. Comsa, *J. Chem. Phys*. 97 (1992) 6773.

57.   R. Deng, E. Herceg, M. Trenary, *Surf. Sci*. 560 (2004) L195.

58.   P. S. Cremer, X. Su, Y. R. Shen, G. A. Somorjai, *Catal. Lett*. 40 (1996) 143.

59.   E. G. Seebauer, A. C. F. Kong, L. D. Schmidt, *Surf. Sci*. 176 (1986) 134.

60.   R. D. Cortright, J. A. Dumesic, *J. Catal*. 148 (1994) 771.

61.   P. S. Cremer, X. C. Su, Y. R. Shen, G. A. Somorjai, *J. Am. Chem. Soc*. 118 (1996) 2942.

62.   T. A. Dorling, M. J. Eastlake, R. L. Moss, *J. Catal*. 14 (1969) 23.

63.   M. Boudart, *J. Mol. Catal*. 30 (1985) 27.

64.   M. Neurock, R. A. van Santen, *J. Phys. Chem. B* 104 (2000) 11127.

65.   D. L. Thorn, R. Hoffman, *J. Am. Chem. Soc*. 100 (1978) 2079.

66.   N. Sheppard, C. De La Cruz, *Adv. Catal*. 41 (1996) 1.

67.   N. Sheppard, C. De La Cruz, *Adv. Catal*. 42 (1998) 181.

68.   F. B. Passos, M. Schmal, M. A. Vannice, *J. Catal*. 160 (1996) 118.

69. T. P. Beebe, J. T. Yates Jr., *J. Am. Chem. Soc*. 108 (1986) 663.

70. D. K. Paul, T. P. Beebe, Jr., K. J. Uram, J. T. Yates, Jr., *J. Am. Chem. Soc*. 114 (1992) 1949.

71. T. P. Beebe, Jr., J. T. Yates, Jr., *Surf. Sci*. 173 (1986) L606.

72. M. Che, C. O. Bennett, *Adv. Catal*. 36 (1989) 55.

73. R. van Hardeveld, F. Hartog, *Adv. Catal*. 22 (1972) 75.

74. F. Zaera, G. A. Somorjai, *J. Am. Chem. Soc*. 106 (1984) 2288.

75. K. S. Hwang, M. Yang, J. Zhu, J. Grunes, G. A. Somorjai, *J. Mol. Catal. A Chem*. 204 (2003) 499.

76. M. E. Levin, M. Salmeron, A. T. Bell, G. A. Somorjai, *J. Catal*. 106 (1987) 401.

77. M. A. Vannice, *J. Catal*. 370 (1975) 449.

78. M. A. Vannice, *J. Catal*. 40 (1975) 129.

79. R. N. Pease, L. Stewart, *J. Am. Chem. Soc*. 47 (1925) 1235.

80. H. D. Burnham, R. N. Pease, *J. Am. Chem. Soc*. 62 (1940) 453.

Chapter 8

Removal of polymer from PVP-stabilized Pt nanoparticles encapsulated by mesoporous silica for applications in heterogeneous catalysis

8.1   Introduction

The production of nanoparticles via solution based reduction methods followed by their encapsulation in oxide matrices have enabled control of particle size [1-3] and shape [4] that has not been achieved with classical catalyst synthesis methods (*i.e.* incipient wetness, ion exchange).   In most solution-based methods, metal precursors are decomposed in a solvent via pyrolysis, reduction or oxidation in the presence of a surfactant.   Surfactants that have been employed for nanoparticle synthesis are molecular, polymeric or macromolecular (dendrimers) prevent particle aggregating while in solution. The mechanism by which these organic phases interact with metal ions and nanoparticles in solution has been investigated [5] and the mechanism by which some surfactant and polymers stabilize particles has been postulated [6].

A number of studies have shown that colloidal nanoparticles are capable of adsorbing carbon monoxide and catalyzing a variety of reactions in solution [6].   While these studies demonstrate that catalysis occurs on organic capped nanoparticles in solution, it generally accepted that the presence of the organic phase will have a negative

effect on the catalytic activity of such colloids. The extent of polymer influence maybe related to the solubility of the polymer in the supporting solvent. The influence of the protecting organic phase may change when the nanoparticles are removed from solution, dried out and placed on a solid support. Dendrimer stabilized aqueous solutions of Pt nanoparticles adsorbed carbon monoxide [7], while under dry conditions, the dendrimer completely blocks CO adsorption, presumably due to collapse of the dendrimer on the nanoparticle [8]. Similar aqueous phase behavior has been observed for colloidal nanoparticles stabilized by vinyl polymers, such as poly(vinylpyrrolidone) (PVP) [9]. The molecular structure of PVP monomer is shown in Figure 1. Complete removal of the polymer from the nanoparticle surface is critical for maximum catalytic activity and
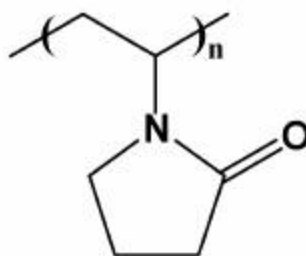
Figure 8.1. Monomer unit of polyvinylpyrrolidone (PVP). PVP with an average molecular weight of 29,000 was used for the synthesis of 1.7, 2.9 and 3.6 nm Pt particles, while PVP with an average molecular weight of 55,000 was used for the synthesis of 7.1 nm particles.

measurement of catalytic properties free of artifacts. Little work has been done with regards to PVP removal from nanoparticle surfaces even though it is a commonly used surface regulating polymer for solution phase nanoparticle synthesis of various metals, including Pd, Rh, Au and Ag [9]. Approximately, 40-50% of the surface of PVP-stabilized Pt nanoparticles dispersed in butanol is covered by PVP as determined by H_2 chemisorption and H_2-O_2 titration. Coverage dependent dipole coupling between

adsorbed carbon monoxide molecules suggested that the free sites were grouped together [10].

Recently, the removal of polyamidoamine dendrimers from Pt particles [11-15] has been investigated. Dendrimers protecting Pt nanoparticles begin decomposing at low temperatures, but complete decomposition and removal from the surface is not accomplished in oxygen until temperatures ≥ 723 K [11]. The number of Pt sites accessible to CO adsorption was greatest after oxidation (1 h) at 698 K. Calcination at 573 K for 3 h led to complete disappearance of dendrimer amide stretches, although the highest catalytic activity was achieved after a 16 h calcination [13]. In the case of dendrimer encapsulated Pt nanoparticles, relatively high temperatures (573–723 K) and variable calcination times (1–16 h) are required for dendrimer decomposition. It appears that dendrimer thermolysis is catalyzed by the presence of Pt [11] but forcing conditions which may lead to particle agglomeration are required for complete dendrimer removal [13]. It is evident from decomposition of dendrimer-stabilized Pt nanoparticles that the type of pretreatment (gas, length of treatment) determines the extent of removal of the organic phase and the stability of the as-synthesized nanoparticle. Pretreatments are therefore considered optimal when the organic phase can be completely removed with perturbing the size and/or shape of the as-synthesized particles.

The interaction and removal of PVP from nanoparticle surfaces has been studied to a lesser extent [16]. Thermolysis of free PVP and PVP-stabilized nanoparticles has been studied under inert and oxidative environments; decomposition is more facile in oxygen and platinum is a catalyst for PVP decomposition in both environments [17, 18]. Previous work on supported PVP-stabilized Pt nanoparticles has demonstrated that Pt

catalysts retained organic fragments even after a heat treatment in O_2/Ar mixtures at 573 K [16].

In this chapter, numerous oxidation-reduction schemes are applied to remove PVP from Pt nanoparticle surfaces supported in polymer template filled SBA-15 (i.e. uncalcined). The catalysts are prepared by a novel method called nanoparticle encapsulation (NE) in which SBA-15 is grown via a hydrothermal process in aqueous solution containing PVP-stabilized Pt nanoparticles [3, 4] (Figure 2). After synthesis, the
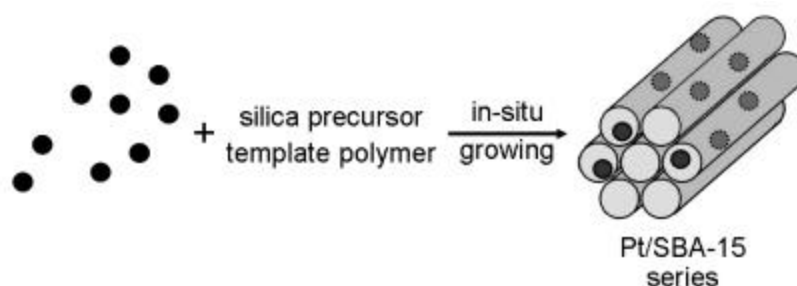
Figure 8.2. Schematic of the nanoparticle encapsulation method for the synthesis of heterogeneous catalysts.

void volume (*i. e.* mesopores) contains polymer template and the Pt nanoparticles are still capped with PVP. A standard *ex-situ* calcination procedure has previously been developed for the initial catalytic studies [3]. Infrared investigations of polymer absorption bands before and after calcination demonstrate that >95% of the polymer was removed by *ex-situ* calcination. The decomposition of polymer template and PVP from the silica pores and Pt nanoparticles, respectively from a series of Pt(X)/SBA-15 (where X = 1.7, 2.9, 3.6 and 7.1 nm) was studied by a variety of thermal methods (*i.e.* thermal gravimetric analysis (TGA), differential scanning calorimetry (DSC) and temperature programmed oxidation (TPO)). These techniques demonstrate that PVP is decomposed at lower temperatures in the presence of Pt as compared with free PVP, but the extent of

PVP decomposition is dependent upon the synthetic PVP monomer: Pt molar ratio and the as-synthesized particle size. Removal of PVP by calcination with dilute NO_2 demonstrated that stronger oxidants were not necessarily better for PVP removal. *In-situ* oxidation-reduction treatments were found to be the most effective method for PVP removal for large Pt particles (7.1 nm) while the same method was less effective on smaller particles (2.9 nm). The effectiveness of the various thermolysis methods was assessed by infrared investigations of CO adsorption, selective gas adsorption and the hydrogenation of ethylene. The research suggests that optimal catalyst pretreatment method (oxidation, reduction) are most likely sample specific; pretreatments appear to depend mostly on the PVP:Pt molar synthesis ratio, Pt particle size and pretreatment protocol (primarily extrinsic properties like batch size).

8.2   Experimental

8.2.1   *Thermal degradation of poly(vinylpyrrolidone) (PVP)*

The decomposition of free poly(vinylpyrrolidone) (PVP, M_w = 55 K (*ave.*), Sigma-Aldrich) was studied in inert (He or N_2) and reactive (O_2 and H_2) atmospheres. PVP decomposition was studied at temperatures ranging from 623 K $\leq$ T $\leq$ 723 K for variable times (2-36 h) in O_2 (Praxair, 99.9%), 0.981% NO_2/He (Praxair) or He (Praxair, UHP, 99.999%) at a flow rate of 100 cc(STP) min^{-1} in a horizontal tube furnace (Blumberg Blue). Samples of PVP (~100 mg) were placed in ceramic weigh boats (CoorsTek) and heated at 10 K min^{-1} to the stated temperature in a particular gas mentioned above. The sample temperature was measured by a thermocouple located in the center of the furnace heating zone. Decomposition of PVP in physical mixtures of

PVP:Pt/SiO$_2$ catalyst (EUROPT-1, 6.3 wt. % Pt) 10:1 weight ratio was studied in the same furnace set-up. The weight loss was determined from the difference in weight before and after treatment of dehydrated PVP.

8.2.2 Nanoparticle Synthesis

Dihydrogen hexachloroplatinate (H$_2$PtCl$_6$·6H$_2$O, 99.9%, metals basis) was purchased from Alfa Aesar. Poly(vinylpyrrolidone) (PVP, M$_w$ = 29,000 and 55,000) was obtained from Sigma-Aldrich. Methanol, ethanol, and ethylene glycol were of analytical grade and used without further purification.

Pt particles were synthesized according to literature methods [2, 19, 20]. Briefly, 1.7 nm Pt particles were prepared by adding NaOH solution (12.5 mL, 0.5 M) in ethylene glycol to a solution of H$_2$PtCl$_6$·6H$_2$O (250 mg, 0.48 mmol) in 12.5 mL of ethylene glycol. The mixture was heated at 433 K for 3 h with N$_2$ bubbling. After reaction, particles were precipitated by adding 1 mL of 2 M HCl, and dispersed in ethanol containing 12.2 mg of PVP (M$_w$ = 29,000). 2.9 nm Pt particles were synthesized by refluxing a mixture of PVP (26.6 mg, M$_w$ = 29,000) and H$_2$PtCl$_6$·6H$_2$O (124.3 mg) in water (40 mL)/methanol (360 mL) solution for 3 h. 3.6 nm Pt particles were formed by mixing the 2.9 nm Pt colloidal solution (100 mL) in a water/methanol (1:9) mixture with 10 mL of 6.0 mM H$_2$PtCl$_6$·6H$_2$O aqueous solution and 90 mL of methanol. The mixture was refluxed for 3 h. 7.1 nm Pt particles were synthesized by adding a total 3 mL of 0.375 M PVP (M$_w$ = 55,000) and 1.5 mL of 0.0625 M H$_2$PtCl$_6$·6H$_2$O solutions in refluxing ethylene glycol every 30 s over 16 min. The mixture was refluxed for an additional 5 min [21].

All Pt colloidal solutions were purified by sequential precipitation/redispersion (three times) in ethanol/*n*-hexane solution, and eventually dispersed in an appropriate

amount of deionized water necessary for a 3×10^{-3} M solution based on Pt salt concentration. The particle sizes were measured by transmission electron microscopy (TEM) and X-ray diffraction (XRD). Estimated particle sizes were 1.73 ± 0.26 (1.7), 2.80 ± 0.21 (2.9), 3.39 ± 0.26 (3.6), and 7.16 ± 0.37 (7.1) nm by TEM (XRD) respectively, indicating high uniformity and monodisperse nanoparticles ($\sigma \sim 8\%$) [2]. The mean TEM particle size is based on a Gaussian distribution fit to the experimentally observed particle size distribution.

8.2.3   Synthesis of mesoporous silica under neutral conditions

Pluronic P123 ($EO_{20}PO_{70}EO_{20}$, EO = ethylene oxide, PO = propylene oxide, BASF), tetramethyl orthosilicate (TMOS, 98%, Aldrich), and sodium fluoride (99.99%, Aldrich) were used as received. 2.5 g of Pluronic P123 was completely dissolved in 50.5 mL of deionized water and stirred for 1 h at 313 K to ensure a homogeneous solution. 0.375 mL of 0.5 M NaF aqueous solution was added, and 3.91 mL of TMOS was quickly added to the reaction mixture, followed by stirring for a day at 313 K.   The resulting slurry was aged for an additional day at 373 K. The white precipitates were separated by centrifugation, thoroughly rinsed with ethanol, and dried in an oven at 373 K to remove residual water and ethanol. The standard ethanol rinse was 500 mL (total volume) under low vacuum.

8.2.4   Catalyst Synthesis

Pluronic P123 ($EO_{20}PO_{70}EO_{20}$, BASF), tetramethyl orthosilicate (TMOS, 98%, Aldrich), and sodium fluoride (99.99%, Aldrich) were used as received. 2.5 g of Pluronic P123 was completely dissolved in 50.5 mL of deionized water. The Pt colloidal aqueous solution (27.0 mL, 3×10^{-3} M) was mixed with the polymer solution and stirred for 1 h at

313 K. 0.375 mL of 0.5 M NaF aqueous solution was added, and 3.91 mL of TMOS was quickly added to the reaction mixture, followed by stirring for a day at 313 K. The resulting slurry was aged for an additional day at 373 K. The brown precipitates were separated by centrifugation, thoroughly washed with ethanol, and dried in an oven at 373 K. The standard wash procedure was identical to pure mesoporous silica. Catalysts were prepared for nominal Pt weight percent of 3%, but post-rinse catalysts had Pt weight loadings ranging from 2.3-2.9 %. It is believed that during synthesis some fraction of the nanoparticles included in the Pluronic P123 micelles are removed during the ethanol rinse.

Previously, these materials were calcined and reduced by a sample dependent standard protocol [3]. 1.7 nm particles were calcined at 623 K for 24 h, while 2.9 and 3.6 nm catalysts were calcined at 723 K for 24 hours. The 7.1 nm catalyst was calcined at 723 K for 36 hours. Calcination times were based on the previous attempts to remove PVP from Pt nanoparticles located in pre-calcined SBA-15 channels [2]. In the NE samples used in this chapter, the SBA-15 channels are filled with silica polymer template suggesting that additional calcination time may be required or even stronger oxidants (such as NO_2, O_3) are necessary. All catalysts were reduced according the following protocol prior to chemisorption or reaction; heat to 473 K in 50 cc (STP) He min^{-1} and hold for 1 h, followed by heating to 673 K in He after which the flow was changed to 50 cc (STP) H_2 min^{-1} and the catalyst was reduced for 75 minutes. After reduction, the catalyst was cooled to 623 K and purged with He for 1h and subsequently cooled to the chemisorption or reaction temperature. Previous unpublished results from our group have proven that the reduction temperature and duration had little effect on Pt dispersion. The purpose of this work is to determine the most effective calcination method for removal of

PVP. A distinction is made in the paper between *ex-situ* and *in-situ* calcination. *Ex-situ* calcination refers to calcination of ~300-400 mg catalyst in a horizontal tube furnace, while *in-situ* calcination occurs in the catalytic reactor (or chemisorption cell) before reduction on a small batch of catalyst (~ 5-20 mg). Experimental conditions (flow rates, heating rates) were identical whether calcination was *ex-situ* or *in-situ*. *In-situ* pretreatment consisted of oxidation-reduction cycles; 1 h calcination in O_2 (Airgas, 99.99%) followed by purging in He (Praxair, 99.999%) for ½ h and reduction in H_2 (Praxair, 99.999%) at a specified temperature (373–673 K) for 1 h.

8.2.5   Catalyst Characterization

Physical characterization of as-synthesized catalyst

TEM experiments were carried out on a Philips CM200 microscope operated at 200 kV at the National Center for Electron Microscopy at Lawrence Berkeley National Laboratory. Catalysts were sonicated in acetone for 10 s, dropped on lacey carbon film coated copper grids (Ted Pella), and dried in air. XRD patterns were measured on a Bruker D8 GADDS diffractometer using Co Kα radiation (1.79 Å). XRD scans were conducted from $10 \leq 2\theta \leq 90°$ at a scan rate of $5°$ min^{-1}. Elemental analyses by inductively coupled plasma–atomic emission spectroscopy (ICP–AES) were conducted at Galbraith Laboratories, Inc. (Knoxville, TN.)

Thermal analysis (gravimetry and temperature programmed oxidation) of SBA-15 and Pt/SBA-15

Thermogravimetric analysis (TGA) experiments on the as-synthesized NE silica as well as the decomposition of PVP from as-synthesized Pt 7.1 nm nanoparticles were conducted on a Seiko Instruments SSC 5200 TG/DTA 220 under a 100 cc (STP) O_2 min^{-1}

flow. The PVP decomposition from the 7.1 nm Pt particle surface was conducted at 10 K min^{-1}. Temperature programmed oxidation (TPO) measurements of PVP powder, uncalcined SBA-15 and Pt/SBA-15 catalysts were conducted in a quartz U-tube flow reactor developed in-house. Samples (50-100 mg) were heated linearly (2 K min^{-1}) by a temperature controller (Cole Parmer Digi-Sense 89000-10) with a 0.5 mm-OD thermocouple extending into the center of the catalyst bed. Effluent lines to the mass spectrometer (Stanford Research Systems quadrupole residual gas analyzer, 100 amu) were heated to 550 K to prevent condensation of H_2O and liquid hydrocarbons. Under 70 cc (STP) min^{-1} oxygen flow, the total combustion products, CO_2 (44 amu), H_2O (18 amu) and nitrogen oxides (NO_x) (30 amu) were monitored. It was difficult to distinguish between the nitrogen containing oxides due to their efficient splitting in the mass spectrometer, so their measured values are collectively reported as NO_x. Carbon monoxide/nitrogen (28 amu) and small hydrocarbons (C_1-C_3 alkanes) were monitored but it proved difficult to determine if they were present in the effluent. Attempts at following ammonia (17 amu) were unsuccessful due to the large signal from evolved water. Results were quantified using standard mixtures of carbon dioxide, water and NO_x with O_2 as the balance gas. The effluent curves were integrated numerically using the rectangular rule with data recorded at 0.5 Hz.

FTIR measurements of PVP decomposition and CO adsorption on Pt/SBA-15

In-situ diffuse reflectance infrared Fourier transform spectroscopy (DRIFTS), using a Nicolet Nexus 670 spectrometer equipped with a Thermo Spectra-Tech controlled atmosphere-diffuse reflection cell was used to study the adsorption of CO on Pt/SBA-15 catalysts. Catalysts were loaded in the diffuse reflectance cell and given a pretreatment

identical to those used for catalytic studies using a gas handling manifold equipped with mass flow controllers (Porter Instruments Company). He (99.999%, Praxair), 10% H_2/He (99.999% both gases, Praxair), H_2 (99.999%, Praxair), 20% O_2/He (99.9 % purity O_2, Praxair) and CO (99.9%, Airgas) were used without further purification. A single beam (128 scans, 2 cm^{-1} resolution) of the freshly reduced catalyst was obtained at 300 K under 30 cc (STP) He min^{-1} and used as the background for the same sample after exposure to CO at 300 K. Samples (10–15 mg) were exposed to a 30 cc (STP) min^{-1} flowing mixture of 10% CO/He for 30 min at 300 K, followed by purging in 30 cc (STP) He min^{-1} at 300 K. After He purging, spectra were recorded. The evolution of Pluronic P123/PVP bands were followed as a function of the pretreatment (heating in inert or reactive atmosphere). Single beam spectra of the catalyst sample were measured during *in-situ* treatment. A single beam spectrum of a silica sample completely free of template polymer was used as the background for absorbance spectrum.

Chemisorption on Pt/SBA-15 catalysts: Determination of exposed metal surface area

Selective chemisorption measurements were conducted to determine the number of Pt surface atoms. Adsorption measurements were conducted on an automated sorption analyzer (Quantachrome 1C). *Ex-situ* calcined catalysts were reduced with 50 cc (STP) H_2 min^{-1} at 673 K for 75 min after activation in 50 cc (STP) He min^{-1} at 473 K for 1h. Prior to chemisorption measurements, catalyst samples were evacuated to 10^{-6} Torr for 1h at 623 K and cooled to room temperature under vacuum. H_2-O_2 isotherms were collected on the same sample (*ca.* 200 mg). After the initial reduction, catalysts were subsequently reduced with 50 cc (STP) H_2 min^{-1} at 673 K for 30 min. Oxidation-reduction treatments were performed *in-situ* in the chemisorption cell on the automated selective gas

adsorption apparatus (Quantachrome 1C) after which H_2-O_2 titration measurements were performed at room temperature. Prior to H_2-O_2 titration measurements, catalyst samples were evacuated to 10^{-6} Torr for 1 h at 623 K and cooled to room temperature under vacuum. Adsorption uptakes extrapolated to zero pressure (monolayer uptake) were used to calculate the metal dispersion. Spherical particle sizes were calculated from dispersion measurements, d(nm) = 1.13/D where D is the dispersion assuming a Pt atom density of 1.27×10^{19} m^{-2} [22].

8.2.6 Ethylene hydrogenation on Pt/SBA-15 catalysts

Kinetic measurements were conducted in a quartz plug flow reactor (PFR) connected to gas flow manifold made of ? " stainless steel tubing. *Ex-situ* or *in-situ* calcined Pt/SBA-15 catalysts (2-30 mg) diluted in acid washed low surface area quartz (~10-150 mg) (Aldrich) were initially reduced if calcined *ex-situ.* He (Praxair, 99.999%), O_2 (Praxair, 99.99%), and C_2H_4 (Airgas, CP grade) were delivered to the reactor with mass flow controllers (Unit Instruments Corporation, Model UFC 1200) at a total flow rate of 90 cc (STP) min^{-1}. Initial conversions were as high as 30 % for some catalyst samples but decreased to ≤ 10 % after 20 hours time on stream (time required for steady state behavior). Turnover rates were corrected to standard conditions of 10 Torr C_2H_4, 100 Torr H_2, and 298 K. Reactant and product concentrations were measured by gas chromatography (Hewlett Packard 5890 Series II) equipped with a flame ionization detector (FID) and a homemade alumina column (6 ft. $\times$ 1/8-in. o.d.). Comparison of catalyst activity (reported in μmol g^{-1} s^{-1}) is a direct measure of exposed surface area and an indication of the extent of PVP removal from the surface) because the starting

catalysts were from the same batch and ethylene hydrogenation rate is directly proportional to the metal surface area (*i.e.* a structure insensitive reaction).

8.3   Results

8.3.1   *Solution phase nanoparticle and mesoporous silica supported Pt catalyst synthesis and characterization*

Monodisperse Pt particles of 1.7-3.6 nm were synthesized by modified alcohol reduction methods according to the literature [2]. Methanol, ethanol, and ethylene glycol (EG) served as solvents for dissolving Pt salts and PVP, and as a reducing agent of Pt according to the following reaction: $H_2PtCl_6 + 2RCH_2OH \rightarrow 2Pt^0 + 2RCHO + HCl$. The generated Pt ions associate with a PVP most likely through the carbonyl group most likely in a 1:1 stoichiometry. The mechanism by which PVP stabilized Pt ions form nanoparticles form is through two possible pathways; collision of Pt ions bound to a single PVP chain through intrapolymer interactions or by interaction between Pt ions bound to separate polymer chains (*i.e.* interpolymer interactions). Pt particle size increases from 1.7 to 2.9 nm as the reaction temperature decreases from 433 K in ethylene glycol to 338 K in boiling methanol. This indicates that reduction of Pt salts at high temperature produces more Pt nuclei leading to more seeds to create nucleation sites, results which results in smaller Pt particles and an increment in the number of particles [23]. The 3.6-nm Pt particles were obtained by the addition of $H_2PtCl_6 \cdot 6H_2O$ (0.06 mmol) to a 100 mL solution of 2.9-nm particles as a seed for stepwise growth. The 7.1-nm Pt particles were generated by slow and continuous addition of the Pt salt and PVP to boiling ethylene glycol, described elsewhere in detail [21]. In all cases PVP was used to

stabilize Pt particles during synthesis, except for the 1.7 nm particles in which PVP was added after the particles had been formed with a PVP monomer to Pt molar equivalency of ~ 1. 2.9 and 3.6 nm particles were synthesized with PVP (M_w = 29,000) and an equivalency of 10 and 5, respectively, while 7.1 nm particles were synthesized at an equivalency of 12. After synthesis, all particles are purified three times by a sequential precipitation/redispersion in ethanol/*n*-hexane. This step is believed to remove excess PVP (presumably PVP multilayers) leaving only a single monolayer.

Weight loss from the as-synthesized washed particles as determined by TGA is due only to the removal of PVP. The maximum weight loss (due to the complete removal of PVP with no residue remaining) is determined by the amount used during synthesis with no post-synthetic precipitation/redispersion. Maximum weight losses from the particles are 11.5% (1.7 nm), 36.2% (2.9 nm), 25.5% (3.6 nm), and 87.2% (7.1 nm). Particles are purified after synthesis which removes an unknown fraction of PVP. Comparison of actual weight loss from the as-synthesized washed particles by TGA analysis with the maximum weight loss determined from the synthetic procedure should enable the amount of removed PVP during purification to be determined. For example, the weight loss from 7.1 nm particles was determined to be 14% suggesting that 86% (or 5.8 g_{PVP}/g_{Pt}) of the PVP is removed by the precipitation-redispersion purification. The amount of PVP remaining on the nanoparticle surface is believed to constitute the monolayer (possibly multilayers) that stabilizes the nanoparticles.

Pt particle sizes were measured by XRD and TEM. Figure 3 are particle size distributions for all four particle sizes from TEM micrographs. Average Pt particle sizes estimated by XRD are 1.7, 2.9, 3.6, and 7.1 nm, and match very well with TEM results.
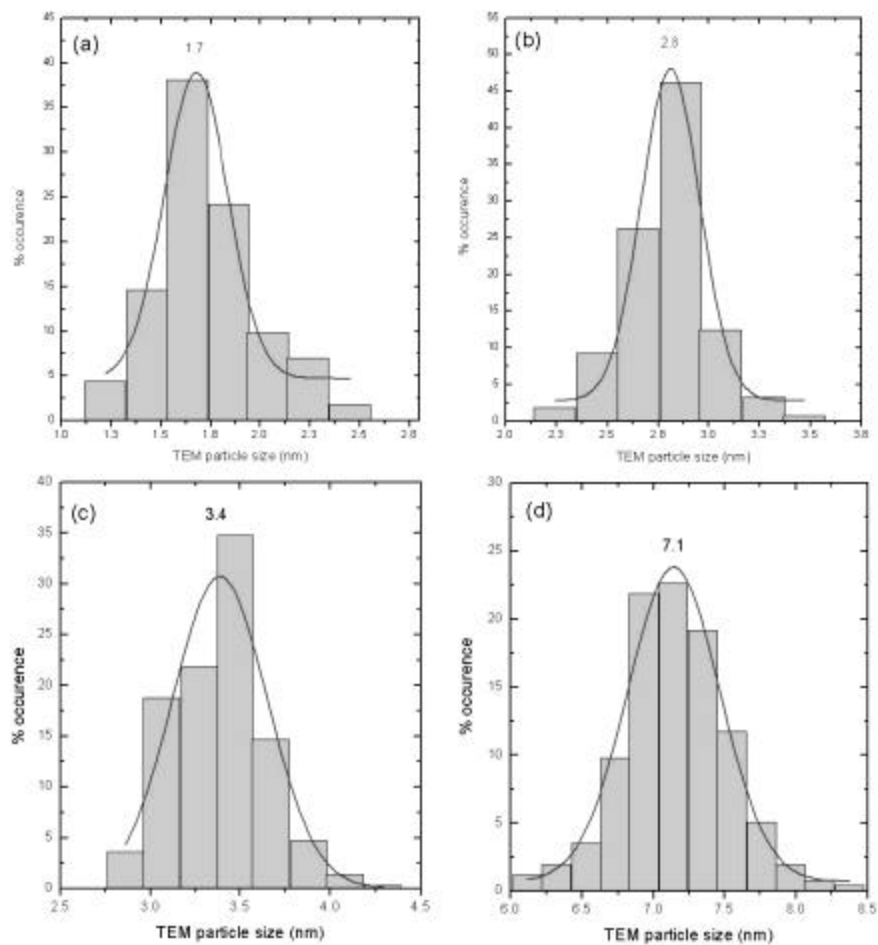
Figure 8.3. Particle size distributions (PSD) for as-synthesized Pt nanoparticles. Statistics based on counting > 250 particles for all samples. Gaussian fit to histogram shown.

SBA-15 was synthesized under neutral conditions using sodium fluoride and tetramethyl orthosilicate (TMOS). PVP-capped Pt particles with sizes of 1.7, 2.9, 3.6, and 7.1 nm were introduced into the neutral pH reaction mixture. In a typical reaction, Pt colloidal solution was mixed with aqueous polymer solution at 313 K and stirred for 1 h to ensure complete dissolution of Pt particles. Brown precipitates were formed 5 min after the addition of NaF solution and TMOS. The supernatant was colorless and transparent, indicating that Pt colloids were incorporated into the silica matrix. The

slurry was aged for a day at 313 K, and placed in an oven at 373 K for an additional day. The product was washed with water and ethanol, and dried in air at 373 K. Pt/SBA-15 catalysts were obtained by calcination of the raw materials under optimal conditions (*vide infra*). In the final composite product, Pt nanoparticles are encapsulated by mesoporous silica structures (Figure 4).
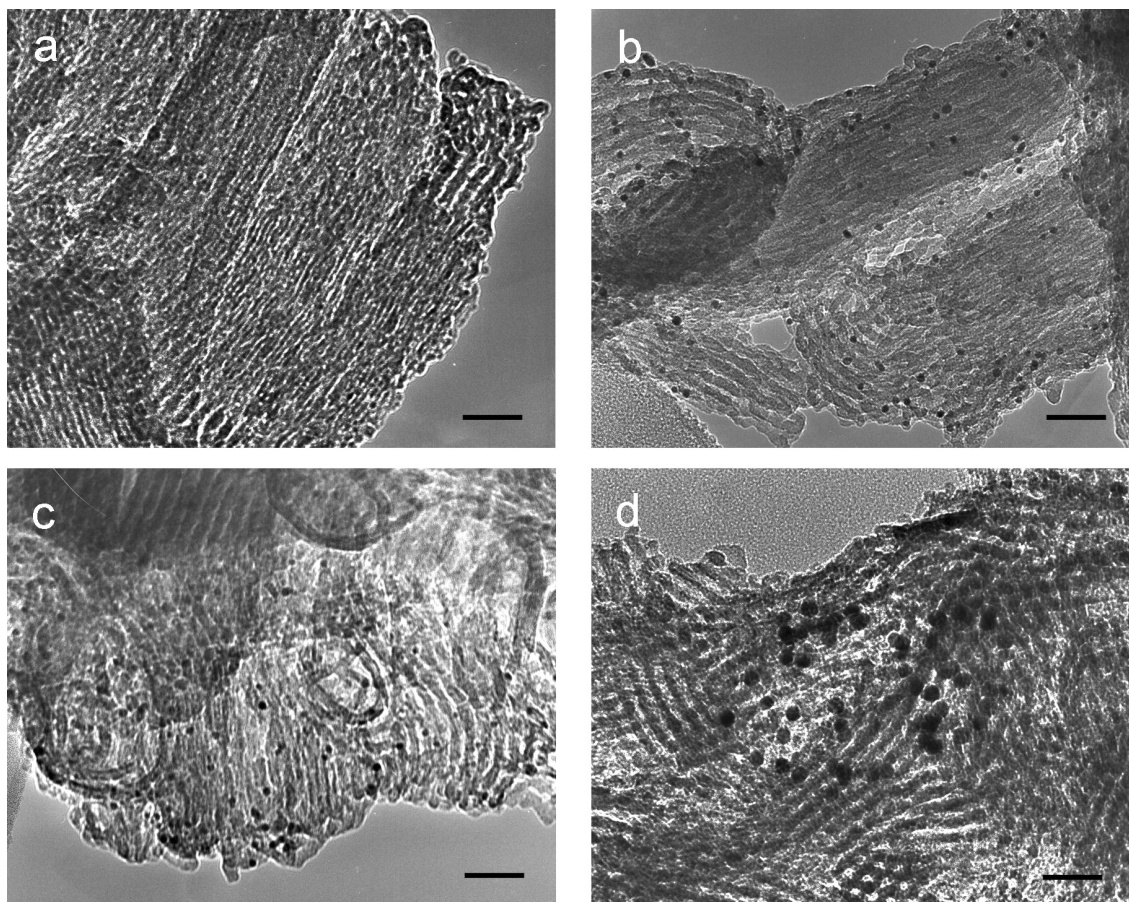
Figure 8.4. TEM images of Pt(X)/SBA-15 catalysts. X = (a) 1.7 nm, (b) 2.9 nm, (c) 3.6 nm, and (d) 7.1 nm. The scale bars represent 40 nm.

8.3.2   *Thermal degradation of PVP and PVP/Pt physical mixtures*

The decomposition of free PVP was studied under inert and oxidizing atmospheres under temperature programmed and isothermal conditions. The oxidation of PVP has been studied by isothermal and transient thermal analysis methods and

temperature programmed oxidation. Upon heating PVP in O_2 to T = 773 K, 92% of the

carbon in PVP is present in CO_2, while 83% of the hydrogen is present in H_2O. No other

carbon based products were accounted for, although the effluent was monitored for C_1-C_3

alkanes during temperature programmed oxidation (Figure 5). The actually fate of
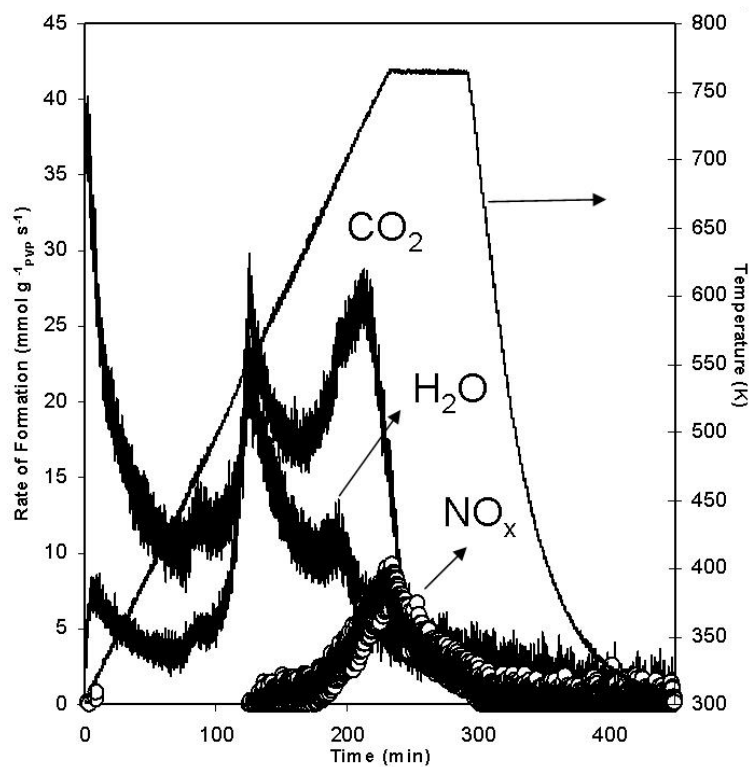
Figure 8.5. Temperature programmed oxidation (TPO) of PVP (M_w = 55,000 K).

the remaining carbon and hydrogen is unknown, but previous studies of PVP

decomposition have shown that alkanes, alkenes and oxygenates (aldehydes and ketones)

are products of decomposition. Only ~10 % of the nitrogen in PVP can be accounted for

in the effluent. Under oxidative conditions, NO_x products were identified with no ability

to determine the exact oxygen content. The missing nitrogen is not present as N_2 as this

was followed mass spectroscopically and could not be identified. The nature (solid, gas)

of the specie(s) containing the product maybe inferred from the decomposition of free

PVP during TGA; Figure 6B demonstrates that at 773 K only 74.3% of the PVP has
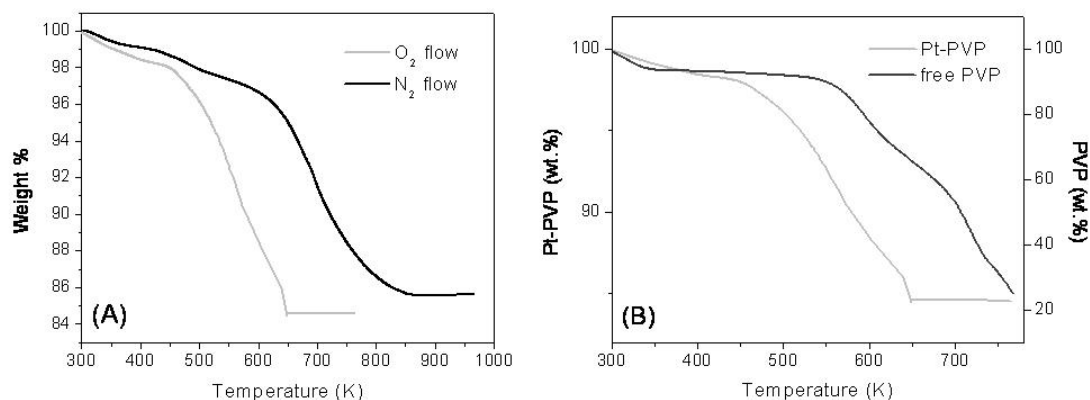
Figure 8.6. Thermogravimetric analysis of PVP ($M_w = 55,000$) decomposition from (A) as-synthesized 7.1 nm and (B) pure PVP in the nitrogen or oxygen.

decomposed to gaseous products. Therefore, 25.7% of the PVP decomposition product(s) are solid. Assuming from the TPO experiment in O_2 that the carbon, hydrogen and nitrogen which is unaccounted for is in solid form, 17.4% of the decomposed polymer is solid. Comparison of the TGA and TPO results in oxygen, it is likely that some fraction of the PVP decomposes to gaseous products which were not identified by TPO. The lines of the TPO apparatus were heated to 550 K, therefore it is unlikely that any of the known decomposition products of PVP condensed in the lines before reaching the mass spectrometer. If all unaccounted carbon, hydrogen, and nitrogen remain in the decomposed solid, the atomic ratio is C (1), H (3.3) and N (2.1).

The addition of a Pt/SiO_2 catalyst to 55 K molecular weight PVP had a tremendous impact on the extent of PVP removal during isothermal decomposition experiments. Figure 7a demonstrates that after oxidation for 2 h, 33 % of the PVP was decomposed in the absence of catalyst, while ~90 % of the PVP decomposed in the

presence of physically mixed Pt/SiO$_2$ at 523 K. In the absence of catalyst, the extent of

PVP decomposition increased with time, while in its presence, the percent of decomposed
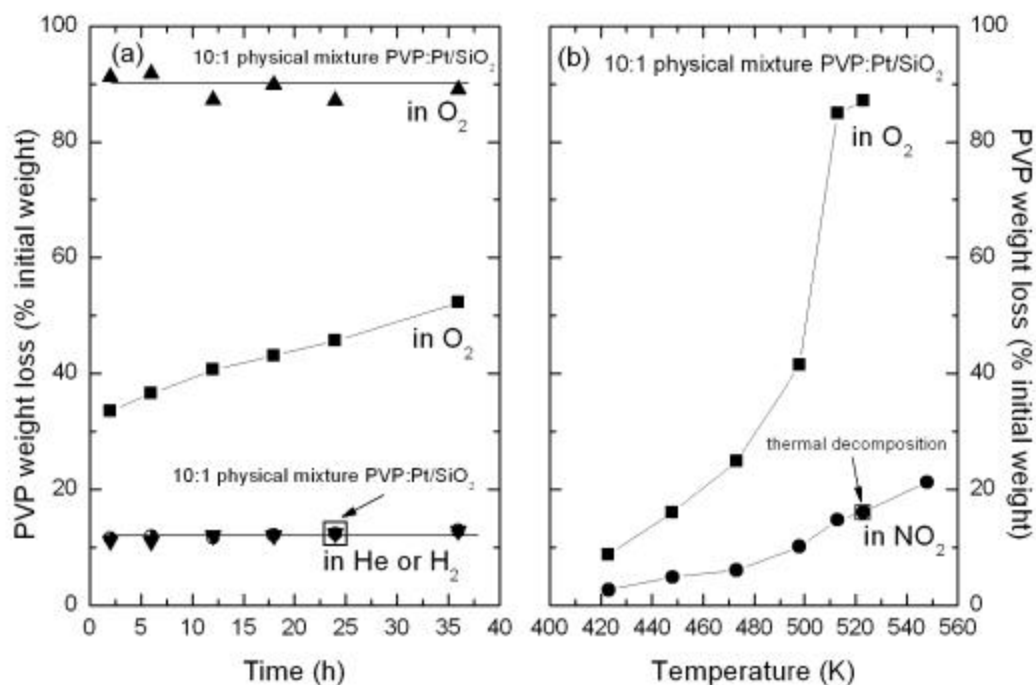
Figure 8.7. Thermal decomposition of (a) free PVP (M_w = 55,000) in oxygen, helium and hydrogen and 10:1 weight ratio physical mixtures of PVP-supported Pt/SiO$_2$ catalyst at 523 K for various times. (b) Influence of temperature on PVP decomposition in oxidizing atmosphere (O$_2$ or 1% NO$_2$/He). The amount of PVP decomposed was identical under thermal and catalytic conditions. Higher concentrations of NO$_2$ (10%) had no influence on the decomposition rate.

PVP was ~90 % for all times at 523 K. The addition of catalyst to free PVP had no

influence on the extent of PVP decomposition in inert (He) or reducing (H$_2$) atmospheres

at 523 K (Figure 7a). The fraction of PVP decomposed in He or H$_2$ in the absence or

presence of catalyst at 523 K never exceeds 0.15 regardless of treatment time. It appears

that the presence of Pt even as a physical mixture catalyzes PVP oxidative decomposition

probably due to the generation of reactive O atoms. The extent of PVP decomposition in

physical mixtures of PVP and a Pt/SiO$_2$ catalyst depends strongly on temperature (Figure

7b). The effectiveness of PVP decomposition by exothermic process (DTA trace, not shown) demonstrated that oxygen was effective for PVP removal but required relatively high temperatures (> 573 K). It was postulated that stronger oxidants may remove comparable amounts of PVP at lower temperatures. Previous studies of the removal of photoresist from Pt nanoparticle arrays demonstrated that low pressure NO_2 treatments were more effective than O_2 treatments for photoresist removal [24]. Figure 7B demonstrates that NO_2 was ineffective for free PVP decomposition and the presence of catalyst had little influence on the extent of decomposition.

8.3.3 *Removal of polymer from as-synthesized mesoporous silica and Pt nanoparticles.*

The removal of polymer by ethanol extraction was studied by thermal gravimetry from a series of NE mesoporous silica rinsed with varying amounts of ethanol. Figure 8 demonstrates the oxidative decomposition of residual polymer after a standard ethanol wash on SBA-15. CO_2 and H_2O both evolve from the sample at ~453 K. The amount evolved is significantly lower than expected from synthesis values. Experimentally, when the white powders are rinsed with ethanol while under a low vacuum, the triblock copolymer is removed as evidenced by the soapy film formed on the surface of the collected ethanol. This method has been previously shown to be effective for polymer extraction from MSU-H matrices [26]. The maximum weight loss expected if all Pluronic used during synthesis is incorporated into the final silica product is 61.3%.

8.3.4 *Decomposition of template polymer and PVP from Pt/SBA-15 catalysts*

The decomposition of Pluronic P123 and PVP from Pt/SBA-15 catalysts was studied by thermal gravimetric analysis (TGA), differential scanning calorimetry (DSC) and temperature programmed oxidation (TPO). Experimental results on the thermal degradation of free PVP (section 10.3.2) and as-synthesized mesoporous silica (section

10.3.3) enable the complex thermal behavior of the as-synthesized catalysts to be interpreted assuming that most Pluronic P123 is removed during ethanol washing [25]
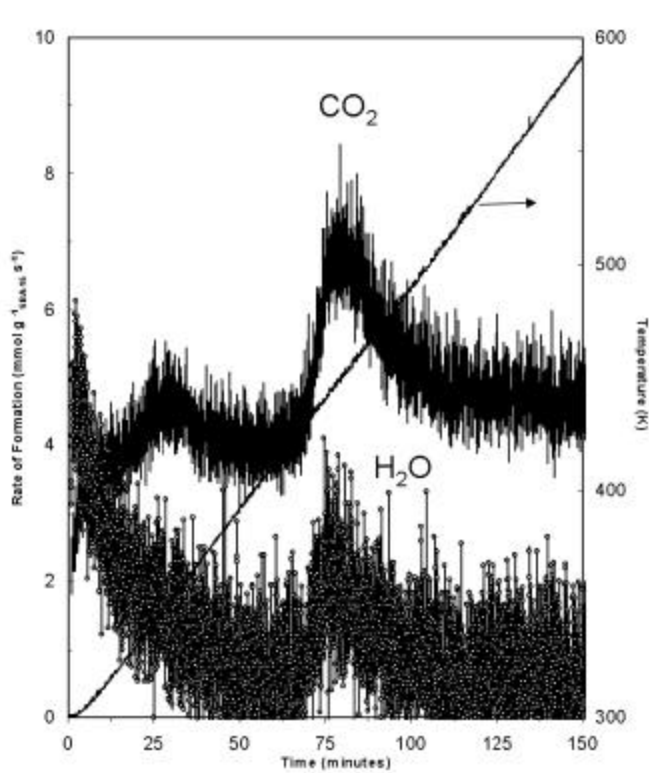
Figure 8.8. Temperature programmed oxidation (TPO) of SBA-15-NE.

and the remaining polymer template is removed by 473 K. One of the difficulties of determining the extent of polymer removal and the optimal treatment method for polymer removal is due to the different synthetic ratios of PVP:Pt used which are necessary to synthesize Pt nanoparticles with different particle sizes. TGA and TPO data is shown for the 2.9 nm particles and TPO data for the 1.7 and 7.1 nm particles are not but shown, but differ from the 2.9 nm sample primarily because these nanoparticles are synthesized with different PVP monomer to Pt molar ratios. The data for the 3.6 nm particles is similar to the 2.9 nm particles and therefore not shown. The decomposition of the Pt(2.9 nm)/SBA-15 catalyst has three distinct weight loss regimes as demonstrated in Figure 9A. Water

desorbed below 373 K, residual Pluronic P123 decomposed from 450 – 500 K (from TPO

on pure SBA-15), and PVP decomposed at ~500 – 773 K under O_2.
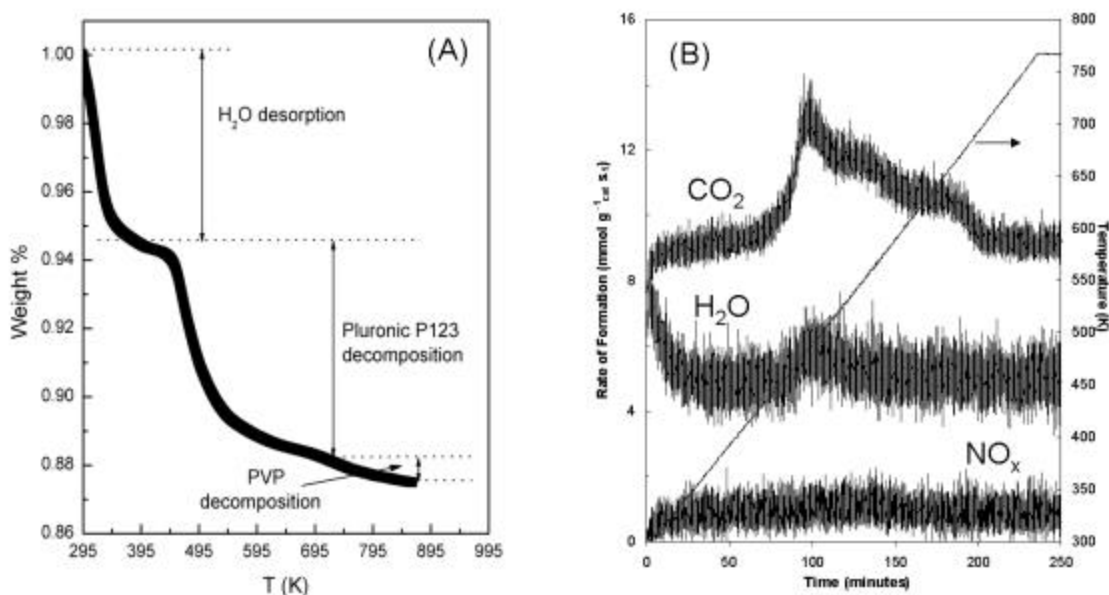
Figure 8.9. (A) TGA and (B) temperature programmed oxidation (TPO) for a 2.69%
Pt(2.9 nm)/SBA-15.

TPO of a 2.69% Pt(2.9 nm)/SBA-15 sample is shown in Figure 9B. The residual

Pluronic peak from Figure 8 is present at approximately the same temperature (453 K) for

the 2.9 nm sample. The CO_2 peak now has a broad shoulder at higher temperatures with

CO_2 production still occurring at temperatures >650 K. TPO data for a 2.33% Pt(1.7

nm)/SBA-15 sample (not shown) is slightly different; the residual Pluronic peak is again

unchanged, but the CO_2 peak due to PVP decomposition is at the baseline by 573 K, at

least 75 K lower than the 2.9 nm particles. The TPO trace (not shown) for the 2.86%

Pt(7.1 nm)/SBA-15 sample is completely different than both the 1.7 and 2.9 nm particles;

all combustion products are released over a very narrow temperature range with

maximum evolution at 448 K [27].

8.3.5   Infrared spectroscopy investigation of carbon monoxide on as-synthesized and ex-situ calcined Pt/SBA-15

The adsorption of CO has been used as a probe molecule because of its sensitivity to underlying metal structure and neighboring adsorbates. Neighboring adsorbates can influence the adsorption of CO by perturbing the electronic structure of the underlying metal surface. Therefore, CO may be a particularly sensitive chemical probe of the influence of residual PVP on the properties of the nanoparticle surface. The adsorption of CO on a 2.62% Pt(3.6 nm)/SBA-15 sample after no calcination, and a 12 and 24 h calcination in oxygen is shown in Figure 10. All samples were reduced at 673 K prior to
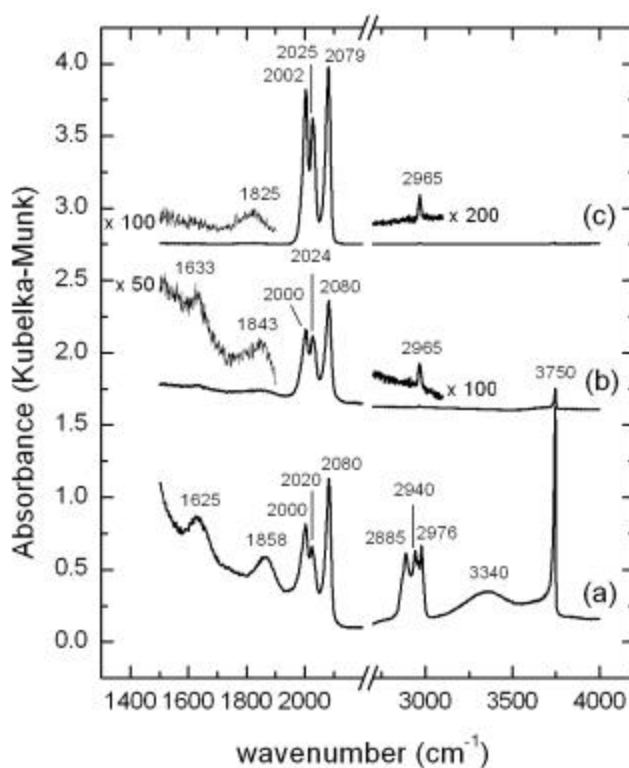
Figure 8.10. Diffuse reflectance infrared spectra of carbon monoxide adsorbed on 2.69% Pt(2.9 nm)/SBA-15: (a) before calcination, (b) after a 12 h 723 K calcination and (c) after a 24 h 723 K calcination.

CO adsorption at room temperature. On all samples exposed to CO, the intense bands at ~2000 and 2020 cm^{-1} are attributed to CO associated with SBA-15 while the band at

2080 cm^{-1} is associated with CO linearly bounded to Pt. The position of this band doesn't change with pretreatment suggesting that CO adsorption is unaffected by the presence of PVP and residual Pluronic. Intense bands in the C-H stretching region which are attributed to -CH$_2$- stretches of the vinyl side chain of PVP and PPO and PEO units comprising the silica template copolymer (Figure 12a). A weaker peak (1625 cm^{-1}) associated with the carbonyl group in the pyrrolidone ring is evident in Figure 10a. This peak is redshifted by 25-50 cm^{-1} (based on comparison with FT-IR spectra of 2-pyrrolidone [28]) suggesting that it is coordinated to the Pt surface. After calcination (Figures 10b and 10c), the peak blueshifts slightly to 1633 cm^{-1} after a 12 h calcination and after a 24 h calcination, this peak has disappeared. Correspondingly, the shape and intensity of the C-H band changes as the sample is calcined. These band assignments are in the presence of adsorbed CO, although *in-situ* studies of these bands in the absence of carbon monoxide demonstrate their position is unaffected by the presence of coadsorbed CO.

8.3.6 *Ethylene hydrogenation on ex-situ and in-situ calcined Pt/SBA-15*

The hydrogenation of ethylene was chosen as a test reaction for PVP removal because it is well-known that the rate is proportional to the exposed metal surface area (*i.e.* structure insensitive reaction) and a significant database of reaction rates measured for a number of catalysts by independent researchers is available for comparison. Rates were measured on catalysts calcined *ex-situ* and *in-situ* (distinction explained in section 10.2.4). Rates of ethylene hydrogenation on an *ex-situ* calcined 2.86% Pt(7.1 nm)/SBA-15 catalyst are shown in Figure 11 as well the weight loss of the sample upon *ex-situ* calcination. Although the weight loss doesn't change after a 2 h calcination, the rate (per

gram catalyst basis) increases by a factor of 50 for catalysts calcined between 0 and 36 h.

Ex- situ weight loss is attributed to water desorption, Pluronic and PVP decomposition.
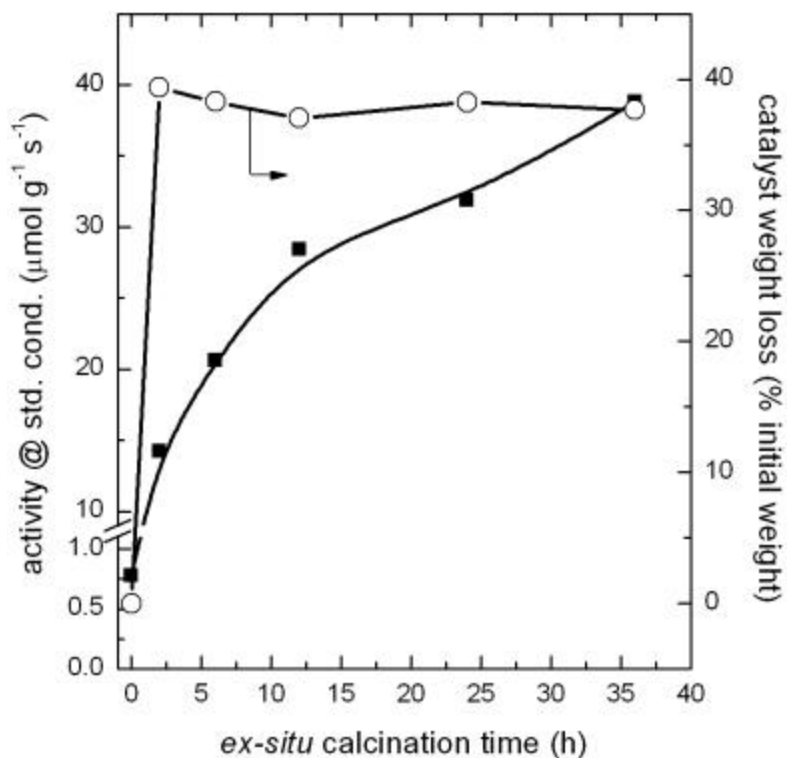
Figure 8.11. Ethylene hydrogenation activity for a 2.86% Pt(7.1 nm)/SBA-15 catalyst calcined *ex-situ* for various times at 723 K. All catalysts had the same weight loss after calcination.

The increasing rate is attributed to an increase in the exposed Pt surface area. The highest rate reaction (39 μmol g^{-1} s^{-1}) is achieved after 36 h calcination at 723 K, while the initial ethylene hydrogenation rates on *in-situ* pretreated samples were as high as ~ 430 μmol g^{-1} s^{-1} (473 K oxidation-reduction, one cycle). Initial and steady state ethylene hydrogenation rates after oxidation-reduction treatments are compiled in Table 1. Activities up to an order of magnitude higher are measured on the *in-situ* calcined samples. There is a consistent trend with the activity (both initial and steady state) decreasing with increasing cycle number at a given temperature, except in the case of

Table 1. Ethylene hydrogenation rates on in-situ oxidation-reduction treated 2.86% Pt(7.1 nm)/SBA-15.

Temperature (K)	Cycle Number[a]	Activity (μmol g^{-1} s^{-1})[b]		Turnover frequency[b,e] (s^{-1})	
		Initial[c]	Steady state[d]	Initial[c]	Steady state[d]
373	1	19	16	0.8	0.7
	2	27	22	1.2	0.9
	3	60	49	2.6	2.1
	4	225	159	9.6	6.8
	5	266	199	11.4	8.5
	6	300	212	12.9	9.1
473	1	427	291	18.3	12.5
	2	413	258	17.7	11.1
	3	416	216	17.8	9.3
573	1	274	151	11.7	6.5
	2	214	120	9.2	5.1
	3	145	105	6.2	4.5
673	1	248	101	10.6	4.3
	2	172	99	7.4	4.2
	3	162	93	7	4.0

[a]Complete cycle is 1 h. oxidation step, followed by ½ h He purge and 1 h. reduction step at stated temperature.

[b]Corrected to standard conditions of 10 Torr C_2H_4, 100 Torr H_2 and 298 K.

[c]Rate after ~7 minutes on stream.

[d]Rate after ~ 12 h on stream.

[e]Assuming entire surface area of as-synthesized 7.1 nm particle is exposed (*i.e.* Pt_s/Pt_T = 0.159).

the 373 K treated sample, in which the activity increased with cycle number. At the

relatively mild calcination conditions of 373 K, the rate increased from 19 µmol $\dot{g}^1$ s^{-1}

after the first cycle to 300 µmol g^{-1} s^{-1} after six cycles, a rate which is ~10 higher than the

most active *ex-situ* 723 K treated 2.86% Pt(7.1 nm)/SBA-15 sample (Figure 11). The

steady state behavior of the *in-situ* treated samples is shown in Figure 12. Steady state

activity follows similar trends as the initial activity; decreases with increasing cycle

number except for the 673 K treated sample in which steady rates are approximately the

same.
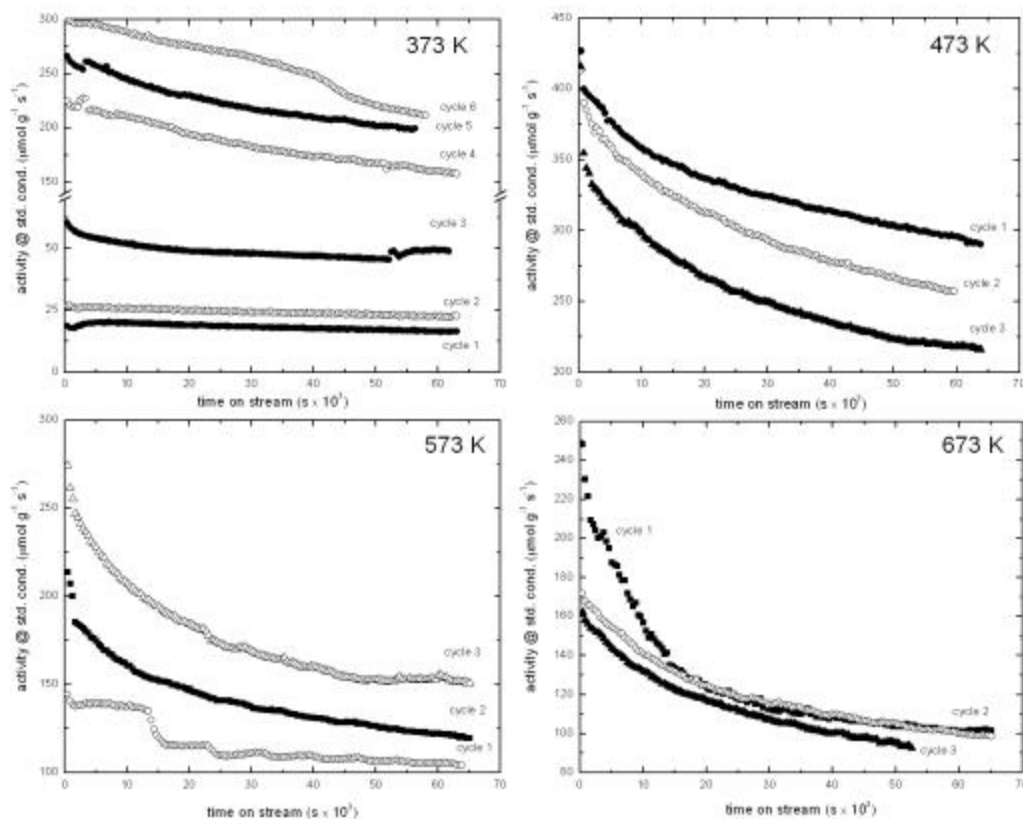
Figure 12. Effect of cycle temperature and cycle number on the activity of 2.86% Pt(7.1 nm)/SBA-15: (A) 373 K, (B) 473 K, and (C) 573 K. A 1 h oxidation step followed by ½ h He purge and 1 h reduction step constitute a complete cycle.

8.4   Discussion

8.4.1   *Formation mechanism of PVP-stabilized Pt/SBA-15 composite materials*

Free PVP is very hydrophilic because of the polar pyrrolidone functionality attached to the main vinyl chain. It dissolves in water, ethanol, and chloroform, while PVP-stabilized Pt nanoparticles are poorly soluble in water. The addition of Pluronic P123 helps to form a stable colloidal solution of Pt nanoparticles in water. Water contact angles have been measured to check the hydrophilicity of materials used during catalyst synthesis. A PVP layer on the Si substrate exhibits a contact angle of 15º, the lowest value of all the surfaces measured and therefore the most hydrophilic. PVP-capped Pt nanoparticle layers made by drop casting and Langmuir-Blodgett techniques [21] are relatively hydrophobic with contact angles of 39º and 53º, respectively. The more hydrophobic nature of the PVP-capped Pt nanoparticle layers is due to the strong interaction between the pyrrolidone rings of PVP and Pt, resulting in the exposure of the hydrophobic main chain at the surface. Pluronic P123 is known to form spherical micelles in water at room temperature, with the hydrophobic propylene oxide unit in the core and the hydrophilic ethylene oxide unit comprising the sphere surface [29] Therefore, PVP-stabilized Pt nanoparticles are likely to be encapsulated within the core of Pluronic P123 micelles. After NaF and TMOS are added to the reaction mixture, silica species polymerize on the surface of Pluronic P123 micelles, and the final product contains Pt particles inside the mesoporous framework. The separate formation of SBA-15 with Pluronic P123 and adsorption of the Pt particles on its surface cannot be excluded but the enhanced solubility of PVP-stabilized Pt nanoparticles in a Pluronic solution suggests that Pt quickly associates with the Pluronic upon its introduction to the solution.

8.4.2   Thermal decomposition of free PVP in inert and PVP-stabilized Pt nanoparticles

The removal of polymers from the surface of Pt nanoparticles is critical if the full catalytic potential of nanoparticles with their extremely high surface to volume ratio is to be taken advantage.   In the case of polymer encapsulated nanoparticles, complete removal including the residues of the decomposition products is critically important. The thermal degradation behavior of the free polymer, PVP has studied by thermal analysis techniques.   It is apparent that the rate and possibly the mechanism by which PVP decomposes is different in N_2 and O_2.   The decomposition of free PVP by various methods have demonstrated two possible decomposition pathways: release of the side chain (pyrrolidone) group followed by decomposition of the vinyl chain or vinyl chain fragmenting and decomposition followed by pyrrolidone decomposition [17].   PVP decomposition by ozone [30], ultrasonic irradiation [31] and high speed stirring [32] have been previously reported. Products such as CO, CO_2, CH_2O, CH_3CHO, CH_4, C_2H_4 and C_2H_6 evolved from aqueous PVP solutions exposed to ultrasonic irradiation [31]. Very little CO_2 was measured during the decomposition of PVP in aqueous solution by ozone; suggesting that reactions other than vinyl side chain breakage are occurring although the nature of these reactions are unknown [30].

After heating PVP-capped 2.5 nm Pt particles in N_2, the absorption band attributed to the $-CH_2-$ stretch of vinyl side chain disappears while the carbonyl band of pyrrolidone decreases in intensity but is still apparent. The loss of methylene absorption bands suggests that decomposition occurs initially through the degradation of the vinyl side chain [33].   Conversely, during thermal treatment in N_2 or O_2, the dominant decomposition of PVP proceeds by the release of the pyrrolidone side group and the

subsequent decomposition of polyenic sidechain [17]. In the presence of oxygen, these sidechains are oxidized to CO_2 and H_2O and in an inert atmosphere aliphatic and aromatic hydrocarbons of low molecular weight are anticipated. Infrared spectra of PVP residues after treatment up to 648 K in either oxygen or nitrogen demonstrated that the carbonyl stretch had blue shifted from 1661 to 1750 cm^{-1}, as well as the appearance of weak absorption bands at 1633 and 3480 cm^{-1}, typically of N–H groups in a cyclic amide. The proposed species is pyrrolidone [17]. TPO of free PVP (Figure 5) suggests that the mechanism by which it decomposes in oxygen is very complex; CO_2 and H_2O are initially evolved at 553 K followed by a smaller H_2O peak at ~690 K and another CO_2 peak at 720 K. In oxygen, the first N bearing compound is not observed until 760 K. This complex decomposition behavior may indicate PVP decomposition by multiple mechanisms. The lack of N in the effluent may suggest the decomposition mechanism proposed by Peniche occurs at lower temperatures; while at higher temperatures rather than releasing intact, the pyrrolidone ring decomposes.

Elemental analyses of PVP-capped Pt nanoparticles after heating in N_2 at 773 K demonstrated that significant more carbon (~38 % weight basis) was retained compared with hydrogen (13 %), oxygen (30 %) and nitrogen (24 %) [33]. The same authors also found that free PVP decomposed to a greater extent (> 95 %), than PVP-stabilized Pt nanoparticles, although the decomposition of PVP from the nanoparticle surface occurred at temperatures 30 K lower than observed for pure PVP [33]. TGA data presented in Figure 6 also confirms the catalytic effect of Pt on PVP decomposition. Similar results were found during the decomposition of dendrimer covered nanoparticles [11]; generation-4 polyamidoamine dendrimer decomposed at temperatures up to one hundred

degrees higher than decomposition from a Pt nanoparticle surface in air, suggesting that Pt also catalyzes the decomposition of dendrimers. This was recently confirmed independently, research which reported that if the treatment conditions (primarily temperature) are not appropriate, carbonaceous residues left behind by the particle template will remain on the particle surface. Chandler and co-workers [13, 14] have suggested that N containing products may be responsible for poisoning dendrimer stabilized Pt nanorparticles. Similarly, TPO results (Figure 5) combined with TGA results of free PVP demonstrate that N containing oxides evolve at high temperatures ($\geq$ 773 K) and most of the nitrogen is unaccounted for (~ 90%), while 25 % of PVP decomposed in oxygen is in the form of a solid. It is likely that this solid material contains a significant fraction of nitrogen. If all the unaccounted carbon, hydrogen, and nitrogen from TPO measurements remain in the decomposed solid, the atomic ratio of the solid residue is C (1), H (3.3) and N (2.1).

8.4.3 *Removal of template polymer from mesoporous silica structures by ethanol extraction and thermal calcination*

A significant fraction (~ 98 %) of the template polymer located in the void volume of the silicate framework after synthesis is presumably removed by ethanol rinsing. The remaining template polymer is removed by calcination by 453 K (Figure 9A). The extent of polymer extraction is typically dependent on the type of surfactanct silicate template interaction. For mesoporous silica (*i.e.* MCM-41) prepared by electrostatic interactions between structure directing and inorganic silicate precursors, template extraction by ethanol amounts to only ~25 % due to the strong interactions between cationic template and anionic silicate precursor [34]. For hexagonal mesoporous

molecular sieves (HMS) [35] prepared by a neutral templating method, ethanol extraction

at 318 K leads to removal of 75 % of the template; the remaining 25% may be related to

the occlusion of EO chains in the silica wall which are less accessible to ethanol [25].

Recent work has shown that EO chains in the silica wall disappear after calcination in air

at 473 K. Therefore the authors contend that the preferred method of template removal is

ethanol rinsing followed by calcination [35]. Similar behavior (~ 75% template removal)

was observed for SBA-15 silica prepared in the presence of the nonionic triblock

copolymer, Pluronic P123, although in this case the ethanol was acidified with HCl [36].

Temperature programmed oxidation studies of Pluronic P123 combustion suggest

that ~98% of the Pluronic is removed by ethanol rinsing if all products of Pluronic

oxidative decomposition are combustion products (H_2O and CO_2) assuming that ethanol

washing removes no template polymer. TGA has not been used to determine the weight

loss which would be useful because while not identifying what is evolved, it measures the

total weight loss. If the fraction of polymer removal determined by TPO is higher than

that determined by TGA, it is possible that products other than CO_2 and H_2O are released

during decomposition. It must be noted that no CO or H_2 evolved from the sample

during temperature programmed measurements. Previous studies of the decomposition

of Pluronic F127 ($EO_{101}PO_{56}EO_{101}$, *ave.* MW = 12,600) have shown that products other

CO_2 and H_2O are detected at low temperatures (353 K) in the presence of oxygen starved

air, products such as 1,2 propanediol, 1-hydroxy-2-propanone, formic acid and acetic

acid [37, 38]. It is believed that these products originated from the poly(propylene oxide)

(PPO) chains because they are more sensitive to thermal oxidation than poly(ethylene

oxide) (PEO) chains due to the more stable tertiary radical that can be formed on the PPO

chains [39]. At higher temperatures (423 K) in oxygen, organics such as acetone, acetic acid, acetaldehyde and 2,3-butane-dione was identified during the decomposition of PPO chains [40]. In a separate study of polypropylene decomposition from 370-413 K, formaldehyde, methanol and a significant fraction of H_2O was identified [41]. Similar products were found for the radiolysis of PEO in H_2O at 298 K; formic acid was the major product with minor products such as formaldehyde ethylene glycol, 1,2-ethanediol, monoformate and diformate [42].

8.4.4   Possible mechanism for PVP stabilization in solution

The mechanism by which PVP protects the nanoparticle has been previously investigated during the synthesis of anisotropic Ag structure growth [43] and for the synthesis of Pt-Au coreshell particles [44]. It is primarily believed that PVP coordinates to metal ions or nanoparticles through its carbonyl group [44], although some experimental evidence suggests that the nitrogen in the pyrrolidone ring may be bonded to the surface of larger particles [45]. Most of the previous work found a distinction between PVP coordination to the nanoparticle surface for nanometer and (sub)micron sized particles, but the critical particle size where this coordination change occurs is unknown. The interaction between PVP and metal ions is proposed to through the carbonyl group of the pyrrlidone side group along the chain and the ability of the polymer chain to interact with other sections of the polymer chain containing Pt ions enable the encounter of zero valent metal ions and the formation of Pt nanoparticles. It has been suggested that for PVP an optimal synthetic temperature leads to increased mobility of the polymer chains enabling a more facile reduction of Pt ions, both of which lead to an increase in the formation of nanoparticles [44].

Water contact angle measurements of PVP-capped Pt nanoparticle Langmuir-Blodgett films suggest that the more hydrophobic nature of the PVP-capped Pt nanoparticle layers (relative to pure PVP) is due to the strong interaction between the pyrrolidone rings of PVP and Pt, resulting in the exposure of the hydrophobic main chain at the surface. In the fact, PVP-capped Pt nanoparticles may only be soluble in H_2O due to some sections of PVP chain dangling off the nanoparticle surface thereby increasing the solubility of the Pt colloid in polar solvents. Likewise, high mobility of the polymer leading to intra- and inter- polymer chain entanglement may affect the solubility of Pt nanoparticle by sterically hindering pyrrolidone rings from adsorbing the nanoparticle surface. The thickness of the PVP layer also suggests that the relative stability of PVP-capped Pt nanoparticles may be due to multilayer adsorption, where the multilayer exposes the polar carbonyl oxygen to the water phase. STM measurements of PVP-capped particles have shown that the thickness of the PVP shell is ~ 0.5 ± 0.2 nm with a 1:1 molar ratio of PVP (monomer basis) to Pt used during the synthesis of 2.6 nm Pt particles [46], while using the same molar PVP:Pt ratio, the thickness of the PVP shell of 3.8 nm particles was ~13 nm [47]. The thickness of the protective layer for Pd nanoparticles stabilized by tetraalkylammonium salts was dependent on the length of the alkyl chain [48]. An analogous situation may occur in the case when PVP with different molecular weights are used to synthesized nanoparticles. PVP with a molecular weight of 29,000 (260 monomer units) is used to stabilize 1.7 – 3.6 nm Pt particles, while PVP with a molecular weight of 55,000 (495 monomer units) is used to stabilize 7.1 nm particles. Removal of PVP from particles may be complicated by the molecular weight

of PVP if such property influences the thickness of the PVP coating and the ability of Pt to catalytically decompose bound PVP.

8.4.5   Influence of residual PVP on CO adsorption and hydrogenation of ethylene

The overall objective of this study to determine the most effective treatment to remove PVP from the Pt nanoparticle surface without causing particle agglomeration, sintering or any other action which causes the as-synthesized particle size to change. Dendrimer stabilized Pt nanoparticles are capable of adsorbing carbon monoxide in solution but the materials are no longer able to adsorb CO in the dried state, presumably due to the collapse of the dendrimer around the nanoparticle [7, 8]. The observed results are consistent with the lack of H_2 chemisorption on dried dendrimer covered Pt nanoparticles. As the calcination temperature increased the amount of adsorbed CO increased consistent with the decomposition and desorption of dendrimer. The authors found that the optimal pretreatment temperature was 698 K for calcination and 473 K for reduction. Conversely, PVP-stabilized Pt nanoparticles adsorb a significant fraction of carbon monoxide after reduction at 673 K (*i.e.* no calcination) (Figure 10a). Upon calcination, it was apparent that both Pluronic and PVP were removed from silicate channels and nanoparticle surface, respectively, but no increase in CO adsorption was observed.   Actually, in the case of a Pt(2.9 nm)/SBA-15 catalyst, CO adsorption decreased after a 12 h calcination at 723 K but recovered (to approximately the same as on an uncalcined, reduced sample) after a 24 h calcination at 723 K. The CO adsorption behavior is contrary to measured rate of hydrogenation on materials calcined for different times at 723 K (Figure 11). The rate of hydrogenation increases as the calcination time is increased. For catalysts subjected only to a 673 K reduction, the ethylene hydrogenation

rate was 0.8 μmol g^{-1} s^{-1} and increased by a factor of 50 after calcination at 723 K for 36 h. The reason for this discrepancy may be related to the ability of carbon monoxide to adsorb onto a carbonaceous covered surface. There is no evidence (XRD or chemisorption) which suggests that high temperature, long time calcination leads to particle agglomeration. Conversely, calcinations at lower temperature lead to samples with lower H_2 adsorption capacity suggesting a carbon covered surface. Partially decomposed dendrimer entities have been speculated to partial poison the catalyst surface after a mild calcination procedure (423 K, 16 h in O_2) [13].

There are still unanswered questions why the *in-situ* calcination-reduction cycles (especially the low temperature ones) produce such active catalysts. One potential explanation has been proposed for dendrimer covered Pt nanoparticles [13]. Potentially, the low temperature decomposition products of PVP decomposition are not volatile enough to oxidize or desorb from the Pt surface but migrate to the silica surface. It has been reported that the support may serve as a sink for coke precursors [49]. Another possibility is the particle size dependence of PVP coordination – infrared spectra of metal complexes of cyclic amides shows characteristic stretches when the nitrogen or carbonyl are coordinated to the metal [45]. Based on this argument, it is proposed that the PVP coordinates to the 7.1 nm particle through the C–N bond; which is more weakly coordinated to the nanoparticle surface as evidenced by the evolution of CO_2 and H_2O at ~ 463 K compared with the 2.9 nm, where CO_2 and H_2O attributed to PVP combustion is evolved at temperatures $\geq$ 523 K. Oxidation-reduction cycles at temperatures $\geq$ 473 K on a Pt(7.1 nm)/SBA-15 catalyst were much more effective than the oxidation-reduction

cycle at 373 K (see Figure 12). Activity increased with each 373 K oxidation-reduction cycles suggesting that more Pluronic and PVP is removed during each successive cycle.

8.5   Summary

The synthesis of Pt nanoparticles in the 1.7–7.1 nm range has been accomplished by the reduction Pt(IV) salts in alcohol in the presence of a surface templating polymer, poly(vinylpyrrolidone) (PVP).   Purification of the particles by continuous precipitation/redispersion rendered stable colloidal Pt nanoparticle aqueous solutions capped with approximately one monolayer of PVP. Addition of a poly(ethylene oxide)-poly(propylene oxide)-poly(ethylene oxide) triblock copolymer to a PVP-capped Pt nanoparticle solution under neutral pH conditions led to the spontaneous formation of rod copolymer micelles with the PVP-capped Pt nanoparticles associated with the hydrophobic poly(propylene oxide) core of the micelle. Upon addition of alkoxy silica source and a hydrolysis catalyst, PVP-capped Pt nanoparticles were encapsulated by mesoporous silica. The type of catalyst purification method on the removal of triblock copolymer from the silica channels and PVP from the nanoparticle surface was assessed with a variety of thermal analytical techniques. Solvent extraction was effective for the removal of triblock copolymer from the silica channels. Residual co-polymer was oxidized at low temperatures (448 K) as determined by temperature programmed oxidation of mesoporous silica. Once encapsulated in silica, thermal treatment was the most effective method for PVP removal from the Pt nanoparticle surface.   PVP decomposition on PVP-capped Pt nanoparticles was catalyzed by platinum.   The

evolution of CO_2 and H_2O occurred at much lower temperatures for PVP-capped Pt nanoparticles compared with free PVP which is in agreement with total weight loss measurements by thermal gravimetry. The thermal behavior of polymer oxidation in Pt/SBA-15 materials demonstrated that combustion products originating from the triblock copolymer evolved first over a rather narrow temperature range while the products of PVP decomposition were detected at higher temperatures and over a broader temperature range as the PVP content increased. High temperature calcination of large catalyst batches were apparently effective (> 95 %) at the removal of PVP determined by infrared spectroscopy of pretreated catalysts. These catalysts were active for ethylene hydrogenation and the surface was apparently clean as determined by the band position for adsorbed carbon monoxide. The use of stronger oxidants, such NO_2 had little benefit compared to oxygen on the removal of PVP as evidenced by infrared characterization of the pretreated catalyst and the comparable ethylene hydrogenation rates. Catalysts containing 7.1 nm particles pretreated by low temperature oxidation-reduction cycles were extremely effective in producing highly active ethylene hydrogenation catalysts, although the hydrogen chemisorption capacity of the materials was extremely low. Adsorption of CO on these catalysts suggests that surface is free of PVP residues. Ethylene hydrogenation rates were two orders of magnitude higher after a 473 K oxidation-reduction treatment than a catalyst calcined at 723 K for 36 hours. Catalysts containing 2.9 nm particles pretreated by the same oxidation-reduction cycles were not as active as 7.1 nm particles suggesting that complete removal of PVP is more difficult on smaller particles. This study emphasizes that the effective pretreatment methods depend on the synthesis PVP: Pt molar ratio, the purification method and the Pt particle size. The

removal of the surface stabilizing organic phase from nanoparticle surfaces is complex and still requires extensive research. In the case of PVP, it appears that Pt catalyzes the decomposition of PVP but removal of residual carbon is extremely difficult and its presence unavoidable.

8.6   References and Notes

1.   Z. Kónya, V. F. Puntes, I. Kirisci, J. Zhu, A. P. Alivisatos, G. A. Somorjai, *Catal. Lett*. 81 (2002) 137.

2.   R. M. Rioux, H. Song, J. D. Hoefelmeyer, P. Yang, G. A. Somorjai, *J. Phys. Chem. B* 192 (2005) 2192.

3.   H. Song, R. M. Rioux, R. Komor, K. Niesz, J. D. Hoefelmeyer, P. Yang, G. A. Somorjai, Submitted to the *J. Am. Chem. Soc*., 2005.

4.   R. M. Rioux, H. Song, M. Grass, S. E. Habas, K. Niesz, P. Yang and G. A. Somorjai. Submitted to *Top. Catal.*, 2005.

5.   H. Bönnemann, R. M. Richards, *Eur. J. Inorg. Chem*. 10 (2001) 2455.

6.   G. Schmid, *Chem. Rev*. 92 (1992) 1709.

7.   D. X. Liu, J. X. Gao, C. J. Murphy, C. T. Williams, *J. Phys. Chem. B* 108 (2004) 12911.

8.   D. S. Deutsch, G. Lafaye, D. X. Liu, B. D. Chandler, C. T. Williams, M. D. Amiridis, *Catal. Lett*. 97 (2004) 139.

9.   B. L. Cushing, V. L. Kolesnichenko, C. J. O'Connor, *Chem. Rev*. 104 (2004) 3893.

10.   D. de Caro, J. Köhler, W. Busser, J. Bradley. *Macromol. Symp.* 156 (2000) 53.

11.   O. Ozturk, T. J. Black, K. Perrine, K. Pizzolato, C. T. Williams, F. Parsons, J. S. Ratliff, J. Gao, C. J. Murphy, H. Xie, H. J. Ploehn, D. A. Chen, *Langmuir* 21 (2005) 3998.

12.   G. Lafaye, C. T. Williams, M. D.Amiridis, *Catal. Lett*. 96(2004) 43.

13.   A. Singh, B. D. Chandler, *Langmuir* 21 (2005) 10776.

14.   H. Lang, A. May, B. L. Iverson, B. D. Chandler, *J. Am. Chem. Soc.* 125 (2003) 14832.

15.   L. W. Beakley, S. E. Yost, R. Cheng, B. D. Chandler, *Appl. Catal. A: Gen.* 292 (2005) 124.

16.   D. G. Duff, T. Mallat, M. Schneider, A. Baiker, *Appl. Catal. A* 133 (1995) 133.

17.   C. Peniche, D. Zaldívar, M. Pazos, S. Páz, A. Bulay, J. San Román, *J. Appl. Poly. Sci.* 50 (1993) 485.

18.   D. Radic, L. H. Tagle, A. Opazo, A. Godoy, L. Gargallo, *J. Therm. Anal.* 41 (1994) 1007.

19.   Y. Wang, J. Ren, K. Deng, L. Gui, Y. Tang, *Chem. Mater.* 12 (2000) 1622.

20.   T. Teranish, M. Hosoe, T. Tanaka, M. Miyake, *J. Phys. Chem. B* 103 (1999) 3818.

21.   H. Song, F. Kim, S. Connor, G. A. Somorjai, P. Yang, *J. Phys. Chem. B* 109 (2005) 188.

22.   J. R. Anderson, *Structure of Metallic Catalysts.* Academic Press New York 1975.

23.   P. Y. Silvert, K. Tekaia-Elhsissen, *Solid State Ionics* 82 (1995) 53.

24.   J. Grunes, J. Zhu, E. A. Anderson, G. A. Somorjai, *J. Phys. Chem. B* 106 (2002) 11463.

25.   J. Patarin, *Angew. Chem. Int. Ed.* 43 (2004) 3878.

26.   P. T. Tanev, T. J. Pinnavaia, *Science* 267 (1995) 865.

27.   R. M. Rioux, T. J. Toops, M. Grass, K. Niesz, J. D. Hoefelmeyer, P. Yang, G. A. Somorjai. *Manuscript in preparation*, 2005.

28.   P. S. Peek, D. P. McDermott, *Spectrochim. Acta, Part A* 44 (1988) 371.

29. P. Alexandridis, J. F. Holzwarth, T. A. Hatton, *Macromolecules* 27 (1994) 2414.

30. J. Suzuki, N. Taumi, S. Suzuki, *J. Appl. Poly. Sci.* 23 (1979) 3281.

31. S. Koda, H. Mori, K. Matsumoto, H. Nomura, *Polymer*, 35 (1994) 30.

32. A. Nakano, Y. Minoura, *J. Appl. Poly. Sci.* 21 (1977) 2877.

33. Y. K. Du, P. Yang, Z. G. Mou, N. P. Hua, L. Jiang,. *J. Appl. Poly. Sci.* 99 (2006) 23.

34. R. Prins, S. Hitz, *J. Catal.* 168 (1997) 194.

35. P. T. Tanev, T. J. Pinnavaia, *Chem. Mater.* 8 (1996) 2068.

36. M. Kruk, M. Jaroniec, C. Hyun Ko, R. Ryoo, *Chem. Mater.* 12 (2000) 1961.

37. G. Gallet, S. Carroccio, P. Rizzarelli, S. Karlsson, *Polymer* 43 (2002) 1081.

38. G. Gallet, B. Erlandsson, A. –C.Albertsson, S. Karlsson, *Poly. Degrad. Stab.* 77 (2002) 55.

39. L. Yang, F. Heatley, T. G. Blease, R. I. G. Thompson, *Eur. Polym. J.* 32 (1996) 535.

40. J. Sedlár, J. Pác, J. *Polymer* 15 (1974) 613.

41. P. J. F. Griffiths, J. G. Hughes, G. S. Park, *Eur. Polym. J.* 29 (1993) 437

42. C. Decker, J. Marchal, *Makromol. Chem*. 166 (1973) 155.

43. Y. Sun, Y. Yin, B. T. Mayers, T. Herricks, Y. Xia, *Chem. Mater.* 14 (2002) 4736.

44. D. I. Garcia-Gutierrez, C. E. Gutierrez-Wing, L. Giovanetti, J. Ramallo-López, F. G. Requejo, M. Jose-Yacaman, *J. Phys. Chem. B* 109 (2005) 3813.

45. F. Bonet, K. Tekaia-Elhsissen, K. Vijaya Sarathy, *Bull. Mater. Sci.* 23 (2000) 165.

46. M. Su, C. Bai, C. Wang, *Solid State Commun.* 106 (1998) 643.

47.   M. Sastry, V. Patil, K. S. Mayya, D. V. Paranjape, P. Singh, S. R. Sainkar, *Thin Solid Films* 324 (1998) 239.

48.   M. T. Reetz, W. H. Helbig, S. A. Quaiser, U. Stimming, N. Breuer, R. Vogel, *Science*, 267 (1995) 367.

49.   J. M. Parera, N. S. Figoli, E. M. Traffano, J. N. Beltramini, E. E. Martinelli, *Appl. Catal*. 5 (1983) 33.

Chapter 9

Monodisperse platinum nanoparticles of well-defined shape: Synthesis, characterization, catalytic properties and future prospects

9.1   Introduction

The surface structure of small metal crystallites changes most dramatically in the 1-5 nm size range and in the case of some reactions catalytic activity is sensitive to particle size changes in this regime [1-6]. As crystal domains become smaller, the ratio of corner and edge atoms to terrace atoms increases [7-10] and the surface topology becomes increasingly roughened. Dimensional control of particles and resulting changes in surface and electronic states, presents an opportunity to tailor particle surfaces to affect substrate interactions. Substrate adsorption on corner and edge atoms, that possess open coordination spheres, can be significantly different, in terms of bond enthalpies, desorption energies, and adsorption geometry, than adsorption occurring on terrace sites. An illustrative example of the concept is the dissociation of CO on Rh surfaces, which is nine orders of magnitude faster on Rh(211) than Rh(111), due to the presence of exposed sites on the step edges of Rh(211) that do not exist on Rh(111) [11].

Boudart has classified catalytic reactions whose rate varies as a function of particle size as structure sensitive [12]. Significant advances in understanding catalytic phenomena, such as the concept of structure sensitive/insensitive reactions, are the result of studying such phenomena on model catalytic systems [13]. The most recent extension of model catalytic systems, or at the very least the simplification of a complex supported catalyst, is the synthesis of monodisperse transition metal nanoparticles with uniform size and shape and their incorporation into typical high surface area oxide support matrices [14-17]. The materials are intended as three dimensional model catalysts, where particle characteristics, such as size, shape, or crystallinity, are controllably varied to probe for influence on catalytic activity and selectivity [15, 16, 18-21]. Solution syntheses of Pt particles yield monodisperse samples with tunable size and shape. Catalyst materials that are prepared by the combination of the proper support and monodisperse particles have unprecedented uniformity, which is difficult to achieve with conventional catalyst synthetic methods.

The effect of metal nanoparticle size on catalytic activity is better understood than the influence of nanoparticle shape on catalytic activity, since size control of crystallites has generally been easier to achieve than shape control.

Introduction of foreign ions during solution phase synthesis of metal nanoparticles is a major parameter for controlling particle shape. Xia *et al*. have extensively studied morphology changes of noble metal nanoparticles (Ag, Pd, and Pt) by adding various foreign ions [22]. They observed that chloride ions and oxygen in the reaction mixture preferentially dissolved twinned particles initially formed during reduction and led to selective formation of single crystalline products such as truncated tetrahedra and

cuboctahedra. In another study by Xia *et al*. [23], trace amounts of iron chloride slowed the reduction of Pt(II) species, inducing optimal anisotropic growth condition during a polyol process to form agglomerates of single-crystalline Pt nanowires rather than small (< 5 nm) Pt crystallites which formed without iron chloride. The addition of large amounts of $NaNO_3$ to a Pt salt solution led to the formation of branched nanostructures due to platinum nitrate formation, which alters the reduction kinetics of Pt [24]. Addition of silver ions in a polyol synthesis of Pt nanoparticles results in lower nucleation temperatures, which favor anisotropic growth to form Pt multipods [25]. Although several foreign ions have been reported to substantially affect particle morphologies, the exact mechanism has not been determined. It is thought that selective adsorption of the additive ion on one or more crystal surfaces changes the selective growth rate of crystal faces leading to the change of shape [26].

In this paper, we demonstrate the synthesis of Pt nanocrystals of well-defined shape using silver ions [27] and poly(vinylpyrrolidone) (PVP) in solution and encapsulation in mesoporous silica (SBA-15) during *in-situ* hydrothermal synthesis. Physical and chemical properties are determined and the prospect of these catalysts serving as models of complex technical catalysts is discussed. The study of reaction selectivity during the hydrogenation of α,β unsaturated aldehyde is suggested as a probe of nanoparticle surface structure.

9.2   Experimental

9.2.1   *Nanoparticle synthesis*

A detailed description of the synthesis of the nanoparticles has been published elsewhere [27]. A brief description of the synthesis is given here. Synthesis of Pt cubes began with the introduction of 0.5 mL of 2×10^{-3} M silver nitrate (AgNO$_3$, 99+%, Sigma-Aldrich) solution in ethylene glycol (EG) to boiling EG followed by the immediate introduction of 3 mL of poly(vinylpyrrolidone) (PVP, MW = 55 K, Sigma-Aldrich, 0.375 M) and 1.5 mL of hexachloroplatinic acid (H$_2$PtCl$_6$•6H$_2$O, 99.9%, metals basis, Alfa-Aesar, 0.0625 M) EG solutions dropwise over 16 min. The resulting mixture was heated at reflux for an additional five minutes followed by centrifugation. After separation of the supernatant and precipitate in acetone, the precipitate was redispersed and washed with ethanol twice and finally dispersed in ethanol. Increasing the molarity of the AgNO$_3$ solution to 2×10^{-2} M and 6×10^{-2} M led to the selective formation of cuboctahedral and octahedral particles, respectively.

9.2.2 *Catalyst Synthesis and Characterization*

A detailed procedure for the synthesis of catalysts by nanoparticle encapsulation (NE) in high surface area mesoporous silica can be found elsewhere [28]. A brief description is given here. A Pt colloid aqueous solution (27.0 mL, 3×10^{-3} M) was mixed with 50.5 mL of aqueous polymer solution (Pluronic P123, EO$_{20}$PO$_{70}$EO$_{20}$, EO = ethylene oxide, PO = propylene oxide, BASF, 2.5 g) and stirred for 1 h at 313 K followed by the quick addition of 0.375 mL of 0.5 M sodium fluoride (NaF, 99.99%, Aldrich) aqueous solution and 3.91 mL of tetramethyl orthosilicate (TMOS, 98%, Aldrich) to the reaction mixture, followed by stirring for a day at 313 K. The resulting slurry was aged for an additional day at 373 K. The brown precipitate was separated by centrifugation, thoroughly washed with ethanol, and dried in an oven at 373 K.

Elemental analysis of the catalysts for Pt and Ag content were determined by inductively coupled plasma-atomic emission spectroscopy (ICP-AES) at Galbraith Laboratories Inc. (Knoxville, TN). Catalysts were made to have a nominal weight loading of 1 % Pt, but ranged from 0.5-0.7 % by weight as determined by ICP-AES. XRD diffractograms of the supported Pt catalysts were measured on a Bruker D8 GADDS diffractometer using Co Kα radiation (1.79 Å) and the particle size was calculated by the Scherrer equation. Catalysts used for ethylene hydrogenation were calcined in 20% O_2/He (total flow 50 cc (STP) min^{-1}) for 1 h at 473 K, purged with He for ½ h at 473 K, followed by reduction in H_2 (50 cc (STP) min^{-1}) for 1 h at 473 K. Cyclic oxidation-reduction experiments confirmed that ethylene hydrogenation activity was maximized after one treatment cycle [29].

9.2.3 *Reactivity studies: Ethylene hydrogenation as a surface probe*

Catalytic reactions were studied in a Pyrex plug flow reactor connected to a ¼" stainless steel manifold containing mass flow controllers (Unit Instruments) for delivery of reactant gases. Ethylene (AirGas, CP grade), hydrogen (Praxair, UHP, 99.999%) and helium (Praxair, UHP, 99.999%) were used as received. Reaction temperatures were measured with a thermocouple extending into the catalyst bed. Reactants and products were detected by gas chromatography (Hewlett Packard 5890) and quantified using Dietz tables [30]. Reaction rate measurements were conducted at differential conditions (all conversions, X < 10%). Typically the catalyst (5 – 15 mg) was diluted with low surface area acid washed quartz in a 1:3 ratio (catalyst: quartz). The Madon-Boudart test [31] verified the absence of heat and mass transfer limitations.

9.3   Results and Discussion

9.3.1   Nanoparticle and catalyst synthesis.

The results for both nanoparticle [27] and catalyst syntheses [28] have been previously published. Details of both syntheses are summarized here. The slow addition of separate PVP and $H_2PtCl_6 \cdot 6H_2O$ solutions to boiling EG caused the color of the solution to change from yellow to dark brown indicating the fast reduction of Pt(IV) species to Pt(0) species. If Ag ions were not added prior to the introduction of the Pt salt, a distribution of Pt particle shapes were obtained [26]. Only upon addition of varying concentrations of $AgNO_3$ is preferential growth of the Pt nanoparticles observed. At a $AgNO_3$ concentration of 1.1 mol % (relative to Pt salt concentration), cubes are formed with ~80% selectivity (Figure 1A), while at 11% and 32 mol % $AgNO_3$, cuboctahedra and octahedra are synthesized with ~100% and 80% selectivity, respectively (Figure 1B and C). In the case of cube and octahedra synthesis, the minor shape is tetrahedral. In all cases, the largest vertex-to-vertex distance is ~9.5 nm ($\sigma \sim 7\%$) regardless of shape . Size and shape of the as-synthesized particles were dependent upon the addition rate of PVP and $H_2PtCl_6 \cdot 6H_2O$. A single addition led to the formation of 4 nm particles with no dominant shape, while slow addition (over 30 min. time period) led to polycrystalline particles with diameters ≥ 13 nm. It was determined that the addition of PVP and Pt salt over a 16 min. time period was optimal. A summary of the Pt particle shapes and yield is shown in Table 1.

UV-Vis absorption spectroscopy under synthetic conditions in the presence of Ag ions suggested the presence of reduced Ag_4^{2+} species during the early stages of synthesis;
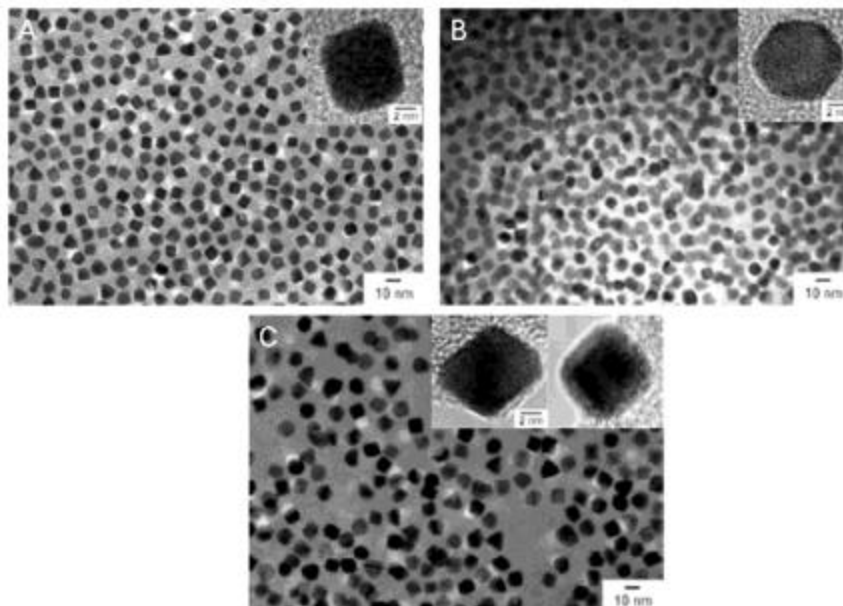
Figure 9.1. TEM micrograph of as-synthesized Pt nanoparticles with distinct shapes: (A) cubes, (B) cuboctahedra and (C) octahedra. Inset: HRTEM images of major particle shape.

with the formation of Ag particles at longer synthesis times [27]. It is believed that the mechanism for Pt nanoparticle growth involves enhanced growth along <100> and/or suppressed growth along <111> due the introduction of Ag ions and their strong adsorption on (100) terminated Pt surfaces. The growth of Ag thin films on single crystalline Pt surfaces has shown that the desorption activation energy of Ag on Pt(100) is higher than on Pt(111) [31]. Some of the silver is removed by repetitive centrifugation and dispersion after Pt particle formation as determined by UV-Vis spectroscopy [27]. This work represents one of the first reports of control over both nanoparticle size and shape under the same synthesis conditions [27].

After purification of the Pt nanoparticles, they were introduced into an aqueous solution of Pluronic P123. In a typical reaction, a Pt colloid solution was mixed with the aqueous polymer solution at 313 K, and stirred for 1 h to ensure complete dispersion of

the Pt particles. Brown precipitates were formed in 5 min after the addition of NaF solution and TMOS. The supernatant was colorless and transparent, indicating that all Pt colloids were incorporated into the silica matrix. The slurry was aged for a day at 313 K and placed in an oven at 373 K for an additional day. The product was washed with water and ethanol, and dried in air at 373 K. Figure 2 shows a schematic of the nanoparticle encapsulation (NE) method and a TEM micrograph of the 0.55% Pt(cubes)/SBA-15 catalyst. The Pt particles are isolated and located within the silica framework without severe aggregation. This method has been successfully utilized with PVP capped monodispersed Pt nanoparticles ranging in size from 1-7-7.1 nm [28].
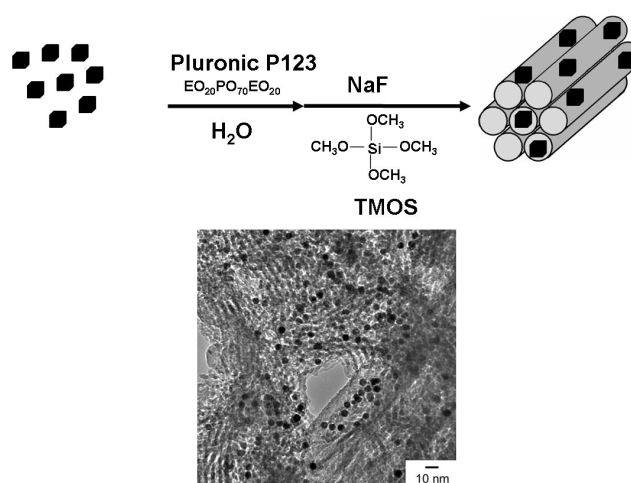
Figure 9.2. Scheme for nanoparticle encapsulation (NE) synthesis of Pt/SBA-15 catalysts and TEM micrograph of a 0.55% Pt(cubes)/SBA-15 catalyst.

Removal of PVP or any other surface stabilizing polymer represents a significant challenge. In most circumstances, these organic molecules are bound strongly to the nanoparticle surface at approximately monolayer coverage. Thermal degradation or calcination of the adsorbed organics are two possible methods for removal and cleansing of the Pt surface. These methods generally require high temperatures and local hot spots

Table 9.1. Yield and average size of Pt nanoparticles

Amount of Ag added[a]	Major shape yield[b] and average size[c]	Minor shape yield[b] and average size[c]
0 mol %	Cubes with rounded edges ~40%	Spheres, ~30% Irregular rods, ~20% Tetrahedra, ~10%
1.1 mol %	Cubes ~80%, 9.4 ± 0.6 nm	Tetrahedra ~10%, 9.8 ± 0.7 nm
11 mol %	cuboctahedra ~100%, 9.1 ± 0.6 nm	--
32 mol %	Octahedra ~80%, 9.8 ± 0.6 nm	Tetrahedra ~10%, 9.9 ± 0.7 nm

[a]With respect to the Pt salt concentration.
[b]Statistically determined values based on counting 250 particles.
[c]Largest vertex to vertex distance.

can be generated at the nanoparticle surface during calcination. In this study, hot spots were avoided by calcination in dilute oxygen (20% O_2/He, Praxair, UHP both gases). Thermal gravimetric analysis of unsupported Pt cubes demonstrates that calcination is much more effective for PVP removal than thermal treatment in N_2 (Figure 3A). PVP decomposes at 473-623 K under O_2 flow; 150 K lower than with N_2. Figure 3B demonstrates that free PVP decomposes at ~573 K. Pt apparently catalyzes the combustion of PVP by the diffusion of O_2 through the randomly tangled alkyl chains of
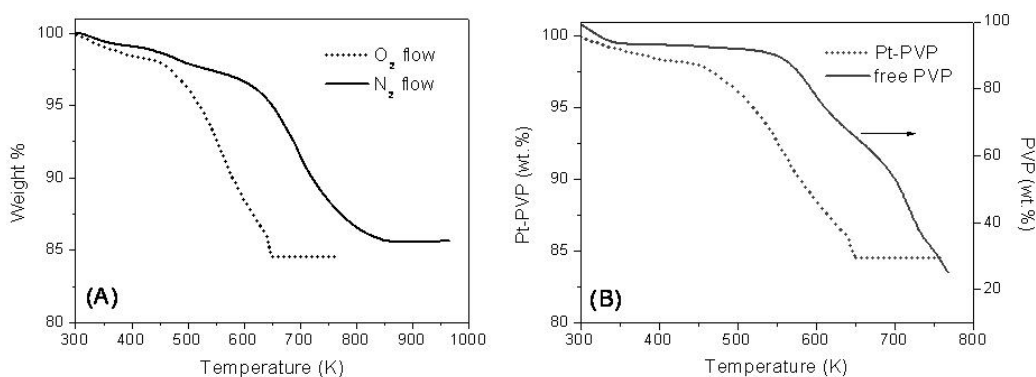
Figure 9.3. (A) Thermogravimetric analysis (TGA) of free PVP and PVP capped Pt cubes and (B) influence of thermal treatment atmosphere on PVP decomposition from Pt cubes.

PVP and dissociation on a clean ensemble of Pt atoms, whereupon catalytic decomposition occurs. Isothermal treatments of free PVP and PVP-Pt/SiO$_2$ physical mixtures in inert (He) and reactive (oxygen) atmospheres confirm that O_2 is more effective toward PVP degradation, and clean Pt catalyzes PVP decomposition at 523 K [29]. While thermal treatments in N_2 or He are effective for removing PVP, both require relatively high temperatures. *In-situ* vacuum transmission electron microscopy imaging of these same nanoparticles adsorbed to amorphous silica grids at temperatures up to 1073 K demonstrate that Pt nanoparticles become truncated at ~623 K, then spherical and

finally the particles spread on the support as the temperature increases [33]. These temperatures are close to those required to remove PVP from the nanoparticle surface. Recently, it has been shown that cyclic oxidation-reduction treatments are effective for removal of PVP with each cycle removing more surface bound PVP or carbon as indicated by ethylene hydrogenation reaction rates [29]. Most of the PVP is removed by calcination at 473 K as determined by infrared spectroscopy, thermal gravimetric analysis and temperature programmed oxidation [29].

9.3.2   *Characterization and Ethylene Hydrogenation Studies of Pt/SBA-15 catalysts*

Elemental analyses of the Pt/SBA-15 catalysts by ICP-AES showed that Pt loadings were in the range of 0.5 – 0.7 wt.%, while the Ag residues were at levels corresponding to a Ag/Pt molar ratio of 0.014, 0.102, and 0.123 for the cubes, cuboctahedra, and octahedra, respectively, based on Pt and Ag content as shown in Table 2. No detectable Ag signals were found in previous XRD and Energy Dispersive X-ray spectroscopy (EDX) studies and AgCl, a product of the reaction between Ag and H_2PtCl_6 was found to precipitate out due to its low solubility in ethylene glycol [27]. BET N_2 adsorption measurements were carried out on the Pt/SBA-15 catalysts and summarized in Table 2. The surface areas of the catalysts are ~ 500 m^2 g^{-1}, slightly lower than pristine SBA-15 [28]. The pore volumes are in the range of ~ 1.9 cc(STP) g^{-1}, and the average pore diameters calculated from desorption branches are around 9 nm. Table 2 contains the Pt particle size determined by line-broadening techniques. Measured XRD particle sizes agree with previous results [27].

Rates of ethylene hydrogenation were measured at low conversions over all catalysts. Initial specific rates for ethylene hydrogenation varied from ~0.1 to 37 μmol g^{-}

^{1} s^{-1}, while turnover frequencies (TOF, s^{-1}) differed by three orders of magnitude over the three catalysts (Table 3). The cubes, with the lowest level of Ag incorporation (Table 2) had the highest rate (~9 s^{-1}), in good agreement with measurements on Pt(111) [34] and other types of Pt catalysts [28, 34–42] (Table 4). Turnover frequencies reported in Table 4 vary from 1–10 s^{-1} confirming that the rate measured over pure Pt catalysts with very different morphologies (*i.e.* single crystals and supported nanoparticles) are similar. In a comprehensive study of the influence of particle size on ethylene hydrogenation, Dorling and co-workers found that the areal rate was invariant with particle size [39]. Pt nanoparticles with higher levels of Ag incorporation are much less active for ethylene hydrogenation on per surface Pt atom basis; the TOF decreased to 0.4 and 2×10^{-2} s^{-1} for the cuboctahedra and octahedra, respectively. These reported turnover rates are nominal and represent a minimum because all surface atoms were assumed platinum. Hydrogenation of ethylene on Ag/SiO$_2$ catalysts does not occur until temperatures $\geq$ 550 K and Ag is only active if highly dispersed [43]; bulk Ag powder was inactive for ethylene hydrogenation at 300 K [44]. The reduction in rate is associated with the presence of Ag present on the surface of the Pt nanoparticles as small clusters which most likely modify the electronic structure of the Pt, as recently shown for a bimetallic Pt-Cu/SiO$_2$ catalyst [45, 46]. Campostrini *et al*. studied the hydrogenation of propylene over a series of Pt-Ag/SiO$_2$ alloy catalysts with Pt/Ag molar ratio ranging from 0.83 to 0.12; the authors found the olefin hydrogenation specific rate decreased substantially as Ag content increased and kinetic parameters such as reaction orders and activation energy changed with more Ag introduction [47]. Pure Pt catalysts were ~50 times more active than a Pt-Ag catalyst with Pt/Ag ratio of 0.12. These catalysts have Ag loadings much

greater than those used in this study, but confirm Ag influences olefin hydrogenation on Pt catalysts. Adsorption and infrared studies of probe gases (H_2, O_2, CO) on Pt-Ag alloy nanoparticles supported on SiO_2 suggest that Pt does not segregate to the surface under reducing conditions, while oxidizing conditions leads to segregation of Ag to the surface for catalysts with Ag atomic compositions as high as 64% [48]. It is worth noting that the pretreatment of all catalysts in this study included a 1 h oxidation step.

Ag incorporation in the cuboctahedra and octahedra was significantly higher than in the cubes, suggesting that Ag may be located on the particle surface or a few atomic layers below surface. Ag is believed to be present on the surface because XRD measurements do not indicate the formation of a PtAg alloy, consistent with their complete immiscibility in the bulk [49]. Lahiri *et al.* [50] have shown that Pt and Ag do not alloy at the nanoscale (2 nm Pt core particle), but rather form a Ag-Pt coreshell nanoparticle. The deposition and growth of Ag adlayers on Pt(111) leads to monolayer confined mixing; *i.e.* Ag is confined to the topmost layer [32, 51]. Mixing at the Pt-Ag interface occurs at step edges and Ag is present as small clusters at submonolayer Ag coverages [51].

9.3.3   Future prospects: Influence of surface structure on reaction selectivity

The ability to synthesize monodispersed Pt nanoparticles of catalytically relevant size ($\leq$ 10 nm) with well-defined shape is a significant achievement in the development of a supported model catalyst. Our agenda with regards to these well-defined nanoparticle/silica catalysts is to study the influence of surface structure on catalytic reaction selectivity. Low temperature ($\leq$ 400 K) multi-path reactions have been targeted

Table 9.2. Elemental analysis and physical properties of Pt/SBA-15 catalysts

Catalyst	Pt loading[a] (wt. %)	Ag loading[a] (ppm)	Physisorption parameters			XRD partice size[c] (nm)
			BET surface area $(m^2\ g^{-1})$	BJH pore size (Å)	Pore volume $(cc(STP)\ g^{-1})^b$	
Pt(cubes)/SBA-15	0.55	43	498	9.0	1.86	7.5
Pt(cuboctahedra)/SBA-15	0.67	378	505	9.2	1.78	8.4
Pt(octahedra)/SBA-15	0.48	326	511	9.3	1.90	8.9

[a]Determined by inductively coupled plasma atomic emission spectrometry (ICP-AES).
[b]Based on the Kelvin equation at $P/P_0 = 0.975$.
[c]Based on the Scherrer equation.

Table 9.3. Kinetics of ethylene hydrogenation on Pt/SBA-15 catalyst series

Catalyst[a]	Activity[b] (μmol g^{-1} s^{-1})	Turnover Frequency[b,c] (s^{-1})	E_a[d] (kcal mol^{-1})
0.55% Pt(cubes)/SBA-15	36.6	8.6	9.9
0.67% Pt(cuboctahedra)/SBA-15	1.9	0.4	10.8
0.48% Pt(octahedra)/SBA-15	0.07	2×10^{-2}	13.4

[a]Catalysts were pretreated in 20% O_2/He for 1 h followed by reduction in H_2 for 1 h at 473 K.
[b]Reaction conditions were 10 Torr C_2H_4, 100 Torr H_2, and 298 K.
[c]Normalized to the number of surface atoms using the following relationship, D = 1.13/d(nm) where D is the dispersion and d is the particle diameter determined by XRD.
[d]Reaction conditions were 10 Torr C_2H_4, 100 Torr H_2 and 273-373 K (catalyst dependent).

Table 9.4. Comparison of ethylene hydrogenation rates on various types of Pt catalysts

Catalyst	Ethylene turnover frequency (TOF)[a] (s^{-1})	Reference
Pt(111)	9.3	34
Pt(100)-(5 × 20)	3.6	35
Pt(210)	7.8	36
Pt nanoparticle array/Al_2O_3	6.5	37
Pt nanoparticle array/SiO_2	4.7	38
~ 0.7% Pt(X)/SBA-15, X = 1.7, 2.9, 3.6 or 7.1 nm	3.5	28
2.45% Pt/SiO_2	9.3	39
0.05% Pt/SiO_2	1.3	40
Pt wire	3.0	41
0.04% Pt/SiO_2	4.4	42

[a]Corrected to standard conditions of 10 Torr C_2H_4, 100 Torr H_2 and 298 K.

due to the instability of the nanoparticle surface structure above ~573 K as demonstrated by electron microscopy [33]. A likely prototype reaction for this type of study is the hydrogenation of α,β unsaturated aldehydes; acrolein (C_3H_4O), crotonaldehyde (C_4H_9O) and cinnamaldehyde (C_9H_8O). Acrolein and crotonaldehyde have proven more difficult to selectively hydrogenate than cinnamaldehyde [52].

Selective hydrogenation of the carbonyl group in acrolein and crotonaldehyde is very difficult and with many catalysts both the C=C and C=O bonds are hydrogenated to yield the primary alcohol. The selective formation of the allylic alcohols is preferred because they are valuable intermediates for the production of perfumes and pharmaceuticals [52]. The reaction scheme for crotonaldehyde hydrogenation is shown in Figure 4A. Reported selectivities to crotyl alcohol for SiO_2 supported Pt catalysts are generally low ($\leq$ 10 %), but selectivities as high as 43 % have been reported for Pt/SiO_2 catalysts with no additives [53-55]. Santori and co-workers [54] have shown that the selectivity to crotyl alcohol during liquid phase crotonaldehyde hydrogenation increases from 9% to 35% at 80% conversion as the Pt particle size on SiO_2 and Al_2O_3 supported catalysts increases from 2 to 6 nm.

Higher selectivity to crotyl alcohol on catalysts containing larger Pt particles suggest that low index faces of fcc metals such as Pt(111) are required for C=O hydrogenation rather than open, low coordination step and kink sites which facilitate hydrogenation of both C=C and C=O bonds [56, 57]. Theoretical results of crotonaldehyde adsorption and hydrogenation have shown hydrogenation of the carbonyl bond is preferred on Pt(111) over other Pt single crystal surfaces [58, 59].
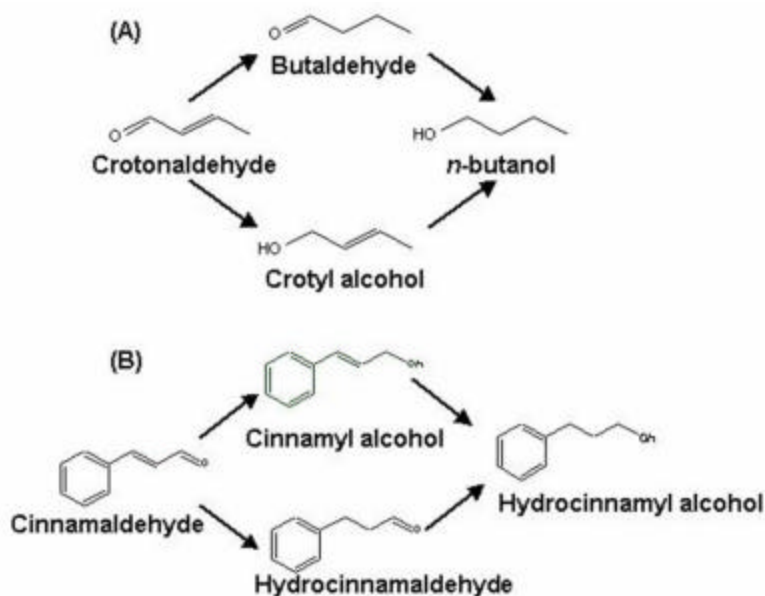
Figure 9.4. Reaction scheme for hydrogenation of α,β unsaturated aldehydes: (A) crotonaldehyde and (B) cinnamaldehyde.

A low temperature reaction involving the hydrogenation of an aromatic α,β unsaturated aromatic aldehyde, cinnamaldehyde is similarly suited for a study of selectivity versus surface structure. The reaction scheme is shown in Figure 4B. As in the case of crotonaldehyde hydrogenation, the unsaturated alcohol is the favored product. Gallezot and co-workers have shown the selectivity to cinnamyl alcohol from cinnamaldehyde has a strong dependence on Pt particle size. The selectivity to the alcohol varied from 83% to 98% (at 50% conversion) as the particle size was increased from 1.3 to ~5 nm [60]. The increased selectivity of larger particles is attributed to a steric repulsion between the flat metal surface and aromatic ring causing hindered adsorption and preferential hydrogenation of the carbonyl group [60, 61]. Crotonaldehyde and cinnamaldehyde hydrogenation may serve as probe reactions of the Pt nanoparticle surface structure because the (111) surface is more selective for the formation of the unsaturated alcohol. The fraction of exposed (111) faces is greatest in

the octahedra (and tetrahedra) followed by the cuboctahedra while cubes are terminated on all sides by (100) surfaces.

9.4   Summary

The synthesis of ~9 nm Pt nanoparticles of well-defined shape with the use of silver ions and surface templating polymers in protic solvents has been demonstrated. Addition of increasing amounts of $AgNO_3$ to refluxing ethylene glycol followed by slow introduction of $H_2PtCl_6 \cdot 6H_2O$ leads to the formation of cubes, cuboctahedra and octahedra with shape uniformity greater than eighty percent. The Pt nanoparticles are incorporated into a mesoporous silica matrix by hydrothermal growth and encapsulation of Pt nanoparticles in aqueous solution. Removal of the surface templating polymer was achieved with thermal oxidation-reduction treatments. The catalysts are active for ethylene hydrogenation and are promising materials for future studies on the influence of catalyst particle shape on reaction selectivity during the low temperature hydrogenation of α,β unsaturated aldehydes.

9.5   References and Notes

1.   M. Boudart, *J. Mol. Catal*. 30 (1985) 27.

2.   M. J. Yacamán, S. Fuentes and J. M. Dominguez, *Surf. Sci*. 106 (1981) 472.

3.   M. Gillet and A. Renou, *Surf. Sci*. 90 (1979) 91.

4.   B. Coq and F. Figueras, Coord. *Chem. Rev*. 178-180 (1998) 1753.

5.   A. S. McLeod and L. F. Gladden, *J. Catal.* 173 (1998) 43.

6.   L. F. Gracia and E.E. Wolf, *Chem. Eng. J*. 82 (2001) 291.

7.   R. Van Hardeveld and F. Hartog, *Surf. Sci*. 15 (1969) 189.

8.   S. Ladas, *Surf. Sci*. 175 (1986) L681.

9.   R. B. Greegor and F. W. Lytle, *J. Catal.* 63 (1980) 476.

10.   J. J. Burton, *Catal. Rev*. 9 (1974) 209.

11.   M. Mavrikakis, M. Bäumer, H. J. Freund and J. K. Nørskov, *Catal. Lett*. 81 (2002) 153.

12.   M. Boudart, *Adv. Catal*. 20 (1969) 153.

13.   M. Boudart, *Top. Catal*. 13 (2000) 147.

14.   H. Lang, R. A. May, B. L. Iverson and B. D. Chandler, *J. Am. Chem. Soc*. 125 (2003) 14832.

15.   R. M. Rioux, H. Song, J. D. Hoefelmeyer, P. Yang and G. A. Somorjai, *J. Phys. Chem. B* 109 (2005) 2192.

16.   J. W. Yoo, D.J. Hathcock and M.A. El-Sayed, *J. Catal*. 214 (2003) 1.

17.   J. W. Yoo, D. Hathcock, and M.A. El-Sayed, *J. Phys. Chem. A* 106 (2002) 2049.

18. Z. Kónya, V. F. Puntes, I. Kiricsi, J. Zhu, A. P. Alivisatos, and G. A. Somorjai, *Catal. Lett*. 81 (2002) 137.

19. Z. Kónya, V. F. Puntes, I. Kiricsi, J. Zhu, A. P. Alivisatos, and G. A. Somorjai, *Nano. Lett*. 2 (2002) 907.

20. Z. Kónya, V. F. Puntes, I. Kiricsi, J. Zhu, J. W. Ager III, M. K. Ko, H. Frei, A. P. Alivisatos and G. A. Somorjai, *Chem. Mater*. 15 (2003) 1242.

21. J. Zhu, Z. Kónya, V. F. Puntes, I. Kirisci, C. X. Miao, J. W. Ager III, A. P. Alivisatos and G. A. Somorjai, *Langmuir* 19 (2003) 4396.

22. B. Wiley, Y. Sun, B. Mayers and Y. Xia, Chem. Eur. J. 11 (2005) 454.

23. J. Chen, T. Herricks, M. Geissler and Y Xia, *J. Am. Chem. Soc*. 126 (2004) 10854.

24. T. J. Herricks, J. Chen, and Y. Xia, *Nano Lett*. 4 (2004) 2367.

25. X. Teng and H. Yang, *Nano Lett*. 5 (2005) 885.

26. Y. –W Jun, J. –H. Lee, J.-sil Choi and J. Cheon, *J. Phys. Chem. B* 109 (2005) 14795.

27. H. Song, F. Kim, S. Connor, G. A. Somorjai and P. Yang, *J. Phys. Chem. B* 109 (2005) 188.

28. H. Song, R. M. Rioux, R. Komor, J. D. Hoefelmeyer, K. Niesz, M. Grass, P. Yang and G. A. Somorjai, Submitted to *J. Am. Chem. Soc*. (2005).

29. R. M. Rioux, M. Grass, T. Toops, K. Niesz, H. Song, J. D. Hoefelmeyer, P. Yang and G. A. Somorjai, To be published (2005).

30. W. A. Dietz, *J. Gas. Chrom*. 5 (1967) 68.

31. R. J. Madon and M. Boudart, *Ind. Engr. Chem. Fund*. 21 (1982) 438.

32. U. Strüber, A. Kastner, and J. Küppers, *Thin Solid Films* 250 (1994) 101.

33. R. Yu, H. Song, X. –F. Zhang, and P. Yang, *J. Phys. Chem. B* 109 (2005) 6940.

34. F. Zaera and G.A. Somorjai, *J. Am. Chem. Soc*. 106 (1984) 2288.

35. A. L. Backman and R. I. Masel, *J. Vac. Sci. Technol. A* 6 (1988) 1137.

36. L.P. Ford, H.L. Nigg, P. Blowers and R.I. Masel, *J. Catal*. 179 (1988) 163.

37. J. Grunes, J. Zhu, E. A. Anderson and G. A. Somorjai, *J. Phys. Chem B* 106 (2002) 11463.

38. A. M. Contreras, J. Grunes, X. -M. Yan, A. Liddle and G. A. Somorjai, *Catal. Lett*. 100 (2005) 115.

39. T. A. Dorling, M. J. Eastlake and R. L. Moss, *J. Catal*. 14 (1969) 23.

40. J. C. Schlatter and M. Boudart, *J. Catal*. 24 (1972) 482.

41. V. B. Kazanskii and V. P. Strunin, Kinet. Katal. 1 (1960) 553.

42. R. D. Cortright, S. A. Goddard, J. E. Rekoske and J. A. Dumesic, *J. Catal*. 127 (1991) 342.

43. H. Ehwald, A.A. Shestov, and V.S. Muzykantov, *Catal. Lett*. 25 (1994) 149.

44. H Imamura, M. Yoshinobu, T. Mihara, Y. Sakata and S. Tsuchiya, *J. Mol. Catal*. 69 (1991) 271.

45. V.Y. Borovkov, D. R. Luebke, V. I. Kovalchuk, and J. L. d'Itri, *J. Phys. Chem. B* 107 (2003) 5568.

46. V. I. Avdeev, V. I. Kovalchuk, G. M. Zhidomirov, and J. L. d'Itri, *Surf. Sci*. 583 (2005) 46.

47. R. Campostrini, G. Caruran and R. M. Baraka, *J. Mol. Catal*. 78 (1993) 169.

48. K. P. De Jong, B. E. Bongenaar-Schlenter, G. R. Meima, R. C. Verkerk, M. J. J. Lammers and J. W. Geus, *J. Catal*. 81 (1983) 67.

49. M. Hansen, *Constitution of Binary Alloys* (McGraw-Hill, New York, 1958).

50. D. Lahiri, B. Bunker, B. Mishra, Z. Zhang, D. Meisel, C. M. Doudna, M. F. Bertino, F. D. Blum, A. T. Tokuhiro, S. Chattopadhyay, T. Shibata and J. Terry, *J. Appl. Phys.* 97 (2005) 094304.

51. H. Röder, R. Schuster, H. Brune and K. Kern, *Phys. Rev. Lett*. 71 (1993) 2086.

52. P. Claus, *Top. Catal*. 5 (1998) 51.

53. M. A. Englisch, A. Jentys and J.A. Lercher, *J. Catal*. 166 (1997) 25.

54. G. F. Santori, M. L. Casella, G. J. Siri, H. R. Adúriz and O. A. Ferretti, React. *Kinet. Catal. Lett*. 75 (2002) 225.

55. M. A. Vannice and B. Sen, *J. Catal*. 115 (1989) 65.

56. T. Birchem, C. M. Pradier, Y. Berthier and G. Cordier, *J. Catal*. 146 (1994) 503.

57. C. M. Pradier, T. Birchem, Y. Berthier and G. Cordier, *Catal. Lett*. 29 (1994) 371.

58. F. Delbecq and P. Sautet, *J. Catal*. 152 (1995) 217.

59. F. Delbecq and P. Sautet, *J. Catal*. 211 (2002) 398.

60. A. *Giror-Fendler*, D. Richard and P. Gallezot, *Catal. Lett*. 5 (1990) 175.

61. M. Lashdaf, J. Lahtinen, M. Lindblad, T. Venäläinen and A. O. I. Krause, *Appl. Catal. A Gen.* 276 (2004) 129.

Chapter 10

Conclusions and Future Work

10.1   Conclusions

The objective of this thesis was to develop a catalyst design project in which transition metal heterogeneous catalysts could be synthesized by methodologies which incorporated the ability to rationally change catalyst properties for systematic structure-function (activity and selectivity) studies in heterogeneous catalysis. The main catalyst property chosen was the size and shape of the supported nanoparticles. The three aspects of catalyst design were emphasized in this study: synthesis, characterization and reactivity studies. The reactions chosen were hydrocarbon conversion reactions which have been studied extensively on conventional prepared heterogeneous catalysts and model catalysts (*i.e.* single crystals) in our laboratory.

Two novel synthetic methods for catalyst synthesis were developed to gain exquisite control over the physical and chemical properties of the catalytic structures which could rationally tuned during synthesis. Solution phase reduction methods based in protic solvents were used to synthesize Pt nanoparticles in the presence of poly(vinylpyrrolidone) (PVP), a surface templating polymer, which serves to stabilize particles in solution. Particle size was controlled during synthesis by altering either the

PVP: Pt salt ratio, temperature, reaction media and by the addition of preformed Pt seed particles. Pt particles with sizes of 1.7 ± 0.26, 2.6 ± 0.22 and 2.9 ± 0.21 nm were synthesized in aqueous methanol or ethanol solutions. A seeded growth method was used to synthesize 3.6 ± 0.26 nm nanoparticles, by the addition of Pt precursor to a methanolic solution of 2.9 nm particles. Larger particles (7.1 ± 0.37 nm) were synthesized by the addition of ethylene glycol solution of Pt precursor to refluxing ethylene glycol. In all these syntheses, the solvent served as the reaction media and metal precursor reductant.

After synthesis, number average and volume average nanoparticle sizes were confirmed with transmission electron microscopy (TEM) and x-ray diffraction (XRD), respectively, while crystallinity and morphology of the particle was determined by electron diffraction. After purification, Pt nanoparticles were loaded onto metal oxide supports by one of two methods developed in our laboratory. The first method, named capillary inclusion (CI) utilized low power sonication in aqueous methanolic solution to anchor Pt nanoparticles in the 7 nm straight pores of the mesoporous SBA-15 which had been synthesized and calcined to remove the template polymer. The method was called capillary inclusion because capillary forces along with the mechanical agitation due to sonication enabled stabilized nanoparticles in solution to diffuse into the pores. An alternative approach to the anchoring of nanoparticles to the surface of SBA-15 utilized a direct growth process, in which the mesoporous silica encapsulated the nanoparticles in solution by an *in-situ* hydrothermal synthesis of the mesoporous silica. This method called nanoparticle encapsulation (NE) guaranteed particles were located on the interior of the silica matrix due to hydrophobic-hydrophilic interactions. The triblock copolymers used to template the silica structure spontaneously form micelles in aqueous solution in which the

hydrophobic portion of the copolymer compose the core of the micelle while the more hydrophilic section interacts with aqueous solution. Pt nanoparticles are stabilized in the same solution by PVP, infrared investigations suggests that PVP bonds to the Pt surface via the carbonyl group of the pyrrolidone ring, thereby exposing the vinylic side chain of the polymer to the solution. The hydrophobic side chain is stabilized in the micelle core due to favorable hydrophobic interactions. Attempts to encapsulate the nanoparticles under optimal conditions (*i.e.* acidic) for well-ordered mesoporous silica formation were unsuccessful due to the agglomeration of particles. The instability of these nanoparticles is most likely due to the protonation of PVP causing the particles to precipitate out of solution. The growth of the silica framework in the Pt nanoparticle solution under neutral conditions required the addition of a catalyst for hydrolysis of soluble silica species. Synthesis under neutral conditions led to a catalyst in which the nanoparticles were dispersed throughout the silica matrix. After synthesis, the two catalysts were synthesized by a number of physical methods; such as nitrogen adsorption to determine total surface area, pore volume and pore size distribution. After inclusion and encapsulation, TEM and XRD confirmed that the particle size of the nanoparticles had not been altered by either synthetic procedure. The mesoporous silica was characterized by TEM and small angle x-ray scattering (SAXS) to determine the ordering of the mesoporous matrix. Capillary inclusion catalysts were prepared with mesoporous SBA-15 silica that had been prepared under acidic conditions and calcined prior to catalyst synthesis. The resultant silica had a high degree of long range order as evidenced by the SAXS data and verified by TEM, which was not disrupted by sonication. Nanoparticle encapsulation samples had less long range order which was evident from TEM and

SAXS data. Silica synthesis in the presence of PVP-capped Pt nanoparticles led to a material with a higher degree of order than silica synthesized in neutral conditions in the absence of nanoparticles. It appears that the PVP-capped nanoparticles have enhanced templating effect, which is probably due to favorable interactions between the vinyl sidechains of PVP and the poly(propylene oxide) (PPO) units of the triblock copolymer.

The role of the surface templating polymer, poly(vinylpyrrolidone) (PVP) during nanoparticle synthesis is stabilization of the nanoparticles while in solution. Removal of the polymer while maintaining the integrity of the particle size and shape distribution is challenging. Long calcination times (12-24 h) in oxygen followed by *in-situ* reduction were required to remove PVP from the nanoparticle surface of capillary inclusion samples. The length and temperature of the calcination procedure was particle size dependent. Significantly more effort was placed on the removal of PVP from the NE samples because they also contain the triblock copolymer used to template the silica matrix in the as-synthesized state. *Ex-situ* calcination procedures similar to those used for the CI samples but with longer calcinations times (24-36 h sample dependent) were applied to the NE samples. Diffuse reflectance infrared spectroscopy investigations demonstrated that a significant fraction ($\geq 90\%$) of the PVP was removed from the catalyst surface after calcinations compared with the as-synthesized sample. The length and temperature of the reduction treatment had little influence on the removal of residual PVP. Temperature programmed oxidation (TPO) studies of PVP oxidation demonstrated that CO_2 and H_2O evolved around 553 K, while TPO results from a Pt(1.7 nm)/SBA-15 catalyst suggested that the evolution of CO_2 and H_2O from PVP decomposition began at ~480 K demonstrating that Pt catalyzes the decomposition of PVP. Separate studies of

physical mixtures of free PVP and a Pt/SiO$_2$ catalyst confirm that Pt catalyzes the oxidative decomposition of PVP. TPO studies of a Pt(2.9 nm)/SBA-15-NE demonstrated that PVP was removed from the Pt surface over a broad temperature range as the PVP:Pt ratio increased. Thermal gravimetric analysis demonstrated that weight loss from a nanoparticle encapsulation catalyst occurred over three distinct regimes; desorption of water (< 373 K), decomposition of Pluronic triblock (453–573 K) copolymer and PVP (573–773 K). Rather than applying long *ex-situ* calcination – *in-situ* reduction pretreatments, short *in-situ* calcinations-reduction treatments from 373–473 K were implemented. Catalysts pretreated by this method were up to 7-10 times more active than their *ex-situ* calcined counterpart. It was demonstrated in the case of low temperature pretreatments (373 K), the activity of a Pt(7.1 nm) catalyst for ethylene hydrogenation increased with each oxidation-reduction cycle up to five cycles. In the case of the same Pt(7.1 nm) catalyst, a calcination-reduction single cycle at 473 K led to the highest measured activity for this catalyst.

Catalysts were characterized by selective gas adsorption and infrared spectroscopy after catalyst activation and reduction. Adsorption of H$_2$, CO and H$_2$ titration of adsorbed oxygen were three independent methods for determination of exposed surface area of both Pt/SBA-15 catalyst series. These surface average particle sizes were in relatively good agreement with particle sizes determined by bulk measurements (XRD and TEM), further confirming their monodisperse nature. The surface chemistry of the nanoparticles was probed with infrared investigations of CO adsorption. The peak position of carbon monoxide is an indicator of the local environment around which the CO is bound, including neighboring adsorbates and the

underlying metal structure. It was confirmed with CO adsorption that the average coordination number of the surface atoms decreases with decreasing particle size. The decreased coordination number of surface atoms in nanoparticles leads to an increased charge transfer from the metal to CO causing the CO bond to redshift in frequency.

Reaction studies were conducted on both sets of catalysts. Hydrocarbon conversion reactions which the Somorjai group has studied extensively on single crystals were the initial focus. Ethylene hydrogenation was used as a probe reaction because the kinetics have been measured for this reaction for a number of catalytic materials and the insensitivity of this reaction to surface structure is well known. This reaction is also an indicator of the cleanliness of the Pt surface as the fraction of surface covered by PVP is inactive for olefin hydrogenation. Rates of ethylene hydrogenation were lower on the CI catalyst series than the NE series, by about a factor of five. Hydrogenation rates on the NE catalysts were in good agreement with previously reported single crystal measurements, while the CI samples were an order of magnitude lower in activity. The hydrogenolysis of ethane to methane was studied on both sets of Pt/SBA-15 catalysts. Unlike ethylene hydrogenation, the sensitivity of this reaction to the metal surface structure is well known. In this present investigation, we found that both samples yielded kinetics suggesting structure sensitivity, although the change in rate on the CI sample was only a factor of three primarily due to a limited range of Pt dispersion. Conversely, the rate of ethane hydrogenolysis decreased by two orders of magnitude with particle size on the NE samples and a corresponding increase in the apparent activation energy was measured as the particle size increased. Smaller particles were more active for hydrogenolysis suggesting that coordinatively unsaturated surface atoms prevalent in

small crystallites were more reactive for C-H and C-C bond activation. CO adsorption experiments qualitatively confirm that surface site heterogeneity (*i.e.* surface roughness) increases with decreasing particle size. The most reactive of these unsaturated sites are assumed responsible for ethane decomposition to surface carbon during hydrogenolysis. The degree of surface carbon deposition was structure sensitive, with smaller Pt nanoparticles demonstrating higher carbon coverage after reaction. Larger particles are more selective for methane formation; smaller particles are more active for methane formation and carbon deposition.

The influence of particle size on reaction selectivity was studied using cyclohexene hydrogenation-dehydrogenation in excess hydrogen as a model reaction. It was determined that that the particle size influenced the selectivity to either product; due to multiple heterogeneous catalytic kinetic effects. Namely, the coverage of hydrogen at a constant temperature was particle size dependent which influenced the rate of cyclohexene hydrogenation.   The dehydrogenation pathway is not influenced by hydrogen coverage effects. Concurrently, the apparent activation energy for cyclohexene dehydrogenation increased as the particle size increased suggesting that the coordinatively unsaturated atoms are more active for C-H bond activation, as was shown in the case of ethane hydrogenolysis.   This initial study of reaction selectivity demonstrated that the effect of particle size can be complex but further supporting that control of nanoparticle size can potentially be a design parameter to develop more selective catalysts.

The adsorption of carbon monoxide and ethylene by selective gas adsorption measurements and infrared spectroscopy was studied over a series of Pt/SBA-15 catalysts

with monodisperse particle sizes ranging from 1.7 – 7 nm. The dependence of the band position on atop CO on clean Pt is examined as a function of particle size and compared with literature values on low and high coordination Pt single crystals. The peak position of the CO vibration suggests that it is bonded to sites with average coordination ranging from 7–9 atoms indicating binding on the smaller particles is dominated by CO interactions with steps and with terraces on larger particles. Compared with previous reported spectra of CO adsorption on Pt catalysts, spectra on the Pt/SBA-15 catalyst series demonstrate only one maximum which is associated with a single type of Pt-CO interaction. The peak position for adsorbed CO decreased with increasing temperature due to anharmonic coupling between the C-O stretch and the frustrated parallel translational mode of adsorbed CO. The corresponding temperature dependent CO coverage on clean Pt can be modeled by the Temkin isotherm. Adsorption of ethylene on catalysts at room temperature led to the formation of π-bonded, di-σ bonded ethylene, which either desorb or convert to ethylidyne at higher temperatures. Ethylidyne and π-bonded ethylene were formed in comparable amounts on small Pt particles ($\leq$ 1.7 nm) at room temperature with trace amounts of di-σ bonded ethylene present at room temperature. All three ethylene derived surface species were formed on larger particles ($\geq$ 2.5 nm), although ethylidyne was the major surface species, and upon heating, ethylidyne was the only identifiable surface species. The conversion of ethylene to ethylidyne is facile on larger particles than small particles presumably because the surfaces are terminated by closed packed planes, primarily (111) which are capable of stabilizing ethylidyne because of their 3-fold symmetry. Sequential co-adsorption studies were also followed by diffuse reflectance infrared spectroscopy to determine the

influence of co-adsorption on the prevailing surface intermediates. Ethylene uptake decreased markedly on a CO covered surface, with the largest decrease in the amount of π- and di-σ bonded ethylene; formation of ethylidyne appeared to be less sensitive to the presence of adsorbed carbon monoxide, especially on the larger particles. Very little change in the CO stretching frequency occurred upon adsorption of ethylene on a CO covered surface because only minor amounts of ethylene were adsorbed in this circumstance. The adsorption of ethylene on this surface was severely hindered due to the large and compact high coverage CO unit cell which forms. The adsorption of ethylene on a clean Pt surface leads a relatively open unit cell presumably with maximum coverage of 0.25 because of steric hindrance of the ethylidyne methyl group. The relatively open surface enables the adsorption of smaller molecules such as CO to occur. Adsorption of CO on an ethylidyne covered surface at 298 K resulted in a reduced CO adsorption capacity and the peak position for the linear bond CO redshift by $\sim$30 cm^{-1}, suggesting donation of electron density from adsorbed ethylidyne to carbon monoxide mediated through the metal surface. The close proximity between adsorbed CO and ethylene is supported by proposed mixed unit cells in which the different adsorbates are located in mixed, compact unit cells. The implications poisoning and promotion of co-adsorption on the observed surface chemistry is emphasized.

Kinetics for the CO poisoned hydrogenation of ethylene were measured on the NE catalyst series. The apparent activation energy, ethylene and hydrogen order changed in the presence of low pressure CO (0.2–1 Torr). In the absence of CO at temperatures greater than 340 K and low ethylene partial pressures, ethylene inhibits the reaction by occupying sites suitable for H_2 dissociation and correspondingly the dependence on H_2 is

~1st order. In the presence of CO, the reaction rate is first order in ethylene and ½ order in H$_2$. Kinetic measurements demonstrate that C$_2$H$_4$ dependence is invariant with CO pressures greater than 0.2 Torr, suggesting that the surface is saturated with CO by this pressure. Measured apparent activation energies double for all samples regardless of particle size. This increase is a consequence of an adsorption equilibrium maintained between adsorbed and gas phase CO and not a change in the rate-determining step. Surface species observed by *in-situ* diffuse reflectance spectroscopy during the hydrogenation of ethylene in the presence of CO was linear bound CO whose frequency position was redshifted relative to CO adsorption on a clean surface of the same catalyst, suggesting that ethylene derived species are present on the surface at concentrations lower than detectable by infrared spectroscopy. Inclusion of the CO adsorption-desorption equilibrium to the noncompetitive Horiuti-Polanyi mechanism for ethylene hydrogenation reproduces the experimentally measured kinetics. The hydrogenation of ethylene on clean Pt catalysts is structure insensitive, while a small influence (2× difference in rate) of particle size is observed reaction is poisoned by CO. This study suggests that particle size is not a decisive parameter for the design of CO tolerant hydrocarbon conversion catalysts.

The synthesis of ~9 nm Pt nanoparticles of well-defined shape with the use of silver ions and surface templating polymers in protic solvents was demonstrated. Addition of increasing amounts of AgNO$_3$ to refluxing ethylene glycol followed by slow introduction of H$_2$PtCl$_6$•6H$_2$O lead to the formation of cubes, cuboctahedra and octahedra with shape uniformity greater than eighty percent. The Pt nanoparticles are incorporated into a mesoporous silica matrix by hydrothermal growth and encapsulated of Pt

nanoparticles in aqueous solution. Removal of the surface templating polymer was achieved with thermal oxidation-reduction treatments. Rates for ethylene hydrogenation decreased in accordance with the amount of Ag retained in the Pt nanoparticles after synthesis. It appears that presence of Ag on the surface or in the bulk of the Pt particle has a substantial influence on the hydrogenation of ethylene. Ag reflections were not observed in XRD studies of the shape-controlled particles, suggesting that Ag is present as small clusters on the Pt surface after reduction.

10.2   Recommendations for Future Work

The project has been successful in many areas considering its relative infancy. The project started in fall 2000 prior to my arrival in Berkeley. The initial work was published in a number of manuscripts with all of the work focusing on the synthesis and characterization of Pt and Au nanoparticle catalysts by an acidic pH based encapsulation method [1-4]. Upon my arrival and construction of a combined chemisorption-reactor setup, it was determined that these catalysts had very little catalytic activity regardless of catalyst pretreatment. Alternative approaches to catalyst synthesis resurrected the project and these materials were found active for catalysis. The natural progression of the project requires that we have had less time to concentrate on reactivity studies. At this point, synthetic procedures for size-controlled Pt nanoparticles are optimized and nanoparticle encapsulation has become our standard catalyst synthesis method. This work has been published [5] or submitted for publication [6]. An area of continued research is related to the removal of the PVP coating from supported Pt nanoparticles. While this topic itself constitutes Chapter 8 of this thesis, it will continue to be a critical

area for future research. There is a number of on-going characterization and reactivity studies occurring in the project as these recommendations are being written. A few will be highlighted and commented on. A high surface area reactor setup complete with heat traced lines, syringe pump for delivery of liquid phase reactants and a combined TCD/FID gas chromatograph for analysis of hydrocarbons and light gases has been constructed for the study n-hexane reforming. Preliminary studies have shown that SBA-15 is totally inert for this chemistry at temperatures relevant for Pt catalyzed reforming reactions; Pt catalyzed reaction products are in excess of thirty different species, primarily hydrogenolysis ($< C_6$), dehydrocyclization (C_6H_6), isomerization products (2- and 3- methylpentane) and C_6 unsaturated compounds (2- and 3- hexenes, methylcyclopentenes). Previous studies of n-hexane reforming in our group on a series of Pt single crystals with different surface structure have shown that a number of the primary reforming reactions are structure-sensitive. The catalytic chemistry is very complex, with significant changes in initial and steady state activity due to catalyst deactivation. The influence of particle size on reaction selectivity during n-hexane conversion in hydrogen is an on-going project in our laboratory.

The development of a model supported catalyst based on shape-controlled products is currently underway. Our initial efforts on nanoparticle synthesis have been published previously [6], and our first catalytic results on these materials is discussed in Chapter 9. Characterization of the as-synthesized nanoparticles initially suggested that Ag was entirely removed from the nanoparticle surface. XRD, x-ray energy dispersive (EDX) spectroscopy confirmed no Ag was located on the Pt surface after purification and UV-visible spectroscopy provided evidence for Ag species in solution. Ethylene

hydrogenation on supported catalysts by nanoparticle encapsulation with shape controlled nanoparticles suggested that significant quantities of Ag were located on the octahedra and cuboctahedra particles, which was subsequently confirmed by elemental analyses. The apparent conflict between reference [7] and [8] may be related to an extrinsic parameter, nanoparticle batch size. Large quantities of particles are needed for catalyst synthesis, which prove to be more difficult to purify. Current efforts are related to developing a characterization method for detection of Ag (besides elemental analysis) and the galvanic exchange of surface Ag with Pt complexes. Initially, we believed that these were promising catalytic materials for future studies on the influence of catalyst particle shape on reaction selectivity during the low temperature hydrogenation of α,β unsaturated aldehydes, but extensive work to date has demonstrated that Ag removal from as synthesized particles in challenging. Alternative non-metal routes to shape-controlled particle synthesis are being explored in the laboratory of Professor P. Yang and his colleagues. Polymers which serve not only stabilizers but also structure-directing agents are being explored.

Preliminary work in collaboration with Dr. Heinz Frei of the Physical Biosciences Division of the Lawrence Berkeley National Laboratory on time resolved infrared spectroscopy of ethylene hydrogenation on Pt/SBA-15 catalysts has been started. Time resolved spectroscopy (TRS) on Pt/Al$_2$O$_3$ catalysts has provided evidence for the kinetic relevance of surface ethyl and ethane production [9, 10]. Preliminary results on Pt/SBA-15 demonstrated that rate constant for ethane evolution was the same of the Pt/Al$_2$O$_3$ catalysts [9, 10] but identification of surface ethyl was complicated by absorption by the silica support. Frei and co-workers identified the CH$_2$ wagging mode of a surface ethyl

species which is located at 1200 cm^{-1}. Attempts at increasing the sensitivity in the region of the ethyl absorption band by exchange of a Mercury-Cadmium-Telluride (MCT) detector with an Indium-Antimony (InSb) detector, which is twice as sensitive as the MCT detector in the same mid-IR spectral region. The replacement of the detector was unable to resolve the 1200 cm^{-1} band associated with ethyl. Further applications of TRS on SBA-15 based catalytic materials are currently being configured.

A second project in collaboration with Dr. Heinz was the development of a delivery system of liquid phase reactants for time resolved infrared spectroscopy measurements of cyclohexene hydrogenation/dehydrogenation, the subject of Chapter 8. Two methods for precise and controlled delivery of cyclohexene to a N_2/H_2 gas stream were developed. The first was based on the same pulsed valve system used for delivery of gas. In the case of cyclohexene, it was stored in a calorimeter bomb pressurized by He (85 psi). Delivery was reproducible and transmission studies in an empty reactor suggested that similar amounts were released during each pulse. Preliminary results have shown the existence of adsorbed benzene with no substantial change in cyclohexene absorption bands on a Pt/Al_2O_3 catalyst at 573 K. The second method developed had the advantage of improving the time resolution of the experiment from the ms timescale to microseconds. The method is a "pump-release" technique, in which a porous (5 µm pores) stainless steel tube with a quartz window filled with amorphous carbon (Norit SX-1) was saturated with cyclohexene. Subsequently, the stainless steel tube was pumped by near infrared light (1064 nm) from a nanosecond Nd:YAG laser through the quartz (transparent to near IR photons). The stainless steel tube quartz window assembly is shown in Figure 1.
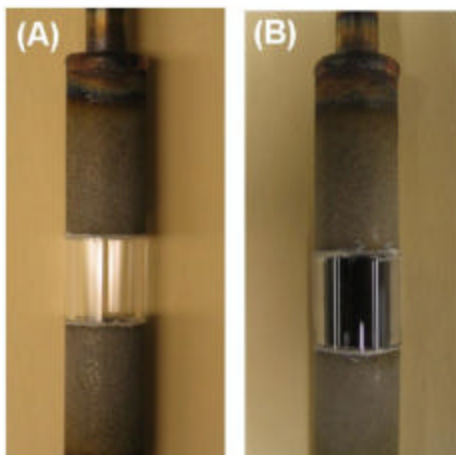
Figure 10.1. (A) Empty porous stainless steel tube with 1" quartz window section. (B) Porous stainless steel tube filled with ~1.5 g of amorphous carbon.

We are currently collaborating with Professor Heinz Frei his postdoctoral associate, Dr. Walter Wasylenko on the poisoning of ethylene hydrogenation by CO using the pulses of CO during the steady state ethylene hydrogenation on a series of Pt/Al$_2$O$_3$ catalysts. The results of pulsed CO TRS experiments should suggest whether the poisoning mechanism involves simple site blocking and a decreased surface concentration of the reactive intermediate, ethyl. TRS experiments allow direct observation of the lifetime of the kinetically relevant surface intermediate, which is 1/TOF, the inverse of the turnover frequency. Therefore, this measured lifetime of the surface ethyl should be identical to the lifetime on the clean surface. TRS requires no prior knowledge of the number of surface sites (usually probed by chemisorption) and therefore will be a true measure of ethylene hydrogenation in the presence of CO.

There are a number of other areas this project should focus on. High resolution electron microscopy characterization of nanoparticles on supports is necessary to understand the evolution of particle size when adsorbed or tethered to a solid surface

from solution. Most likely the adhesion energy associated with the nanoparticle solid

support interaction will perturb the particle shape [11]. Initially, we attempted to support

Pt nanoparticles on nm sized SiO_2 spheres in order to study the supported nanoparticles

by electron microscopy. We searched for a synthetic method which would enable us to

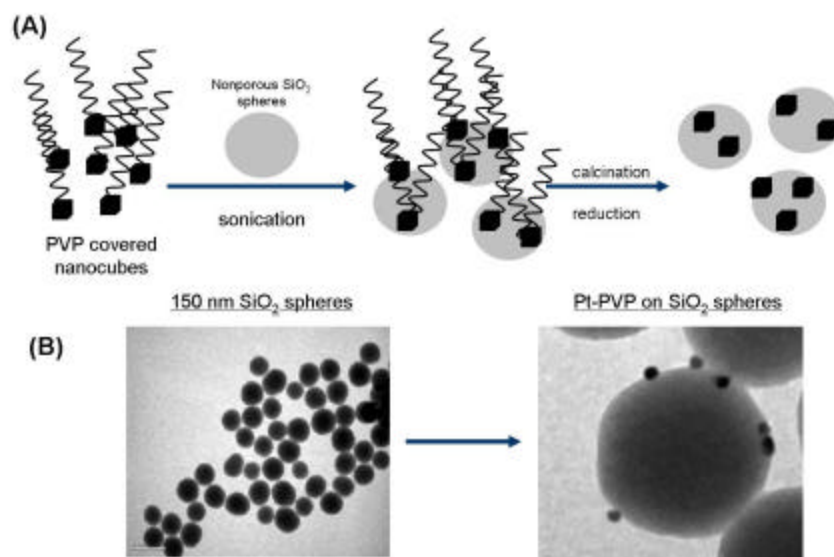place nanoparticles on the surface of ~ 150 nm spheres (Figure 2).

Figure 10.2. (A) Schematic representation of Pt nanoparticle attachment to 150 nm SiO_2 spheres. (B) Electron microscopy image of 150 nm SiO_2 spheres and Pt/SiO_2 spheres after sonication.

The above figure demonstrates that our initial results were unsatisfactory, due most likely

to similar charge on the surfaces both nanoparticles and silica sphere. The dynamics of

nanoparticle adsorption onto solid surfaces is critical if the influence of heterogeneous

catalysis on particle shape is to be studied. Numerous studies by El-Sayed have shown

that the most reactive atoms on unsupported nanoparticles leach from the particle while

in solution under catalytic conditions [12]. It would be interesting to study if there is a

corresponding behavior in gas-phase catalyzed reactions.

A third active area of research related to catalysis on Pt nanoparticles started in the Somorjai laboratory has been sum frequency generation surface vibrational spectroscopy studies of adsorption and reaction on Langmuir-Blodgett (LB) films of 9 nm Pt cubes whose preparation have been previously described [7] (Figure 3).
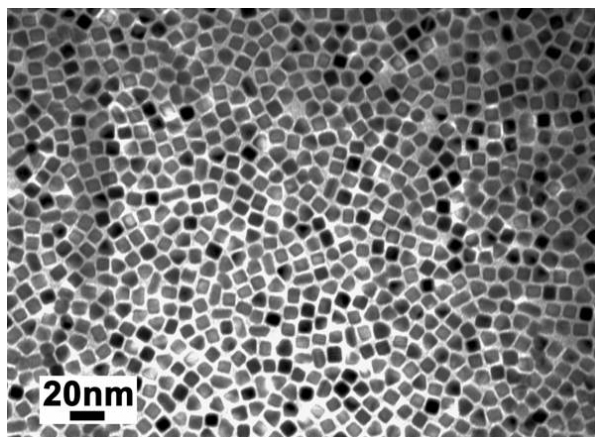

Figure 10.3. Langmuir-Blodgett (LB) film of 7 nm Pt cubes used for SFG studies of carbon monoxide and ethylene adsorption.

The synthesis of these cubes as well as their catalysis when supported in SBA-15 has been discussed in Chapter 9 and accepted for publication [8]. Initial results of this study have included a study of PVP removal and the influence of carbon monoxide adsorption on the restructuring of PVP. The adsorption and oxidation of carbon monoxide on clean Pt has been investigated. An example of CO adsorption on 9 nm Pt cubes and its subsequent oxidation as a function of temperature is shown in Figure 4. Currently, two manuscripts [13, 14] are being written based on our initial findings of CO and ethylene adsorption to clean LB films of 7 nm Pt particles. Future work will consist of the installation of gas chromatograph for continuous analysis of reaction progress during the oxidation of methanol over 7 nm Pt cubes.
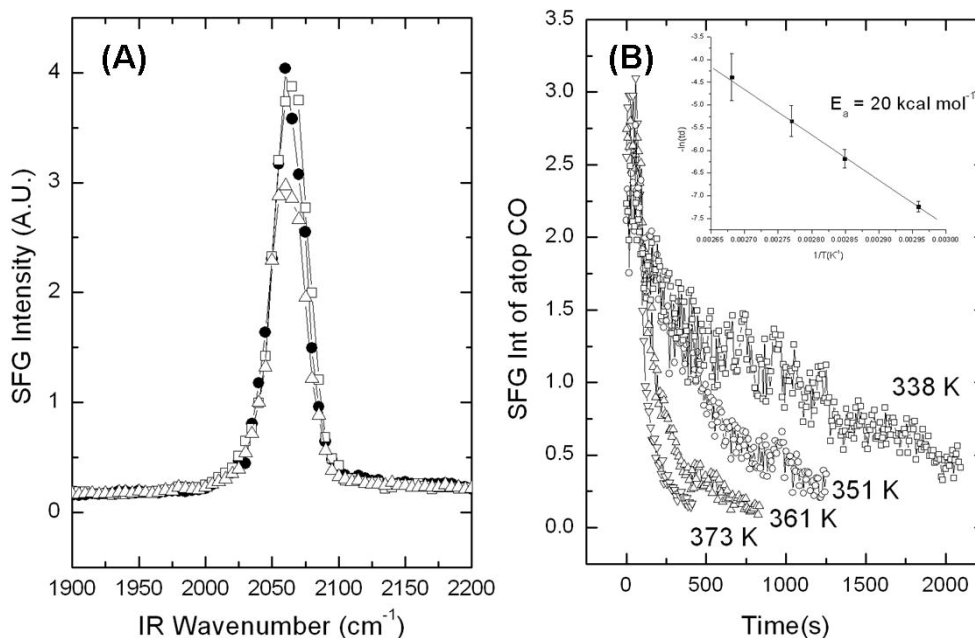
Figure 10.4. (A) SFG spectra collected in *ssp* polarization at sapphire/nanoparticle interface: 35 Torr of CO (?), in flowing helium after five minutes (?), and after < 1 mtorr vacuum for 3 h (?). (B) CO oxidation kinetics at stated temperatures in flowing oxygen. Inset is the measured apparent activation energy for CO oxidation.

Recently, apparent activation energies for CO oxidation on the Pt LB films measured by gas chromatography were in excellent agreement with the activation energy measured by SFG.

10.3   References and Notes

1.   Z. Kónya, V. F. Puntes, I. Kiricsi, J. Zhu, A. P. Alivisatos, G. A. Somorjai, *Catal. Lett*. 81 (2002) 137.

2.   Z. Kónya, V. F. Puntes, I. Kiricsi, J. Zhu, A. P. Alivisatos, G. A. Somorjai, *Nano. Lett*. 2 (2002) 907.

3.   Z. Kónya, V. F. Puntes, I. Kiricsi, J. Zhu, J. W. Ager III, M. K. Ko, H. Frei, A. P. Alivisatos, G. A. Somorjai, *Chem. Mater*. 15 (2003) 1242.

4.   J. Zhu, Z. Kónya, V. F. Puntes, I. Kirisci, C. X. Miao, J. W. Ager III, A. P. Alivisatos, G. A. Somorjai, *Langmuir* 19 (2003) 4396.

5.   R. M. Rioux, H. Song, J. D. Hoefelmeyer, P. Yang, G. A. Somorjai, *J. Phys. Chem*. B 109 (2005) 2192.

6.   H. Song, R. M. Rioux, R. Komor, J. D. Hoefelmeyer, K. Niesz, M. Grass, P. Yang, G. A. Somorjai, Submitted to *J. Am. Chem. Soc* on 10.28.05.

7.   H. Song, F. Kim, S. Connor, G. A. Somorjai, *J. Phys. Chem. B* 109 (2005) 188.

8.   R. M. Rioux, H. Song, S. Habas, M. Grass, K. Niesz, J. D. Hoefelmeyer, P. Yang and G. A. Somorjai, Accepted in *Top. Catal*. on 12.10.05

9.   M. K. Ko, H. Frei, *J. Phys. Chem. B* 108 (2004) 1805.

10.   W. Wasylenko, H. Frei, *J. Phys. Chem. B* 109 (2005) 16873.

11.   P. L. Hansen, J. B. Wagner, S. Helveg, J. R. Rostrup-Nielsen, B. S. Clausen, H. Topsøe, *Science* 295 (2002) 2053.

12.   (a) R. Narayanan, M. A. El-Sayed, *J. Am. Chem. Soc*. 126 (2004) 7194. (b) R. Narayanan, M. A. El-Sayed, *Langmuir* 21 (2005) 2027.

13.   S. J. Kweskin, S. E. Habas, R. M. Rioux, K. Komvopoulos, P. Yang, and G. A. Somorjai. In preparation (2005).

14.   S. J. Kweskin, S. E. Habas, R. M. Rioux, K. Komvopoulos, P. Yang, and G. A. Somorjai. In preparation (2005).